R P A T
A S D
R T

Gary Melady

School of Physics

College of Engineering, Mathematical and Physical Sciences

University College Dublin

Submitted in fulfilment of the requirements

for the degree of Doctor of Philosophy

Head of Department:

Prof. L. Hanlon

Supervisor:

Prof. L. Hanlon

December 2, 2009

Contents

List of Figures

List of Tables

Abstract

Gamma-ray bursts (GRBs) are intense eruptions of high-energy γ-radiation and are the most luminous events observed in the Universe. Ranging in duration from milliseconds to hundreds of seconds, they have isotropic energies of $\sim 10^{53}$ erg. They are thought to be produced by the collapse of a stellar object into a compact remnant accompanied by a rotating accretion disk, with radiation emitted by two anti-parallel collimated jets of material.

The unpredictable nature of GRBs precludes the scheduling of observations and demands automated responses on the shortest possible time-scales. Robotic optical telescopes are particularly well suited to the study of the optical afterglows of these events. Small (< 1 m) telescopes are sensitive enough to detect the optical emission in many cases, particularly since they can carry out observations at very early times when an optical counterpart will be at its brightest. Presented in this thesis is the development, installation and operation of the Watcher system. Watcher is a 40 cm robotic optical telescope dedicated to GRB follow-up observations. The system has been operating fully robotically at Boyden Observatory in South Africa since March 2006, and has carried out extensive observations in response to GRB alerts generated by the *Swift* satellite and other missions.

In order to contribute to the highly competitive field of GRB research it is necessary to have a streamlined, rapid and efficient analysis framework for robotic telescope data. This thesis also presents the development of such a framework for the Watcher project: The *quick* Software Analysis Suite. Based primarily on IRAF, the *quick* suite is a custom built reduction and analysis pipeline. It includes functions for performing photometry,

calculating signal/noise ratios and querying astronomical catalogues for the automatic selection of suitable reference stars.

A summary of the GRB follow-up observations that have been performed to date by Watcher is also presented, including GRB 060526, GRB 060904b and GRB 080905b. Finally, the unusual case of SWIFT J195509 + 261406 is described in detail. Initially appearing to be a standard cosmic GRB, more than 40 flaring episodes were detected from the source in the optical band over a time span of three days, and a faint infrared flare 11 days later, after which the source returned to quiescence. Radio observations confirmed a Galactic nature for the source and established a lower distance limit of ~3.7 kpc. It is suggested that the source could be an isolated magnetar whose bursting activity has been detected at optical wavelengths, and for which the long-term X-ray emission is short-lived. If this is the case, a new manifestation of magnetar activity has been recorded and it can be considered that SWIFT J195509 + 261406 is a link between the 'persistent' Soft γ-ray Repeaters (SGRs) / Anomalous X-ray Pulsars (AXPs) and dim isolated neutron stars.

Chapter 1

Introduction to Gamma-Ray Bursts

1.1 Introduction

Gamma-ray bursts (GRBs) were discovered accidentally in the late 1960's by the US Vela satellites. These satellites were designed to monitor potential violations of the US-Soviet nuclear test-ban treaty but instead detected brief flashes of highly energetic γ-ray radiation (Klebesadel et al., 1973). The burst durations ranged from milliseconds to hundreds of seconds and the emission extended up to energies of $\sim$1 MeV. The first GRB lightcurve detected by Vela 4 is shown in Fig. 1.1.

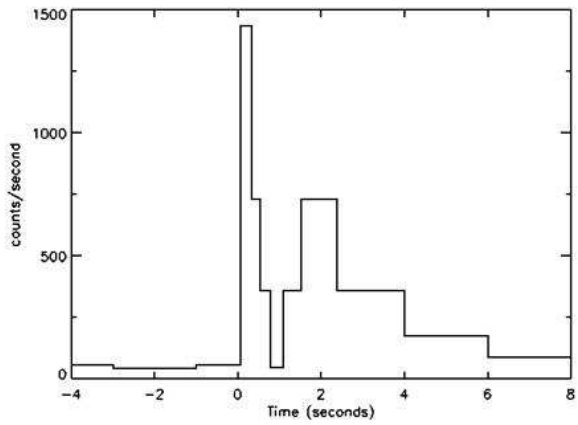

Figure 1.1: GRB 670702, the first gamma-ray burst lightcurve, detected by the Vela 4 satellite on July 2 1967. *Credit: Klebesadel et al. (1973).*

The relatively crude imaging and localisation capabilities of γ-ray instruments at the time made progress towards the understanding of GRBs difficult. As additional Vela satellites were launched with better instruments, the inexplicable detections of γ-ray bursts continued. By analysing the different arrival times of the bursts detected by different satellites, it was possible to determine rough estimates for the sky positions of certain bursts and definitively rule out a terrestrial or solar origin. The intensity of the photon fluxes observed suggested a nearby origin and early theories proposed a link to neutron stars within our own Galaxy (e.g. Higdon and Lingenfelter, 1990). In 1991 however, NASA launched the *Compton Gamma Ray Observatory* (CGRO) with a dedicated GRB instrument on board called BATSE (the Burst Alert And Transient Source Experiment). Over its 9 year lifespan BATSE detected 2704 GRBs (Fishman and Meegan, 1995).

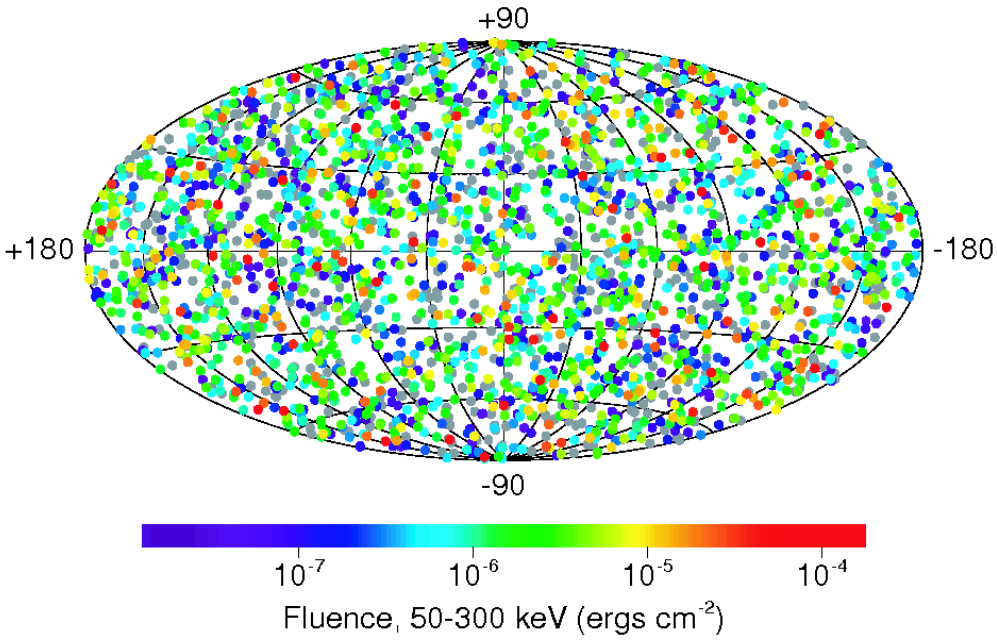

Figure 1.2: The spatial distribution in Galactic coordinates of the 2704 bursts observed by BATSE, which shows the isotropic nature of the GRB distribution. *Credit: http://www.batse.msfc.nasa.gov/batse/grb/skymap/*

The positions of the bursts detected by BATSE shows an isotropic distribution over the entire sky (Fig. 1.2), rather than clustered around a particular direction, for example along the Galactic disk (Meegan et al., 1992). This suggested a cosmological origin for

GRBs, rather than a Galactic one. The idea was strengthened by the cumulative peak flux distribution of BATSE GRBs (Fig. 1.3). The power-law slope of $-3/2$ at high fluxes in the $log(N) - log(P)$ plot (where N is the number of bursts and P is the peak flux) indicates a homogeneous distribution in a Euclidean space model. The slope becomes shallower at lower fluxes, implying a relative under abundance of faint sources detected.

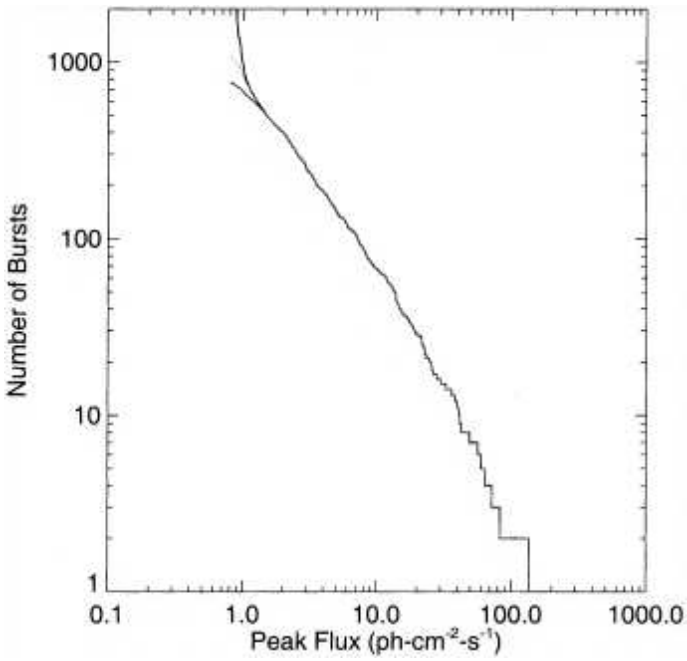

Figure 1.3: The peak flux distribution of the BATSE GRBs, showing the cumulative distribution of the flux at the peak of the light curve versus the log of the number of bursts. The $-3/2$ slope at high γ-ray peak fluxes indicates a uniformly distributed population. The slope of the distribution is shallower at lower fluxes, indicating a relative under abundance of faint bursts. *Credit: Paciesas et al. (1999).*

Predictions were made regarding the possibility of afterglow counterparts at longer wavelengths following the prompt emission (e.g. Paczynski and Rhoads, 1993) caused as the ejected γ-ray producing material interacts with the surrounding environment. However, ground-based multi-wavelength follow-up observations were hampered by the poor localisation capabilities of γ-ray instruments and long time delays before these localisations were made available. GRB localisations were greatly improved with the launch of the Italian-Dutch satellite BeppoSAX. Launched in 1997, BeppoSAX detected the first X-ray afterglow (Costa et al., 1997) about 8 hours after the burst onset of GRB 970228.

Its more accurate and rapid localisation also allowed for ground-based follow-up observations to be made, which resulted in the first detection of a GRB optical afterglow (van Paradijs et al., 1997). Optical spectroscopy performed on the afterglow of a subsequent burst, GRB 970508 (Frail et al., 1997), provided a redshift of $z = 0.835$, thus confirming the cosmological origin of GRBs for the first time. Distance measurements allowed the energy output of the bursts to be constrained, with a typical burst having an isotropic energy of $\sim 10^{53}$ erg. More recent theories and observations suggest that GRB emission is not isotropic but rather in the form of beamed jets (with an opening angle of $1/\Gamma$, where Γ is the Lorentz factor of the outflow), which reduces the energy requirement to $\sim 10^{51}$ erg (e.g. Bloom et al., 2003).

1.2 GRB Classification

To further understand the nature of GRBs and their progenitors, efforts were made to classify bursts. A study of the large BATSE catalogue revealed a bimodal distribution based on the prompt emission duration (Kouveliotou et al., 1993). This division is based on the T_{90} of the burst, the time over which 90% of the γ-rays are detected. Fig. 1.4 shows a dip at ~ 2 s, which strongly suggests two distinct groups, short (< 2 s) and long (>2 s) GRBs. This ~ 2 s minimum is also apparent in spectral hardness vs. duration studies, where the hardness is defined as a ratio of the counts in the detectors' high energy band to the counts in its low energy band. Fig. 1.5 (Qin et al., 2000) shows that short GRBs tend to be spectrally harder, i.e. have a higher proportion of high-energy photons, while long GRBs tend to be somewhat spectrally softer.

Since the two peaks of the distribution can be modelled as two overlapping log-normal distributions (Quilligan et al., 2002), classification into 'short' and 'long' bursts may not be as straightforward as $T_{90} < 2$ s or $T_{90} > 2$ s. Donaghy et al. (2006) states that the dividing time should be at ~ 5 s and several papers propose a third sub-division of GRBs with intermediate duration (Horváth et al., 2006). To add to this, a significant number of

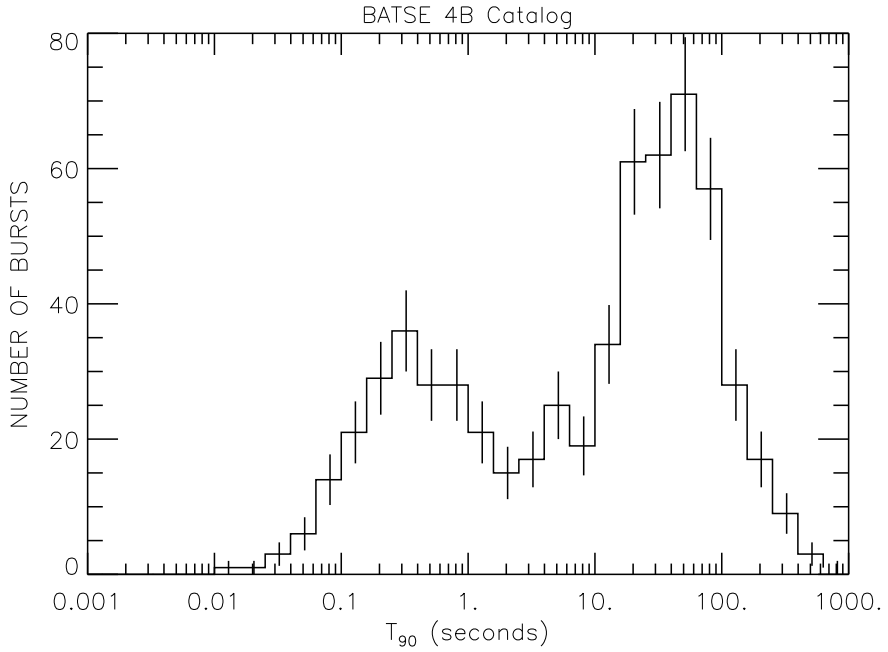

Figure 1.4: T_{90} duration distribution of the GRBs in the BATSE 4B Catalogue. The distribution is bimodal and consists of the two overlapping lognormal distributions of short ($T_{90} < 2$ s) and long ($T_{90} > 2$ s) GRBs. *Credit: Paciesas et al. (1999).*

short GRBs may be incorrectly classified. The GRBs in question have extended, spectrally soft emission which can last for tens to hundreds of seconds after the initial short pulse. About 1/3 of the BATSE short bursts exhibit this behaviour (Norris and Bonnell, 2006). Other indicators that may be used to aid in GRB classification, i.e. short-hard or long-soft, include the spectral lag, the host galaxy type and the detection or non-detection of an accompanying supernova (Donaghy et al., 2006).

1.2.1 Temporal Properties

GRB lightcurves are highly variable and complex in nature, displaying rapid changes in flux over time-scales as short as milliseconds (McBreen et al., 2001; Quilligan et al., 2002). Fig. 1.6 shows a sample of long-duration GRB lightcurves from the BATSE catalogue illustrating some of the possible variations in temporal structure. While the majority of lightcurves are highly variable, many are smooth and exhibit a rapid rise and slower decay, known as a Fast Rise Exponential Decay (FRED). Some rare cases involve a pre-

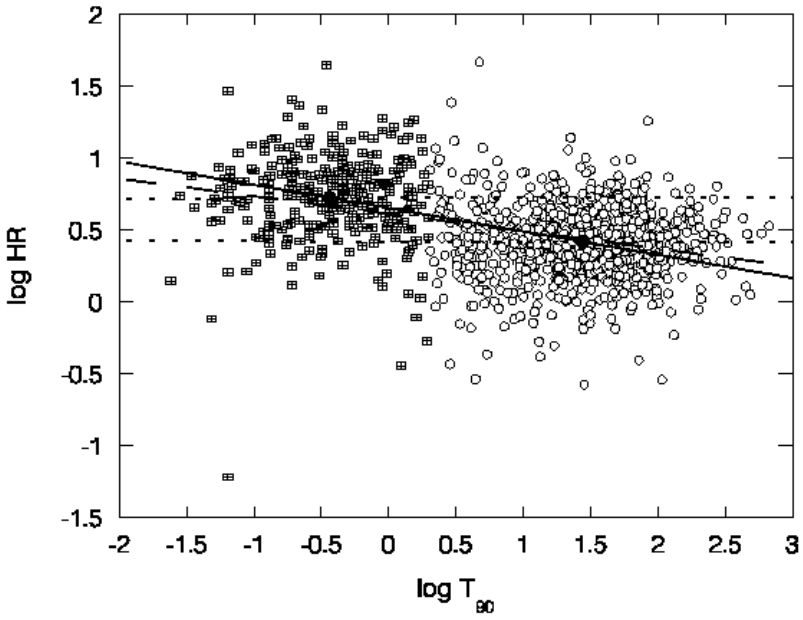

Figure 1.5: BATSE hardness ratio (HR)–T_{90} correlation showing the two distinct classes of GRBs. Short GRBs are shown as squares and tend to be spectrally harder. Long GRBs are shown as circles are in general spectrally softer. The dotted lines are the regression lines for the short and long GRBs and the solid line is the regression line for the whole sample. *Credit: Qin et al. (2000).*

cursor pulse followed by a quiescent stage, that may last from tens to hundreds of seconds, followed by an apparent restart of the central engine with subsequent emission.

1.2.2 Spectral Properties

Prompt emission spectra for both long and short bursts tend to be relatively simple, non-thermal spectra spanning a broad energy range. Weak GRBs are best fit by a single power-law, due to the limited statistics, given by:

$$N(E) = AE^{\alpha} \tag{1.1}$$

where $N(E)$ is the photon flux (photons $\mathrm{cm}^{-2}\,\mathrm{s}^{-1}$), α is the photon index and A is the amplitude (photons $\mathrm{cm}^{-2}\,\mathrm{s}^{-1}\,\mathrm{keV}^{-1}$). When statistics are good enough, GRB spectra can be well described by the Band model (Band et al., 1993), an empirical model consisting

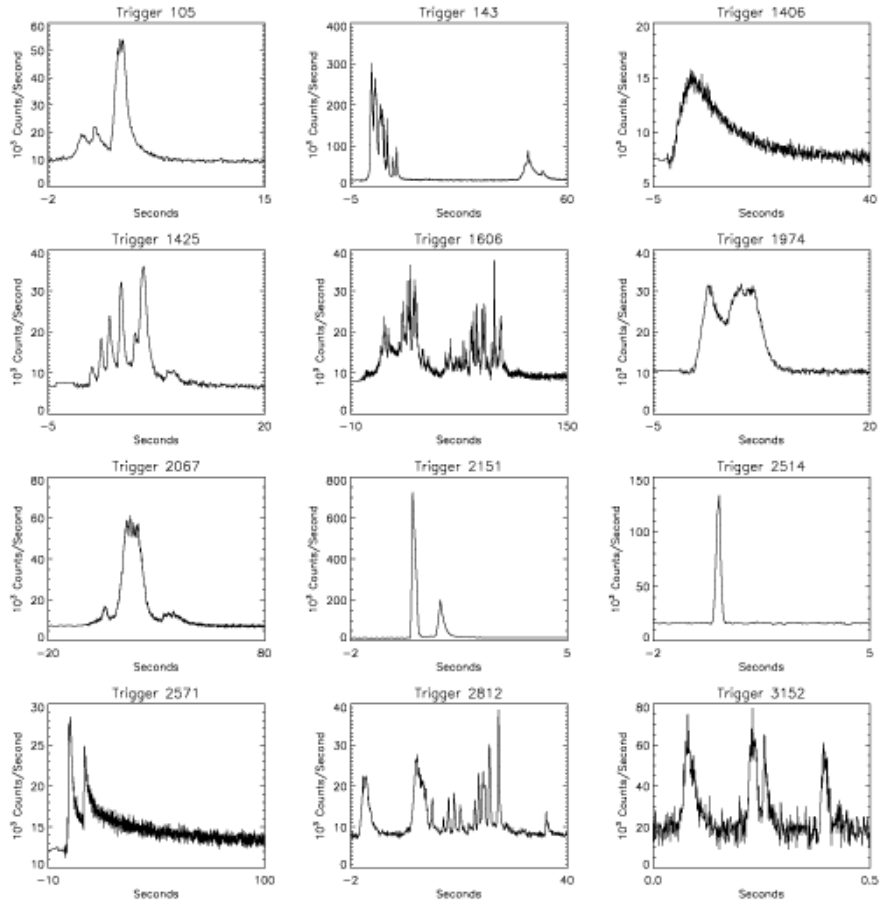

Figure 1.6: Sample lightcurves of long-duration GRBs detected by BATSE, showing the diversity in temporal structure observed in bursts. *Credit: http://heasarc.nasa.gov)*.

of two smoothly connected power-laws of the form:

$$N(E) = \begin{cases} A\left(\dfrac{E}{100\,\mathrm{keV}}\right)^{\alpha} \exp\left(\dfrac{E}{E_0}\right), (\alpha-\beta)\,E_0 \geq E \\ A\left[\dfrac{(\alpha-\beta)E_0}{100\,\mathrm{keV}}\right]^{\alpha-\beta} \exp(\beta-\alpha)\left(\dfrac{E}{100\,\mathrm{keV}}\right)^{\beta}, (\alpha-\beta)\,E_0 < E \end{cases} \tag{1.2}$$

where α is the low energy photon index, β is the high energy photon index and E_0 is the break energy. Working from a sample of 156 bright BATSE bursts, Preece et al. (2000) determined typical values for the low-energy power-law index to be around -1 and the high-energy power-law index to be around -2.2. The typical E_0 value is distributed lognormally within a narrow range around ~240 keV (Fig. 1.7).

The peak energy (E_P) is used as a measure of a burst's spectral hardness. It is the energy of the peak of the burst's power output and can be represented by plotting the νF_ν

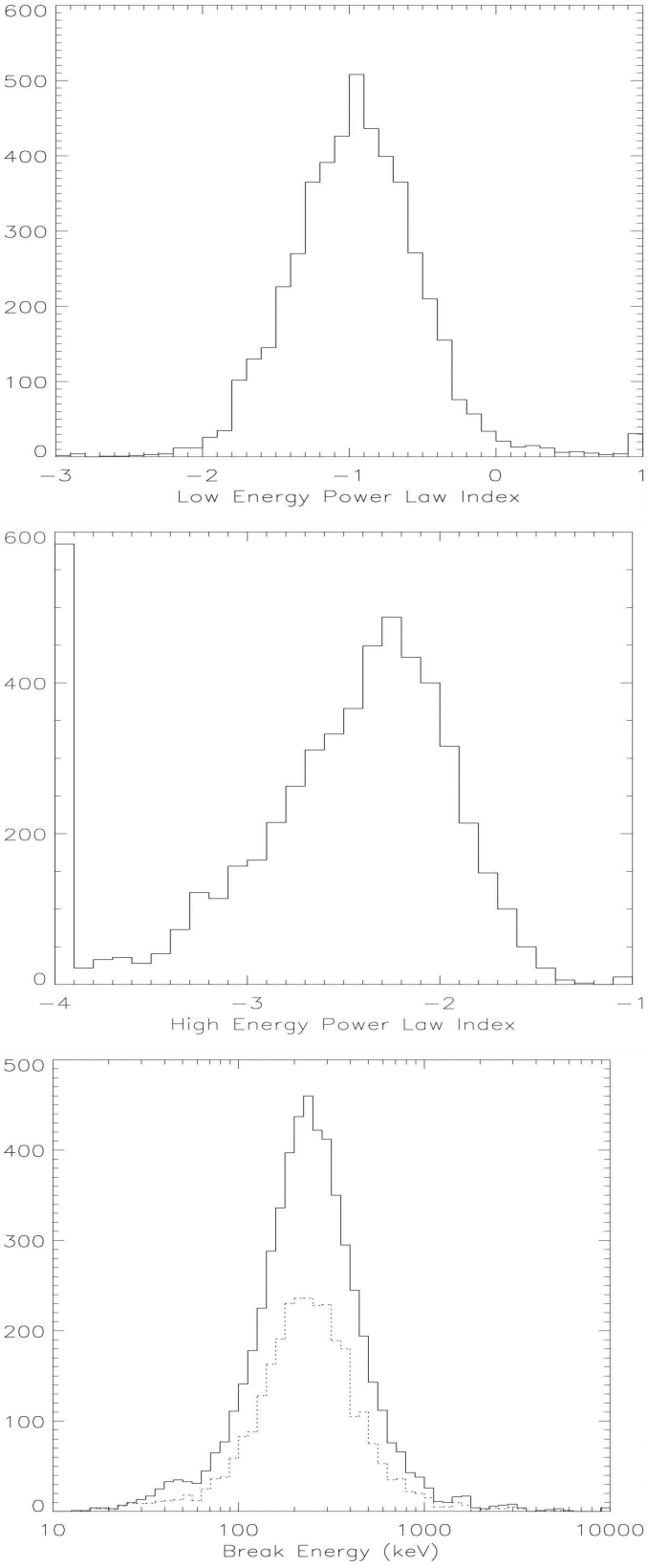

Figure 1.7: Distributions of the spectral parameters for the low-energy power-law index α, the high-energy power-law index β and the break energy E_0 obtained by using the Band model on spectral fits of the brightest 156 BATSE GRBs. *Credit: Preece et al. (2000).*

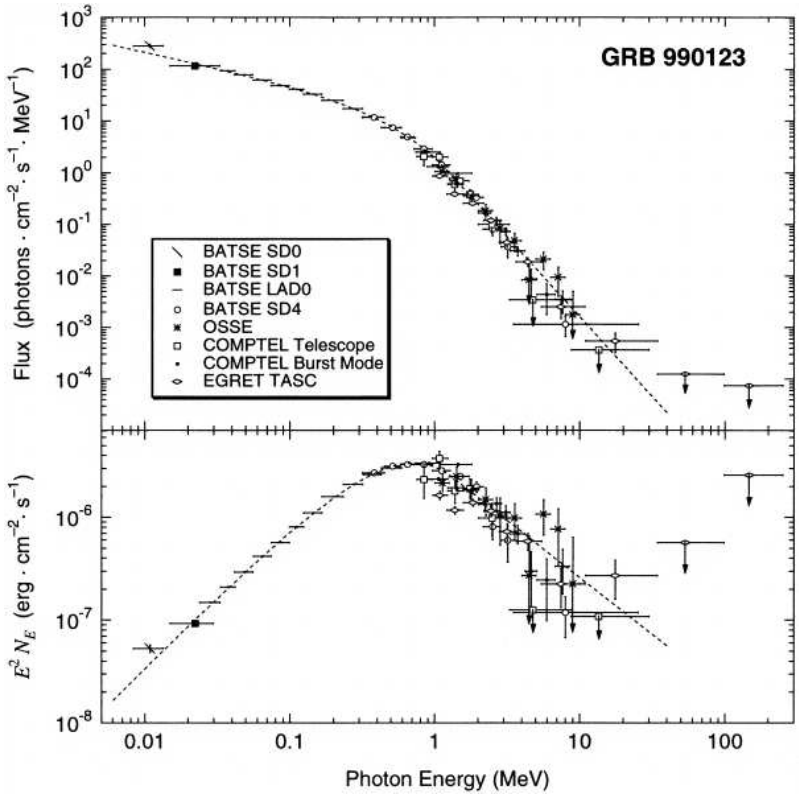

Figure 1.8: The differential photon spectrum and νF_ν spectrum of the prompt emission of GRB 990123 detected by BATSE, OSSE, COMPTEL and EGRET. *Credit: Briggs et al. (1999).*

spectrum (or $E^2 N(E)$), where ν is the photon energy and F_ν is the specific energy flux. E_P is related to the break energy E_0 by $E_P = (2 + \alpha)E_0$ when $\beta < -2$. This spectral shape is valid both for integrated emission over the whole burst duration and for the emission during shorter segments of the burst. Fig. 1.8 shows a photon spectrum and νF_ν spectrum of the bright burst GRB 990123. Long GRBs tend to evolve from hard to soft over time, with the prompt emission (the first ~2 s) of a long burst being of a similar hardness to that of a short GRB.

A type of X-ray transient event called an X-Ray Flash (XRF) was discovered by Heise et al. (2001) to have very similar observational characteristics to GRBs. The XRFs have a larger X-ray fluence than γ-ray fluence thus they have a lower νF_ν peak energy ($E_P \leq$ 30 keV). There is also an intermediate group of bursts with E_P values between XRFs and GRBs called X-Ray Rich GRBs (XRRs). There is a continuum of spectral properties

and similar duration distributions (Sakamoto et al., 2005) across these three groups of transients, suggesting a similar origin. The low E_P values may arise due to an intrinsic property of the source e.g. an under-powered central engine. Another possible explanation for XRFs is that they are 'typical' GRBs at very high redshifts. This possibility has been ruled out however, by confirming the redshifts of a number of XRFs. An alternative hypothesis is that XRFs / XRRs are typical GRBs, but are being observed at an angle off-axis to the beamed jet (D'Alessio et al., 2006).

Extremely high energy emission has been seen from some GRBs, including the detection of an 18 GeV photon by the EGRET instrument on-board CGRO (Dingus, 2003). Tentative evidence for TeV emission has been reported by ground-based very high energy air-shower telescopes in the cases of GRB 970417a by MILAGRITO (Atkins et al., 2003) and GRB 971110 by the GRAND array (Poirier et al., 2003). The processes whereby such high energy emission can be produced are still poorly understood and the *Fermi* satellite, with its advanced high-energy detectors, will allow GRB high energy emission to be studied in much greater detail.

1.3 Empirical Correlations

Due to increased ground-based spectroscopic follow-up measurements, GRBs with robust redshifts are increasing in number, e.g. GRB 090423 with $z = 8.2$, allowing astronomers to potentially use GRBs for cosmological study. It was initially thought that GRBs could not be used as standard candles since the measured isotropic energies for typical long bursts range from $\sim 10^{50}$ to $\sim 10^{54}$ erg. Frail et al. (2001) find that, if the beaming effect is taken into account, the corrected energies cluster around a standard energy of $\sim 10^{51}$ erg. In an attempt to ascertain distance estimates for bursts of unknown redshift, a number of correlations have been proposed based on the observed properties of some of the events with known redshifts.

The Lag-Luminosity Relation The spectral lag is the time delay between the arrival of high-energy and low-energy γ-ray photon emission and is a common feature of most GRBs (e.g. Norris et al. (2000); McBreen et al. (2006); Hakkila et al. (2007)). It is a natural consequence of the hard to soft spectral evolution observed in GRBs (Kocevski and Liang, 2003). The spectral lag of a burst can be measured by cross-correlation of the lightcurves in the low and high energy channels of a detector. The peak of the cross-correlation function then corresponds to the spectral lag of the GRB. Norris et al. (2000) reported an anti-correlation between the spectral lag and the isotropic peak luminosity of GRBs, based on a limited sample of 6 long-duration GRBs detected by BATSE and BeppoSAX. This implies that bursts with long lags are intrinsically weaker than short-lag bursts and allows the correlation to be used, in principle, as a distance indicator for long GRBs. Short bursts, however, are inconsistent with the correlation and tend to have exclusively very small or negligible lags (e.g. Norris and Bonnell (2006); Yi et al. (2006)). On this basis, spectral lag has been suggested as one of the indicators to determine whether a burst is long or short (Donaghy et al., 2006).

The Amati Relation A correlation between E_P, the peak energy in the νF_ν spectrum measured in the source frame, and E_{iso}, the isotropic energy emitted in γ-rays was identified by Amati et al. (2002). Originally based on a sample of 12 GRBs detected by BeppoSAX, the relation was subsequently extended to GRBs detected by HETE-2 (Lamb et al., 2004; Sakamoto et al., 2006). The HETE-2 detections also included a number of XRFs, providing further evidence of a link between XRFs and GRBs. Short GRBs are shown to be inconsistent with the relation (Amati, 2006), providing another method for distinguishing between long and short bursts.

The Ghirlanda Relation Evidence that GRB emission takes the form of a collimated, beamed jet, rather than isotropic emission, has been provided by achromatic temporal breaks in the afterglow lightcurve. A correlation has been found between the luminosity of the GRB and the time of the afterglow jet break, with more luminous GRBs having earlier

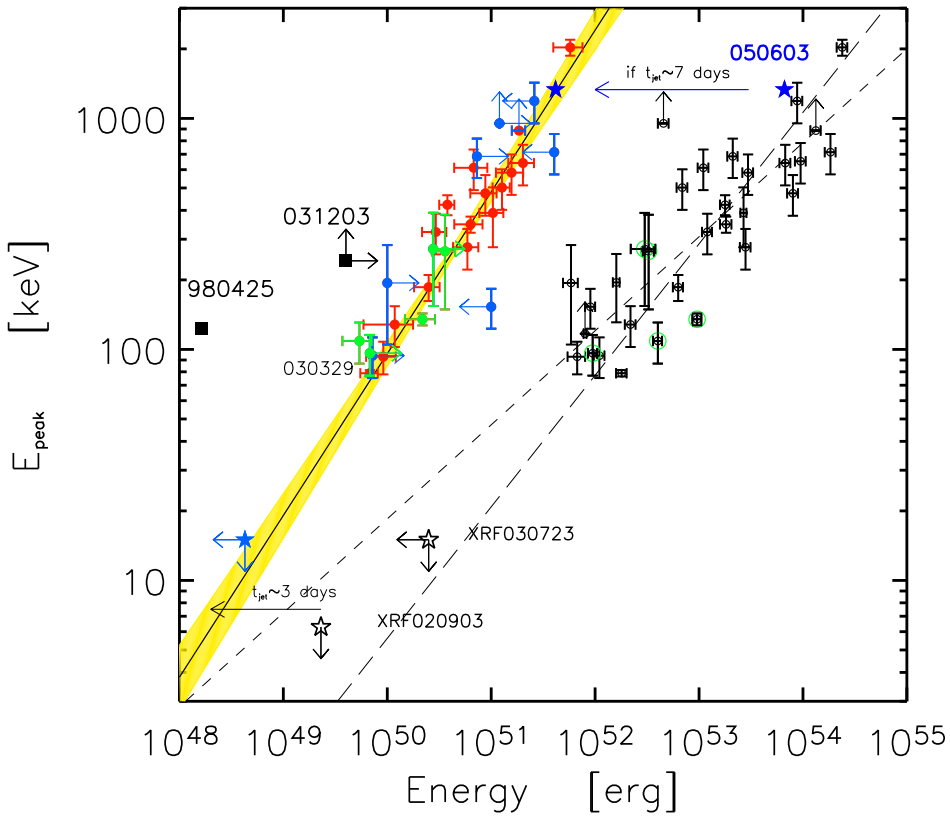

Figure 1.9: The Amati relation (black symbols) shows the correlation between E_P and the equivalent isotropic energy, E_{iso}. The Ghirlanda relation (red, green and blue symbols) shows the correlation between E_P and the collimation-corrected energy, E_γ. *Credit: http://www.brera.inaf.it*

jet break times and therefore smaller jet opening angles (Frail et al., 2001; Panaitescu and Kumar, 2001). A modification of the Amati relation, correcting for this collimation effect, was proposed by Ghirlanda et al. (2004). It provides a better correlation between E_P and the collimation-corrected energy emitted in γ-rays, E_γ (Fig. 1.9).

1.4 Progenitors

Any model to describe the central engine of a GRB clearly must take the observed properties into account. Variability of the prompt emission can be of a time scale as short as 1 ms, which requires a compact object (see § 2.1.2). The typical duration of a GRB is

much longer than the variability time scale, suggesting prolonged central engine activity which may be explained by an accretion mechanism. The central engine must be capable of producing a collimated, relativistic outflow in the form of a jet (see § 2.1.1) and must also be able to produce the huge amount of γ-ray energy observed ($\sim 10^{51}$ erg). This energy is comparable to the binding energy of a compact object.

The only known objects capable of supplying such a large release of energy in such a short time-scale are compact objects, such as neutron stars or black holes, surrounded by a massive accretion disk ($\sim 0.1\,M_{\odot}$). The accretion disk can form from the remnant stellar material during the formation of the compact object itself and can account for the prolonged central engine activity and variability in the lightcurves.

Energy from the compact-object/accretion-disk system is converted into a relativistic jet. This energy is provided either by the binding energy of the torus or the rotational energy of the compact object itself. Usov (1992) suggests an alternative method of energy extraction to the accretion method, involving a Poynting flux dominated relativistic flow provided by the rotational and magnetic energy of a newborn neutron star. The temperature of accreted matter increases before falling into a black hole and energy may be extracted from the system in the form of neutrinos. The baryon density at the poles of the rotating compact object is reduced and neutrinos from opposite sides of the accretion disk will be likely to annihilate here. This process produces $e^{\pm}$ pairs in the jet and helps to collimate the outflow (Fig. 1.10; MacFadyen and Woosley (1999)).

An alternative method of energy extraction is described by the Blandford-Znajek mechanism (Blandford and Znajek, 1977), which describes how torque is applied to the accretion disk by magnetic field lines threaded throughout the black hole. The torque is in the opposite direction to the rotation of the black hole and can cause Poynting-dominated jets to be ejected at the poles.

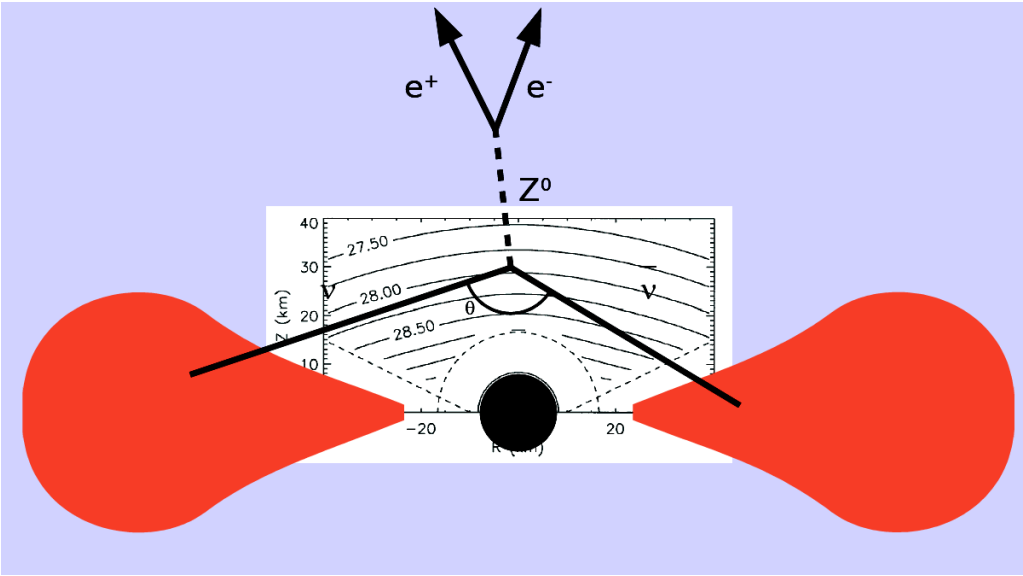

Figure 1.10: Neutrinos from opposite sides of the accretion disk annihilate over the poles of a compact object creating an $e^{\pm}$ pair. *Credit: http://www.mpa-garching.mpg.de/lectures/ADSEM/WS0304_Kretschmer.pdf*

1.4.1 Collapsars

The leading model for the formation of long GRBs is the collapsar model. It involves the collapse of the iron core of a rapidly rotating massive star ($\geq 30\,M_{\odot}$). The core collapse produces a black hole of ~2-3 $M_{\odot}$ and the remaining stellar matter forms an accretion disk of ~0.1 $M_{\odot}$, formed by the angular momentum of the star (Woosley, 1993). The disk is formed along the rotational axis of the black hole, reducing the density at the rotational poles. This facilitates the formation of jets, which are further collimated by their passage through the stellar mantle. As the jet emerges through the stellar surface it has a high Lorentz factor. Internal and external shocks subsequently produce the GRB and afterglow respectively (e.g. Mészáros and Rees, 1993) after the jet has traversed several stellar radii. The Lorentz factor of the jet can be highly variable, most likely due to instabilities in the accretion disk which causes a variable accretion rate.

The collapsar model has a significant amount of observational evidence to support it. There is strong evidence of a link between long GRBs and massive stars. The discovery of GRB 030329 and its associated supernova SN 2003dh (Hjorth et al., 2003; Stanek et al., 2003) has secured the link between long GRBs and stellar collapse. Supernovae observed

since then have been determined to be Type Ib/c, which are characterised by a lack of hydrogen absorption lines, consistent with the prediction of progenitor stars that have lost their hydrogen envelopes. Studies of GRB host galaxies have found that long GRBs occur exclusively in regions of active star formation in star-forming galaxies, such as irregular galaxies and in the arms of spiral galaxies (Fig. 1.11; Bloom et al. (2002)). Due to the short lives of massive stars ($\leq 10^7$ yr) they collapse close to the region in which they were formed and so are never found in regions where star formation has ceased. This implies that long GRBs are expected to occur in galaxies undergoing star formation but not early type galaxies. The hosts of long GRBs are observed to be predominantly blue, sub-luminous, star-forming galaxies, indicating a significant abundance of young, massive stars (Le Floc'h et al., 2003). GRBs tend to be located at the very brightest regions of their host galaxies (Fruchter et al., 2006) which also suggests that GRBs are produced by the most massive stars.

1.4.2 Binary Compact Object Mergers

Binary mergers of compact objects are the leading progenitor model for short GRBs (e.g. Blinnikov et al. (1984); Eichler et al. (1989); Paczynski (1991); Narayan et al. (1991); Fryer et al. (1999)). These events also result in a black-hole/accretion-disk system and occur when binary stars lose energy and coalesce as their orbits decay. This energy loss is thought to occur naturally due to the emission of gravitational radiation, provided the binary system remains bound and is not disrupted by a supernova. Both stars must have originally been in the mass range of $\sim 8\,M_\odot$- $25\,M_\odot$ to form neutron stars. Due to the scale of the energy released in a GRB, the preferred models involve two neutron stars (Eichler et al., 1989), or a neutron star and a black hole (Paczynski, 1991). The system is rotating rapidly when it merges, resulting in a black hole of $\sim 2.4\,M_\odot$, with the necessary angular momentum to form a neutron rich accretion disk of $\sim 0.1\,M_\odot$- $0.2\,M_\odot$. The event occurs within a few seconds, which accounts for the short duration of these bursts. No supernova is expected to accompany the merger, as there is no conventional star to explode.

Most of the energy released during a merger ($\sim 10^{53}$ erg) is emitted in the form of low energy neutrinos and gravitational waves. The remaining energy is sufficient to power a short burst however, and is only a fraction of the energy released during the merger ($\sim 10^{51}$ erg; Rees (1999)). The relativistic outflow may be driven by neutrino annihilation producing $e^{\pm}$ pairs, which in turn produce γ-rays (Eichler et al., 1989). The favoured energy source for this process is a massive accretion disk surrounding a black hole (Jaroszynski, 1996).

The rate of binary star mergers is estimated to be $\sim 10^{-6}\,\mathrm{yr}^{-1}\,\mathrm{galaxy}^{-1}$ (Narayan et al., 1991) which agrees with the rate of short GRBs (Piran, 1992). With a typical long lifetime of $\sim 10^{8}$ - 10^{9} yr (Narayan et al., 1992), these mergers are expected to occur far from the place of birth of the compact object due to their high spatial velocities and also an occasional kick velocity provided by supernovae during their evolution. This is not always the case however, as there is evidence for a population of short lived binaries with very close orbits and lifetimes of $\sim 10^{5}$ yr (Belczynski et al., 2002), so that mergers may occur close to their birth site. Short GRBs tend to occur in early type host galaxies, such as ellipticals, with some occurring in star forming regions. At least some short GRBs have been detected on the outskirts of elliptical galaxies, e.g. GRB 050509 (Gehrels et al., 2005) and some have been found in star forming galaxies, e.g. GRB 050709 (Fox et al., 2005) (Fig. 1.11). The star formation rate in these galaxies, however, has been found to be less intense than in typical host galaxies of long GRBs. Studies by Berger (2008) show that short GRB host galaxies exhibit higher luminosities and higher metallicities than those of long GRBs, and are not consistent with a young population. Supernovae have never been associated with any short GRBs, despite deep observations of a number of nearby bursts.

1.4.3 The GRB-Supernova Connection

The collapsar model predicts the collapse of a massive star ($\sim 30\,\mathrm{M}_{\odot}$) to a compact object as a mechanism to produce long GRBs. The resulting release of energy must lead to the

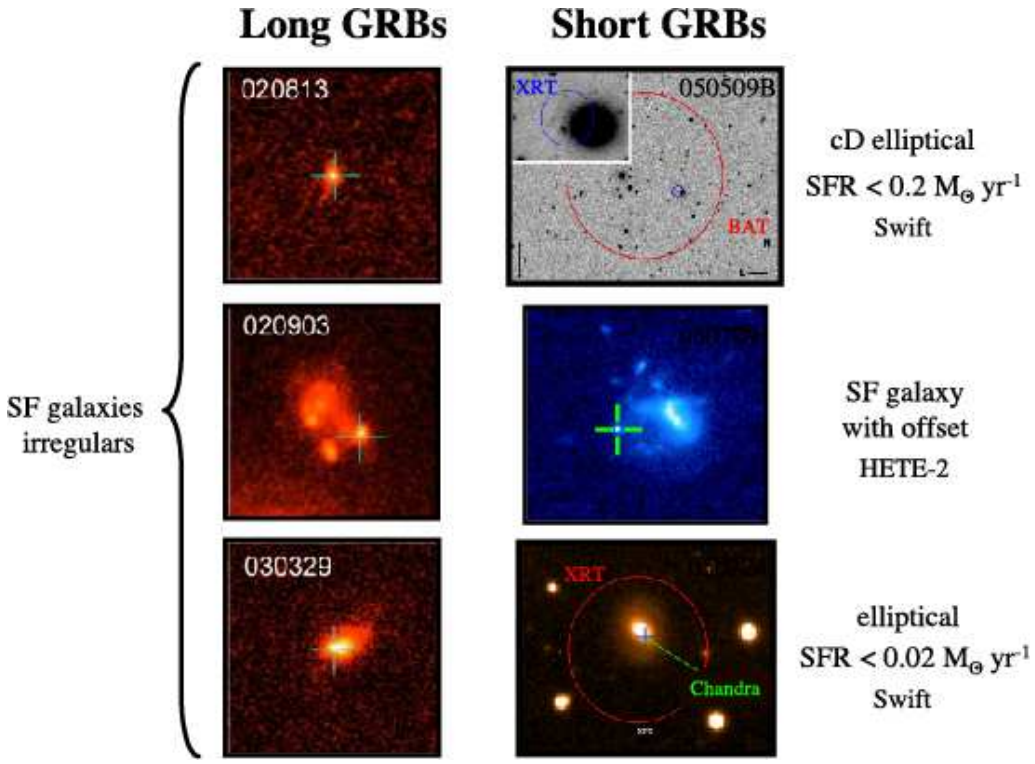

Figure 1.11: Host galaxies of long GRBs are typically irregular and with a high star-formation rate. Short GRBs have been observed on the outskirts of elliptical galaxies and also in star forming regions. *Credit: Gehrels et al. (2007).*

ejection of the star's envelope at high velocities, producing a supernova (SN). The SN emission is non-relativistic, spherical and $\sim 10^{51}$ erg is emitted over weeks and months. Once the cosmological origin of long GRBs was firmly established (Metzger et al., 1997), the total isotropic energy in γ-rays was determined to be $\sim 10^{51}$ erg, comparable to the total kinetic energy in a supernova explosion. The association of long GRBs with active star-formation indicated massive stellar death as a likely progenitor, further hinting at a supernova connection.

An association between GRBs and SNe was initially proposed long before a connection was verified observationally (Colgate, 1968; Paczynski, 1986). The first strong evidence for such an association came with the detection of the highly unusual supernova SN 1998bw (Galama et al., 1998), which was spatially and temporally coincident with GRB 980425. The observed properties of the prompt GRB emission were fairly typical but a very bright, peculiar SN, was also detected in the host galaxy at a redshift of

$z = 0.0085$. This low redshift burst, at a distance of ~ 35 Mpc, was very under luminous, with an isotropic γ-ray energy of $8.5 \pm 0.1 \times 10^{47}$ erg, more than three orders of magnitude fainter than typical long bursts. An X-ray source in the galaxy allowed for a more refined localisation of the burst and tightened the correlation between the GRB and the SN. The probability of the association between GRB 980425 and SN 1998bw being a chance coincidence has been estimated to be $\sim 10^{-4}$ (Galama et al., 1998). Therefore this detection provided the first convincing evidence for the link between long-duration GRBs and SNe.

This link has subsequently been confirmed with the direct spectroscopic detection of SN 2003dh associated with GRB 030329 at $z = 0.1685$ (Hjorth et al., 2003; Stanek et al., 2003). The bright, slowly fading afterglow ($R \sim 13$ mag) and low redshift of the burst made it well suited to extensive spectroscopic follow-ups . Additional spectroscopic and photometric studies of the afterglow several days after the burst (Della Valle, 2005; Matheson, 2005; Fynbo et al., 2004) showed a deviation from a pure power-law decay and the emergence of broad SN spectral features (e.g. Hjorth et al., 2003). As the afterglow faded, a red supernova bump became prominent, showing remarkable similarity to SN 1998bw. Several other GRBs have been reported to be associated with SNe, based on spectroscopic as well as lightcurve signatures, including GRB 031203 (Bailyn et al., 2003; Malesani et al., 2004), GRB 021211 (Della Valle et al., 2003), and GRB 050525 (Della Valle et al., 2006b).

Short-duration GRBs are not expected to have associated SN emission if the prevailing merger theory for their origin is correct. Secure limits on the lack of SN emission have been placed on several short bursts, including GRB 050509b (Bloom et al., 2005; Hjorth et al., 2005a) and GRB 050609 (Fox et al., 2005; Hjorth et al., 2005b). Afterglow observations are therefore consistent with the merger hypothesis for short GRBs at present.

The validity of the theory that all long GRBs are associated with SNe was called into question with the detections of two nearby *Swift* GRBs without SNe, GRB 060505 at $z = 0.089$ (Fynbo et al., 2006; Ofek et al., 2007) and GRB 060614 at $z = 0.125$ (Fynbo

et al., 2006; Gal-Yam et al., 2006; Della Valle et al., 2006a). Due to their proximity and apparent membership of the long duration class (T_{90} of 4 ± 1 s and 102 ± 1 s respectively (Hullinger et al., 2006; Barthelmy et al., 2006)), SN searches were initiated by many observers, which failed to detect a SN down to limits ~ 100 times fainter than the prototypical SN1998bw. The lack of an associated SN to such deep limits may be evidence for a new phenomenological type of massive stellar death. It has been suggested that these bursts may be related to merger events like short bursts and therefore not have SN emission.

Chapter 2

Gamma-Ray Bursts: Theoretical Models and Afterglow Behaviour

2.1 Introduction

A viable theoretical model for GRBs must account for various physical processes and explain the vast diversity found in both the prompt emission and subsequent afterglows. Most models involve the collapse of a stellar object, the creation of an accretion disk and a pair of jets which interact with the circumburst medium. Considering the massive release of energy involved in a GRB ($\sim 10^{53}$ erg isotropic) the progenitor must be a compact object such as a black hole or neutron star, since no other object is capable of such emission over such a short time-scale. The compactness problem (§2.1.2) dictates that the outflow must be moving relativistically, with a Lorentz factor of $\Gamma \geq 100$. Taking into account the relativistic beaming factor (see § 2.1.1), the total energy required for a GRB is decreased to $\sim 10^{51}$ erg (Frail et al., 2001), since the material is beamed into an angle of $1/\Gamma$ rather than being emitted isotropically. The energy must be dissipated within this collimated, relativistic jet for the release of the prompt and afterglow emission. Dissipation is thought to occur in the form of collisionless shocks. Most models are based on synchrotron radiation from relativistic electrons accelerated within these shocks.

2.1.1 Jets

The outflow emitted from the central engine moves relativistically and is collimated along the axis of rotation of the central engine. The outflow is referred to as a jet and is a common structure in astrophysical objects, including active galactic nuclei and micro-quasars. The geometric opening angle of the jet is called θ_j. When a source is radiating isotropically in its own rest frame but moving relativistically in the observer frame, the emitted radiation is beamed into a small cone about its direction of motion. If the object is moving with a bulk Lorentz factor Γ, the relativistic opening angle is $1/\Gamma$. The effect of relativistic beaming of the jet reduces the required energy output of the burst from 10^{53} to 10^{51} erg. The interaction between the geometric and relativistic opening angles can produce measurable effects in the afterglow lightcurve.

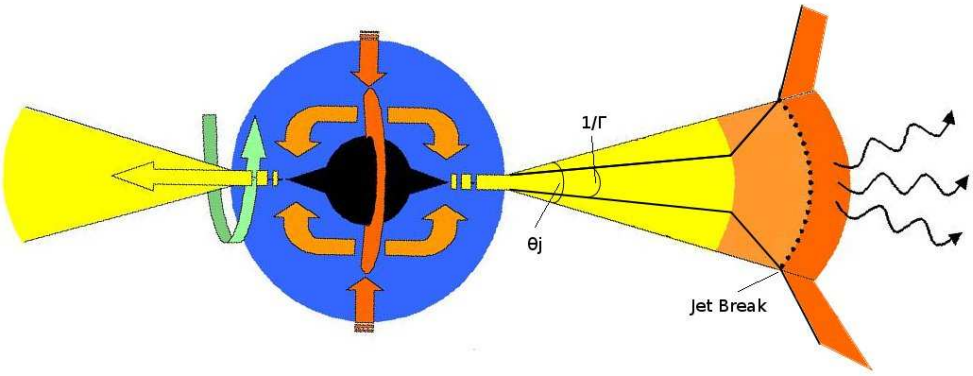

Figure 2.1: The collimated outflow from the GRB, with a geometric opening angle θ_j, is moving with a bulk Lorentz factor Γ. The jet is relativistically beamed with an opening angle of $1/\Gamma$. As the jet slows the relativistic beaming effects decrease until the relativistic cone eventually becomes wider than the geometric, causing the 'jet break'.

Initially the jet is moving with a large Lorentz factor and is thus highly beamed, with $1/\Gamma < \theta_j$. At this point the fireball evolution appears similar to the isotropic case, as an observer can only detect emission from within the relativistic cone. Under these conditions Γ is predicted to decay as a power-law proportional to the radius r and the afterglow

lightcurve decays as a power-law $\propto t^{-1}$. The relativistic beaming effects decrease as the jet slows down, due to interaction with the inter-stellar medium, and the relativistic cone gradually expands (Fig. 2.1). When the relativistic cone eventually becomes wider than the geometric opening angle, i.e. $1/\Gamma > \theta_j$, then Γ changes to decay as an exponent of the radius and the late-time afterglow lightcurve decays much faster, as a power-law $\propto t^{-2}$ (Sari and Piran, 1999a). The 'jet break' in the power-law lightcurve is a hydrodynamical effect and should occur in all wavelengths simultaneously. The time at which the break occurs is an important measurement as it can be used to calculate the opening angle, θ_j, of the jet. θ_j can then be used, along with the isotropic energy E_{iso}, to infer the geometrically corrected energy radiated in γ-rays, E_γ, given by (Piran, 2005):

$$E_\gamma = \frac{\theta_j^2}{2} E_{iso} \tag{2.1}$$

2.1.2 The Compactness Problem

The short time-scale variability of GRB prompt emission implies that the source of γ-ray emission must be smaller than cδt, where δt is the variability time-scale. The radius of the compact source combined with the observed photon energies of $\sim$1 MeV imply a high photon density at the source. At this density $\gamma\gamma$ interactions would produce $e^\pm$ pairs which creates a large optical depth, meaning high-energy photons should not be observed. However, the photon spectra observed from GRBs are predominantly non-thermal, which implies an optically thin source region.

This apparent contradiction can be resolved by invoking a relativistic expansion of the outflow, with a Lorentz factor of Γ. The effect of relativistic beaming confines the view of the source to $1/\Gamma$, meaning that the source may be a factor of Γ^2 larger and still maintain the same short time scale variability. The incoming photons have also been blue-shifted in the observer frame, due to the relativistic Doppler effect, which also results in the appearance of higher observed energies. This means that there is a smaller fraction of photons energetic enough to undergo pair production and contribute to opacity. In order

to eliminate the compactness problem, the source of a typical burst becomes optically thin for Lorentz factors $\Gamma \geq 100$ (Piran, 2005). Baryonic contamination of the outflow must be kept low, however, as the motion will cease to be relativistic if the energy of the flow is converted to kinetic energy of the baryons.

2.1.3 Emission Mechanisms

Synchrotron radiation may be used to explain the observed spectral behaviour of GRBs (Lloyd and Petrosian, 2000) and is currently considered the dominant mechanism for energy dissipation. Synchrotron emission occurs when a relativistic charged particle, usually an electron, is accelerated in a magnetic field and cools rapidly, emitting a high energy photon. The direction of motion of the electron must have a component perpendicular to the magnetic field (i.e. a non-zero pitch angle). One characteristic feature of synchrotron radiation is the polarisation of the emission, which has been tentatively observed in several bursts (McGlynn et al., 2007). The strength of the magnetic field plays an important role in the emission, however a high level of polarisation can be produced from either a uniform magnetic field in the jet or a random magnetic field in the plane of the shock.

Tavani (1996) details a synchrotron shock model which predicts an optically thin synchrotron spectrum from a power-law electron energy distribution with a sharp minimum cut off energy and an isotropic pitch angle distribution. This provides a good fit to many observed spectra, but requires modification to explain some of features of the low energy spectra (Preece et al., 2002). A large range of low-energy spectral behaviour can be explained when taking into account an anisotropic electron pitch angle distribution and the effects of synchrotron self-absorption (Lloyd-Ronning and Petrosian, 2002). A variation on synchrotron radiation is jitter radiation, which involves emission from electrons in small-scale, non-uniform magnetic fields (Medvedev, 2000). This approach can account for the rapid spectral variability and hard to soft evolution in GRBs, as well as the presence of a soft X-ray component in some GRBs.

Compton processes can also be used to explain the observed spectral features of GRBs.

Inverse Compton scattering occurs when a relativistic electron scatters off a photon. The electron may deposit a fraction of its energy to the photon in the collision, thus boosting the photon to higher energies by factor of γ_e^2, where γ_e is the electron Lorentz factor (Piran et al., 2008). The types of spectra observed in GRBs could be produced by inverse Compton scattering of synchrotron emission (Panaitescu and Mészáros, 2000). An alternative method for γ-ray production is the synchrotron self-Compton process. This involves the photons that were originally created in the synchrotron mechanism being up-scattered to higher energies by the same electrons initially responsible for their creation. This effect is dominant at low photon energies and high photon energies.

2.2 The Fireball Model

The standard theoretical framework for the interpretation of GRB emission is called the fireball model (Mészáros, 2002) and has been extremely successful at describing the observed properties of the prompt and afterglow emission. The basic premise of the model is the formation of a relativistically expanding, high-temperature outflow of matter, called a fireball, which is created from the release of a large amount of energy from a compact region over a short period of time, irrespective of the nature of the progenitor. Prompt γ-ray emission is produced by collisionless internal shocks within the fireball. As the fireball progresses into the surrounding external medium it shock heats electrons in the medium, which results in the longer wavelength afterglow emission. The model is shown schematically in Fig. 2.2.

With an observed luminosity greatly exceeding the Eddington luminosity, the radiation pressure within the fireball is sufficient to allow it to expand relativistically (e.g. Paczynski, 1986). The bulk Lorentz factor Γ of the fireball increases linearly until reaching a maximum value, after which it remains constant. The fireball consists mainly of an $e^{\pm}$ plasma and γ-rays, with a smaller component of baryons. The relativistic expansion of the fireball implies a low baryonic component, as the baryonic load determines the ex-

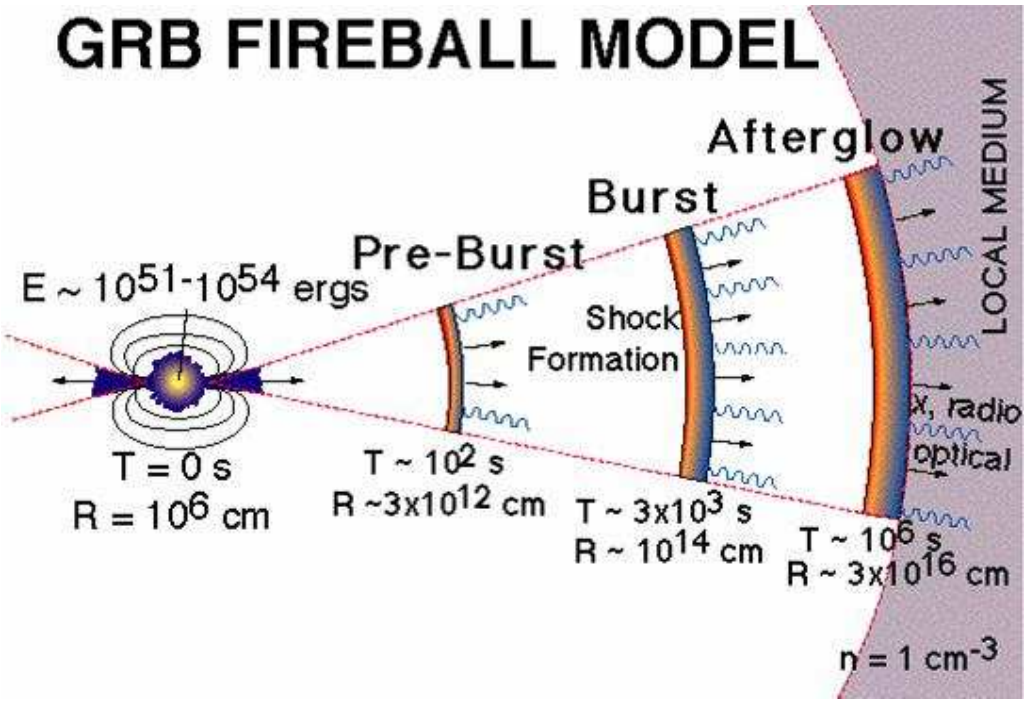

Figure 2.2: Schematic of the Fireball Model. Prompt γ-ray emission is created by internal shocks, while the longer-wavelength afterglow emission occurs at larger radii as the interaction of the relativistic outflow with the external local medium decelerates the fireball. *Credit: http://gsfc.nasa.gov*.

pansion velocity. As the fireball expands it changes from being optically thick to optically thin at a radius of $\sim 10^{12} - 10^{13}$ cm. A thermal component to the spectrum is introduced at this point due to photospheric emission from the expanding fireball (Pe'er, 2008).

2.2.1 Internal Shocks

The central engine of a GRB is variable and emits matter in shells. The overall Lorentz factor of the outflow will reach a constant value, but each shell within the jet develops its own Lorentz factor. When a shell of a lower Lorentz factor is overtaken by one with a higher Lorentz factor, a shock is formed. The shocks are collisionless, i.e. the transition from pre-shock to post-shock states occurs on a length scale much smaller than a particle collisional mean free path. The synchrotron radiation produced within the shocks is the non-thermal γ-radiation observed in the prompt emission (Piran, 2005). Magnetic inhomogeneities in the shock region cause the electrons within the shell to undergo multiple

reflections, becoming flash-heated and Fermi accelerated. The higher energy electrons then radiate γ-rays due to synchrotron emission within the magnetic field. The shocks form within the jet itself and are not affected by the external medium. The multiple emission episodes and high variability seen in GRB lightcurves can be successfully explained by the internal shock model.

2.2.2 External Shocks

As the fireball progresses away from the central engine it sweeps up matter from the surrounding medium. At a radius of $\sim 10^{16} - 10^{18}$ cm the internal shells have combined into a single relativistic shell and the amount of matter swept-up from the external medium becomes significant enough to decelerate the fireball. This creates a shock front that moves through the external medium, heating the matter therein to extreme temperatures (e.g. Rees and Mészáros, 1992). These flash-heated particles are accelerated to relativistic speeds and then radiate via synchrotron emission, producing the afterglow emission of the GRB, which shifts to progressively lower wavelengths as the fireball decelerates. Even in the presence of a low-density surrounding medium, the external shock model allows the kinetic energy of the fireball to be converted to photons.

2.2.3 Reverse Shocks

The process of creating the external forward shock also creates a reverse shock, which propagates back into the ejecta (Mészáros and Rees, 1997; Sari and Piran, 1999b). These two shocks are separated by a contact discontinuity and the energy contained in both are comparable. The reverse shock is short-lived and has a lower temperature than the internal shock. It is mildly relativistic and as it crosses back over the remnant star it heats and accelerates electrons. The reverse shock takes tens of seconds to sweep through the ejecta and produce a bright flash. The lower Lorentz factor of the shock predicts emission in the optical band (Sari and Piran, 1999b), distinguishable from the late afterglow emission

due to the fact that the shock only crosses the shell once, producing a single flash. The shocked hot matter then expands adiabatically and the emission weakens and shifts to lower frequencies. A reverse shock generated optical flash was observed simultaneously with γ-ray emission in GRB 990123 (Sari and Piran, 1999a). If the jet is Poynting-flux-dominated, the large magnetic pressure prevents the formation of a strong reverse shock.

2.3 GRB Afterglows

A multi-wavelength GRB afterglow, from X-ray to radio, was predicted before the discovery of GRB 970508 which was the first GRB observed to have a radio afterglow (Frail et al., 1997). With a measured redshift of z = 0.835 it confirmed an unambiguous cosmological origin for GRBs. The Italian/Dutch satellite BeppoSAX revealed more of the cosmological nature of bursts with the identification of the first X-ray afterglow in 1997 (Costa et al., 1997). With a more accurate localisation of the burst the first successful follow-up observations at optical wavelengths were made possible (van Paradijs et al., 1997). There is also extensive observational evidence for collimated emission from GRBs, provided by breaks in the X-ray or optical lightcurves of their afterglows. This break is commonly interpreted as a jet break enabling an estimate of the jet opening angle.

The quality of GRB afterglow observations has dramatically improved in the *Swift* era. The *Swift* mission combines improved sensitivity to GRBs with multi–wavelength instruments and, crucially, rapid localisation and slewing capabilities, which has led to routine observations of GRBs at X-ray and UV/optical wavelengths ~100 s from the trigger. These capabilities have allowed the prompt and early afterglow phases to be explored in far greater detail than was previously possible. *Swift* also provides GRB positions with unprecedented speed and accuracy, which has greatly assisted ground-based follow-up observations with robotic optical/IR telescopes, a significant number of which have come online in recent years.

2.3.1 Afterglow Emission

As the relativistic fireball sweeps up matter from the ambient medium and is decelerated, the resulting forward shock propagates into the ambient medium. This generates the long-lived multi-wavelength afterglow, while a short-lived reverse shock propagates back into the ejecta. Most of the fireball kinetic energy is transferred into the shocked external medium. The fireball Lorentz factor evolves with radius r and with observer's time t as:

$$\Gamma \propto r^{-3/2} \propto t^{-3/8}, \quad r \propto t^{1/4} \tag{2.2}$$

$$\Gamma \propto r^{-3} \propto t^{-3/7}, \quad r \propto t^{1/7} \tag{2.3}$$

The first case describes adiabatic fireball evolution in which the energy is constant, which is generally valid at late times (~hours). The second case describes radiative evolution, in which a significant fraction of the kinetic energy is lost due to radiative processes (Mészáros and Rees, 1997). This phase is thought to apply to the prompt emission and early afterglow.

In the simple afterglow model (Sari et al., 1998), electrons in the external medium are shock-accelerated to a power-law distribution of Lorentz factors given by:

$$N(\gamma_e) \propto \gamma_e^{-p}, \quad \gamma_e > \gamma_m \tag{2.4}$$

where γ_m is the minimum Lorentz factor of the distribution. The lower limit is set by the assumption that a constant fraction of the shock thermal energy is acquired by the electrons in the shock. The electrons radiate via the synchrotron process to produce the afterglow spectrum shown in Fig. 2.3. The spectrum is composed of a series of broken power-laws connected at the characteristic frequencies ν_a, ν_m, and ν_c. At frequencies below the self-absorption frequency ν_a, the flux undergoes synchrotron self-absorption and is described by the Rayleigh-Jeans part of the blackbody spectrum. The absorption

cross-section is higher at longer wavelengths and so as the observing frequency increases, the total flux density increases. Above ν_a, self-absorption effects are no longer significant and the underlying power-law distribution is recovered. The synchrotron frequency ν_m corresponds to the typical electron Lorentz factor, which is determined by the minimum Lorentz factor $\gamma_{e,min}$. Since electrons cool on time-scales $\propto \gamma_e^{-1}$, electrons with $\gamma_e > \gamma_c$ (corresponding to ν_c, the cooling frequency) cool very rapidly. This gives rise to two types of spectra. Fast-cooling occurs during the prompt emission and early afterglow, where $\nu_m > \nu_c$, i.e. the typical electron frequency is much higher than the cooling frequency (Fig. 2.3a). Slow-cooling is dominant when $\nu_m < \nu_c$, which describes the afterglow at late times (Fig. 2.3b). The transition from fast to slow cooling occurs at a time t_0 when $\nu_m = \nu_c$. For a given observed frequency, either $t_0 > t_m > t_c$ (typical for high frequencies), or $t_0 < t_m < t_c$, where t_m and t_c are the times when the break frequencies ν_m and ν_c cross the observed frequency ν.

Given values for the isotropic equivalent energy of the initial explosion and the micro-physical parameters (p, ϵ_e, ϵ_B, and ζ_e), and for a certain fireball Lorentz factor evolution (i.e. adiabatic or radiative), the temporal evolution of the characteristic frequencies can be determined. The observed light curve at a specific frequency (in the observer frame) can then be described by the temporal variation of the characteristic frequencies and of $F_{\nu,max}$, the peak flux. The flux at a given frequency ν can be expressed as:

$$F_\nu(t, \nu) \propto t^\alpha \nu^\beta \tag{2.5}$$

where α and β are the temporal and spectral decay indices (Sari et al., 1998).

Observational evidence has proved the simple afterglow model to be successful. It is based, however, on a number of simple assumptions that need to be modified in order to explain some features of the lightcurves. The fireball is taken to be isotropic, resulting from an impulsive injection of energy from the central engine, and the density of the external medium into which the forward shock propagates is assumed to be constant. However, it is more likely that the surrounding environment could be a stellar wind, such

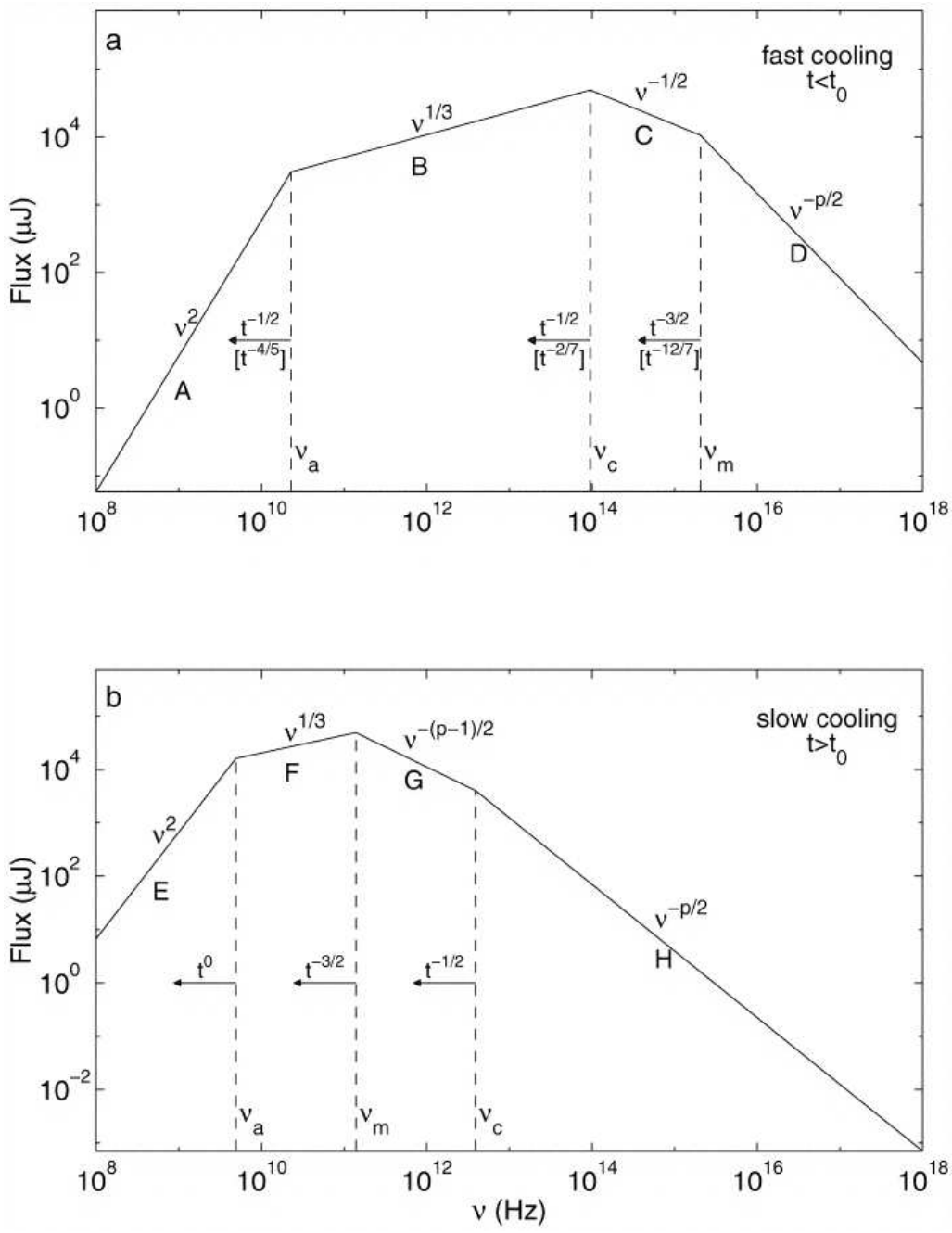

Figure 2.3: Synchrotron spectrum of a relativistic shock with a power–law electron energy distribution. (a) Fast cooling, which is expected at early times ($t < t_0$). Self–absorption is important below ν_a. The frequencies ν_m, ν_c, and ν_a decrease with time as indicated; the scalings above the arrows correspond to an adiabatic evolution, and the scalings below, in square brackets, correspond to a fully radiative evolution. (b) Slow cooling, which is expected at late times ($t > t_0$). The evolution in this case is always adiabatic. *Credit: Sari et al. (1998)*

as in the collapse of a Wolf-Rayet star. Predictions for a forward shock moving through such an environment suggest a steeper decline in the optical afterglow than expected from the standard model (Chevalier and Li, 1999).

2.3.2 Modified Afterglow Models

The assumptions in the basic afterglow model serve to simplify the analysis, and are not expected to be realistic in all cases, though they work remarkably well for many events. Many authors have proposed modifications to the simple afterglow model by considering cases in which the first-order assumptions are not satisfied. Table 2.1 shows the expected temporal and spectral indices corresponding to the forward shock spectral regimes in the simple afterglow model, and also presents values for some modified cases, as well as cases where the electron power-law index $1 < p < 2$ (e.g. Dai and Cheng (2001)). Some of the main modifications are discussed below (for further details see Zhang and Mészáros (2004)).

Wind Medium

The simple afterglow model assumes that the forward shock propagates into a constant density ISM. However, the massive star progenitor which has been proposed for long GRBs suggests that the ambient medium may be a stellar wind environment, as seen in Wolf-Rayet stars. The density profile of such an environment is $\rho \propto r^{-2}$. The optical afterglow in this case is expected to decline more steeply than for the simple fireball (Chevalier and Li, 1999, 2000). Concurrent X-ray, optical, and radio afterglow observations are particularly useful for distinguishing between the wind and ISM environments.

Energy Injections

If the central engine is still active when the fireball is decelerated (the onset of the afterglow), or if the ejecta shells have a range of bulk Lorentz factors, then shells emitted later or with lower Lorentz factors can catch up and refresh the forward shock (Rees and

	β	α ($p > 2$, $p \sim 2.3$)	$\alpha(\beta)$	α ($1 < p < 2$, $p \sim 1.5$)	$\alpha(\beta)$
ISM, slow cooling					
$\nu < \nu_a$	2	$\frac{1}{2}$		$\frac{17p-26}{16(p-1)} \sim -0.06$	
$\nu_a < \nu < \nu_m$	$\frac{1}{3}$	$\frac{1}{2}$	$\alpha = \frac{3\beta}{2}$	$\frac{p+2}{8(p-1)} \sim 0.9$	
$\nu_m < \nu < \nu_c$	$-\frac{p-1}{2}$	$\frac{3(1-p)}{4} \sim -1.0$	$\alpha = \frac{3\beta}{2}$	$-\frac{3(p+2)}{16} \sim -0.7$	$\alpha = \frac{3(2\beta-3)}{16}$
$\nu > \nu_c$	$-\frac{p}{2}$	$\frac{2-3p}{4} \sim -1.2$	$\alpha = \frac{3\beta+1}{2}$	$-\frac{3p+10}{16} \sim -0.9$	$\alpha = \frac{3\beta-5}{8}$
ISM, fast cooling					
$\nu < \nu_a$	2	1		1	
$\nu_a < \nu < \nu_c$	$\frac{1}{3}$	$\frac{1}{6}$	$\alpha = \frac{\beta}{2}$	$\frac{1}{6}$	$\alpha = \frac{\beta}{2}$
$\nu_c < \nu < \nu_m$	$-\frac{1}{2}$	$-\frac{1}{4}$	$\alpha = \frac{\beta}{2}$	$-\frac{1}{4}$	$\alpha = \frac{\beta}{2}$
$\nu > \nu_m$	$-\frac{p}{2}$	$\frac{2-3p}{4} \sim -1.2$	$\alpha = \frac{3\beta+1}{2}$	$-\frac{3p+10}{16} \sim -0.9$	$\alpha = \frac{3\beta-5}{8}$
Wind, slow cooling					
$\nu < \nu_a$	2	1		$\frac{13p-18}{8(p-1)} \sim 0.4$	
$\nu_a < \nu < \nu_m$	$\frac{1}{3}$	0	$\alpha = \frac{3\beta-1}{2}$	$\frac{5(2-p)}{12(p-1)} \sim 0.4$	
$\nu_m < \nu < \nu_c$	$-\frac{p-1}{2}$	$\frac{1-3p}{4} \sim -1.5$	$\alpha = \frac{3\beta-1}{2}$	$-\frac{p+8}{8} \sim -1.2$	$\alpha = \frac{2\beta-9}{8}$
$\nu > \nu_c$	$-\frac{p}{2}$	$\frac{2-3p}{4} \sim -1.2$	$\alpha = \frac{3\beta+1}{2}$	$-\frac{p+6}{8} \sim -0.9$	$\alpha = \frac{\beta-3}{4}$
Wind, fast cooling					
$\nu < \nu_a$	2	2		2	
$\nu_a < \nu < \nu_c$	$\frac{1}{3}$	-$\frac{2}{3}$	$\alpha = -\frac{\beta+1}{2}$	-$\frac{2}{3}$	$\alpha = -\frac{\beta+1}{2}$
$\nu_c < \nu < \nu_m$	$-\frac{1}{2}$	$-\frac{1}{4}$	$\alpha = -\frac{\beta+1}{2}$	$-\frac{1}{4}$	$\alpha = -\frac{\beta+1}{2}$
$\nu > \nu_m$	$-\frac{p}{2}$	$\frac{2-3p}{4} \sim -1.2$	$\alpha = \frac{3\beta+1}{2}$	$-\frac{p+6}{8} \sim -0.9$	$\alpha = \frac{\beta-3}{4}$
Jet, slow cooling					
$\nu < \nu_a$	2	0		$\frac{3(p-2)}{4(p-1)} \sim -0.8$	
$\nu_a < \nu < \nu_m$	$\frac{1}{3}$	$-\frac{1}{3}$	$\alpha = 2\beta - 1$	$\frac{8-5p}{6(p-1)} \sim 0.2$	
$\nu_m < \nu < \nu_c$	$-\frac{p-1}{2}$	$-p \sim -2.3$	$\alpha = 2\beta - 1$	$-\frac{p+6}{4} \sim -1.9$	$\alpha = \frac{2\beta-7}{4}$
$\nu > \nu_c$	$-\frac{p}{2}$	$-p \sim -2.3$	$\alpha = 2\beta$	$-\frac{p+6}{4} \sim -1.9$	$\alpha = \frac{\beta-3}{2}$

Table 2.1: Predicted temporal and spectral indices α and β from various afterglow models, following the convention $F_\nu \propto t^\alpha \nu^\beta$. The assumption $\nu_a < \min(\nu_m, \nu_c)$ is made. *Credit: Zhang and Mészáros (2004)*

Mészáros, 1998). Generally, a total injection energy comparable to that of the impulsive energy in the initial fireball is required to make a detectable signature in the afterglow light curves (Zhang and Mészáros, 2002). Energy injections can produce a variety of signatures in afterglow light curves, including flattening, bumps, and temporal breaks on cessation of energy injection.

2.3.3 X-Ray Afterglows

Before the launch of the *Swift* satellite, observed X-ray afterglow lightcurves were characterised by a single power-law decay given by:

$$F_X(t, \nu) = t^{\alpha}\, \nu^{\beta} \tag{2.6}$$

where α and β had typical values of $\sim$ -0.9 and $\sim$1.4 respectively (Piro et al., 2002). The early afterglow period from $\sim 10^2$ to $\sim 10^4$ s remained largely unexplored until the launch of *Swift*. Rapid follow-ups, typically $\sim$ 100 s, with the XRT instrument on-board *Swift* allowed the early afterglow regime to be studied for the first time. Consistent X-ray observations at early times revealed an unexpectedly complex structure and have led to a canonical X-ray afterglow lightcurve which consists of a number of distinct power-law segments. The main lightcurve features are shown in Fig. 2.4 (Zhang et al., 2006) and consist of 5 main components, which may not all be present in all bursts.

- **I Steep decay phase:** A steep decay phase is first observed, which is usually smoothly connected to the prompt γ-ray emission (phase 0), with a temporal decay slope ~ -3 or steeper, extending to $\sim 10^2 - 10^3$ s. The spectral slope is usually different from those of the later afterglow phases. The initial steep decay is generally interpreted as being late prompt emission due to the curvature effect when the prompt emission ceases abruptly (Kumar and Panaitescu, 2000; Zhang et al., 2007). The conical geometry of the GRB jet results in the emission at large angles to our line of sight being delayed relative to on-axis emission.

- **II Shallow decay phase:** The temporal decay slope is typically ~ -0.5 or flatter, extending to $\sim 10^3 - 10^4$ s, when a temporal break is observed before the normal decay phase. The shallow decay is thought to be related to the external shock, possibly due to energy injection from the jet when low-Γ shells pile up behind a decelerating high-Γ shell (Rees and Mészáros, 1998), continuous energy injection

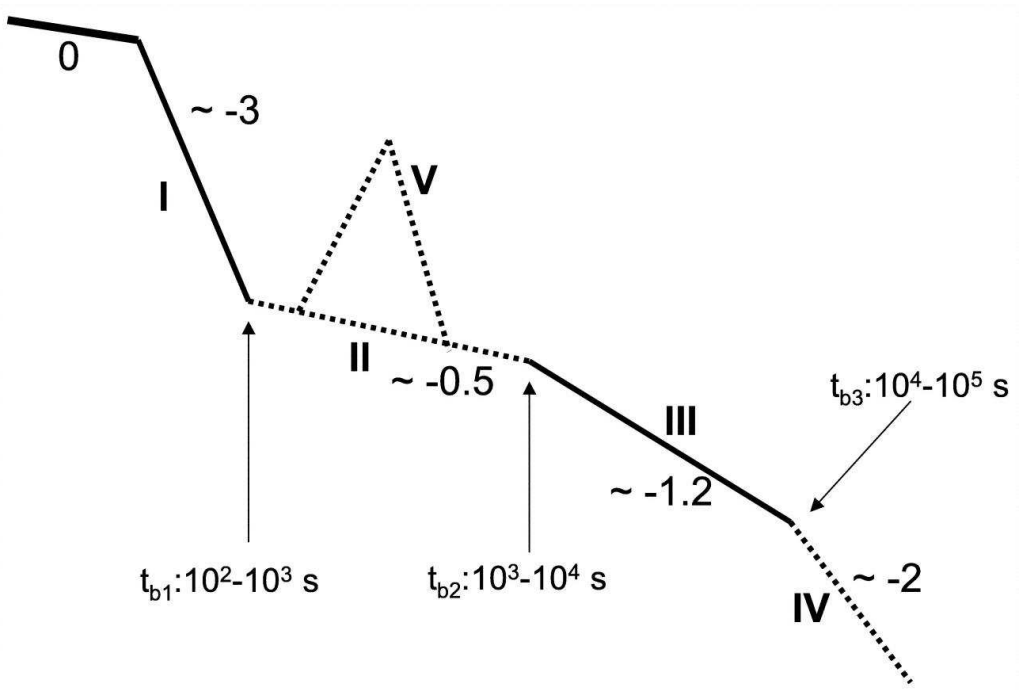

Figure 2.4: Canonical X-ray afterglow lightcurve based on *Swift* XRT data. The phase "0" denotes the prompt γ-ray emission. Segments I and III are most commonly observed and they are marked with solid lines. The other three components are only observed in a fraction of bursts and are marked as dashed lines. Typical temporal indices (α) are indicated in the figure. *Credit: Zhang et al. (2006).*

from the central engine at later times (Zhang et al., 2006), or a delay in transfer of energy from the fireball to the surrounding medium.

- **III Normal decay phase:** The normal decay phase usually follows the predictions of the standard afterglow model, with a temporal decay slope of ~ -1.2, and seems to be in agreement with predictions of the standard afterglow model (Mészáros and Rees, 1997).

- **IV Post jet-break phase:** Occasionally observed following the normal decay phase, this final break is the so-called jet break with a typical temporal decay slope of ~ -2 it is in agreement with predictions of the jet model.

- **V X-ray flares:** Observed in nearly half of GRB afterglows, occasionally with multiple flares in a single burst. Rise and decay slopes are typically very steep (Burrows et al., 2005a).

2.3.3.1 X-Ray Flares

Since the launch of *Swift*, X-ray flares have been observed in ~50% of *Swift* GRBs with early X-ray afterglow observations. The overall energy emitted in X-rays is usually a few percent of the prompt γ-ray emission, but there have been cases from *Swift* where flares have been observed with a comparable flux to the γ-ray emission. The flares can occur from hundreds of seconds after the prompt emission to up to a day later and have been observed in long and short duration GRBs. They are generally superimposed on the underlying decay in the steep or shallow phases of the X-ray afterglow. The rise and fall times of the flares are much shorter than the time since the burst onset and the flares tend to soften with time, with later flares being broader and less energetic than earlier ones.

A number of interpretations for X-ray flaring have been proposed, such as refreshed external shocks (Zhang and Mészáros, 2002) and late-time central engine activity, either continued or restarted (Zhang et al., 2006). The observed characteristics imply an internal shock origin, which would require just a fraction of the total prompt emission energy to explain the flares. The internal shock model can explain the rapid rise and decay of the flares, because the trigger time for the flare has to be reset every time the central engine restarts. The fact that the flares are observed 10^2 – 10^3 s after the prompt emission suggests that there is a long period of time before the central engine restarts, which must be explained by the theoretical models. Suggestions for restarting the central engine include fragmentation or gravitational instabilities, either in the star's envelope or the accretion disk, or different binary progenitors in the case of short GRBs, e.g. NS-BH mergers or white dwarf-NS mergers, both of which would cause extended accretion (e.g. King et al., 2007).

2.3.4 Optical Afterglows

Observations of optical afterglows since the launch of *Swift* have revealed early faintness to be more the norm than the exception, contrary to previous expectations. In pre-*Swift*

observations, the late-time optical flux was described by:

$$F_O(t, \nu) = t^{\alpha}\, \nu^{\beta} \tag{2.7}$$

with typical values of $\alpha \sim -1$ and $\beta \sim -0.7$ (Zhang and Mészáros, 2004). Late breaks in the optical afterglow light curves have been observed in a number of cases, interpreted as jet breaks e.g. GRB 990510, (Harrison et al., 1999). Optical afterglow behaviour in general has been unexpectedly complex and varied at early times (Panaitescu and Vestrand, 2008) and reverse shock optical flashes have been much less common than had been suggested by previous early optical observations. There is also a large fraction of GRBs that have no detectable afterglows at optical wavelengths, called "dark bursts" (§ 2.3.4.4).

Some GRBs show significant rebrightenings e.g. GRB 060206 (Woźniak et al., 2006) and GRB 060607a (Nysewander et al., 2007) and short time scale variability (e.g. Stanek et al., 2007). Others have plateau phases during which the flux stays approximately constant e.g. GRB 050801 (Rykoff et al., 2006a) and GRB 060210 (Stanek et al., 2007). Proposals for possible explanations for the observed optical afterglow characteristics include: refreshed external shocks, long-lived activity of the central engine and density variations in the external medium (Rees and Mészáros, 1998; Wang and Loeb, 2000). Early optical afterglow lightcurves can be divided into 4 types: fast-rising with an early peak, slow-rising with a late peak, flat plateaus and steep decays (Panaitescu and Vestrand, 2008). In most cases, the optical afterglow fades after several weeks. At this stage, the afterglow becomes significantly dimmer than its host galaxy, and the lightcurve reaches a plateau stage corresponding to the host galaxy emission. In several cases, a "bump" in the lightcurve is observed at late times, usually interpreted as evidence for an underlying supernova.

The luminosities of optical afterglows have a bimodal distribution (e.g. Kann et al., 2006). The majority of afterglows belong to the brighter of the two populations, while low redshift afterglows are, on average, less luminous than more distant ones. This provides possible evidence for the existence of a nearby, sub-luminous population of GRBs as

proposed by several authors (Norris, 2002; Soderberg et al., 2004; Foley et al., 2008).

2.3.4.1 Reverse Shock Emission

GRB 060111b was a bright, double-peaked burst detected by *Swift* (Perri et al., 2006), with $T_{90} = 59 \pm 1$ s. A $\sim 13^{th}$ mag, rapidly decaying, optical transient was detected at $\sim T_0 + 29$ s by both the ROTSE-III and TAROT robotic telescopes (Yost et al., 2006; Klotz et al., 2006a). The high-time resolution light curve obtained by TAROT revealed a lack of fine time structure during the decay of the optical flare, while the γ-ray light curve showed a peak during the same time interval. The clear anti-correlation between the optical and γ-ray flux rules out a common emission mechanism, and the rapid ($\alpha = 2.4$) decay of the optical afterglow unambiguously identifies the reverse shock as the source of the prompt optical emission (Klotz et al., 2006c).

GRB 060117 was an extremely intense burst detected by *Swift* (Campana et al., 2006a), with $T_{90} = 16 \pm 1$ s. Observations by the robotic telescope FRAM, beginning at $T_0 + 124$ s, detected a very bright optical transient at $R = 10.1$ mag (Kubánek et al., 2006a; Jelínek et al., 2006a). The early optical emission decayed rapidly, and later observations by other instruments failed to detect an optical or radio transient (Nysewander et al., 2006; Schmidt et al., 2006), setting strong limits on the fluxes which indicated an unexpectedly rapid further decay. Jelínek et al. (2006b) interpreted the light curve as a transition between reverse and forward shock emission, with a relatively steep electron-distribution index $p \simeq 3.0$. Evidence for a transition from the reverse shock to forward shock phase was also present in the optical emission from GRB 050525a (Shao and Dai, 2005), the first bright, low-redshift burst to be observed by both the narrow field instruments on *Swift*, resulting in one of the most comprehensive multiwavelength descriptions of the early evolution of a GRB afterglow (Fig. 2.5).

Several bursts for which early optical data is available have displayed no evidence of reverse shock emission. The ROTSE-IIIa robotic telescope detected prompt optical emission from GRB 050401, 33 s after its detection by *Swift* (Barbier et al., 2005). After

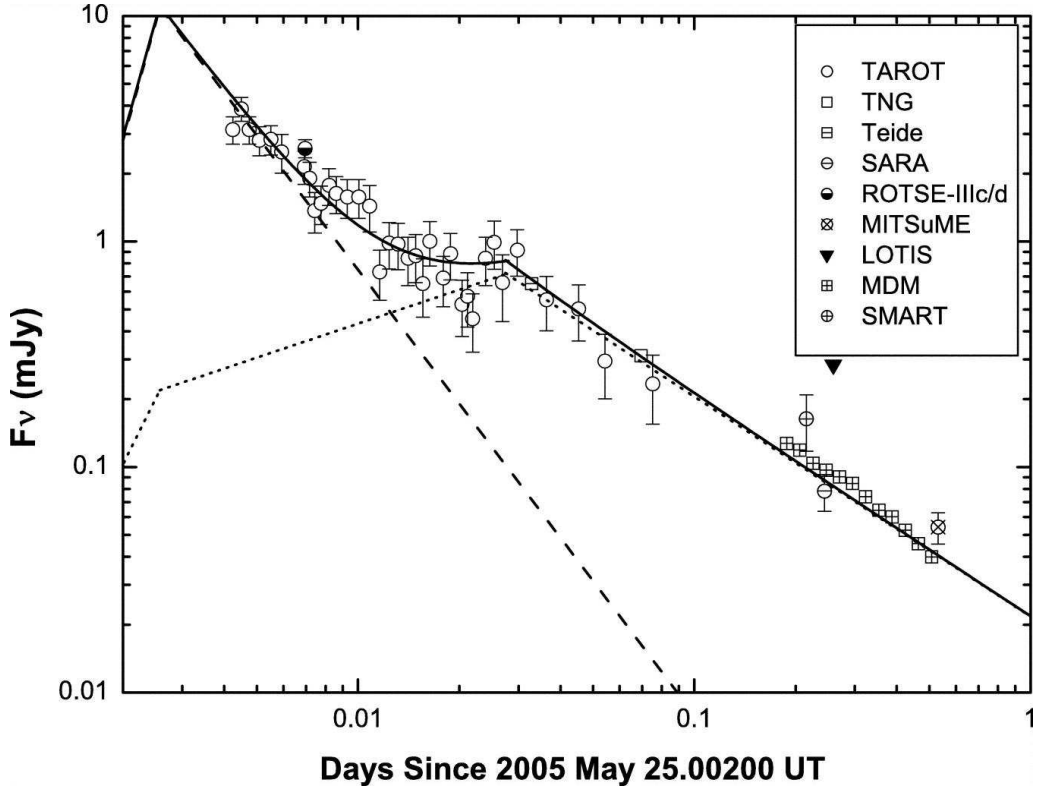

Figure 2.5: R-band light curve of GRB 050525a. The fitting curve (*solid line*) is generated by superposition of the forward shock emission (*dotted line*) and reverse shock emission (*dashed line*). *Credit: Shao and Dai (2005).*

the prompt optical detections of GRB 990123 and GRB 041219a, this was just the third GRB that had been detected optically while still active in γ-rays, and the first detection for a burst of average duration and luminosity. The early optical behaviour showed no similarity to that of either GRB 990123 or GRB 041219a. No correlation with the γ-ray emission was observed, and the prompt optical emission was well fitted by a backward extrapolation of the afterglow at late times, indicating a very rapid rise of the forward shock emission, and a negligible contribution from internal shocks (Rykoff et al., 2005). Early dominance of the forward shock emission was also suggested by the simple power-law decay observed from very early times in GRB 061007 (Mundell et al., 2007), which reached a peak magnitude of $R \sim 10.3$. The well-sampled early optical light curves of GRB 060418 and GRB 060607a were shaped by the forward shock only (Fig. 2.6), and by determining the time at which the afterglow peaked, Molinari et al. (2007) could infer the original Lorentz factor of the fireball to be ∼400.

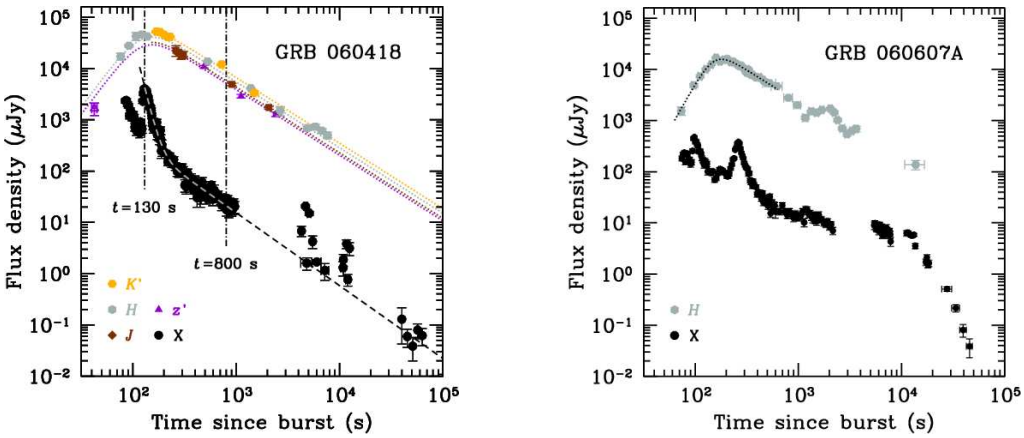

(a) (b)

Figure 2.6: NIR and X-ray light curves of (a) GRB 060418 and (b) GRB 060607a. The dotted lines show the fit of a broken power-law model to the NIR data. *Credit: Molinari et al. (2007).*

2.3.4.2 Emission from Internal Shocks

An alternative to the reverse shock interpretation was proposed for the bright optical flare observed from GRB 050904. This burst had a spectroscopically measured redshift of 6.29 ± 0.01 (Kawai et al., 2005) and a bright optical counterpart was detected during the γ-ray emission in unfiltered observations by TAROT (Boër et al., 2006), beginning 86 s after the trigger. The 30 cm BOOTES telescope failed to detect an optical counterpart at early times in its R-band observations (Jelínek et al., 2005), since the high redshift placed the Lyα cutoff redward of the R-band. GRB 050904 was similar to GRB 990123 in that it had a large isotropic equivalent energy, high intrinsic peak energy, and displayed similar optical behaviour. Unlike GRB 990123 however, an X-ray flare was observed contemporaneous with the optical flare. While the optical flare can be accounted for in the context of the reverse shock model, this emission process is expected to have a negligible contribution in the X-ray band. Wei et al. (2006) suggest that, with the proper parameters, both the optical and X-ray flashes can be explained by the late internal shock model, first proposed by Fan et al. (2005) to interpret the prompt emission from GRB 041219a.

Further confirmation of a link between prompt emission at γ-ray and optical wavelengths was discovered in GRB 050820a. This burst was composed of an initial period

of γ-ray emission from $T_0 - 17$ s to $T_0 + 22$ s (Page et al., 2005), followed by a second, larger episode of emission from $T_0 + 217$ s to $T_0 + 270$ s, and was detected by both *Swift* (Cummings et al., 2005) and KONUS-Wind (Pal'shin and Frederiks, 2005). The RAPTOR robotic telescope responded to the GCN alert based on the initial BAT trigger, and subsequently detected optical emission contemporaneous with the main outburst of energy in γ-rays. These observations reveal faint optical emission that suddenly flares and varies erratically, tracking the γ-ray emission, before fading over the course of the next hour (Vestrand et al., 2006). Comparison of the optical and γ-ray lightcurves allowed the determination of the temporal relationship and relative strength of the two optical components, one which tracks the γ-ray lightcurve and one from the external shock emission (Fig. 2.7).

2.3.4.3 Optical Flashes

According to the fireball model internal shocks within the jet create the γ-rays, external shocks produce the long-lived afterglow, and a reverse external shock with a lower temperature can propagate back into the ejecta to produce the prompt optical emission (Sari and Piran, 1999b). The robotic telescope ROTSE (Robotic Optical Transient Search Experiment) observed a bright optical flash concurrent with the γ-ray emission for GRB 990123, reaching ~9th magnitude 47 seconds after the onset of the burst (Akerlof et al., 1999). The prompt optical and γ-ray emission were not correlated (Fig. 2.8b), suggesting that the optical emission was not the low-energy tail of the prompt γ-ray emission and was instead emitted in a different physical region. This is consistent with the reverse shock theory (Sari and Piran, 1999a). Conversely, correlated optical and γ-ray emission were detected in GRB 041219a (Fig. 2.8a) indicating that they were related and were both generated by internal shocks (Vestrand et al., 2005).

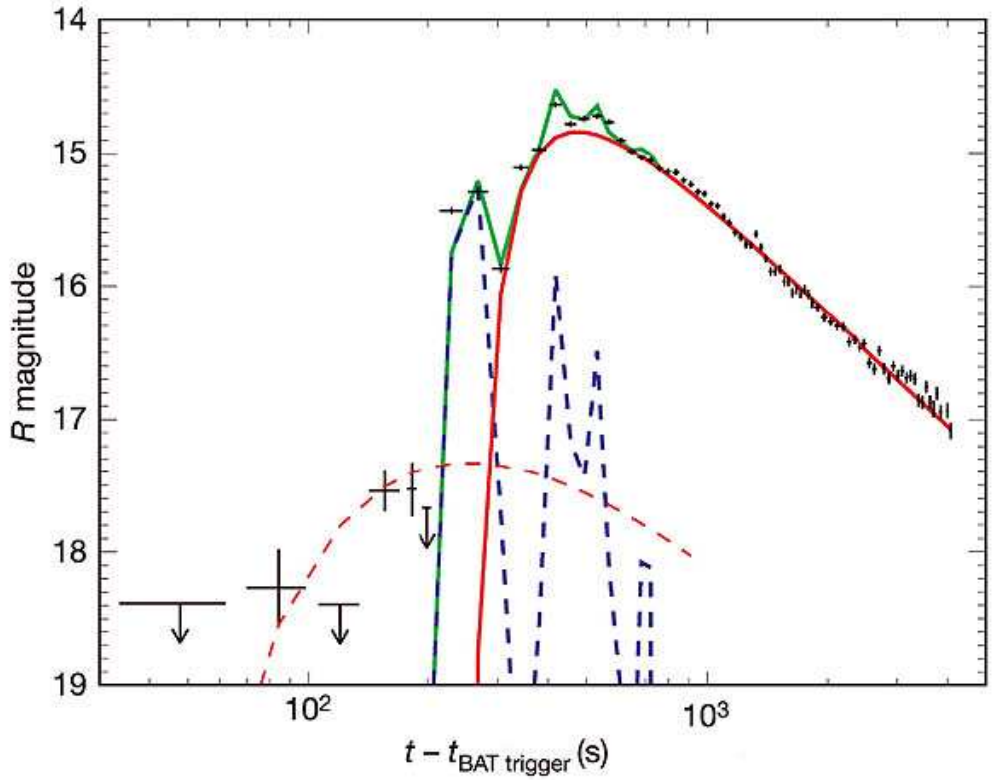

Figure 2.7: RAPTOR observations of GRB 050820a (black crosses). The blue dashed line shows the predicted prompt optical component obtained by scaling the KONUS-Wind γ-ray flux measurements, after re-binning to the same time intervals as the RAPTOR measurements, by a factor $F_{opt}/F_{\gamma} = 7.4 \times 10^{-6}$ and converting to the R-band equivalent magnitude. The solid red line shows the model early afterglow component, with a reference time t_0 set to the start of the second, more intense γ-ray pulse. The green trace shows the sum of these prompt and early afterglow components. The dashed red line shows an afterglow component with the same flux-rise timescale as the dominant afterglow, but with a reference time set to the onset of the precursor pulse, and an amplitude given by the ratio of the γ-ray fluence for the precursor pulse to that of the main pulse. *Credit: Vestrand et al. (2006).*

2.3.4.4 Dark GRBs

A significant proportion of GRBs do not have a detectable afterglow, even though deep observations down to ~21 - 22 magnitudes are carried out for most events within 24 hours of the burst (Coward et al., 2008). Of the 432 GRBs detected by *Swift* up to May 2009, 356 have been observed by UVOT and 135 have resulted in UV/optical detections. Taking ground-based follow-ups into account, the number of UV/optical/IR detections rises to

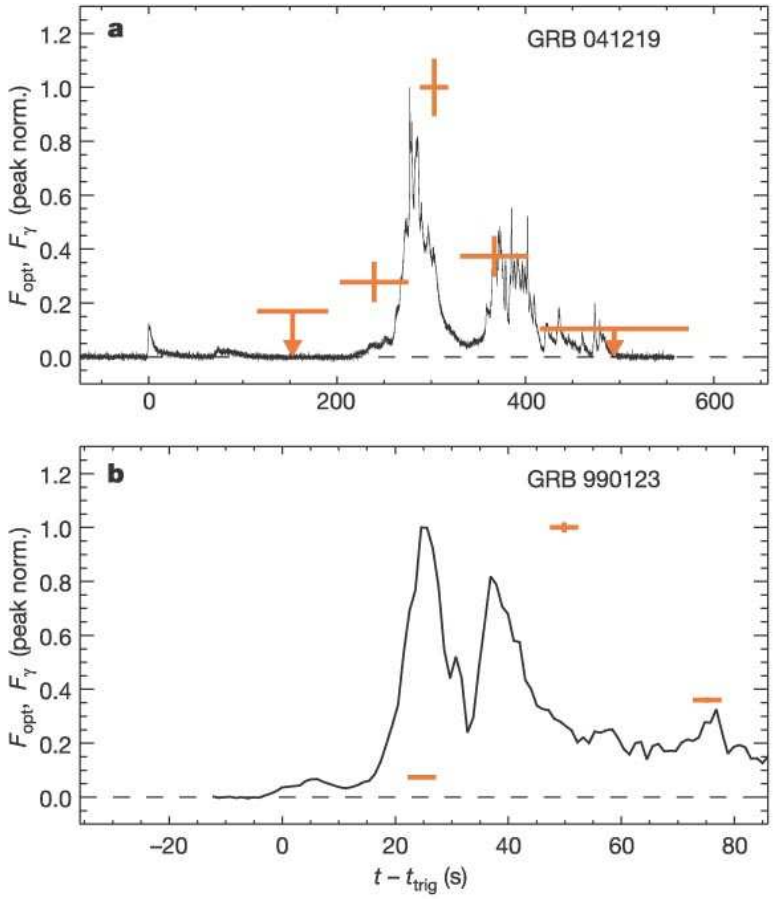

Figure 2.8: Comparison of the γ-ray and prompt optical light curves for GRB 041219a and GRB 990123. (a) For GRB 041219a the optical flash was correlated with the γ-rays suggesting a similar origin for both. (b) For GRB 990123 the optical emission does not follow that of the γ-rays and is consistent with the reverse shock theory. *Credit: Vestrand et al. (2005).*

248, or ~57% of the total number of *Swift* GRBs[1]. Several possible explanations for these dark GRBs have been proposed, such as extinction factors relating to the GRB environment, host galaxy type and redshift.

One possible explanation is that optical emission may have been present, but decayed rapidly to below detectable limits by the time observations began (Groot et al., 1998; Li et al., 2003; Berger et al., 2002), or may have been intrinsically faint to begin with (e.g. Li et al., 2003). The lack of a sufficiently deep detection limit may also be due to adverse observing conditions, e.g. excessive sky brightness due to dawn, twilight or the

[1] Statistics were obtained from the *Swift* GRB table: http://swift.gsfc.nasa.gov/docs/swift/archive/grb_table.html

moon, or the field's proximity to nearby bright stars or the moon. This idea is supported by the detections of radio transients without optical transients (Hurley et al., 2002), and by the association of GRBs with star-forming regions, which are dusty, optically-thick environments. Within the burst environment dust obscuration may be due to a high gas column density (e.g. Lamb, 2001; Castro-Tirado et al., 2007) or dust in the host galaxy along the line of sight to the GRB (∼10% of dark events, Piro et al. (2002)). Since GRBs are at cosmological distances, there may also be significant foreground extinction due to the inter-stellar medium (ISM) (Paczynski, 1998). A low-density ambient medium can result in a sub-luminous afterglow (Groot et al., 1998), since the afterglow peak flux depends on the square root of the density of the ambient medium, leading to reduction of the afterglow peak flux by several magnitudes with respect to bursts that occur in higher density regions (Mészáros and Rees, 1997). Some fraction of bursts are expected to be located beyond $z \gtrsim 5$, so that the UV band is redshifted to optical wavelengths (Fynbo et al., 2001; Jakobsson et al., 2004). However, GRBs at high redshift can only account for ∼10% of these dark bursts (e.g. Gorosabel et al., 2004; Castro-Tirado et al., 2006b). Roming et al. (2006) used early observations of *Swift* GRB afterglows to investigate the most probable cause of dark GRBs. They found that ∼25% of the bursts were extincted by Galactic dust, ∼25% were obscured by absorption in the GRB environment and ∼30% were most probably affected by Ly-α absorption at high redshift. Rapid temporal decay and low-density environments were found not to be significant factors.

2.4 Conclusions

The fireball model provides a good description of the basic properties of observed afterglow behaviour. Other models, such as the Cannonball model (Dar and de Rújula, 2004), have not been developed to the same extent and do not offer the predictive power of the fireball model. However the simplified view of the simple fireball model does not explain some of the more complex afterglow behaviour described here and additional work is required to explain the richness of features observed in the X-ray and optical afterglows.

Chapter 3

The Watcher Robotic Telescope

3.1 Robotic Telescopes

3.1.1 Introduction

The key feature of a robotic telescope is that it can observe completely autonomously. Such telescopes require significantly advanced telescope control systems, drives and encoders to facilitate the location of targets. Unlike an automated telescope, which requires a manually input list of targets to observe every night, the robotic telescope can generate its own dynamic observing schedule based on information in its database. Parameters such as the priority of a target and its altitude during the night are all taken into account. This scheduling is also flexible enough to respond to external requests or events, such as new transient sources or activity, and return to its regular schedule when these observations are complete. Targets are located with a combination of high-precision pointing and star pattern recognition. To confirm that the target has been successfully acquired the system can compare the latest image to a catalogue, which provides feedback if corrections are required. The system must also be capable of safely dealing with an array of external local events, such as bad weather, power failure or the failure of a key component. The system can also be accessed and controlled remotely, if required, and provide remote users with access to data (Baruch, 1995; Williams and Mulherin, 2001).

3.1.2 Robotic Telescope Astronomy

A very large proportion of the available funding for ground-based astronomical hardware has traditionally been directed toward high-profile, large-scale projects which aim to build bigger and bigger telescopes. However, at the other end of the scale, an ever-growing number of science programmes are being carried out by smaller instruments operated in an automated or robotic manner. Scientists have found their research programmes hampered by the inflexibility and limited availability of observing time at large telescopes, and have devoted considerable effort to developing robotic systems better suited to their scientific requirements. Such instruments have become increasingly sophisticated due to a variety of technological advances, in particular the advent of CCD detectors and the widespread availability of powerful, affordable computers since the early 1990s. Overviews of the technological and scientific advances being made in the area of robotic telescope astronomy since the mid 1990s are given by Henry and Eaton (1994); Bode (1995); Chen et al. (2001); Oswalt (2003).

The main advantage of robotic telescopes lies in their flexibility, which allows sources to be studied in ways that are not possible with traditional facilities where observing runs are limited to a few nights at a time (Eaton et al., 2003). The study of variable sources like active galactic nuclei (AGN) (van Breda, 1995) and variable stars (Szabados, 2003) greatly benefits from long-term monitoring programmes that robotic facilities can carry out so effectively. Rapid, automated response capabilities also make robotic telescopes ideally suited to observations of transient sources like supernovae and GRBs. Manually operated and large (> 1 m) telescopes can respond on time-scales of minutes at best whereas small robotic telescopes can begin observing a target in seconds, opening up a previously unexplored regime in the time-domain study of transient sources (Andersen and Pedersen, 2004). Robotic telescopes also excel at carrying out surveys. Cosmological studies of the large-scale structure of the universe have been based on catalogues made by small telescopes (Huchra, 2003), and calibration tasks such as extinction monitoring.

3.1.3 The Gamma-Ray Burst Coordinates Network

Based on the theoretical models for γ-ray bursts, which predicted the presence of GRB counterparts, McNamara et al. (1995) concluded that optical follow-up work required deep imaging of GRB fields with response times of the order of minutes or less. In order to carry out such rapid follow-up observations observers required precise GRB positions to be calculated rapidly and distributed throughout the community. This triggered the development of the BATSE COordinates DIstribution NEtwork (BACODINE), a system to determine the positions of GRBs detected by BATSE and transmit the positions to sites worldwide on a time-scale of seconds (Barthelmy et al., 1995). The BACODINE system was subsequently expanded to include and distribute coordinates of GRBs detected by other orbiting high-energy observatories (Fig. 3.1) and was renamed the Gamma-ray burst Coordinates Network (GCN) (Barthelmy et al., 1998). Every source of GRB detection and localisation information that has come online in the intervening years has been added to the GCN so that it now provides accurate locations over a range of response times (Table 3.1).

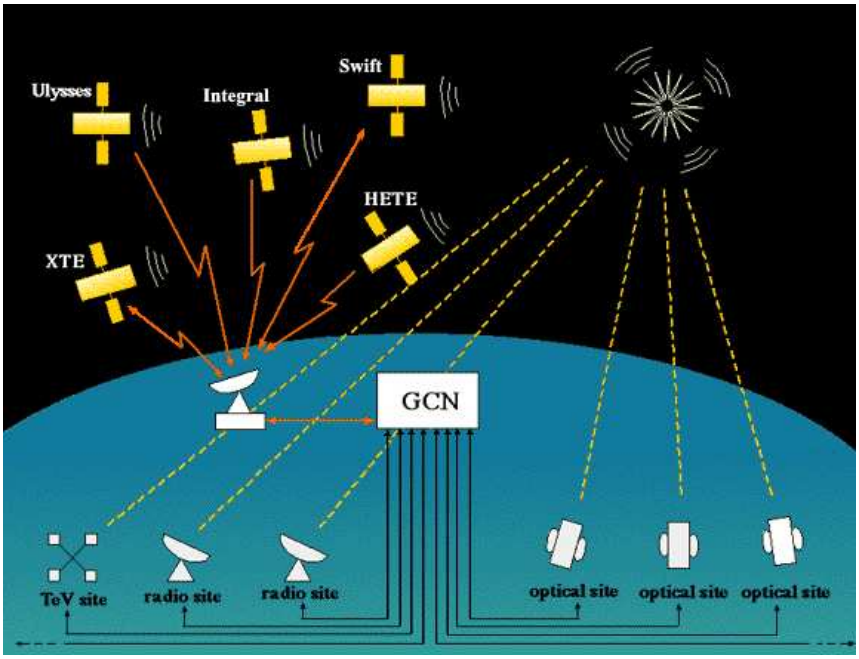

Figure 3.1: The Gamma-ray burst Coordinates Network (GCN). *Credit: http://gcn.gsfc.nasa.gov*

SOURCE	TIME DELAY	ERROR BOX	RATE
Fermi-GBM	~10 s	15′	20/month
Fermi-LAT	2–32 s	10–100′	~5/year
Fermi-LAT_REFINED	2–6 hr	5–30′	~5/year
AGILE_WAKEUP	~30 m	~30″	5–10/year
AGILE_GROUND	1–2 hr	3″	5–10/year
AGILE_REFINED	~2–5 hr	3″	5–10/year
Swift-BAT	13–30 s	1–3′	2–5/week
Swift-XRT	30–80 s	7″	2–5/week
Swift-UVOT	1–3 hr	2″	1–3/week
INTEGRAL_WAKEUP	~1 m	$> 10'$	1/month
INTEGRAL_REFINED	1–2 m	~5′	1/month
INTEGRAL_OFFLINE	1–3 hr	$< 5'$	1/month
IPN	0.5–1.5 days	5–20′	3/month
RXTE-ASM	1–2 hr	$4' \times 15 - 150'$	~8/year
RXTE-PCA	3–5 hr	6–40′	~6/year

Table 3.1: Details of active GRB satellite missions included in the GCN. ‘WAKEUP’ refers to the initial automated localisation of the burst. ‘REFINED / GROUND / OFFLINE’ can refer to either further automated pipeline processing of the burst, usually done when more data becomes available, or manual analysis of the burst, performed by ground personnel. *Credit: http://gcn.gsfc.nasa.gov*

A key feature of the modern GCN system is the distribution of GCN Circulars, short messages from researchers summarising observations that have been made, results, and plans for future observations, thereby allowing the follow-up community to make optimum use of the resources at its disposal. Another product which has recently been made available is the GCN Report. This is a short (1 - 2 page) final description of the observations and results of a group’s follow-up efforts on a specific burst. The main purpose of these reports is to facilitate the publication of data which, by itself, would not be sufficient for a paper, and also to allow the *Swift* team to distribute their γ-ray, X-ray, and optical lightcurves in a more timely manner. All GCN Circulars and Reports are archived on a page on the GCN website, which is updated in real time. In addition, there is a burst information page for each satellite, which is also updated in real time.

3.1.4 Recent GRB Satellite Missions

A summary of some of the satellite missions currently involved in GRB research is given below.

- **INTEGRAL:** The INTEGRAL satellite is an ESA mission primarily designed for high-resolution spectroscopy, imaging and accurate positioning of sources in the γ-ray domain (Winkler et al., 2003). Its main scientific objectives include studies of γ-ray line processes in stellar nucleosynthesis and large-scale structures, the high-energy physics of compact objects, and γ-ray bursts. It is capable of providing rapid and precise localisations to enable afterglow studies. The main instruments are the high-resolution spectrometer, SPI (20 keV - 8 MeV, Vedrenne et al. (2003)), and a high angular resolution imager called IBIS (15 keV - 10 MeV, Ubertini et al. (2003)). INTEGRAL is also capable of multi-wavelength observations with its X-ray monitor (JEM-X, Lund et al. (2003)) and Optical Monitoring Camera (OMC, Mas-Hesse et al. (2003)). All three of INTEGRAL's high-energy instruments use coded aperture techniques to image, localise and resolve γ-ray sources.

- **HETE-2:** The High Energy Transient Explorer (HETE-2) is a multi-wavelength mission dedicated to observations and localisations of γ-ray bursts (Ricker et al., 2003). It is equipped with a wide field γ-ray detector, FREGATE (1 - 500 keV, Atteia et al. (2003)), and two coded aperture X-ray detectors, the Wide-field X-ray Monitor (WXM, 2 - 25 keV, Kawai et al. (2003)), and the Soft X-ray Camera (SXC, 0.5 - 10 keV, Villasenor et al. (2003)), which can determine GRB positions accurate to $10'$ and $30''$ respectively. GRB locations are calculated by on-board software in real time for immediate relay to the GCN, within seconds of the burst trigger. Automated analysis engines process raw data, after it has been transmitted to the MIT control centre, and generate refined positions, typically 15 mins - 2 hours post-burst.

- **AGILE:** Launched by the Italian Space Agency in April 2007 (Tavani et al., 2006)

the primary goals of the AGILE mission is the broadband detection of GRBs and the study of implications for particle acceleration and high energy emission. AGILE is also engaged in studies of AGN, Galactic compact objects, supernova remnants, and unidentified γ-ray sources. Its main characteristic is its ability to simultaneously image sources at γ-ray and hard X-ray energies over a wide field of view with arcminute angular resolution. On-board triggering and localisation algorithms detect bursts and calculate positions, which are rapidly transmitted to ground. It has two primary instruments, the Gamma-Ray Imaging Detector (GRID), with an energy range of 30 MeV - 50 GeV and an angular resolution of $15'$, and the hard X-ray monitor Super-AGILE, with an energy range of 10 - 40 keV and an angular resolution of $2 - 3'$.

- ***Swift:*** Launched into low-earth orbit in November 2004 NASA's *Swift* mission (Gehrels et al., 2004) is a multi-wavelength observatory dedicated to the study of GRBs. As well as determining burst locations with unprecedented accuracy and speed, *Swift* can also study the little known regime of very early X-ray and UV/optical emission due to its rapid, autonomous slewing capabilities. *Swift* is the first GRB mission to cover the UV/optical wavelength range and includes a wide-field γ-ray Burst Alert Telescope (BAT), an X-Ray Telescope (XRT), and a UV/optical telescope (UVOT). BAT (Barthelmy et al., 2005) is a large FOV γ-ray detector which provides GRB triggers and initial positions accurate to $\sim 3'$. Its sensitivity spans the energy range from 15 - 500 keV, with an energy resolution of $\sim$7 keV. The XRT (Burrows et al., 2005b) is a broad-band (0.2 - 10 keV) X-ray imager designed to measure fluxes, spectra and light curves of GRBs and their afterglows, and in particular to provide rapid and accurate positional information. The instrument uses a focusing X-ray telescope and a single thermoelectrically cooled CCD detector yielding a field of view of $23' \times 23'$. For a typical GRB, positions accurate to $7''$ are obtained within 30 s of target acquisition. UVOT (Roming et al., 2005) is a 30 cm modified Ritchey-Chrètien telescope designed for the photometric and spec-

troscopic study of GRB UV/optical counterparts in the 170 - 600 nm wavelength range. The instrument is equipped with filter wheels carrying 11 broadband colour filters, UV/optical grisms, and a clear filter. The telescope's 17′ FOV is co-aligned with the XRT. The telescope's main function is to perform broadband UV/optical photometry of GRB counterparts from early (~100 s) to late times, and provide finding charts accurate to 0.3″ within ~300 s for ground-based follow-up observations. Photometric redshifts can be measured for bursts in the range $1.5 < z < 4.5$ (the Lyman-α cutoff is shifted beyond UVOT's sensitivity range for $z \geq 5$). Low-resolution grism spectroscopy can be performed on bright bursts, which can also facilitate redshift determinations.

- **Fermi:** The key scientific objectives of Fermi (de Angelis, 2001) are to understand the mechanisms of particle acceleration in AGNs, pulsars and SNRs, to resolve the γ-ray sky at high energies, to determine the high energy behaviour of GRBs and other transients, and to probe dark matter and the composition of the early Universe (Panaitescu, 2008). It comprises of two main instruments, the Large Area Telescope (LAT) and the Gamma-ray Burst Monitor (GBM) (Meegan et al., 2007). LAT operates in the range 20 MeV - 300 GeV and has a FOV of 2.4 sr, with the ability to localise GRBs to 10′ or less. GBM consists of 12 NaI detectors operating in the energy range 8 keV - 1 MeV, which will provide burst triggers and locations, and two BGO detectors observing in the energy range 150 keV - 30 MeV. The LAT and GBM can independently trigger on GRBs and spectra will be jointly fit when possible.

3.1.5 Robotic Telescope Systems

In recent years an increasing number of groups have become involved in the development of robotic optical telescopes for GRB follow-up observations. With the launch of *Swift* the availability of accurate GRB localisations at unprecedented response times and regularity

have made such instruments particularly relevant. Different scientific goals and varying levels of funding have resulted in a wide range of approaches being taken in the design of robotic follow-up instruments. Some of the instruments currently in operation are described below.

- **ROTSE-III:** The ROTSE-III telescope system is a worldwide network of 4 identical instruments at different longitudes (Texas, Namibia, Turkey, and Australia), which can provide continuous coverage of the night sky (Akerlof et al., 2003). Each ROTSE-III system is made up of a 45 cm telescope and a detector with a $2\,\mathrm{k} \times 2\,\mathrm{k}$ Marconi CCD chip, resulting in a total field of view of $\sim 2^\circ \times 2^\circ$. The mount was based on a commercially available model which was modified to provide high slewing speeds ($35^\circ\,\mathrm{s}^{-1}$ in both axes), which allows it to begin imaging targets within seconds of receiving alerts.

- **REM:** REM is a 60 cm telescope with a fast slewing capability (60° in 5 s), operating in the La Silla Observatory, Chile, since June 2003 (Antonelli and Team, 2005). The telescope is equipped with a high throughput Infrared Camera (REMIR) and an optical imaging spectrograph (ROSS) which are simultaneously fed by a dichroic. This allows for the collection of high S/N data in a large spectral range (0.45 - 2.3 μm).

- **TAROT:** The 25 cm TAROT telescopes consists of two instruments, one at the Calern Observatory in France and another, TAROT-S, at the ESO facility at La Silla. The relatively small size of these telescopes allows for slewing speeds of up to $80^\circ\,\mathrm{s}^{-1}$, resulting in extremely short target acquisition times of 1 - 1.5 s (Boer et al., 2003). TAROT-S serves as a very rapid wide-field companion to the REM experiment.

- **PROMPT:** The PROMPT experiment is a robotic telescope system comprising six 40 cm telescopes (Reichart et al., 2005) located at the Cerro Tololo Inter-American Observatory, Chile. Each telescope uses a Paramount ME mount (see § 3.2.6) and

can slew at $7^\circ\ s^{-1}$. Five of the telescopes are designed for imaging and are fitted with Alta U47+ cameras by Apogee, with each one optimised for a different wavelength range from NIR through to UV, while the sixth is equipped with a polarimeter. The system's capabilities for simultaneous multi-colour imaging enable it to construct spectral energy distributions across 8 filter bands and estimate photometric redshifts.

- **RAPTOR:** The RAPTOR experiment (Vestrand et al., 2002) links together eight wide-field monitoring and three narrow-field response telescopes to act as an autonomous system capable of identifying optical transients and carrying out follow-up observations in real-time. The wide-field monitoring system has a FOV of ∼1300 square degrees with a resolution of ∼35″ and is spread over a large geographical area, ∼38 km^2, providing stereoscopic images of the same field. Real-time processors instantly analyse the wide-field images and the positions of interesting transients are fed back to the mount controllers with instructions to point the narrow-field telescopes at the transient. The narrow-field instruments can perform simultaneous multi-colour imaging, low-resolution spectroscopy, and polarimetry.

- **BOOTES:** The BOOTES network (Castro-Tirado et al., 2004) is a system of wide-field imagers and narrow field response telescopes located in Southern Spain. The wide-field imagers consist of commercial 50 mm wide-field lenses (Nikkor, Japan) attached to two ST8 CCD cameras (Santa Barbara Instruments Group, USA). Each pair of the BOOTES wide-field cameras is mounted atop a 0.3 m LX 200 Meade telescope (Meade, USA), allowing long integrations of a previously selected region. The four cameras monitor the same region of the sky, both in the I and V bands. BOOTES-1 is located at El Arenosillo (Huelva) and BOOTES-2 at the Estacion Experimental de La Mayora (Malaga), 240 km apart. BOOTES-IR (Castro-Tirado et al., 2006a), located at Observatorio de Sierra Nevada in Spain, is a 60 cm Ritchey-Chrètien telescope equipped with high-throughput NIR camera featuring a HAWAII

HgCdTe Infrared detector array. BOOTES-IR has a blue-band enhanced optical CCD at one of the telescope's Nasmyth foci along with the NIR camera, using a dichroic to split the incoming light into visible and infrared, thereby allowing simultaneous observations in two bands. It is capable of slew speeds of $10^{\circ}\,s^{-1}$ and can point to any part of sky within 20 s, with a typical slew time of 5 s.

3.1.6 Robotic Telescope Networks

The next level of sophistication is an intelligent network, capable of identifying interesting phenomena and communicating with other instruments to request observations (Vestrand et al., 2004). The advantages of observing with robotic telescopes can be multiplied by combining individual instruments into networks. In its simplest form, a network can comprise several independent instruments operated by the same institution or collaboration. These systems can be distributed around the world with the aim of constantly monitoring the night sky (e.g. ROTSE-III), or can operate at the same site in order to perform simultaneous multi-colour photometry, spectroscopy, and/or polarimetry (e.g PROMPT). Common communication protocols are essential to the operation of advanced networks. One format which has been widely adopted is VOEvent, an XML-based protocol designed to communicate information on transient events (White et al., 2006). The VOEventNet[1] project combines information on transient events from many organisations and observing programmes and distributes alerts in the VOEvent format (Drake et al., 2006). Instruments on the network can then feed their results back into the system using the same messaging format. VOEvent alerts are openly available to the astronomical community, and currently provide information on supernovae, GRBs, and microlensing events.

[1] http://voeventnet.org/

3.2 Watcher System Description

3.2.1 Boyden Observatory

Boyden Observatory is located at 29° 08′ 20″ South, 26° 24′ 20″ East, 26 km from the city of Bloemfontein, South Africa. It has a long history of astronomy, going back as far as 1927 when it was initially set up as Harvard University's Southern Observatory. There are several telescopes on site, including a 13 inch refractor, a solar telescope and the original, recently refurbished, 1.5 m telescope (Fig. 3.2). The University of the Free State Physics Dept., along with a group of local contributors called The Friends of Boyden, have recently finished a visitors' centre at the observatory which includes an indoor and outdoor auditorium, exhibition area, viewing platforms and cooking facilities (for the occasional "brai" or BBQ). There is also a house on the site for an astronomer.

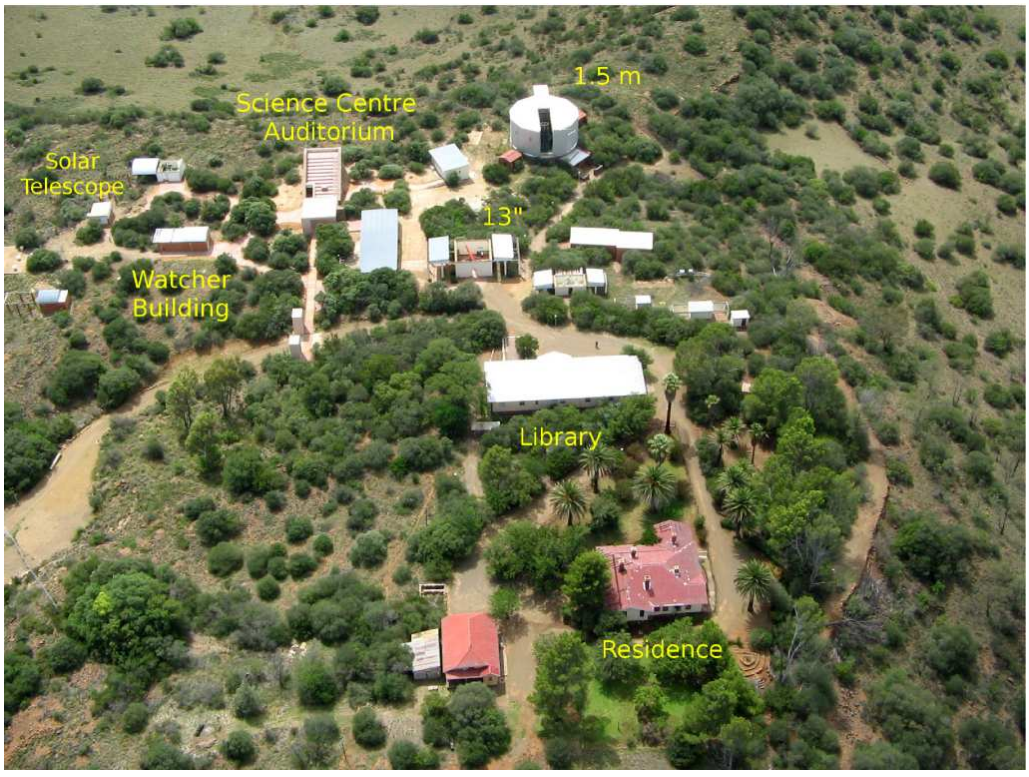

Figure 3.2: Layout of Boyden Observatory. *Credit: Juan Olivier*.

The site was chosen for 2 main reasons; location and weather. Although there are many robotic telescopes in operation worldwide, there are relatively few in the south-

ern hemisphere (ROTSE-IIIc is the only other GRB robotic telescope in southern Africa, located at the HESS site in Namibia (Fig. 3.3)). This leaves a sizeable gap when considering prompt GRB follow-up. When choosing a location for Watcher, this gap was taken into account and South Africa was deemed to be a suitable site to increase sky coverage. The other major factor was seeing conditions. While the site is relatively close to a city, it remains sufficiently remote to maintain low levels of light pollution. Weather conditions in the area are also favourable, especially during the winter, when the chances of cloud cover are minimal. Conditions, however, degrade during the summer months, with frequent afternoon thunder storms and a higher chance of cloud and rain. Lightning protection is provided by a lightning-conductor in the centre of the grounds. Another positive factor was access to on-site support by technicians from the University, which proves invaluable for maintenance and repair. The observatory also provides internet access via a microwave link to the University. Finally, the 1.5 m telescope may also be made available for follow-up observations of particularly interesting targets.

The main system components were tested in UCD before being shipped to Bloemfontein. A temporary structure was erected on the roof of the School of Physics building which allowed the basic functions of the mount, telescope and CCD to be tested. Watcher was installed to Boyden Observatory over the course of three on-site visits. The first trip (July 19 - July 31 2005) dealt primarily with the installation of the instruments and the set up of the PCs. On the second trip (September 09 - October 21) the telescope was properly balanced, polar aligned and the pointing capabilities of the mount were examined. However bad weather and interface problems between the mount and the control software caused delays. The third trip (March 13 - April 04 2006) allowed for the installation of a new mount (a Paramount ME) and the resolution of all other problems. The system began operations during the final week of March 2006.

Figure 3.3: Map of southern Africa showing the location of the Boyden Observatory and the site of the H.E.S.S. high-energy γ-ray project in Namibia, where the ROTSE–IIIc robotic telescope is located. *Source: Google maps.*

3.2.2 Dome

The Watcher building consists of three rooms; the control room, the telescope room and a small storage room (Fig. 3.4). The building itself was refurbished and modified to better suit the needs of an unattended telescope. The roof is of a roll-back design and originally was operated via a manual winch. A three-phase motor powered by a Hitachi SJ 100 Series Inverter was attached to the winch and controlled with custom electronics built in the UCD workshops. This can be operated from a handset or from the computer. Micro-switches at either end of the roof's tracks act as boundary points to stop the motor and also serve to report the status and position of the roof to the control software.

The roof itself had to be significantly modified to ensure that there was no possibility that the telescope could ever come into contact with it. The original horizontal support beams were changed to an angular design (Fig. 3.5) and careful consideration was given to the full range of motion of the telescope. The telescope room measures 4.9 m $\times$ 4.6 m $\times$ 2.82 m and the instrument itself is mounted on a 2 m high pier. This allows Watcher to

Figure 3.4: Front and side views of the Watcher building. The front room, with the roll-off roof, houses the telescope, while the control room housing the computers and other equipment is at the rear. The top image shows the building prior to refurbishment.

observe down to an altitude of ~8° in the east and west. In the north and south directions it is obstructed slightly by the previously mentioned lip (~17° altitude) and the rolled back roof (~25° altitude) respectively.

Figure 3.5: Watcher with the roof opened. The redesigned roof structure allows Watcher to observe close to the horizon while removing the possibility of a collision.

3.2.3 Telescope

The optical tube assembly (OTA) on Watcher is a single 40 cm Classical Cassegrain reflecting telescope (Fig. 3.6), provided by Optical Guidance Systems.[2] A Classical Cassegrain arrangement consists of a concave parabolic primary mirror and a convex hyperbolic secondary mirror positioned at the focus of the primary. The secondary mirror then focuses light back down through an opening in the primary mirror onto a detector (Fig. 3.7). This design serves to reduce spherical and chromatic aberration, especially for a small field of view. The tube is constructed of Tuned Carbon Fibre XZe, which com-

[2] www.opticalguidancesystems.com

Aperture	40 cm
Focal Length	570 cm
f/ratio	f/14.25
Secondary Diameter	10.8 cm
Back Focus	25.4 cm
Tube Diameter	49.5 cm
Tube Length	137.16 cm
Focuser Tube Internal Diameter	6.35 cm
Weight	42 kg

Table 3.2: OGS 40 cm Classical Cassegrain specifications

bines magnesium and aluminium to create a lightweight but thermally stable structure. This allows fast slewing of the OTA with the ability to reach any part of the sky in under 30 s. Detailed characteristics are presented in Table 3.2.

Figure 3.6: The OGS 40 cm Classical Cassegrain telescope

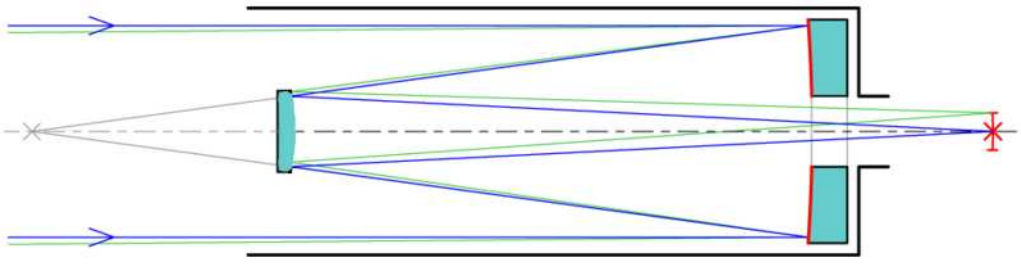

Figure 3.7: The Classical Cassegrain telescope design

3.2.4 CCD

The detector used is an Apogee AP6e CCD supplied by Apogee Instruments.[3] It consists of a scientific grade (< 100 bad pixels) array of 1024×1024, $24\,\mu$m pixels. It has a gain of 8 e^-/ADU and a typical readnoise of ~ 13 - $15\,e^-$ rms. It can read out an image in 1.5 s and is connected to a computer via a PCI card, which also provides the power. The speed of this readout is important, especially during time-sensitive observations such as GRBs. Thermoelectric cooling maintains the chip at $-20.0 \pm 1°$C at which the dark current is $\sim 1.5\,e^-$ pixel^{-1} s^{-1}. The chip itself is a front-illuminated Kodak KAF-1001e with a quantum efficiency greater than 50% over the visible spectrum (from 520 to 840 nm, see Fig. 3.8). The chip specifications are presented in Table 3.3.

Array Size (pixels)	1024 x 1024
Pixel Size	24 x 24 μm
Chip Size	24.6 mm x 24.6 mm
Digital resolution	14 bit
Sat. Signal	200,000 e$^-$
Sensor Noise	13 e$^-$
Dynamic Range	> 83 dB
QE @ 400 nm	40%
Peak QE (550 nm)	72%

Table 3.3: Kodak KAF-1001E CCD specifications

[3] www.ccd.com

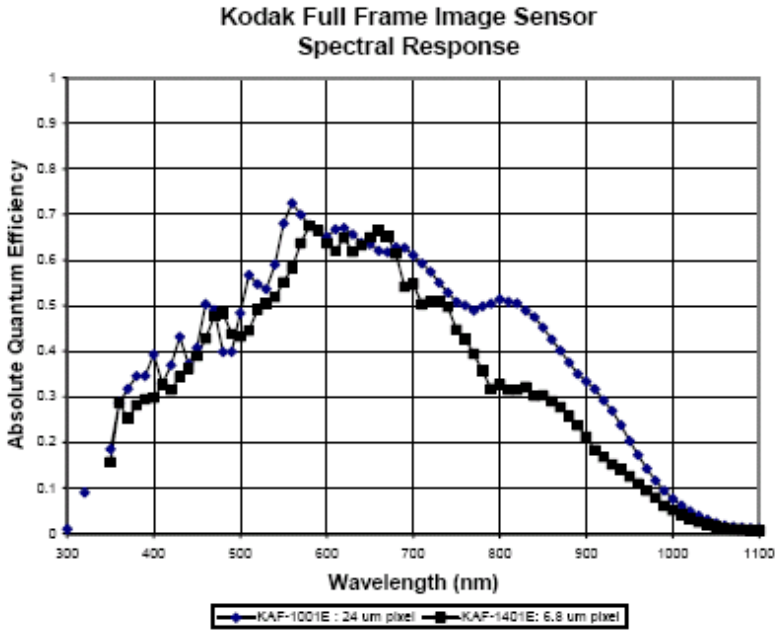

Figure 3.8: Kodak KAF-1001e quantum efficiency curve. *Credit www.ccd.com*

3.2.5 Field of View

Two important properties of any telescope are the field of view and the plate scale. The field of view is a measure of the size of the area of the sky that is covered per image. The plate scale is a measure of how much sky is imaged per pixel. For a CCD user it is convenient to measure this property in arcsec per pixel. To calculate the plate scale we take the focal length of the primary mirror, f in mm, and the CCD pixel size, μ in microns, and use the equation (Howell, 2000a):

$$P = \frac{206265 \times \mu}{1000 \times f} \tag{3.1}$$

where P is the plate scale in arcsec pixel^{-1}; 206,265 is the number of arcseconds in 1 radian[4] and 1000 is the conversion factor between millimetres and microns. The plate scale is then multiplied by the number of pixels on the CCD to calculate the field of view.

[4] 1 radian = 57.3° = 3,438′ = 206,265″

For Watcher this results in a plate scale of 0.86″ pixel^{-1}, and a field of view of 14.8′ × 14.8′ .

3.2.6 Mount

One of the most important parts of a robotic telescope is an accurate and reliable mount. The Paramount ME is a world-leading, high-end amateur mount. Movement is controlled by the MKS 4000 control system which employs brushless DC servomotors which can take instrument loads of 70 kg. These research-grade motors provide fast slew speeds of up to 7° s^{-1} with consistent torque and are designed to be almost frictionless, ensuring a long life span even when taking into account extended periods of operation. Periodic error in the movement of the gears can be corrected in software and errors that occur due to the stopping of the mount after slewing, called backlash, are virtually zero. With a good pointing model in operation the mount can achieve a pointing accuracy of ∼30″ .

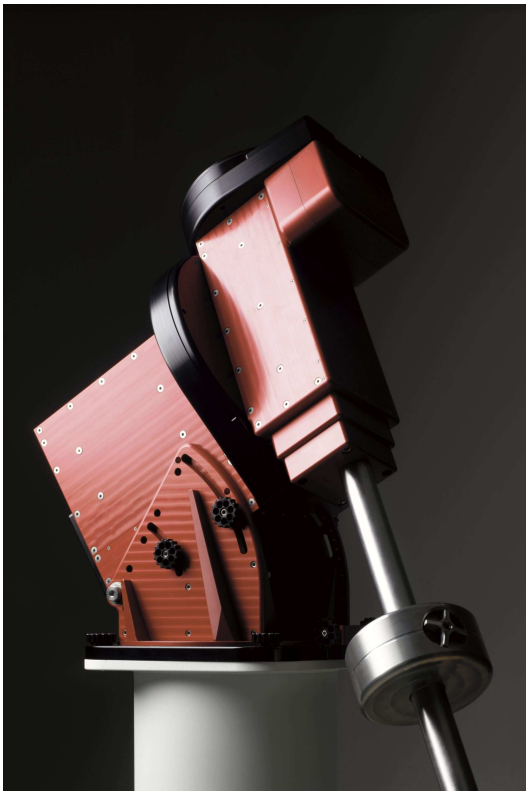

Figure 3.9: Paramount ME. *Credit www.bisqe.com*

Two of the most important aspects of the mount, from a remote observatory point of view, are the in-built safety features and the "AutoHome" system. AutoHome is an automated initialization process that slews both the right ascension and declination axes of the mount to a mechanically fixed position, called the Home Position. The control system must perform this step every time the mount is turned on so that the absolute position of the mount can be established (to the nearest one-third arcsecond). After homing, the mount "knows" its orientation and therefore cannot be slewed into the pier. The right ascension limits are approximately 5 degrees past the meridian in each direction (east and west) and in declination the limit is approximately -90 degrees. Homing also ensures that if there is ever a loss of power the mount can re-establish its position without human intervention. The mount motors are also equipped with current limiters, which means if the mount is accidentally slewed into a stationary object (e.g. the roof or pier) the movement is immediately aborted. Another convenient feature is through-the-mount cabling, which allows cables to be tidied and reduces drag on the OTA, as well as the chance of cables becoming entangled.

3.2.7 Filter Wheel

The Optec IFW[5] filter wheel consists of 5×50 mm diameter filters (Fig. 3.10). These contain the Bessell (Bessell, 1995) photometric filter set of B, V, R, I and clear (Fig. 3.11). Changing filters takes $\sim$3 s per slot. The system is connected to the computer via a handset and can be controlled either from this handset or from the PC. It is mounted at the primary focus of the telescope and the CCD is then mounted to it. The two are then secured with an additional custom mounting bracket, fixed to the drawtube of the telescope at one end and the base-plate of the CCD at the other (Fig. 3.12). The wheel has become unreliable, probably due to dust (as of summer 2008) and has been set to only take images in clear until a replacement can be installed.

[5] www.optecinc.com

Figure 3.10: IFW filter wheel system. *Credit www.optecinc.com*

3.2.8 Focuser

The Robofocus is a basic stepper motor used to drive the telescope's existing focusing mechanism. It is attached to the secondary mirror at the front of the telescope, replacing the original motor supplied which could not be computer controlled. It is mounted at the centre of the support structure holding the secondary mirror in place and black masking tape is used to minimise any light scatter that could be caused by the white power cable.

3.2.9 Weather station

To prevent damage to the system a reliable and accurate method of monitoring weather conditions is needed. The Davis Instruments Vantage Pro[6] wireless weather station is solar-powered and provides a suite of detectors including a rain collector, temperature and humidity sensors and an anemometer. Additional to these are a precipitation event

[6]www.davisnet.com/weather

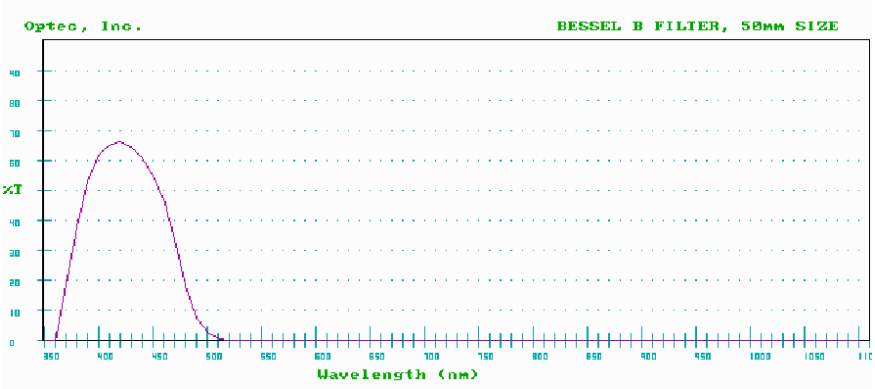

(a) B-band

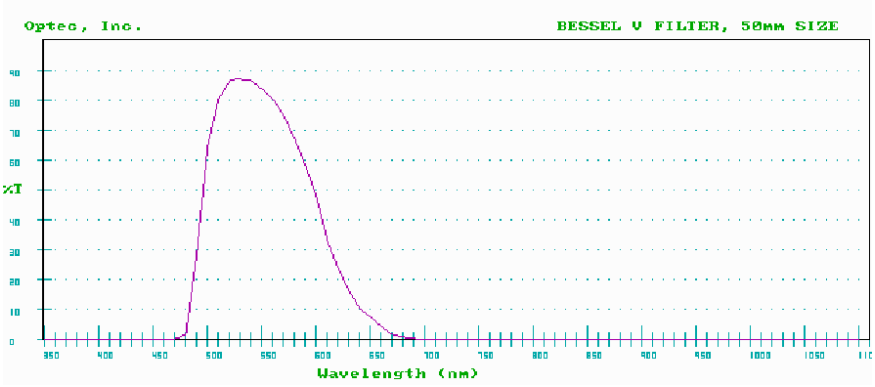

(b) V-band

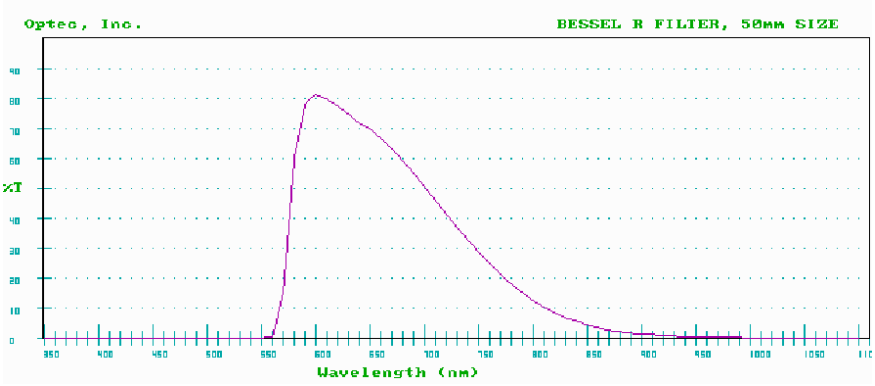

(c) R-band

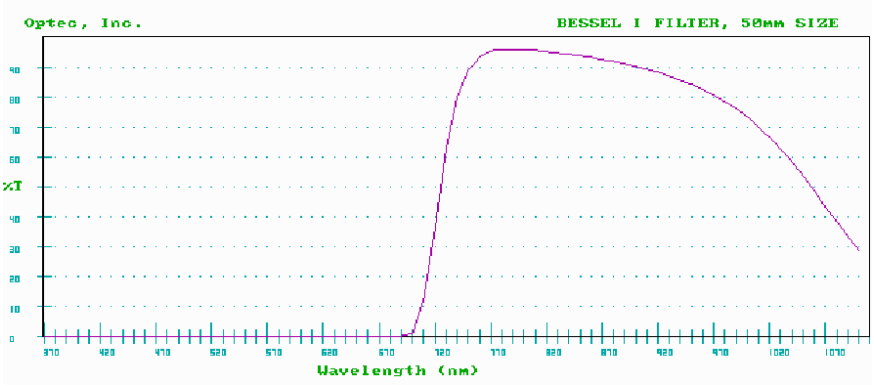

(d) I-band

Figure 3.11: Transmission curves for the Bessell BVRI filters

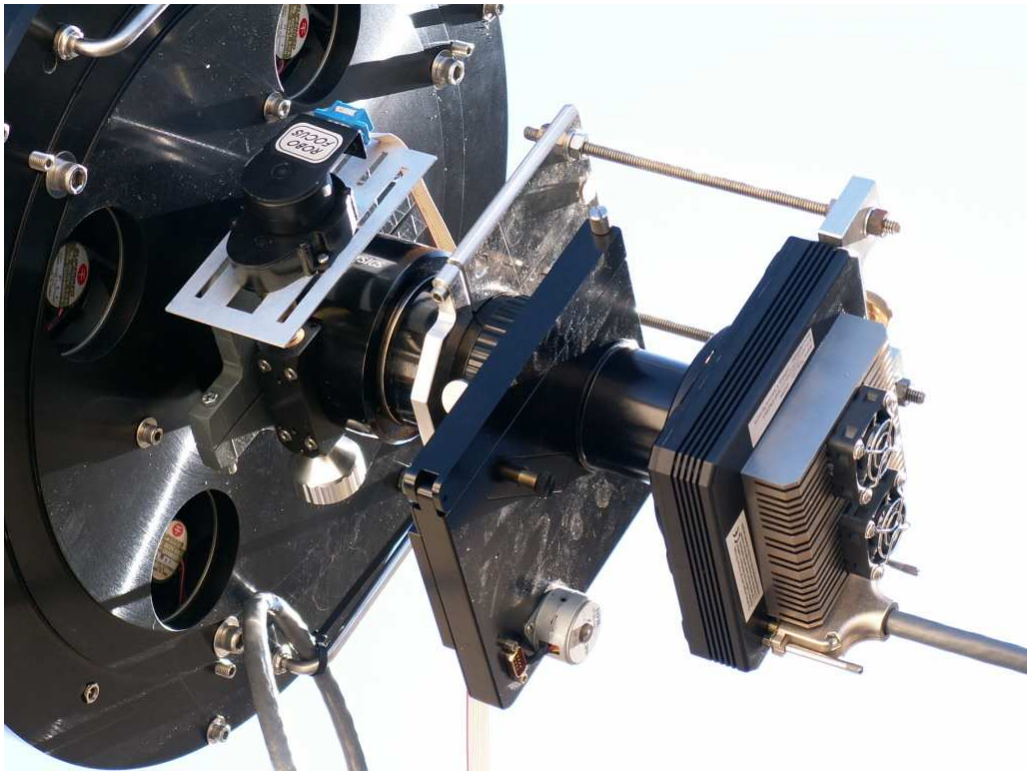

Figure 3.12: Detailed view of the rear of the telescope including the filter wheel, CCD and custom mounting bracket. Note the Robofocus was later moved to the secondary focus at the front of the telescope.

detector, provided by ROBOsky[7], and a cloud sensor, which was custom manufactured in the Czech Republic. The cloud sensor consists of two sheets of temperature probes thermally separated by a heat sink. It works by detecting the difference in temperature between the ground and the sky. A clear sky at night is cooler than the ground by a certain amount, which reduces when clouds pass overhead. With proper calibration this system gives an accurate report of cloud cover.

The system is mounted on the roof of a small auditorium opposite the Watcher building and connects wirelessly to a receiver placed inside the dome. This receiver is then wired into one of the computers in the control room and also contains barometric, temperature and humidity sensors. The system is capable of automatically responding to adverse weather conditions by ceasing observations and closing the dome. It then waits for an hour before attempting to open the dome again, to allow conditions to improve. It will

[7] www.robosky.com

also, as a safety precaution, shut the dome if communications with the weather station are lost. All weather logs are recorded to a database and are accessible through a convenient web interface.

3.2.10 Computers

Two Pentium 4 computers, watcher1 and watcher2, are used to control and coordinate the instruments. Each consists of a 2.4 Ghz processor, 512 Mb of RAM, DVD re-writer, 40 GB system disk and a 200 GB data disk. The data disk on watcher1 serves as the current image archive and is backed up to the data disk on watcher2. A 750 GB external hard disk is also attached to watcher2 to facilitate more long term backups of older data. For reasons of reliability, security and enhanced networking both machines are running distributions of Linux, Suse[8] 9.2 on watcher1 and Suse 10.3 on watcher2 (watcher2 is a newer version as it suffered a hard drive failure in early 2008 and the operating system had to be reinstalled). Watcher1 is also dual-bootable with Windows XP, which is convenient for running Windows-based telescope control and modelling software.

Responsibilities are divided between each machine but the central server is located on watcher1, which coordinates the various hardware and software components. Further details can be seen in Table 3.4. Network connection is provided by a dedicated microwave link from the observatory to the University of the Free State in central Bloemfontein. This allows remote access to the system via secure shell (ssh[9]) and also allows Watcher to email updates, and emergencies, to the Watcher team. It also provides access to the GCN, which gives Watcher the freedom to respond automatically and rapidly to GRBs without any human intervention.

Watcher1	Roof	Focuser	Filter Wheel	UPS
Watcher2	CCD	Mount	Weather Station	Webcam

Table 3.4: Division of hardware control between computers

[8] www.opensuse.com
[9] www.openssh.com

3.2.11 UPS

The Uninterruptible Power Supply used for Watcher is an MGE Systems Pulsar Evolution 2200.[10] It has a power rating of 1.54 kW / 2200 VA and doubles as a surge protector for all devices connected to it. In the event of a power failure the UPS is more than capable of running the entire observatory for about an hour, which allows enough time for main power to be restored in most cases. The load on the UPS in this case is ~20% of its full capacity, leaving ample room for the system to be upgraded with additional components at a later date. Closing the roof, parking the telescope and safely powering down the computers and all other components consumes ~2% of the total battery power. The computers are designed to reboot when main power is restored and are set to restart the system automatically. During a longer power outage the UPS is programmed to shut down the system when the battery charge reaches 30%. This margin is left purposely large to cope with the unlikely event that the mains power might be restored for a short amount of time, with the system booting to a fully operational status and then the mains power fails again. This remaining charge allows the UPS to safely shut the system down once again in this case.

3.3 Software

3.3.1 RTS2

The observatory control software used on Watcher is called RTS2[11] (Kubánek et al., 2006b) It was designed primarily by Petr Kubánek for use on the BART robotic telescope (Jelínek et al., 2004) in the Czech Republic. From the humble beginnings of a final-year computer science project, it is now responsible for the complete operations of the BOOTES telescope network (Castro-Tirado et al., 2006a) in Spain, the FRAM telescope (BenZvi et al., 2007) at the Pierre Auger Observatory, Argentina and Watcher in

[10] www.mgeups.com
[11] http://lascaux.asu.cas.cz/rts2

South Africa. It is written in C++ (an object orientated programming language) which is highly modular and allows for the easy addition of new hardware support. The targets are stored in a PostgreSQL database, which is extremely fast and configurable, and several user scripts are provided for database management. RTS2 has a particular emphasis on GRB follow-up observations and has the capability to monitor the GCN for news of new bursts, which it can then automatically observe. It is designed for the Linux platform and is open source and freely available.

One of the most crucial aspects of a robotic observatory is the ability for the system to automatically schedule a list of targets to observe. There are various approaches to the problem of scheduling (Granzer, 2004) each with their own advantages and disadvantages. Currently RTS2 bases its scheduling decisions on several factors; target altitude, lunar distance, time since last observation, number of observations and priority. Priority is a value set by the user that assigns merit to a target. The higher the priority the higher the chance the target will be observed. This means that the user does not need to interrupt the automatic scheduling routine when observations of a specific target are desired, the system will intelligently choose the best time to make the observations. Taking all these values into account the scheduler uses an algorithm to select targets in real time, including taking calibration frames at dawn and dusk. However, this makes it difficult to predict which targets will be chosen on a given night and at what times they will be observed. There are two methods to ensure observations of a target at a specific time. The first is to disable the scheduler completely and manually select the target. This requires the user to be logged in to the system at the appropriate time and to re-enable the scheduler afterwards to resume automatic observations. The second is to create an observation plan, detailing each target id and the start and end times of each observation. Under automatic scheduling a new GRB will be assigned the highest priority, overriding all other targets in the database. This priority diminishes slowly over the following ~48 hours to ensure follow-up observations are made.

RTS2 consists of a suite of programs which can be divided into four main groups;

hardware control, observation control, the central server and several miscellaneous scripts to aid user control. A schematic representation of RTS2 is shown in Fig. 3.13

3.3.1.1 Hardware Control

Each piece of hardware is managed by its own device daemon.[12] These daemons sit above the drivers of each component and provide a common communication method for operating hardware and returning status reports. This framework allows client programs to request operations from the hardware without the need for that client to have any knowledge of what type of hardware is being used. The following device daemons are currently being used on Watcher:

- `rts2-teld-paramount`: controls the Paramount ME telescope mount
- `rts2-camd-apogee`: controls the Apogee AP6e CCD
- `rts2-filterd-ifw`: controls the Optec IFW Filter Wheel
- `rts2-focusd-robofocus`: controls the Robofocus focuser
- `rts2-dome-dublin`: controls the Watcher observatory dome

3.3.1.2 Observation Control

There are two main scripts that handle actual observations; `rts2-selector` and `rts2-executor`. `rts2-selector` chooses the next target to be observed from the database (the automatic scheduler) while `rts2-executor` coordinates the observation, selecting the filter and exposure for the camera. After the image has been taken `rts2-imgproc` attempts to get astrometry on the image, using a combination of a package called astrometry.net[13] and the custom designed Jibaro astrometry package (de Ugarte Postigo et al., 2005). If this process is successful the image is saved to a directory on the hard drive to await further analysis by a user. If not, it is placed in a temporary directory for the system to attempt

[12] A "daemon" is a program that runs in the background, rather than under the direct control of a user.
[13] www.atrometry.net

astrometry again in the morning. Another program, `rts2-grbd`, waits for incoming alerts from the GCN. A new GRB is processed by creating a new target in the database based on the information contained in the alert. This new target is given the highest priority and so will immediately be selected by the scheduler. All of these daemons interact extensively with the database by reading data on the targets and writing new information on recent observations and images.

3.3.1.3 Central Server

The central server oversees management of the whole observatory and is responsible for tying together hardware control and client scripts. Every device daemon registers with the central server in order to be accessible by the various client programs. A client program contacts the central server which then passes the request for information or actions on to the devices. The devices can also make requests of the central server, for example if the weather station detects bad weather it reports the status to the central server, which then closes the roof and parks the telescope. It is also responsible for managing the time states of the observatory (day, evening, dusk, night, dawn, morning, day).

`rts2-mon` is a monitoring program that displays, and updates in real time, information on the status of the central server, all connected devices and all running client programs. It is based on ncurses, a programming library used to write text-based user interfaces which resemble graphical user interfaces (GUIs). This can be run in a terminal which, when run remotely, results in much less latency than a conventional GUI. It is possible to control various items via `rts2-mon` including; switching the server on and off, changing the currently selected filter and adjusting the cooling temperature of the CCD. It is also possible to disable the scheduler and manually select targets from the database through `rts2-mon`. Work is currently in progress on `rts2-soap`, a program to facilitate access to RTS2 through a web browser using the Simple Object Access Protocol (SOAP).

3.3.1.4 User Tools

A variety of command-line tools are included in RTS2 for accessing and updating the database. `rts2-targetlist` allows the user to see a list of all targets in the database. `rts2-targetinfo` provides more detailed information on an individual target, such as coordinates, priority, observation sequence and a table detailing the altitude of the target at each hour of the day. With the tool `rts2-target` it is possible to change certain values associated with the target, including enabling or disabling the target, changing the priority or changing the observation script (the sequence of exposures and filters used to observe the target). `rts2-user` is used to manage user entries and email lists, while `rts2-nightreport` provides observation reports on a night-by-night basis.

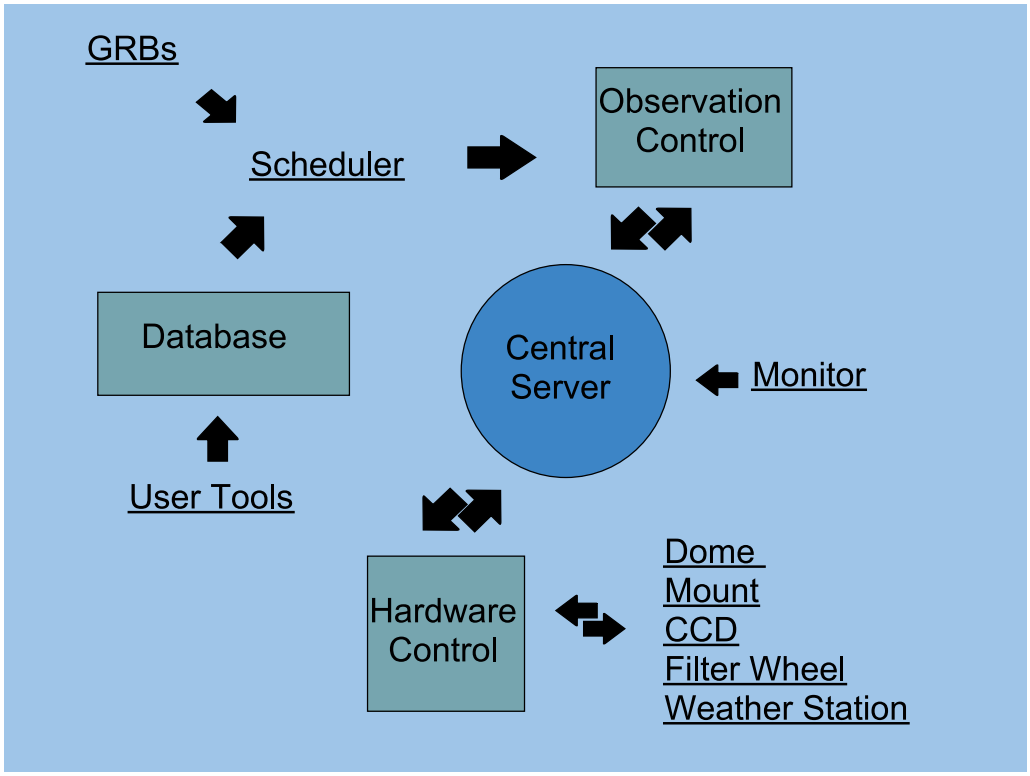

Figure 3.13: Schematic representation of RTS2

3.3.2 Other Software

3.3.2.1 Weather Station

The software used to manage the weather station is called the Meteo package.[14] It is a free suite of programs designed to gather information from the weather station and display it in a series of graphs. The station is polled once every second and the data stored in a MySQL[15] database. It can be viewed using a set of dynamically created graphs and a PHP-based browser interface. This information is also passed to the RTS2 central server which decides if it is safe to continue observing. In the event of bad weather (if it is raining or the wind-speed is above a certain safety threshold) or if communications with the weather station are lost, the central server will put the observatory into a *standby state*. In this state the roof is closed and the telescope is parked, but the CCD is still kept cool in the event that conditions improve and observations can resume.

3.3.2.2 UPS

The UPS is managed by the Network UPS Tools[16] (NUT) package. NUT is an open source suite of programs which provides a common interface for monitoring and administering UPS hardware over a network. The main UPS daemon, `upsd`, manages communications between the driver and the various client programs on the network. The main client program is `upsmon`, which monitors the status of the UPS and manages the safe shut-down of the PC when the battery level reaches a critical state. User scripts can also be run at shutdown using `upsmon`. The current status of the UPS (e.g. battery charge, load etc.) can be viewed using `upsc`.

Since the UPS is connected to watcher1, it acts as the master UPS server. All other computers on the network are slaves and only communicate with watcher1, not the UPS directly. A simple C program, `rts2-upsshutdown`, was written to connect to the central

[14] http://meteo.othello.ch
[15] http://www.mysql.com
[16] www.netowrkupstools.org

server and switch it to the *off* state. In this state the observatory is shut down completely, the roof is closed, the telescope is parked and the CCD is no longer kept cooled. This program is run by `upsmon` on watcher1 in the event that the battery charge becomes critical (set to 30%), before safely shutting down all other computers on the network.

3.3.2.3 Automated SMS System

For any robotic telescope concerned with GRBs the most crucial time is when observations begin on a new GRB. The data must be reduced and analysed as quickly as possible so that a GCN can be published. To facilitate this an automated SMS[17] alert system was designed as part of this work. In the event that Watcher begins observing a new GRB a text message containing details of the burst is sent to the Watcher team. The system is based on the fact that Watcher sends emails to users when starting a new GRB observation (among other events). When an email matching certain keywords is received in Dublin, an SMS is sent. This email keyword search is made easy due to the fact that our team has its own dedicated email server (bermuda.ucd.ie).

The text messages themselves are sent using an open-source script called `o2sms`[18]. `o2sms` is a command line program designed to send SMS messages using the websites of Irish mobile phone operators. It supports all three major Irish operators - O2 Ireland, Vodafone Ireland and Meteor Ireland. Each of these operators provide ~300 free text messages from their websites every month. It is important to note that the SMS is sent from the operator website, not from a physical mobile phone. So there is no need to leave a phone connected to a computer, although the system does require an active account with one of these providers.

The system works by scanning every email received for a certain set of key words (specifically “start GRB observation”). This is done on the email server itself using a `procmail`[19] script. Once a match is made the script parses several pieces of information

[17] Short Message Service or more commonly known as a Text Message
[18] http://www.mackers.com/projects/o2sms/
[19] http://www.procmail.org/

from the body of the email, including the burst name, coordinates, current airmass, which satellite detected the burst and Watcher's response time to the alert. It then passes these values to a short bash script, called `mailtosms`, which organises them into a message. The final part is handled by a perl script called `sendsms.pl`. To prevent multiple text messages being sent about the same burst `sendsms.pl` will first compare the name of the new GRB to a "blacklist". This is a list of older bursts that text messages have already been sent about. If the new GRB is not on that list it will send the message created by `mailtosms` to the Watcher team using `o2sms`. It will then add the burst name to the blacklist.

The system has worked well for over a year and was recently upgraded to include the details of the GRB it is reporting on (the original version only reported the name of the burst being observed). Future planned upgrades for the system include sending an SMS alert for events other than GRB observations, such as hardware failure, the loss of mains power or the roof closing due to bad weather.

3.4 Conclusions

The rapid, automated response capabilities of robotic telescopes make them ideally suited to observations of transient sources like GRBs. Small robotic telescopes can begin observing a target in seconds, opening up a previously unexplored regime in the time-domain study of transient sources. Since May 2006, Watcher has routinely carried out early observations of GRB error boxes on time-scales of tens of seconds to minutes. The system has detected 6 optical transients, three of which were observed while the GRB was still active in γ-rays, and has determined early upper limits to optical emission for a number of other GRBs (see § 6.1).

Chapter 4

CCD Photometry

4.1 Introduction

Charged Couple Devices (CCDs) have revolutionised modern astronomy. They will take their place in astronomical history along with other important technological advances such as the telescope, the prism, photographic plates and diffraction gratings. The increasing use and availability of CCDs for astronomical imagery has resulted in several major impacts upon modern observational astronomy. One impact is that CCDs provide the astronomer with a digital output that can be easily stored, copied and transported. In addition, digital images can be easily manipulated by computers enabling the observer to apply powerful tools that can highlight subtleties not obvious in the original image as well as allowing for the development of software that can automatically process and analyse the images.

CCDs have also allowed users of small to medium sized telescopes to make valuable contributions to observational astronomy. For many imaging projects there are advantages to using a smaller sized telescope, including better accessibility for long term survey work (e.g. searching for extra-solar planets) and better ability to react to targets of opportunity (e.g. GRBs). In order to fully understand the signal on a CCD image, it is necessary to first understand how a CCD works (§ 4.2) and its various limitations. General considerations

regarding photometry are presented in § 4.3. Firstly a brief overview is given of the celestial coordinate system (§ 4.1.1) and the magnitude scale (§ 4.1.2).

4.1.1 The Celestial Coordinate System

The coordinate system used to describe the positions of objects in the sky is based on an extension of the longitude and latitude system used on the surface of the Earth. It is convenient to imagine all stellar objects as lying on the inside surface of an infinitely large celestial sphere, with the Earth at the centre (Fig. 4.1). Extending the north and south poles from the Earth gives the north and south celestial poles. Similarly the celestial equator is an extension of the Earth's equator. Longitude is represented by right ascension (RA) and latitude by declination (δ). Declination is measured in degrees, minutes and seconds with 0° at the equator and ±90° at the north and south poles. Right ascension is measured in hours, minutes and seconds eastwards from Greenwich, London. The celestial sphere is divided into 24 hours of RA and the relationship between RA and δ is given by: 1 hour of RA = 15 $\cos\delta$ degrees. The cosine factor is needed due to the fact that the lines of RA converge at the poles.

Astronomers define several terms to refer to points specific to their observing site. The zenith is the point on the celestial sphere that is directly overhead. The meridian is an imaginary line from the north celestial pole to the south through the zenith. The altitude of an object is the angle between the local horizon and that object on the celestial sphere. At most locations on Earth (except close to the poles), when an object crosses the meridian (or transits) it is at its highest altitude. During the time needed by the Earth to complete a rotation around its axis (a sidereal day), the Earth moves a short distance (approximately 1°) along its orbit around the sun. Therefore, after a sidereal day, the Earth still needs to rotate a small extra angular distance before the sun reaches the same position in the sky relative to the Earth. A solar day is, therefore, nearly 4 minutes longer than a sidereal day. When the local sidereal time is equal to the object's RA the object will be on the meridian. This is the best time to observe the source as the amount of atmospheric

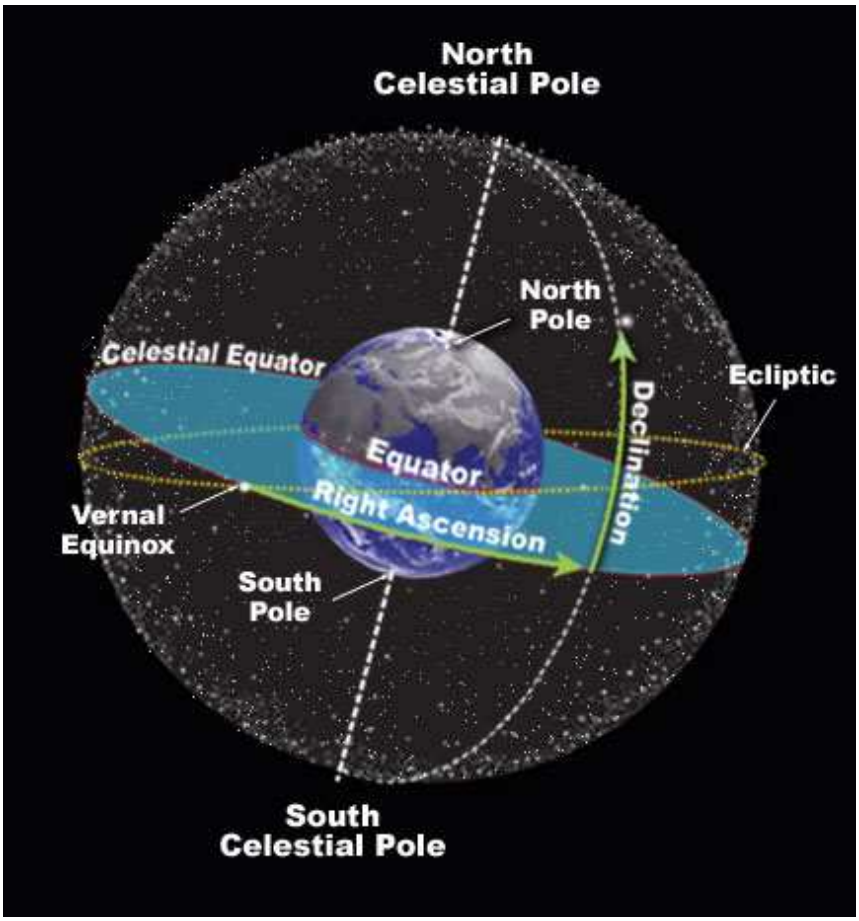

Figure 4.1: The celestial sphere. *Credit: www.onr.navy.mil*.

absorption (airmass) is minimised.

The Earth's pole precesses in space because of the torque of the Sun, Moon and planets with a period of nearly 26,000 yr, or an angular rate of $\sim 55''$ yr^{-1}. Because of this variation, the coordinates of a cosmic body only have meaning when the *epoch* is specified. Astronomers are currently using the J2000 epoch.

Astronomers use a system of dates called the Julian Day. This system was adopted in order to make it easier to work with different calendars and to unify different historical chronologies. It is defined as the number of days and the fraction of the day since Greenwich noon, January 1st, 4713 BC. It is also convenient for astronomers as the day changes at noon, rather than midnight.

4.1.2 The Magnitude System

The astronomical magnitude system provides a measure of the brightness of a celestial object. It is based on a star catalogue compiled by the ancient Greek astronomer Hipparchus ~200 BC. Hipparchus made visual observations of stars and placed the brightness of each on a scale from 1 to 6, with 1 being the brightest and 6 the faintest. When the technology was later developed to make accurate measurements of the brightness (or flux) of stars the magnitude scale was found to be logarithmic, with a difference of 1 magnitude corresponding roughly to 2.5 times the difference in brightness. This scale was formalised by Pogson (Pogson, 1856) where he defined 5 magnitudes to be a difference of exactly 100 times in flux. Thus each magnitude step is defined to be a factor of 2.512 ($\sqrt[5]{100}$) change in brightness.

The magnitude scale is defined by the equation:

$$m_1 - m_2 = -2.5 log_{10}\left(\frac{f_1}{f_2}\right) \tag{4.1}$$

where m_1 and m_2 are the magnitudes of the objects of interest and f_1 and f_2 are the fluxes (erg s^{-1} cm^{-2}) for those objects. For this system to be useful a zero point for the scale was needed. The star Vega was chosen as the reference point and given the magnitude of 0.00. Thus the magnitude of any other star is just the flux ratio between that star and Vega:

$$m_1 = -2.5 log_{10}\left(\frac{f_1}{f_{Vega}}\right) \tag{4.2}$$

- **Instrumental magnitude:** This is the raw measurement for the magnitude of a source. It is specific to a particular set of conditions including telescope, CCD, observing location, airmass, weather, position of the moon etc.

- **Apparent magnitude:** This is the calibrated brightness of a source, based on the comparison of the instrumental magnitudes to known standard stars.

- **Absolute magnitude:** This is the magnitude of a source if it were placed at a distance of 10 parsecs (32.6 light years). To calculate the absolute magnitude both the apparent magnitude and the distance to the source are required.

4.1.3 Filters

A CCD is sensitive to light over a broad range, from infrared through to ultra-violet (Fig. 4.4). To isolate certain parts of the spectrum for scientific measurement a set of standard filters is normally used. One common set of filters is the UBVRI (ultra-violet, blue, visible, red and infrared) system developed by Johnson, Kron and Cousins (Bessell, 1979). This set usually consists of 5 coloured glass filters. Coloured glass filters use chemical dye to restrict the wavelengths that they transmit. Most coloured glasses are cutoff filters, i.e. they only allow light above (or below) a certain wavelength. Originally a bandpass filter, i.e. a filter that only passes light between some upper and lower wavelength limit, was created by combining two coloured glass filters. One filter served to only pass wavelengths below some upper limit, the second only allowed wavelengths above some lower limit. The glasses were joined together with optical cement, which eliminated two air-glass interfaces. Modern bandpass filters are composed of many thin layers of dielectric materials, which have differing refractive indices to produce constructive and destructive interference in the transmitted light. In this way optical bandpass filters can be designed to transmit a specific waveband only.

4.2 Charge Coupled Devices

A Charge Coupled Device (CCD) is comprised primarily of silicon. It consists of an array of metal insulation semiconductor (MIS) capacitors (called pixels) in close proximity (Fig. 4.2). If an incoming photon of light strikes a pixel and is within a certain wavelength (or energy) range it will be absorbed by the silicon. This absorption causes the semiconductor to liberate a valence electron, via the photoelectric effect, and promote it to the

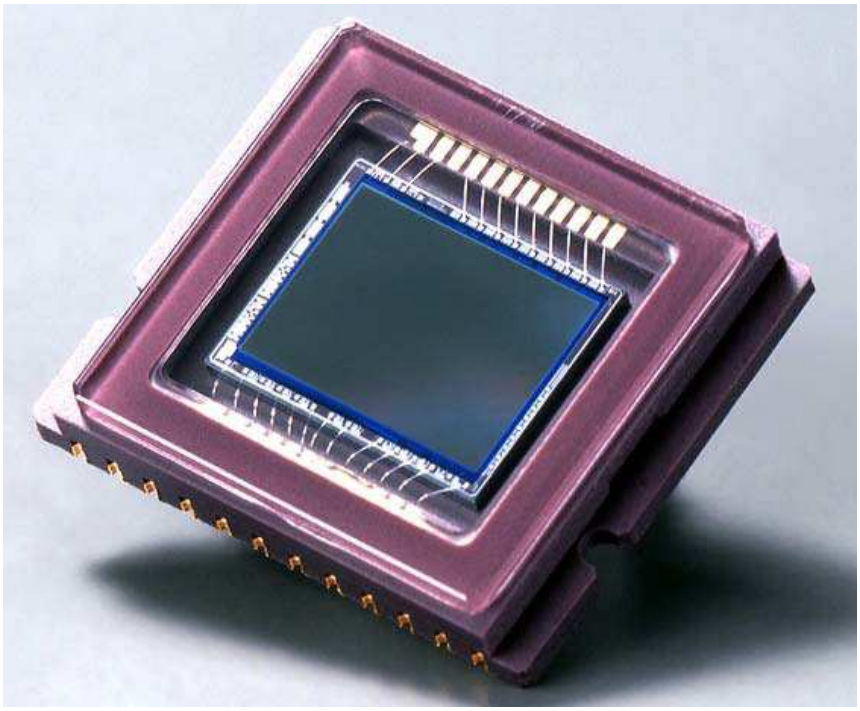

Figure 4.2: CCD image sensor. *Credit: www.fujifilm.com.*

conduction band. Silicon has a bandgap energy of 1.14 electron volts (eV) and a useful photoelectric effect range of 1.1 to about 10 eV, corresponding to a wavelength range from the near-IR to the soft X-ray (Rieke and Visnovsky, 1994). Photons of energies from 1.1 to ~4 eV (~11,000 to 3,000 Å)[1] generate single electron-hole pairs in the semiconductor, whereas those of higher energy (up to 10 eV) produce multiple pairs. The CCD appears transparent to photons above and below these limits.

At the end of an exposure the stored charge must be read out from the CCD. The charge in each pixel is shifted serially along the columns of the CCD from one pixel to the next (Fig. 4.3). In the AP6e CCD used on Watcher each charge transfer is ~99.997% efficient. The charge in the top row of pixels is shifted off the CCD to another row of pixels called the output shift register. This row is not exposed to light and is the bridge between the CCD and the output electronics. The charge in each pixel in the output shift register is read out one pixel at a time as a voltage value. These voltage values are typically in the range of 0.5 to 4 microvolts, so an on-chip amplifier is needed to boost the signal which is

[1]The conversion from wavelength to energy (in eV) of a photon is given by: E = 12,407 / λ (Å)

then digitised by an analogue to digital converter to produce the output signal in analogue to digital units (ADU) also known as counts. The conversion, from incoming photons to digital counts, is dependant on certain factors specific to each CCD including: quantum efficiency, gain, readout noise, dark current and the dynamic range of the chip. Each of these is discussed in turn below.

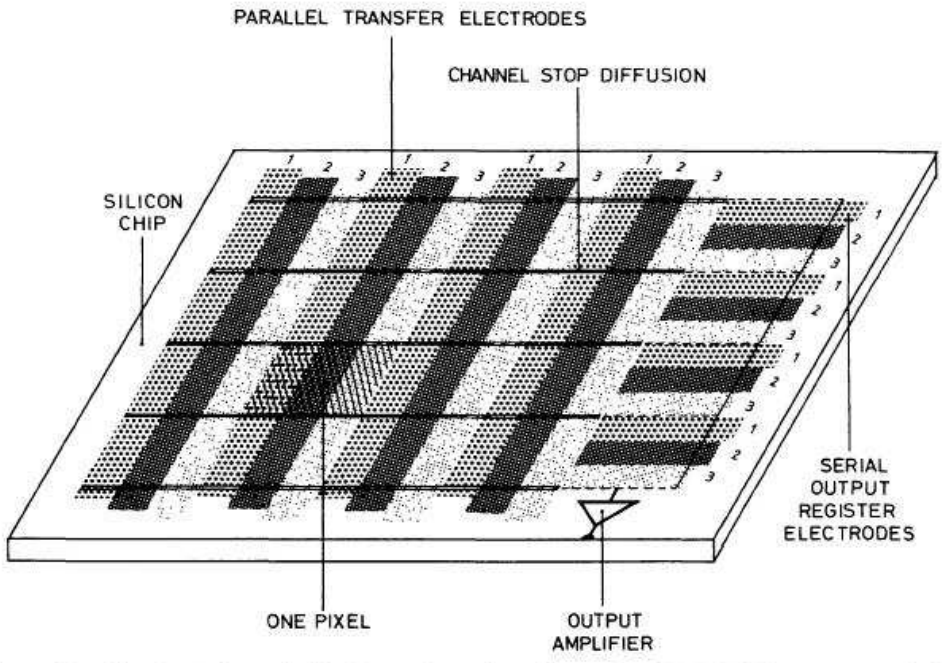

Figure 4.3: The basic layout of a three-phase two-dimensional CCD. The sequence 1, 2, 3 on each set of electrodes indicates the normal direction of charge transfer in the parallel and serial registers. *Credit: Mackay (1986).*

4.2.1 CCD Characteristics

"The only uniform CCD is a dead CCD" - Mackay (1986). Due to slight errors in the manufacturing process and imperfections on the initial silicon wafer, every CCD is slightly different. The characteristics of each CCD must be measured and understood before accurate scientific measurements can be made. Many of these non-uniformities, such as variations in quantum efficiency across the chip, can be reduced / removed with proper calibration frames. Others, such as the readout noise, cannot be removed and must be factored into the uncertainty on the final measurement.

4.2.1.1 Quantum Efficiency

CCDs are sensitive over a range of wavelengths. The total spectral range over which a detector is sensitive is called the bandpass. The efficiency with which the sensor converts an incoming photon into a photo-electron is called its quantum efficiency (QE). This efficiency varies over the bandpass but is typically over 50% for half of the spectral range and would normally peak at ~75% (see Fig. 3.8 for the QE curves of the KAF-1001e chip used in the AP6e CCD on Watcher). This response is governed by the material used to create the CCD, i.e. silicon, and the configuration type of CCD, i.e. a thin or thick detector, front-side or back-side illuminated, etc. Most standard CCD detectors are sensitive from ~300 nm to ~1000 nm. Outside this range the incoming photons will either pass right through the silicon or get reflected off the surface (although more specialised X-Ray CCDs have been developed for missions such as XMM-Newton). Fig. 4.4 shows a comparison of the various quantum efficiency curves for different types of CCDs over the visible spectrum.

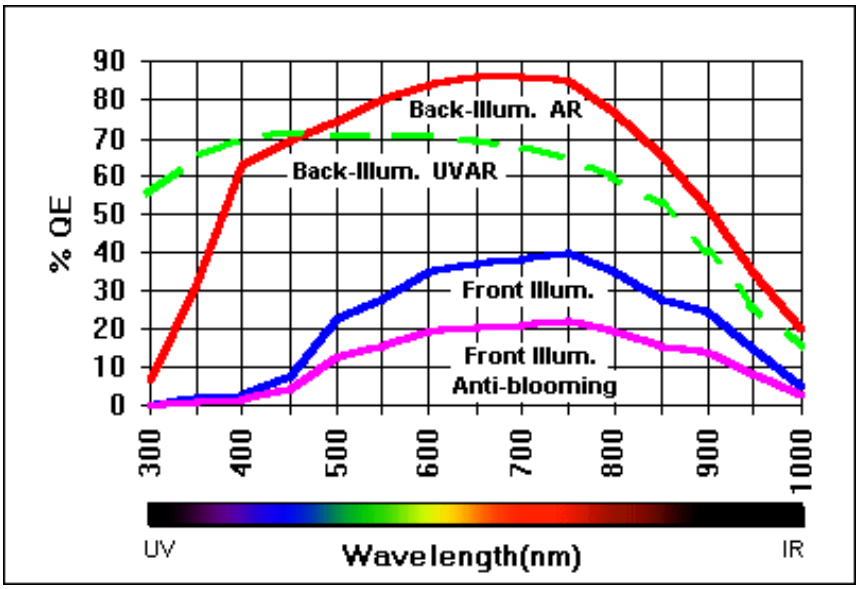

Figure 4.4: Sample quantum efficiency curves for back and front illuminated CCDs. *Credit: www.ccd.com*.

A CCD is manufactured from a single, integrated wafer of silicon. All the gate structures and surface channel layers are located on the front side while the back side, which

is just bulk silicon, is usually covered with gold foil. For a front-illuminated device incoming photons strike the front side of the detector passing through the surface gate structures before being absorbed by the silicon, reducing the overall QE of the chip. A front-illuminated CCD is usually about 300 microns thick, making it susceptible to cosmic ray absorption but providing a flatter imaging surface (Fig. 4.5). For a back-illuminated device the detector is mounted upside down and photons strike the back of the chip. The device is first thinned to ~15 microns by various etching techniques before being mounted in a rigid substrate. The advantage of this set up is that the incoming photons are absorbed directly by the silicon, rather than having to first pass through the gate structures, greatly improving the QE of the device and improving the response to shorter wavelength light. However, the thinning of the chip results in shallower pixel well depths and is more expensive to produce (Fig. 4.5).

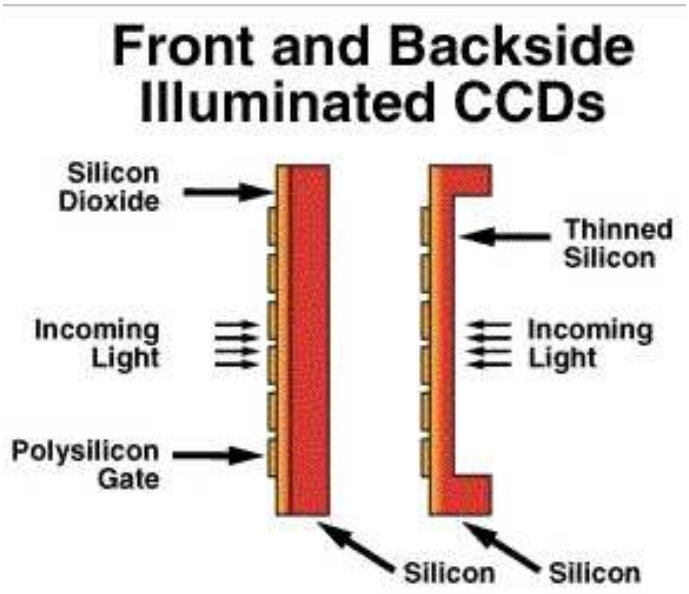

Figure 4.5: Front and Backside illuminated CCDs. *Credit: http://www.astro.virginia.edu/class/oconnell/astr511/lec11-f03.html*.

4.2.1.2 Gain & Readout noise

Readout noise is the noise associated with the readout electronics of a CCD. It is added to each pixel as the electrons are transferred from the CCD image area to the storage device.

For a CCD with a fixed gain value there are two indistinguishable components to readout noise[2]. The first is from random fluctuations due to the electronics while the second is introduced during the analogue to digital (A/D) conversion process (see § 4.2.1.3) and occurs in the on-chip amplifier and A/D converter. These two sources combine to give a statistical distribution of the noise for each pixel centred on a mean value. This distribution is not necessarily Gaussian (Merline and Howell, 1995). The physical size and temperature of the on-chip amplifier play a large role in the level of the readout noise. The readout speed is also a factor since a faster readout results in a hotter amplifier which increases noise (Janesick and Elliott, 1992). Modern CCDs have a readout noise of around 10 electrons per pixel. The value for the AP6e is 13 e^- pixel^{-1}.

The gain of a CCD is the number of electrons required in a pixel to register as one ADU in the A/D converter. The gain directly affects the dynamic range of the CCD and also introduces an inherent uncertainty in the measurement of the incident flux. A large gain setting may be desirable to make use of the full dynamic range of a CCD but it also means that a large number of photo-electrons is required to generate 1 ADU. A stellar magnitude calculation for a star, covering tens of pixels, could have a large uncertainty introduced at this level of gain. In general the gain is a fixed number set by the manufacturer but can by changed on some CCDs.

4.2.1.3 Dark Current

The dark current is a source of noise due to the temperature of the CCD. Thermal excitations in the silicon of the detector may, if high enough, promote electrons out of the valence band. These electrons will then be stored in the pixel well and are indistinguishable from electrons due to incoming photons. After an image has been read off the chip it is impossible to separate these electrons from the electrons generated by a light source. To minimise dark current it is necessary to cool the CCD. It is also important to keep the temperature stable as even a slight change can affect the dark current considerably. There

[2]These components can be separated for any device for which the gain is adjustable.

are two principle methods of cooling a CCD. In major professional observatories a CCD is cooled to about -100°C by using liquid nitrogen. The temperature is then usually kept constant (±0.1°C) by the use of a small on-board heater. This method is expensive and requires regular refills of liquid nitrogen, which is not feasible for a remote, robotic observatory. A more cost efficient method is thermoelectric cooling, which merely requires an electrical power source to operate. Most commercial CCDs use Peltier cooling (Martinez and Klotz, 1998) and can achieve temperatures from -20°C to -50°C, ±1°C. Typical values of dark current in modern thermoelectrically cooled CCDs are below 5 electrons per pixel per second (the dark current on the AP6e is 1.5 e^- pixel^{-1} s^{-1}).

4.2.1.4 Signal To Noise

For a CCD, the signal to noise ratio (S/N) of a detection provides a measure of the significance of that detection. A high S/N means that the source signal is well above the combined sources of noise. This calculation is especially important when trying to identify faint sources, such as some GRBs. For sources close to the level of the background, the S/N will be the major factor in determining whether a source has been detected and the reliability of that detection.

For a bright target the dominant source of uncertainty is the photon noise. The photon noise is described by Poisson statistics, therefore for a signal N, the associated noise term is just $\sqrt{N}$. The simplest form of the S/N equation, in which the only source of noise considered is photon noise, is given by:

$$\frac{S}{N} = \frac{N_{star}}{\sqrt{N_{star}}} = \sqrt{N_{star}} \tag{4.3}$$

where N_{star} is the signal from the star alone. This signal can be from an individual pixel, or from a number or pixels. Most often a source is measured by placing an aperture around the source and counting the total number of ADU from the pixels within that area.

For faint sources, however, the photon shot noise is no longer the dominant factor in the noise and the other sources of noise need to be taken into account. The background, or

sky, level may be another source of noise in an image. It is extremely variable and caused by sources such as urban light pollution, the moon, high level cloud and the airmass. To minimise this noise observations must be made from a dark site i.e. away from an urban area and/or at high altitude. Physical variations across the CCD can also affect the measured background level in different areas of the chip. A source-free region on the CCD is needed to measure the background level of the sky. Most software packages make estimates of the background by placing an annulus around the source. This annulus is typically centred on the source but does not include any signal from the source itself. The software then uses this selection region to determine the mean sky pixel level in ADUs. A larger area is preferred as this provides a better background estimation but taking too large an area may include another nearby star so care must be taken, especially in crowded fields (Fig. 4.6).

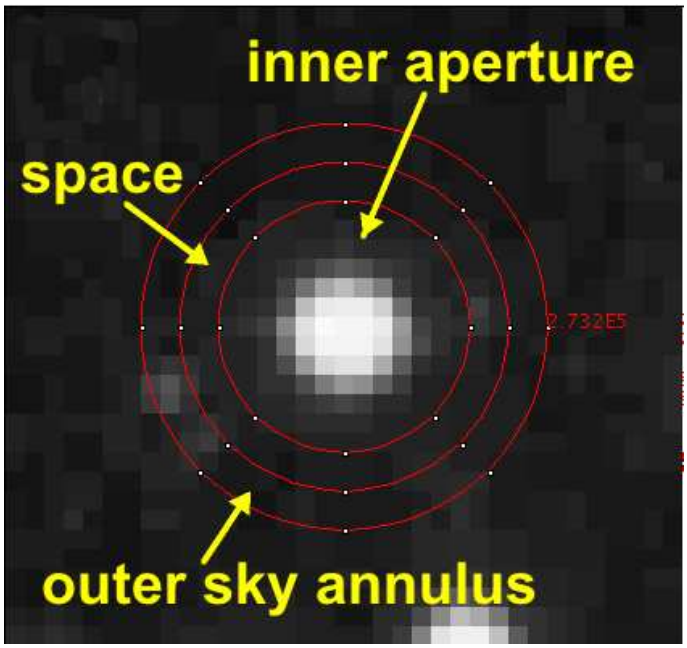

Figure 4.6: In aperture photometry an aperture is used around the source to calculate the signal from the source and a surrounding annulus is used to estimate the background level. *Credit: http://www.astro.physik.uni-goettingen.de/ hessman/ImageJ/Book/Measuring_Brightness/.*

The dark current associated with the CCD is also described by Poisson statistics and the dark noise increases as a function of time. The final source of noise is the readout

noise, which behaves as a shot noise source rather than a Poisson noise source, and therefore is entered into the equation as the value itself and not the square root of the value as Poisson noise sources are. Taking all of these sources into account gives the "CCD Equation" (Mortara and Fowler, 1981):

$$\frac{S}{N} = \frac{G \cdot N_{star}}{\sqrt{G \cdot N_{star} + n_{pix}(G \cdot N_{sky} + t \cdot N_{dark} + N_R^2)}} \tag{4.4}$$

The signal component of this equation is given by N_{star}, the signal from the star, multiplied by G, the gain of the CCD, to convert the value from ADU to the total number of photons collected from the source. The noise component comprises the photon noise from the source in photons (N_{star} multiplied by the gain G), the sky background level in photons (N_{sky} multiplied by the gain G), the dark current (N_{dark} multiplied by the exposure length, t) and the readnoise squared, N_R^2. The latter three components must be multiplied by the number of pixels under consideration, i.e. the area of the aperture used to determine N_{star}.

A more complete version of the "CCD Equation" is given in Merline and Howell (1995):

$$\frac{S}{N} = \frac{G \cdot N_{star}}{\sqrt{G \cdot N_{star} + n_{pix}(1 + \frac{n_{pix}}{n_B})(G \cdot N_{sky} + t \cdot N_{dark} + N_R^2 + G^2\sigma_f^2)}} \tag{4.5}$$

This equation contains two extra terms and is most appropriate in cases of high background level, poor sampling of the background level or large gain values. The first extra term n_B is the number of pixels used to determine the background level. From equation 4.5 it is clear that using as many pixels as possible (within reason) is preferred. The term, $G^2\sigma_f^2$, is used to account for the quantisation error introduced within the A/D converter, where σ_f is an estimate of the 1-sigma error introduced during the conversion from electrons to ADU. It is based on how the A/D converter behaves when dealing with pixels that do not have enough electrons to result in a full ADU step (e.g. a pixel with 4 electrons when using a gain of 8). Under the assumption that a charge level that is half way between two output ADU levels has an equal chance of being assigned to the lower or

the higher ADU value, σ_f is calculated to be approximately 0.289 (Merline and Howell, 1995). Using a high gain value will increase this source of noise.

In discussing other important applications of array detector technology (e.g. infrared CCDs) a term is missing from Eq. 4.5 to take account of the impacts of residual response variations among pixels after flat-field correction. These residual variations are due to slight differences among pixels in their relative spectral response combined with the fact that the flat-fielding source spectrum will not in general match the target source or the sky spectrum. These residual fluctuations can be at the few % level, and in high-background situations, or for bright sources, can become the dominant determining factor in maximum achievable precision, leading quickly to a saturation of achievable S/N as a function of integration / observation time. To take this effect into account the following term would need to be added to the other variance terms under the root sign in the denominator of Eq. 4.5:

$$G^2 \cdot a^2((N_{star} + n_B \cdot N_{sky})^2 + (n_B \cdot N_{sky})^2) \tag{4.6}$$

where a is the rms residual pixel-to-pixel response fluctuation after flat-fielding. This term is the variance on the differential source-background measurement due to residual pixel-to-pixel response non-uniformity.

4.2.1.5 Dynamic Range

The dynamic range of the CCD is the maximum number of photoelectrons that each pixel can register before being filled (or saturated). The dynamic range is often represented as a log ratio of the well depth to the readout noise in decibels. This is given by the equation (Howell, 2000b):

$$DynamicRange = 20 \times log_{10}\left(\frac{D_{well}}{RN}\right) \tag{4.7}$$

where D_{well} is the well depth in electrons and RN is the read noise in electrons. For

the AP6e the dynamic range is $20 \times log_{10}(185000/13) = 83\,dB$.

This ratio D_{well}/RN also gives an indication of the number of digitization levels that might be appropriate for a given sensor. For the KAF–1001E used in the AP6e, the ratio of well depth to read noise is $\sim 185,000/13 = 14,230$. The number of digitization levels is dependent on the number of bits used in the A/D converter. The total range of values that a specific number of bits can represent is given by 2^{bits}. The AP6e CCD has a 14-bit A/D converter, which gives $2^{14} = 16,384$ meaning it can represent numbers between 0 and 16,384 which adequately covers the dynamic range of the pixels. The CCD can be saturated by overloading either the pixel well capacity or the A/D value. The pixel saturation is given by the well depth divided by the gain. The A/D saturation is given by the number of digitization levels multiplied by the gain. For the AP6e pixel saturation will occur at a value of $185,000/8 = 23,125$ ADU and the A/D saturation occurs at $16,384 \times 8 = 131,072$ input photo-electrons.

One of the advantages of a CCD is that it has a linear response over a large range. This means that the relationship between input value (charge collected in each pixel) and output value (digital number, or counts, stored in the output image) is linear over most of the dynamic range of the chip. A CCD can, however, become non-linear at the high end of the input values. Most professional CCDs reach one of the two saturation limits (either pixel full well capacity or A/D saturation) before they enter the non-linear regime of the chip. However care must be taken to ensure this is the case, especially if a chip has an adjustable gain setting (which changes the saturation levels). It is important to know the linear range of the CCD and to be aware of the fact that even though some pixels may not be saturated they may still be within the non-linear range and therefore unusable.

4.2.2 Calibration Frames

A raw CCD image contains a mixture of two types of information, signal due to photons from astronomical sources and unwanted noise due to both background and electronic sources. In an attempt to account for the noise in an image several calibration frames

must be taken. Once the images have been 'cleaned', or reduced, they can be used in scientific analysis. The different calibration frames needed for astronomical photometry are detailed below.

4.2.2.1 Bias & Dark Frames

Bias Frame: A bias frame is a measure of the underlying noise of a CCD due to the on-chip amplifiers. This occurs as low level variation between pixels across the entire array. The bias should remain constant over time and the rms of the bias value is the read-out noise of the CCD. A bias frame is taken by leaving the shutter of the CCD closed and exposing for a time of zero (or as close to it as the settings on the CCD will allow). To accurately sample the bias level it is recommended to create a master bias frame, consisting of the average of at least 10 bias frames. These can be taken at any stage during an observing run.

Dark Frame: A dark frame is primarily a measure of the thermal noise (dark current - see §4.2.1.3) of a CCD. It also contains information about hot or dead pixels on the CCD and the level of cosmic ray strikes at an observing site. If the CCD is cooled using liquid nitrogen then the dark current is usually negligible and a dark frame is unnecessary. For thermoelectrically cooled CCDs, however, there may be a considerable dark current and a sequence of dark frames is required. The dark current of a CCD is related to the length of the exposure, therefore it is necessary to take dark frames for the same exposure lengths as the object frames. A dark frame is taken by leaving the shutter closed and exposing the CCD for the same time as the object frames (e.g. if a mix of 10 s, 30 s, and 60 s images are planned during the night dark frames corresponding to these exposure lengths must be taken). Multiple dark frames should be averaged to create master darks for each exposure length required. The dark current depends on the temperature of the CCD so dark frames should only be taken once the CCD has been cooled to its operational temperature. It can also change with time so darks should be taken frequently e.g. at the start and end of

every observing run. In an ideal situation a dark frame would be taken before and after every object frame, however this would severely affect the duty cycle of the CCD. Since the dark frame is created with the shutter closed it also contains the bias level of the CCD, so it is unnecessary to take separate bias and dark frames. Fig. 4.7 shows an example of a dark frame.

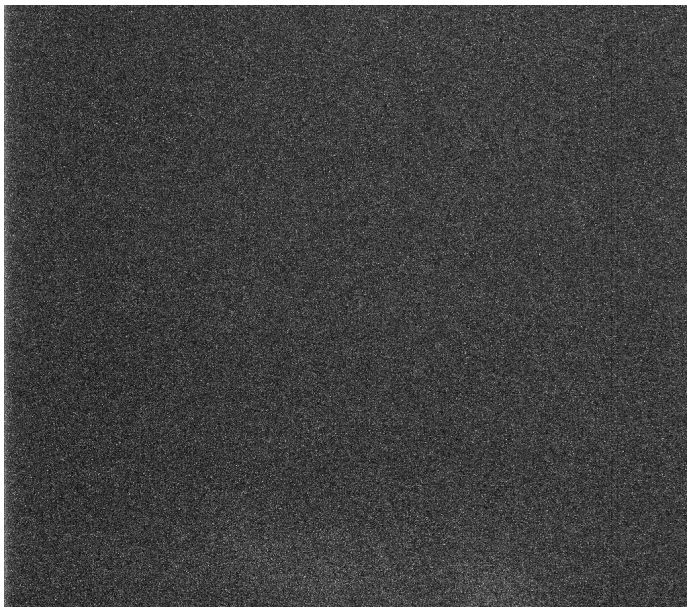

Figure 4.7: An example of a dark calibration frame showing uniformity accross the CCD, taken with the AP6e on Watcher.

4.2.2.2 Flat Fields

A flat field image serves to correct several different problems related to a CCD image. The main purpose of a flat field is to account for quantum efficiency variations across the pixel array. Each pixel has a slightly different QE value and responds differently to the incoming wavelengths of light due to variations in manufacturing. The flat field is also used to compensate for any image vignetting due to the optical tube assembly and dust accumulation on any of the optical surfaces. Ideally, a flat field image consists of uniform illumination of every pixel by a light source of identical spectral response to that of the target images. Since the CCD also responds differently across the range of the bandpass, a flat field needs to be taken for each filter to be used. It is also necessary to have a

high enough S/N level in the frames, in order to identify true fluctuations across the chip, but not so high as to saturate the pixels. In practice it is extremely difficult to achieve a 'perfect' flat field.

There are two methods of taking flats; dome flats and sky flats (Massey and Jacoby, 1992). A dome flat is taken by pointing the telescope at the underside of the closed dome, or a projector screen. This surface is illuminated with a bright light source and the telescope is pointed directly at the bright spot. A sky flat is an image of the sky at dawn or dusk, when there is enough ambient light to illuminate the CCD but not enough to saturate it. Neither of these methods replicate the spectral conditions of night-time imaging exactly but are accurate enough for most astronomical requirements, such as photometry and spectroscopy. As with the dark and bias frames, many flats should be taken in each filter and then averaged to create a set of master flat field frames. Fig. 4.8 shows an example of a flat field.

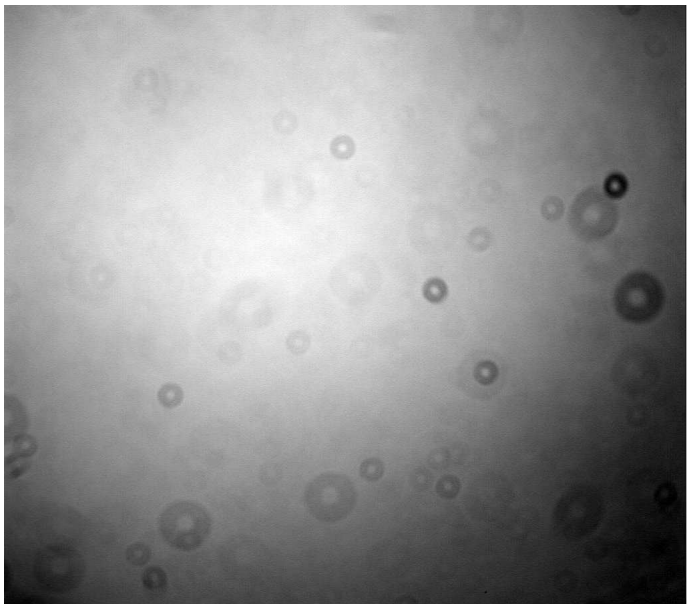

Figure 4.8: An example of a flat field calibration frame taken with the AP6e on Watcher. Note the dust rings and slight vignetting effect.

4.2.2.3 Image Reduction

The final reduction of an astronomical image is a relatively simple process. Taking several sets of the calibration frames described above – bias, dark frame and flat field – provides the user with a good base for creating master calibration frames. It is these master frames that are ultimately applied to each image frame. The calibration equation is given by (Gullixson, 1992):

$$Reduced\ Image = \frac{Raw\ Image - Dark}{\overline{(Flat - Dark)}} \tag{4.8}$$

The dark frame must be subtracted from both the raw image and the flat frame as both have been affected by the dark current and bias level. The signal level in the flat is arbitrary, as it depends on the twilight sky etc., so the dark-subtracted flat field is normalised to 1. The dark-subtracted raw object image is then divided by this normalised, dark-subtracted flat field. This results in a clean, flattened, 'reduced' image ready for scientific analysis.

4.3 Photometry

Photometry is the measure of the brightness of a source. Modern astronomical photometry essentially boils down to the conversion of the flux (counts) of a source on a CCD image to the standard magnitude system. Once the image has been taken and properly reduced, the 'instrumental' magnitude of the target is calculated. The effect of the atmosphere on both the brightness and colour of the target object must then be taken into account. Using multiple observations of standard stars at different airmasses and in different filters it is possible to correct the measured instrumental magnitude. These corrections result in the apparent magnitude of the object if the atmosphere were not present (or at zero airmass).

Standard stars are carefully selected to have known magnitudes and colours. They are stable (i.e. non-variable) and are of an acceptable brightness (i.e. bright enough to

be easily detected but not so bright as to saturate the CCD). The most commonly used stars that fulfil the above criteria are the Landolt standard stars (Landolt, 1992) which and are located close to the celestial equator, making them visible to observatories from both hemispheres. They are distributed in groups approximately every 1 hour in right ascension, so there is always a selection of standard stars available throughout the night.

4.3.1 Instrumental Magnitude

Instrumental magnitude is a measurement of the brightness of a star that is specific to an instrument. It is dependant on many factors, such as the telescope and CCD, the atmospheric seeing conditions, the airmass, the colour of the object and the sky brightness (due to urban light pollution or the proximity of the moon). It would be rare for two different observations of the same source to result in the same instrumental magnitude. The basic process of obtaining an instrumental magnitude is made easy due to the digital nature of CCDs. Each pixel contains a count level representing the number of photons that struck the pixel during the exposure. To calculate the total flux from the target the counts from all the pixels that contain that target are summed. It must also be noted that each pixel contains information from both the target and the sky background level. An estimation of the average background level is then made and subtracted from the total flux to give the signal from the target.

The instrumental magnitude of the measurement is then calculated using the equation:

$$m_I = -2.5 \log_{10} \left(\frac{N_{ap} - A_{ap} S_{sky}}{t_{exp}} \right) \tag{4.9}$$

where m_I is the instrumental magnitude, N_{ap} is the total counts in the aperture, A_{ap} the area of the aperture in pixels, S_{sky} the sky background level per pixel and t_{exp} the exposure time of the image in seconds.

4.3.1.1 Point Spread Function

The shape of a point source of light on a CCD is called the point spread function (PSF). It is assumed that all stars are point sources of light since their angular sizes are smaller than the diffraction limit of most small optical telescopes. With this in mind it is possible to make the assumption that all stars have the same shape and size on the CCD. The PSF is a plot of the flux vs. the radius of a star in an image (Fig. 4.9). The shape is radially symmetric, with a Gaussian 'core' and a large 'halo' surrounding it, which approximates to a power law. The angular size of the PSF can be characterized by the full width at half maximum (FWHM), which is the diameter of the core when the flux falls to half the peak value. There is no 'end' to the PSF, it declines asymptotically to zero with increasing radius.

4.3.1.2 Aperture

When measuring the signal from a star it is important to include as much of the source light as possible. Since the PSF has no definite edge, it is difficult to say where the light from the star ends and the background sky level begins. When counting the flux from a star an 'aperture' is used as a boundary area. Choosing an aperture is an important factor in photometry. Too small an aperture results in the possibility of excluding legitimate light from the star. Choosing too large an aperture means including a large area of background, which increases the noise of the measurement. It also risks including another nearby star, thus contaminating the measurement. The optimum aperture size will depend on the seeing conditions in each image. A growth curve of aperture sizes is the most accurate way to determine which aperture size will yield the highest S/N ratio (Howell, 1989). (As a rough guide an aperture value of $\sim 1.4 \times$ FWHM of the PSF is usually a good starting point.) The aperture size should be kept constant for a given frame when measuring standard stars for comparison.

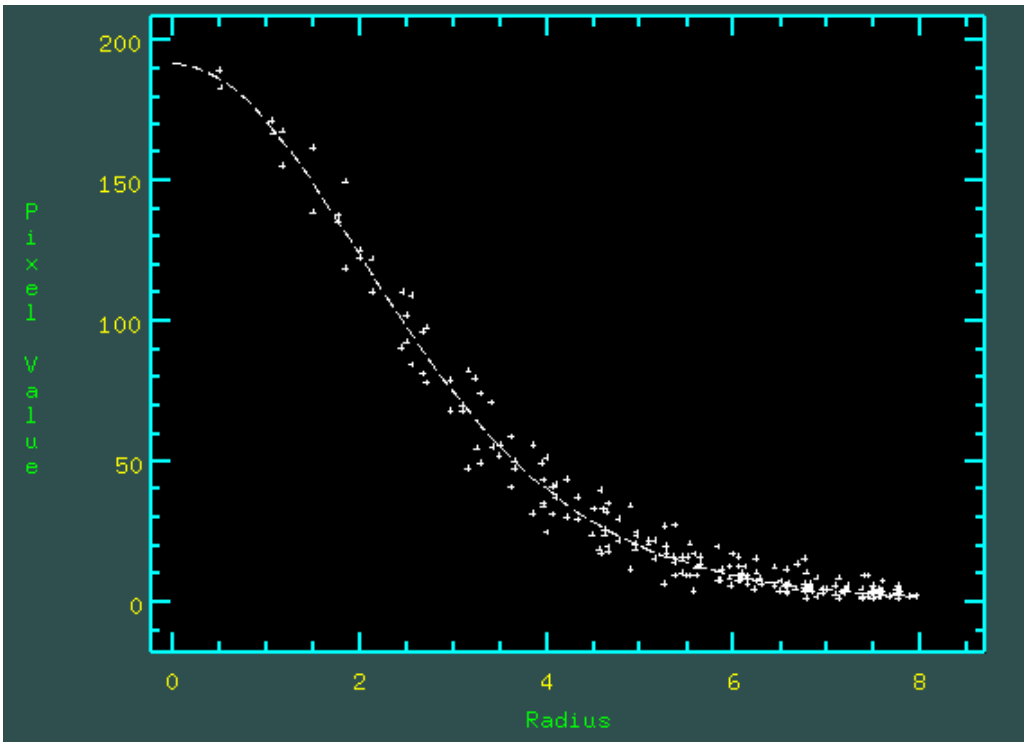

(a) Radial plot

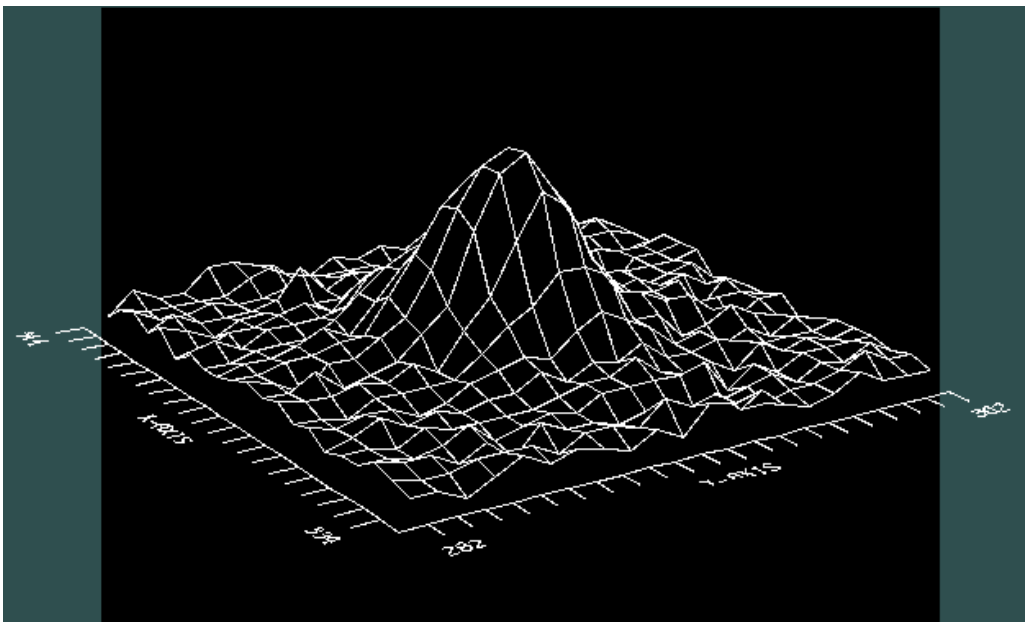

(b) Contour plot

Figure 4.9: Sample point spread function of a star observed by Watcher.

4.3.2 Airmass and The Atmospheric Extinction Coefficient

The Earth's atmosphere absorbs light. As a target moves from the zenith to the horizon throughout the night, the amount of atmosphere that light from the target must pass through increases. The thickness of the atmosphere is called the airmass and has a direct relation on the brightness and colour of a celestial object. To calculate the airmass at a particular altitude it is necessary to first assume that the Earth is flat and that the atmosphere is a uniform layer above the Earth's surface. The length of the light path through the atmosphere varies as the secant of the angle of the object from the observer's zenith (θ_Z). An object at the zenith has the least amount of atmosphere to pass through and is given the airmass value of 1. The amount of absorption at the zenith depends upon the height of the observatory above sea level, the quality of the local sky, the amount of light pollution etc. The equation used to calculate the airmass is given by:

$$\sec\theta_Z = \frac{1}{[\sin\lambda\sin\delta + \cos\lambda\cos\delta\cos h]} \tag{4.10}$$

where λ is the latitude of the observatory, δ is the declination of the target and h is the hour angle of the object at the time of the observation (converted from units of time to degrees). This equation is accurate for most positions in the sky, except near the horizon where the curvature of the Earth is not negligible. The correction term (ΔX) is given by:

$$\Delta X = 0.00186(\sec\theta_Z - 1) + 0.002875(\sec\theta_Z - 1)^2 + 0.0008083(\sec\theta_Z - 1)^3 \tag{4.11}$$

The final equation for airmass is written as:

$$X = \sec\theta_Z - \Delta X \tag{4.12}$$

Most modern observatory computer systems, including RTS2 on Watcher, are capable of automatically calculating the zenith angle and airmass of a target and of writing this

information into the header of the image.

Photometrists characterise the opacity of the atmosphere by a quantity called the extinction coefficient (K). This is the ratio of flux incident on the surface of the atmosphere (f_{inc}) to the observed flux (f_{obs}) at the zenith, expressed in magnitudes. To determine the value of K a sequence of observations of standard stars is made during an observation run. The observed fluxes of these standard stars are measured at various different airmasses as they transit across the sky. Once enough points have been taken (as many as possibly over as wide a range of airmass as possible) a graph can be produced of instrumental magnitude vs. airmass. The extinction coefficient is given by the slope of this graph. It is necessary to generate graphs for each filter being used. This correction is then applied to the instrumental magnitudes of the target object (and the standard stars) to calculate their values at zero airmass (0AM), i.e. outside the atmosphere. For a given instrumental magnitude m_I, observed at airmass X in, say, the V filter with a determined extinction coefficient K_V, the correction equation is given by:

$$m_I^{0AM}(V) = m_I(V) - XK_V \tag{4.13}$$

The extinction coefficient is a measure of how the sky affects a particular filter and is independent of the colour of the target star. It can vary over short time-scales and can change over the course of a week. The humidity levels, changing weather and the changing seasons can all have a noticeable effect on its value. Individual events, such as a nearby volcanic eruption or sandstorm, can also have an effect. It is good practice to make measurements of the atmospheric extinction every night.

4.3.3 Colour Transformation Equations

The filters of any standard system are never uniformly transmissive across their bandpasses, and so they attenuate spectral energy by an amount depending on the spectral shape of the target source. Also, the relative spectral response in the bandpasses of the

working system never matches exactly that of the standard system (e.g. Landolt). Therefore, to convert measured instrumental magnitude values to the standard system, transformation equations are derived which relate the instrumental colours to the standard colours. To do this it is necessary to make multiple observations of standard stars, e.g. the Landolt standards whose magnitudes and colours are well known. These equations take the form (the example used is for V – R but the equation is the same for most colours):

$$(V-R)_S = K'(V-R)_I^{0AM} + M_0 \tag{4.14}$$

where $(V-R)_S$ is the known colour index in the standard system, K' is the colour dependant coefficient (which depends on the colour sensitivity of the filters, the CCD and the optical system) and M_0 is the instrumental offset. $(V-R)_I^{0AM}$ is defined to be:

$$(V-R)_I^{0AM} = m_I^{0AM}(V) - m_I^{0AM}(R) \tag{4.15}$$

where $m_I^{0AM}(V)$ is the instrumental magnitude at zero airmass in the V filter. To calculate K' and M_0 it is necessary to observe a set of standard stars of different colours in a range of filters over a range of airmasses. It is then possible to plot the instrumental colours (corrected to zero airmass) vs. the standard colours of the standard stars (e.g. $(V-R)_I^{0AM}$ vs. $(V-R)_S$). The slope and intercept of this graph gives the value of K' and M_0 respectively. The points should lie along a well defined straight line, with a small scatter about the line. For an optical system that is close to the standard system, K' should be close to 1.00 and M_0 should be close to 0.00.

To determine the relationship between the instrumental magnitudes, e.g. $m_I^{0AM}(V)$, and the standard system apparent magnitudes, V, the following equation is used:

$$V = m_I^{0AM}(V) + V_{ZP} \tag{4.16}$$

where V_{ZP} is the zero point magnitude in the V filter and usually has some colour dependence. This is determined by plotting V_{ZP} using the above equation for standard

stars that span a wide range of colour. This should result in a linear relationship of the form:

$$V_{ZP} = V_{ZP}^{0} + c(V - R) \tag{4.17}$$

where V_{ZP}^{0} is the zero point for a star of colour = 0.00 and c is the colour dependence. The final relation between V and $m_I^{0AM}(V)$ is then given by:

$$V = m_I^{0AM}(V) + [V_{ZP}^{0} + c(V - R)] \tag{4.18}$$

4.4 Conclusions

Modern CCDs have made the process of the measurement of the brightness of celestial objects into a robust science. Once a good understanding of the CCD behaviour is obtained and proper calibration frames are recorded, it is a relatively straightforward process to carry out the necessary data reduction to allow apparent magnitudes of targets of interest to be derived.

Chapter 5

The *quick* Software Suite

5.1 Introduction

In order to contribute to the highly competitive field of GRB research it is necessary to have a streamlined, rapid and efficient analysis framework for robotic telescope data. A number of different analysis applications were examined for the Watcher project, but none were considered fully suitable. The ideal system would need to be able to handle large amounts of data, require a minimum of user input, be capable of mathematical computation and be able to produce high quality lightcurves. It would also be advantageous if the system were free and easy to install on any linux pc. Packages with graphical user interfaces, such as Gaia,[1] require the user to analyse each image manually, which is extremely labour intensive for large amounts of data. A command line application like IRAF[2] (Image Reduction and Analysis Facility) seemed more suitable for dealing with our needs but is notoriously difficult to use. In the end it was deemed necessary to custom build a reduction and analysis pipeline, based on IRAF, which would satisfy our needs, be relatively easy to use and would produce fast and accurate results.

[1] http://star-www.dur.ac.uk/ pdraper/gaia/gaia.html
[2] http://iraf.noao.edu/

The *quick* suite is broken into 3 main parts; reduction, analysis and miscellaneous tools. Each of the larger main scripts relies on several smaller "core" scripts. This makes it easier to implement changes to certain functions, as the edits only need to be made in the core script, rather than each main script individually. Core scripts include functions for performing photometry, calculating signal/noise ratios and querying an astronomical catalogue in order to select reference stars. Although some can be run as standalone applications, most of them are designed in conjunction with the main scripts and cannot be run on their own.

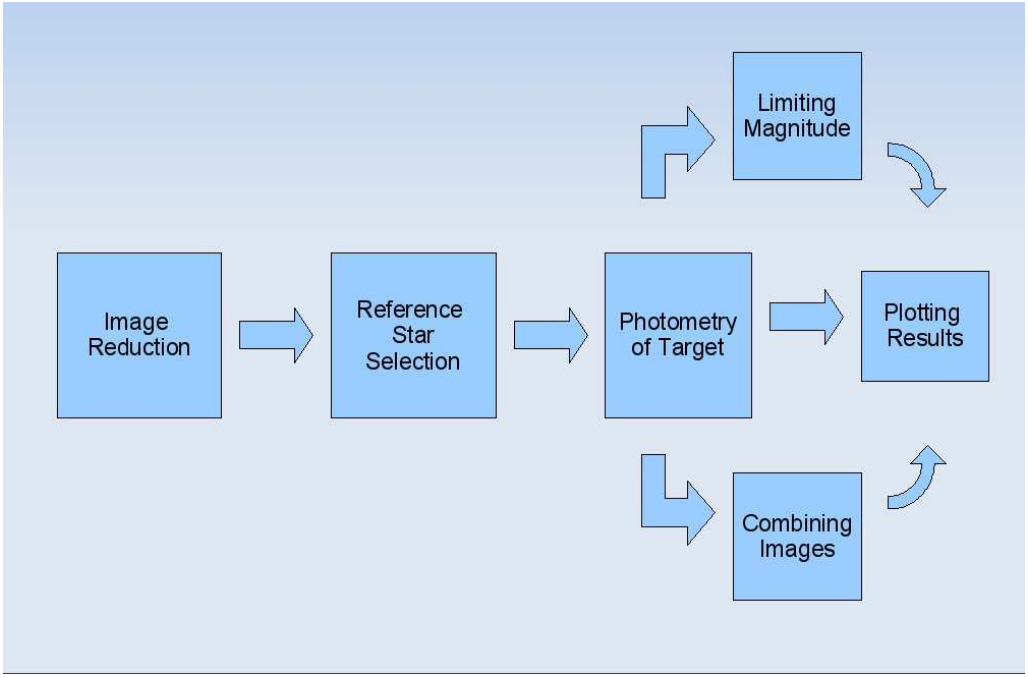

Figure 5.1: Overall schematic representation of the *quick* photometry pipeline.

5.1.1 Suite Overview

Since no individual application was suitable, it was decided to tie together several applications for the multiple tasks needed in the *quick* suite. In order to do this a framework was required to act as a root program, executing the various applications and passing information and commands to them. `Bash`[3] is the shell, or command language interpreter,

[3]http://www.gnu.org/software/bash/

supplied with most distributions of linux. It is a relatively basic programming language but can be easily scripted and does not require a high level of programming skill. It has the ability to queue a list of commands and pass them to another application, as if the user were typing them manually. It also has many tools for operating on text files, such as splitting or combining columns of data from different sources, making it easy to produce high quality tables of results which the user can assess and graph. In order to achieve our goals, 3 different applications are employed: IRAF, Octave and Gnuplot. Some programs from the WCSTools suite are also used, mostly for image header manipulation. The full code listing for the *quick* suite is presented in Appendix A.

5.1.1.1 IRAF

IRAF is the industry standard in image reduction and analysis. It was originally written by the IRAF programming group at the National Optical Astronomy Observatories (NOAO), but has grown over the years to include a huge array of astronomical tasks, from spectral analysis to radial velocity calculations. It is freely available for all major operating systems, but is relatively difficult to install. As powerful as IRAF is, it also has some downsides. Due to its reliance on the older style command shell `xgterm` it is quite difficult to use, especially on large amounts of data. While scripts can be written within IRAF, it is not amenable to large scale automation. Finally the output files from certain tasks in IRAF are of a non-standard form and it can be time consuming for the user to extract and graph the relevant information.

5.1.1.2 Octave

Octave[4] is a powerful, high-level, command line program similar to Matlab. Octave is, however, distributed under the General Public License (GPL) and is freely available on most linux systems. It is mainly aimed at numerical computations and can be easily scripted from `bash`.

[4] http://www.gnu.org/software/octave/

5.1.1.3 Gnuplot

Gnuplot[5] is a command-line driven interactive data and function plotting utility for most major operating systems. It is an extremely powerful 2D and 3D plotter and is freely available and easily installed. Gnuplot has its own scripting language, which is very convenient for saving templates of graph layouts, and can also be executed from within a `bash` script.

5.1.1.4 WCSTools

WCSTools[6] is a package of programs and a library of utility subroutines which is mainly aimed at setting and using the world coordinate systems (WCS) in the headers of astronomical images. It is freely available and is maintained by the Smithsonian Astrophysical Observatory. The main WCSTools utility used in the *quick* software suite is `sky2xy` which converts a coordinate from right ascension and declination to x and y pixels for each specific image. This means that it is not necessary for the user to know where in the frame the target object is located (provided the astrometry is accurate). The other utilities used include `gethead` and `sethead`, which can retrieve and edit image header information, and `getdate`, which converts the time from Julian Date (JD) to Universal Time (UT).

5.2 Reduction

The reduction script, `quick_reduce`, is designed to take in a list of raw images and calibration frames and produce a set of clean, calibrated images. The purpose of the script is to get the images ready for analysis with a minimum of user input. A small amount of preparation is required to run this program. The user must place the images, darks and flats in specific, separate directories to make it easy for the program to find and differentiate them. `quick_reduce` is written in a mix of `bash` and IRAF and is made up of 5

[5] http://www.gnuplot.info/
[6] http://tdc-www.harvard.edu/wcstools/

components: applying a bad pixel mask and trimming some rows and columns from all frames; renaming all frames to a more user-friendly convention; testing the quality of the calibration frames; making a master dark and master flat and finally using the new master dark and flat to reduce the image frames. Each of these components is now described in more detail.

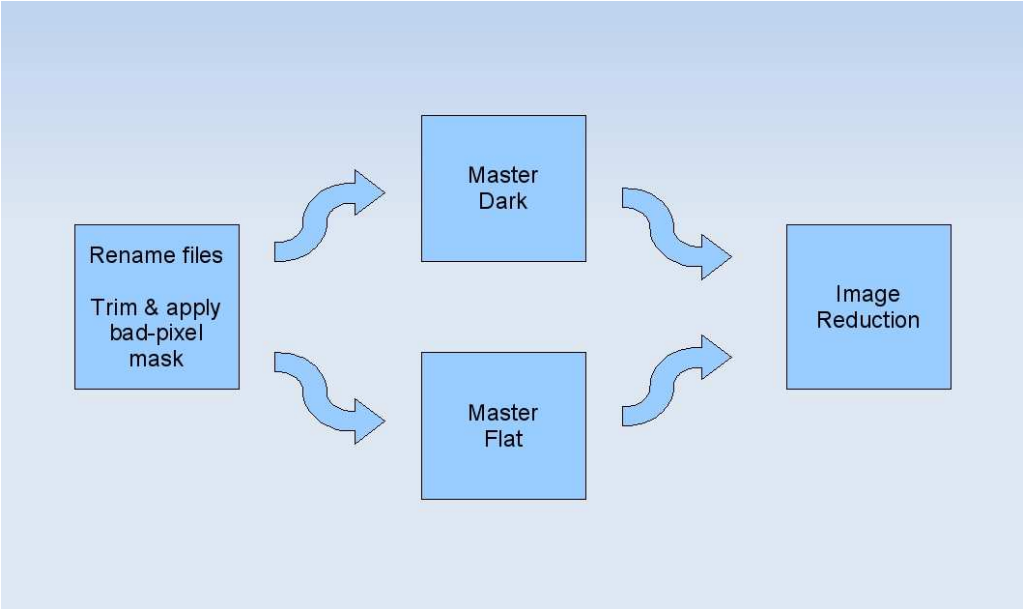

Figure 5.2: Schematic representation of the reduction pipeline, `quick_reduce`.

5.2.1 Bad Pixel Mask & Trim

Applying a bad pixel mask is done using the `fixpix` parameter of `ccdproc` in IRAF. This algorithm takes regions of bad pixels and replaces them by linear interpolation from neighbouring pixels. `Fixpix` can also be used on bad rows or columns. The direction of interpolation can be specified either horizontally for a column or vertically for a row. The bad pixels may be specified by a pixel mask, an image or a text file. For the mask or image, values of zero indicate good pixels and other values indicate bad pixels to be replaced. The text file consists of lines with four fields, the starting and ending columns and the starting and ending lines. Any number of regions may be specified. Currently it is not deemed necessary to apply a bad pixel mask to Watcher data.

The images can also be trimmed using the `trim` parameter in `ccdproc`. Trimming an image completely removes rows and columns from the frame, as opposed to "fixing" them using `fixpix`. If the `trim` parameter is set, the input image will be trimmed to the image section given by the parameter `trimsec`.[7] Since the dimensions of calibration frames must match image frames, this trimming is applied to all frames.

5.2.2 Renaming

All images taken with Watcher (or any system using RTS2) are named with the date and time (to the nearest millisecond) at which the image was taken. This ensures that no file name can be duplicated but makes it difficult to see specific information about the image at a glance. The script `quick_name` renames images based on information found in the image header. It is written in `bash` and makes use of the `gethead` program from WCSTools to access the image headers. `quick_name` places important information such as time, exposure, filter and target name into the file name to make it easier for the user to quickly evaluate the data. Information on the type of image is extracted from the header i.e. whether it is a dark, flat or a data frame, and then the file is renamed using the relevant information for each image type.

- A dark frame is renamed to "Dark- -Time_Exposure.fits"
  e.g. '20060724043937-0910.fits' → 'dark- -2006-07-24T04:39:37.910_60.fits'
- A flat frame is renamed to "Flat- -Time_Filter.fits"
  e.g. '20060724044233-0404.fits' → 'flat- -2006-07-24T04:42:33.404_B.fits'
- An image is renamed to "(Object Name)- -Time_Filter_Exposure.fits"
  e.g. '20060726233824-0641.fits' → 'PKS2155-304- -2006-07-26T23:38:24.641_R_60.fits'

Renaming also makes organisation of the data on the command line much easier as information such as filter or exposure is now in the file name and it is no longer necessary

[7] E.g. In Watcher's case (1024×1024 pixels) we set `trimsec` = [1:1023,1:1020] which cuts off the last column and the top four rows.

to examine each image header.

5.2.3 Testing Calibration Frame Quality

To create a good master dark or master flat it is necessary to combine as many dark and flat frames as possible. Selecting suitable calibration frames can be very laborious if the user has to manually examine a large number of images in order to identify the few problem frames. To automate this process `quick_reduce` performs a filtering of all calibration frames using another script called `quick_imstat`. `quick_imstat` makes use of the `imstat` program in IRAF to generate some basic statistics on the frames, such as the total number of pixels, the mean pixel value, the standard deviation of the mean pixel value and the minimum and maximum pixel values. `quick_reduce` uses the mean pixel value of each frame to decide whether to remove that frame or not. For darks it is more desirable to have a lower mean pixel value, around the average background level of the images, to highlight the low level thermal and electronic noise so a maximum threshold is set (see § 4.2.2.1). Any dark frame with a mean pixel value above that threshold will be removed to a trash directory. Fig. 5.3(a) shows an example of a good quality master dark frame taken with Watcher. A good master dark should have an even distribution of noise, with no gradients or areas of higher / lower response and should not contain any cosmic-ray strikes. For flats the opposite is true; it is more desirable to have a higher mean pixel value, above the average background level of the images, so a minimum threshold is set. A good flat frame must be sufficiently well illuminated to highlight any regular artefacts which may affect an image, such as rings caused by dust on any of the optical surfaces or a non-linear illumination gradient across the CCD (see § 4.2.2.2). Fig. 5.3(b) shows an example of a good quality flat field taken with Watcher. A threshold of roughly twice the noise of an image is usually sufficient to ensure this. Any flat frame with a mean pixel value below this threshold is removed to a trash directory. The master darks and master flats should still be manually examined for stars or unusual artefacts to ensure good image reduction.

5.2.4 Creating Master Calibration Frames

After unsuitable calibration frames have been removed from the lists of darks and flats, `quick_reduce` then creates a master dark and master flat. Two similar programs are used in IRAF to accomplish this. `Darkcombine` is used to create master darks and organises the resulting frames by exposure length. `Flatcombine` is used to create master flats and organises the resulting frames by filter. These programs are merely specialised cases of IRAF's `imcombine` program, with the specific settings needed to create darks and flats already selected. In both cases a median combine is used, which preserves the value of each pixel to two decimal places for greater accuracy. A cosmic-ray rejection (`crreject`) algorithm is also applied to filter out cosmic rays from the frames.

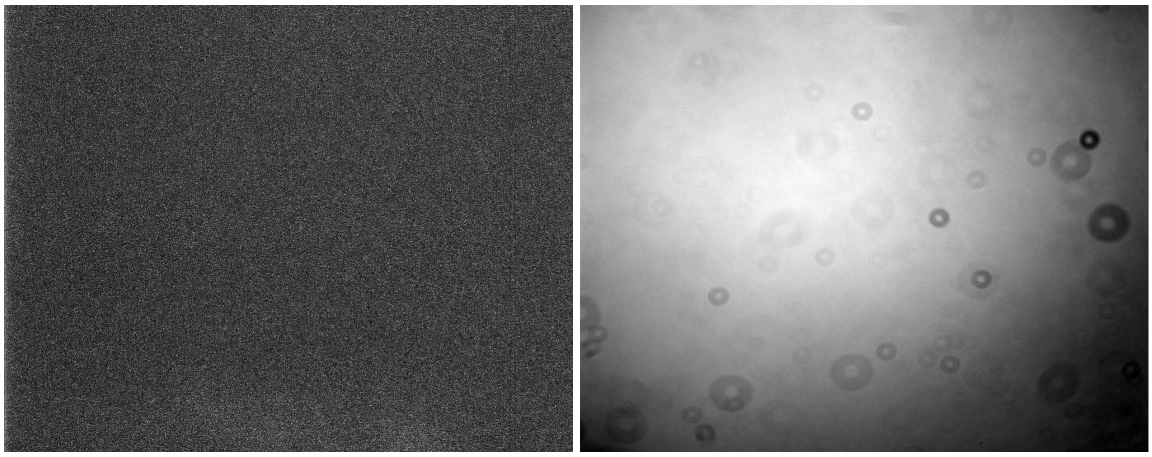

Figure 5.3: (a) A good quality master dark, showing an even distribution of noise (b) A good quality master flat, note the dust rings and slight vignetting.

5.2.5 Image Reduction

The final step of the `quick_reduce` script is to actually reduce the target images. At this point there will exist a master dark for each exposure length supplied and a master flat for each filter supplied. Care must be taken to apply the master calibration frame of the correct exposure length and filter appropriate to a given image. The IRAF program `ccdproc` is used to reduce the images (see § 4.2.2.3), this time specifying the appropriate master dark and master flat. This process is looped until all combinations of exposures

and filters have been dealt with. The resulting reduced images are then saved to a new directory and renamed to indicate that they have been reduced, trimmed and that a bad pixel mask has been applied if required. Fig. 5.4 shows the surface plots of a faint star from an image before and after reduction. For Watcher the mean pixel value of a raw image is ~475 (Fig. 5.4(a)). After reduction the mean pixel value is usually below ~10 (Fig. 5.4(b)). This process is especially important for enhancing faint objects, such as most GRBs, which are close to the background level in an image. As a quick look at the overall quality of the reduced images `quick_imstat` is run once again and a plot is produced of the mean pixel values of each reduced image. This quality plot gives a rough indication of the consistency of the seeing conditions throughout the observing run. Higher mean pixel values indicate worse seeing conditions. A large increase in mean pixel value at the end of the observing run is usually due to the brightening sky of the approaching dawn (Fig. 5.5).

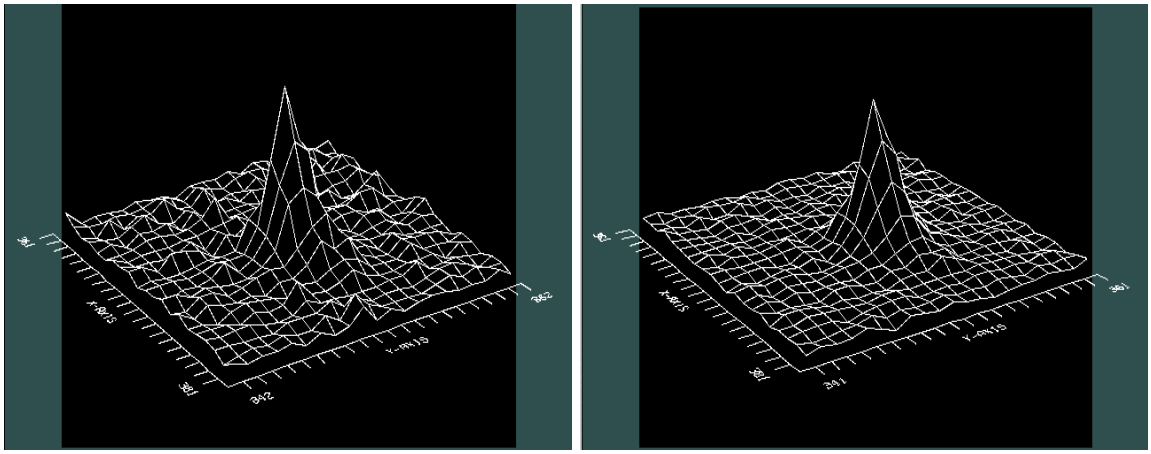

Figure 5.4: (a) Surface plot of a faint star from a raw image taken by Watcher. (b) Surface plot of the same faint star after the image has been reduced. Note that the background noise level is reduced.

5.3 Analysis

The heart of the *quick* suite is the package of photometry scripts. These scripts automate the five main tasks that must be performed in order to analyse astronomical optical

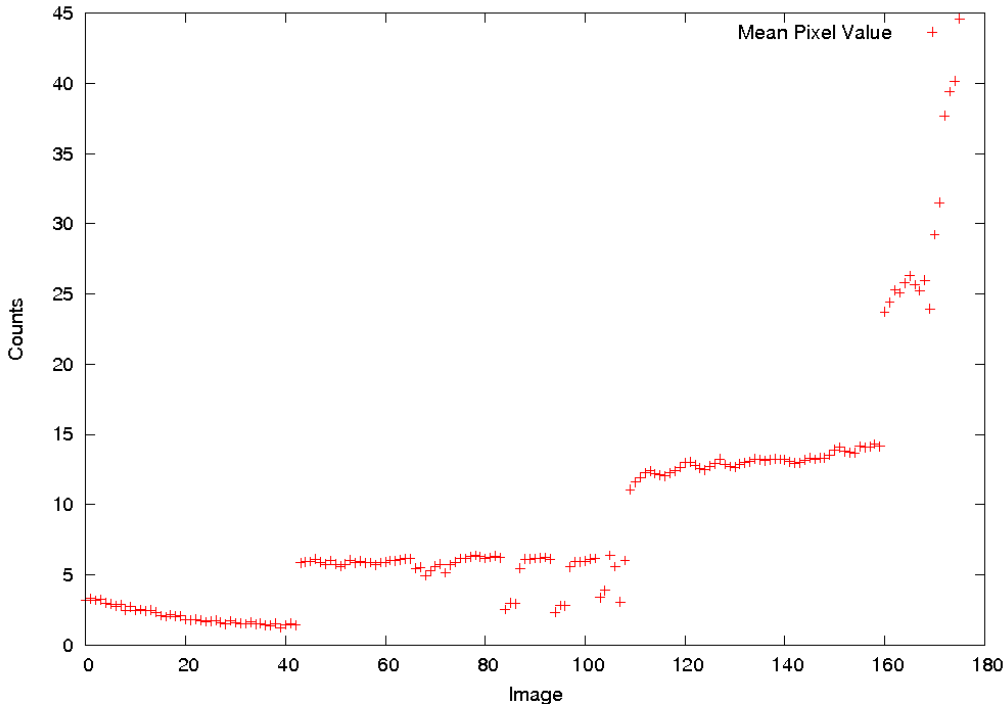

Figure 5.5: Sample plot indicating overall quality of reduced images. The system automatically switches to longer exposure lengths throughout the night, causing a slight increase in mean pixel values. Note the increase in mean pixel value at the end of the run, indicating dawn.

data. The first step is to select suitable reference stars in the field of view. Photometry is then performed on both the target and the reference stars. The resulting instrumental magnitudes of the reference stars must then be calibrated to an astronomical catalogue to calculate the apparent magnitude of the target. In order to determine the significance of the source detection the signal to noise ratio and significance level of the target must also be calculated. These parameters are particularly important when looking at faint objects like GRBs. Finally, if no object is detected at the specified coordinates, the limiting magnitude of the frame must be calculated (Fig. 5.6). The only user input required is the coordinates of the target object, in right ascension and declination, and the initial time of the event, T_0, in JD. This information should be placed in a .roi (region of interest) file in the same directory as the images. The final output of this process is two files: one a list of detections, the other a list of limiting magnitudes. The files are arranged so the user can see all the relevant information at a glance and subsequently create lightcurves of the

target object. Each of the main photometry scripts relies on several core scripts in order to accomplish its tasks.

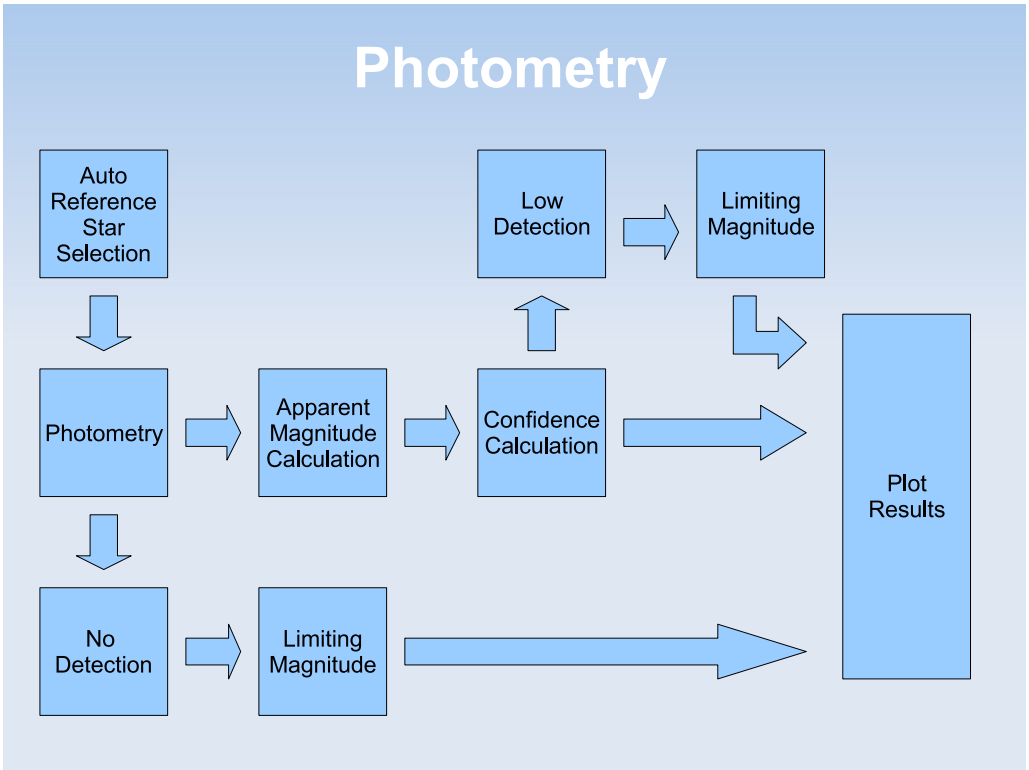

Figure 5.6: Schematic representation of the overall photometry pipeline.

A brief description of the main scripts follows:

- `quick_ref_star`: Automatically selects suitable reference stars.
- `quick_phot`: Performs photometry on a list of targets, calculating signal to noise ratio, significance level and converting instrumental magnitude to apparent magnitude.
- `quick_lim_mag`: Calculates the limiting magnitude of the image.

A brief description of the core scripts follows:

- `quick_time_core`: Converts the exposure time of the image from Julian Date (JD) to seconds and calculates the $T - T_0$, the time since the event started.

- `quick_phot_core`: Performs photometry on a list of targets in an image and outputs the instrumental magnitude, the error on the instrumental magnitude, the mean background level, the area of the aperture and the counts within the aperture.
- `quick_confidence_core`: Calculates the signal to noise and significance level of each target in the image.
- `quick_appmag_core`: Calculates the apparent magnitude of the target object based on the reference stars.
- `quick_cat_core`: Querys a catalogue for the coordinates and magnitudes of stars within a certain radius of the target object.

5.3.1 Reference Star Selection

To calculate the apparent magnitude of the target object, a set of reference stars must be selected. The instrumental magnitudes calculated for these objects are compared to the internationally accepted values in a catalogue. The average of the difference is then applied to the target object to calculate its apparent magnitude. A good reference star must satisfy a set of criteria. The star must be in a catalogue and stable (i.e. non-variable). Its magnitude should be relatively close to the magnitude of the target object and, ideally, it should be physically close to the target object on the CCD (this is to rule out varying seeing conditions in different parts of the frame).

5.3.1.1 Overall vs. Per-Image reference star selection

A given reference star should be well detected in every frame. Due to slight tracking errors or occasional repositioning of the telescope, along with Watcher's relatively small field of view, it is possible for the target object to sometimes drift around the field. This effect can cause some of the candidate reference stars to drop off the edge of the image for certain periods of the observation run. In order to maintain consistency it is desirable to use the same reference stars throughout the observation run. In practice, however, this

limits the user to a very small selection of suitable reference stars. It also causes good reference stars to be eliminated due to the fact that they may be off the edge of the frame for a few, or even only one, of the images. With this in mind two scripts were written: one to select the best overall reference stars that appear in every frame; the other to select the best reference stars on a per-image basis. In the event that the overall method returns only a small number, or possibly no, suitable reference stars, the per-image method can be used. Both scripts are essentially the same, differing only in the final selection of suitable reference stars.

The script `quick_ref_star` starts by querying a catalogue for possible reference stars. The USNO-B1 catalogue was chosen for this task. It is an all-sky catalogue containing over a billion objects and is a combination of various sky surveys over the last 50 years. It is believed to be complete down to V=21 with 0.3 magnitude photometric accuracy in up to three colours and 0.2 arcsecond astrometric accuracy at J2000. The core script `quick_cat_core` starts by getting the target object coordinates from the .roi file (provided by the user) and searching the catalogue within a certain radius around this region and within a certain magnitude range. These limits can be changed easily depending on the type of target being examined. The WCSTool `scat` is used to perform this search. `quick_cat_core` is also able to automatically retrieve the correct filter magnitude from the catalogue to match the filter of the image. When using the clear filter the script chooses the R band catalogue values. This band was chosen as the CCD is most sensitive to this filter. Once the coordinates of possible reference stars have been retrieved from the catalogue `quick_ref_star` then tests the candidates for suitability by running photometry on the list, calling to `quick_phot_core`. This core script returns the instrumental magnitudes of each reference star, along with the information necessary to calculate the significance of each detection.

5.3.1.2 Overall Reference Star Selection

After all the images have been tested `quick_ref_star` discards any star that was not detected in all images. It then calls `quick_confidence_core` to calculate the signal to noise and significance level of the remaining candidates. If any of these detections are weak (< 3 sigma) they too are discarded. The final output of this script is a single list of coordinates and apparent magnitudes of reference stars that have been well-detected in all images in the data set.

5.3.1.3 Per-Image Reference Star Selection

The per-image method is similar to the overall method but only operates on images individually. It calls `quick_confidence_core` to calculate the signal to noise and significance level of the candidates in the current image and also discards any detections that are weak (< 3 sigma). The final output of this script is a separate list of coordinates and catalogue apparent magnitudes of reference stars for each individual image in the data set.

5.3.2 Photometry

The photometry script, `quick_phot`, consists of four main parts: aperture optimisation, the photometry algorithm; the signal to noise and significance level calculation and the apparent magnitude calculation. Once the user has input the coordinates of the target object along with the start time of the event, in JD, to a .roi file `quick_phot` can begin. The reference stars can come from the automatic reference star selection script or they can be manually entered by the user. The WCSTool `sky2xy` converts the coordinates of the list of targets from RA and DEC to x and y pixel values for each image in preparation for `phot` to analyse these locations in the following steps. The final output of this script is an 'apparent_magnitude' file of the target and an 'instrumental_magnitude' file for each reference star. Both files have the same structure and contain columns for: JD, T-T_0, Exposure, Magnitude, Magnitude Error, S/N and significance level.

5.3.2.1 Time

`quick_phot` sets up a time index for the current image. `quick_time_core` is called to convert the time of the image from JD to UT and then calculate the time since the start of the event in seconds. Octave is used for these calculations. The output of this script is a file containing the time of the image in JD, the time since the start of the event in seconds and the exposure time of the image in seconds. This information is later combined with magnitude and signal to noise information for the target to create a final output file that is easy for the user to view and plot.

5.3.2.2 Aperture Optimisation

The distribution of light from a star on a CCD is called the Point Spread Function (PSF). Assuming good optics, proper focusing and good tracking, this PSF is circularly symmetric and consists of a Gaussian 'core' with a large 'halo', which is approximated by a power-law. Since all stars may be treated as point sources of light it follows that all stars in an image have the same size and shape. Due to the halo of the PSF, however, the intensity of the star fades smoothly to zero with increasing radius with no definite edge. This presents a problem in aperture photometry: How big an aperture should be used? If too large an aperture is selected there is a risk of drowning the target in noise related to the background light. There is also a chance of accidentally including a nearby object within the aperture, thus contaminating the signal. If too small an aperture is selected there is a risk of missing a portion of the signal from the target. Neither of these scenarios is acceptable, especially when analysing faint stars. With this in mind an aperture optimisation script, `quick_ape`, was created to test a sequence of apertures and choose the best.

`quick_ape` uses a growth curve method to select the best aperture (Fig. 5.7). Since the PSF of every star in an image should be the same, the brightest reference star is chosen. The script performs photometry on this target, using `quick_phot_core`, and selects an aperture between a lower and upper limit, which can be set by the user. Any range of apertures can be used and the script will loop the process, incrementing the aperture value

by a small amount until the upper limit is reached. The script then calculates the signal to noise and significance level of each measurement using `quick_confidence_core`. When all apertures have been measured `quick_ape` then selects the smallest aperture that gives the highest significance level as the optimum aperture. This value is then used by `quick_phot` as the aperture for all the targets in the image, including the target object.

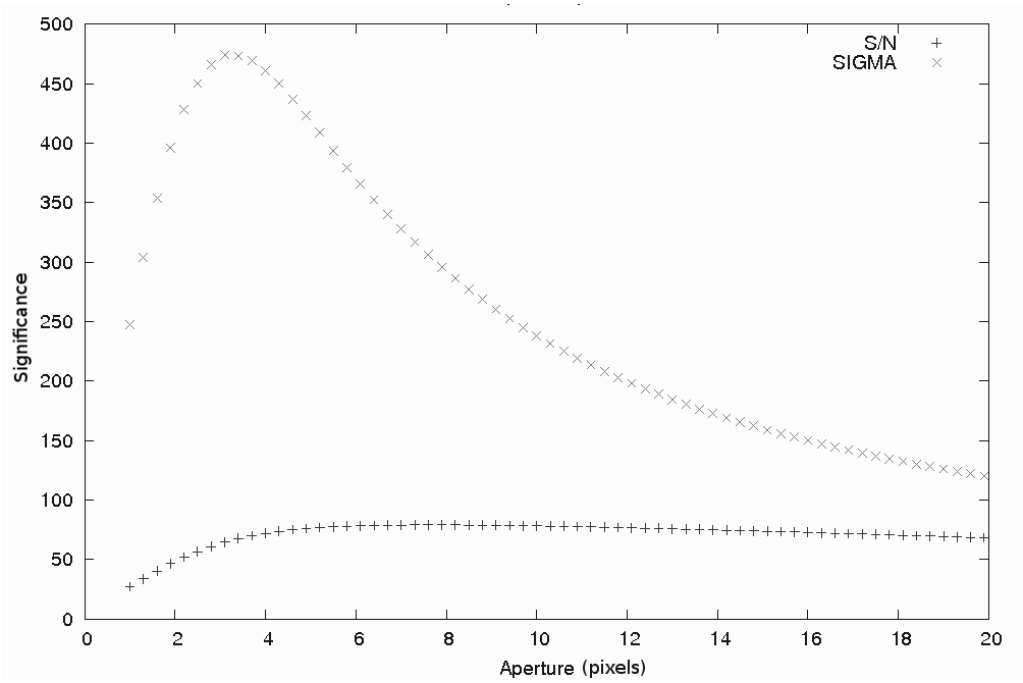

Figure 5.7: Sample plot of a growth curve used for aperture optimisation.

5.3.2.3 Photometry Algorithm

The heart of the photometry process, `quick_phot_core`, starts by gathering some initial information about the image, such as the gain, read noise and aperture. The gain and read noise are fixed values of the CCD and the optimum aperture is calculated by `quick_ape`.

The IRAF program `phot` is used for the actual photometry. `Phot` computes accurate centres, background sky values, and fluxes for a list of objects in the image whose coordinates are read from an input file. These values are then converted to instrumental magnitudes for each object. `Phot` computes accurate centres for each object using a centroid algorithm. The width of the centring box may be defined by the user using the

`cbox` variable. For bright objects this value may be left large without much consequence, there is little chance that `phot` will centre on the wrong object. For faint objects, however, care must be taken to ensure that `phot` centres on the desired object and not a nearby faint object or even a random noise fluctuation. As Watcher is mostly involved in GRB afterglow detection, the centring box can be left small due to the accurate astrometry on the images provided by `rts2` combined with the accurate coordinates and small error box provided by the *Swift* satellite (usually ±3 arcsec from XRT). `Phot` calculates the flux of the object by placing an aperture (calculated by `quick_ape`) around the object. The integral of the counts within the circular aperture is computed by summing all pixels in the aperture. To compute the mean background level of the image, sky pixels in an annular region around the object, the dimensions of which can be defined by the user, are extracted from the image (see § 4.2.1.4). The algorithm used to compute the sky level is called 'mode', which computes the pixel distribution using the computed mean and median (and is recommended by several IRAF guides to photometry). The final flux of the source is calculated using the equation:

$$N_{star} = N_{sum} - A \times N_{sky} \tag{5.1}$$

where N_{star} is the counts from the target object, N_{sum} is the total counts within the aperture, A is the aperture area and N_{sky} is the mean sky background level per pixel. This flux value is then used to calculate the instrumental magnitude of the object. Several important values of the output of `phot`, specifically the magnitude, the error on the magnitude, the mean sky background level, the aperture area and the flux, are then extracted using the IRAF program `txdump`.

5.3.2.4 Apparent Magnitude Calculation

The next part of `quick_phot` is to convert the instrumental magnitudes calculated by `phot` to apparent magnitudes. `quick_aphot_core` is a short script written primarily in Octave which is designed automate this process. The instrumental magnitudes of the

reference stars are compared to their values in the catalogue and the differences between these values are calculated. This offset is then subtracted from the instrumental magnitude of the target object. The average of this set of values gives the apparent magnitude of the target. The equations used for calculating the apparent magnitude and the errors are given by:

$$T_{app} = \frac{((T_{inst} - (R1_{inst} - R1_{cat})) + ... + (T_{inst} - (Rn_{inst} - Rn_{cat}))}{n} \tag{5.2}$$

$$\delta T_{app} = \frac{\sqrt{(\delta T^2_{inst} + \delta R1^2_{inst} + \delta R1^2_{cat}) + ... + (\delta T^2_{inst} + \delta Rn^2_{inst} + \delta Rn^2_{cat})}}{n} \tag{5.3}$$

where T_{app} is the apparent magnitude of the target, T_{inst} is the instrumental magnitude of the target, R_{inst} is the instrumental magnitude of the reference star, R_{cat} is the catalogue magnitude of the reference star and n is the number of stars being used.

The primary goal of the *quick* software suite is the rapid photometric analysis of transient astrophysical sources using a robotic telescope. Therefore, the method of apparent magnitude calculation sacrifices some accuracy for speed. To properly calculate the zero point magnitude, extinction coefficient (see § 4.3.2) and the colour magnitude transformations (see § 4.3.3) would require constant user input. Careful selection of standard stars and the manual scheduling of regular observations of these stars at various airmasses are required and only at the end of the night would it be possible to generate the graphs needed to accurately perform high-precision photometry on the target object. GRBs are unpredictable, variable objects and it is not prudent to divert observations for even a short amount of time.

5.3.2.5 Confidence Level Calculation

The final step in the main photometry process of `quick_phot` is to calculate the confidence level of the detection. Another short script called `quick_confidence_core` is used to calculate the signal to noise and significance level of the detection. The values used are

taken from the output of `quick_phot_core`. The equations used are given by (Mortara and Fowler, 1981):

$$\frac{S}{N} = \frac{G \cdot N_{star}}{\sqrt{G \cdot N_{star} + A(G \cdot N_{sky} + t \cdot N_{dark} + N_R^2)}} \tag{5.4}$$

$$sigma = \frac{N_{star}}{\sqrt{A \cdot N_{sky}}} \tag{5.5}$$

where N_{star} is the counts from the target object within the aperture, A is the aperture area, N_{sky} is the mean sky background level per pixel, N_{dark} is the noise from the dark current, G is the gain of the CCD and N_R is the read noise of the CCD (see § 4.2.1.4).

5.3.2.6 Limiting Magnitude

If the target object is not detected it is necessary to calculate the magnitude of the faintest object in the frame to allow an estimate of the upper limit of the magnitude of the object. The script `quick_lim_mag` calculates this upper limit and can be called at two points during the `quick_phot` script. If the initial photometry does not detect any object at the coordinates provided `quick_phot` will run the `quick_lim_mag` script and move on to the next image. If `quick_phot` does detect an object but its significance level is below a certain threshold then the limiting magnitude script is run. This fail-safe protects the user from spurious detections, e.g. if IRAF accidentally mistakes random noise for a star.

`quick_lim_mag` starts by searching a catalogue for candidate stars and is not limited by radius or magnitude limit. The core script `quick_cat_core_lim` returns all catalogue stars that could possibly be in the image. It then passes all these candidates to `quick_phot_core` which performs photometry on them. Any objects that are not initially detected are discarded. The significance levels of the remaining stars are then calculated using `quick_confidence_core` and the results are sorted by magnitude. `quick_lim_mag` then searches through this list for the faintest object with a significance level above a certain threshold (usually >3 sigma). The catalogue value of this star is then saved to a final

'limiting_magnitude' output file, containing the columns: JD, $T - T_0$, Exposure, Catalogue Magnitude, Instrumental Magnitude, Instrumental Magnitude Error, S/N and Sigma level. This file fits in with the apparent magnitude file created by `quick_phot` and both can be plotted together easily to give both detections and limiting magnitudes of the target object.

5.3.3 Miscellaneous Scripts

Along with the main reduction and analysis scripts detailed above there are a few smaller scripts that have been added to the *quick* suite over time to aid the user in performing various repetitive tasks.

- `quick_combine`: Often when analysing faint objects the first run of photometry does not yield results. This can be especially true if the images are of a short exposure length, e.g. ~10 s. To increase the signal to noise ratio of faint objects the images can be combined. This process increases the chances of a detection but the trade-off is a reduction in the temporal resolution of the data. The ideal scenario would be to combine the images in the smallest groups possible, which would guarantee detection while maintaining a high temporal resolution. The script uses the IRAF program `imcombine` to median combine images into any set of groups defined by the user. For example to combine all the images in a directory into groups of 3 the command '`quick_combine 3`' can be run. This divides the images into groups of 3, combines them, saves the result to a new directory and updates the header of the new image to reflect the new total combined exposure length.

- `quick_region`: This script creates a ds9 region file of a list of targets which is useful when attempting to evaluate the position of the target object or of the reference stars. It places a circle around all reference stars and prints the catalogue magnitudes underneath each one. It also places a circle around the area of the target object and prints the word 'Target' underneath.

- `quick_plot`: This is a set of scripts to plot the output data from `quick_phot` and

quick_lim_mag using Gnuplot. The y-axis displays the brightness of the target in magnitudes and is inverted and the x-axis displays the time of the observations and is converted to log scale. Each axis is labelled with the appropriate title and units. There are various different versions of the plotting script, for example quick_plot_object plots the apparent magnitude of the target vs. time, while quick_plot_object_lim_sn plots the apparent magnitude with the limiting magnitude vs. time in an upper sub-plot and, in a sub-plot below, plots the signal to noise and significance level vs. time. It is the latter script that is automatically called at the end of quick_phot to quickly and cleanly display the result of the latest analysis.

Chapter 6

Watcher GRB Observations & Results

6.1 Introduction

Of the 373 GRBs detected by various missions between April 1 2006 and July 30 2009[1], Watcher carried out follow-up observations of 145. 106 of these bursts were observed within 1 day of the trigger, 27 within 1 hour and 10 within 1 minute. A histogram of times from the GRB trigger to the first Watcher observation for all bursts observed within 1 day of the trigger is shown in Fig. 6.1. Where an optical transient was detected or a useful upper limit could be determined, a notice was distributed to the GRB community through the GCN. In some cases, the observations yielded no useful information due to adverse observing conditions or due to the burst being 'dark' (see § 2.3.4.4).

Response times to GCN alerts are typically ~ 30 s, the fastest response being 12.5 s in the case of GRB 070707. Watcher spends a significant portion of each night pointing at the centre of *Swift's* current field-of-view. A target in the RTS2 database is dynamically updated with the coordinates of the current *Swift* pointing, and its priority is set so that it will be selected by the scheduler if it is observable. The aim of this strategy is to have Watcher pointing in approximately the right direction in order to minimise response times to *Swift* GRBs.

[1] 317 of these were detected by *Swift*, 26 by INTEGRAL, 10 by the IPN, 13 by AGILE and 7 by Fermi. Statistics were obtained from Jochen Greiner's GRB page: http://www.mpe.mpg.de/ jcg/grbgen.html

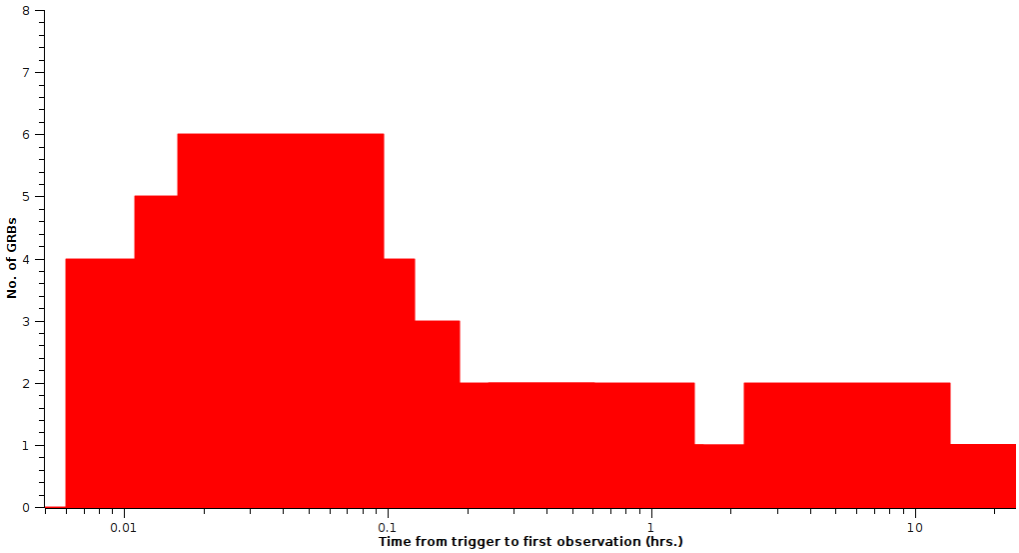

Figure 6.1: Histogram of times from GRB trigger to first Watcher observation for all GRBs observed by Watcher within 1 day of the trigger. The bin size is 0.005 hrs, (18 s). Follow-ups to non-GRB GCN alerts are not included.

A summary of Watcher's highlight follow-up responses to GRBs is presented in Table 6.1, showing rapid response times along with detections and upper limits.

6.1.1 Detections of GRB Prompt Optical Emission & Afterglows

There are three cases of prompt optical emission detected by Watcher while the GRB was still active: GRB 060526, GRB 060904b and GRB 080905b. The case of GRB 060904b, is described in detail in § 6.2.

6.1.1.1 GRB 060526

At 16:28:30 UT on May 26, 2006, the BAT instrument on-board *Swift* detected GRB 060526 (Campana et al., 2006b). The burst was composed of two well separated episodes of emission. The first episode consisted of two FRED-like peaks starting at $T_0 - 3$ s and $T_0 + 6$ s respectively, with the second peak ending at $T_0 + 13$ s. The second episode, from $T_0 + 230$ s and $T_0 + 270$ s, was a symmetric pulse peaking at $T_0 + 270$ s. The BAT light curve is shown in Fig. 6.2.

GRB	GCN	z	Watcher ΔGRB	Watcher ΔGCN	Watcher Result	Watcher GCN
080928	8292	1.692 (GCN 8301)	3h 36m 11s	3h 34m 6s	19.37 m ± 0.11 at 10h 33m 36s	8303
080905b	8182	-	43s	15s	16.2 m ± 0.2 at 1m 52s	8207
080414	7618	-	2m 50s	33s	≥ 14 m	7619
080218b	7314	-	59s	19s	≥ 16 m	7316
070621	6560	-	40 s	24s	≥ 17.9 m	6562
070615	6537	-	1m 22s	45s	≥ 15 m	6538
070611	6494	2.04 (GCN 6499)	1m 18s	41s	18.53 m ± 0.24 at 35m 48s	6528
070330	6232	-	6m 9s	5m 54s	≥ 18.2 m	6233
060926	5612	3.208 (GCN 5367)	1m 1s	47s	≥ 13 m	5615
060912b	5563	-	1m	50s	Upper Limit	5566
060904b	5505	0.703 (GCN 5513)	1m	48s	17.1m ± 0.3 at 8m 11s	5510
060614	5252	0.125 (GCN 5276)	4h 19m 26s	4h 19m 8s	19 m ± 0.3 at 7h 6m	5257
060602b	5200	-	14m 35s	15s	Upper Limit	5199
060526	5162	3.21 (GCN 5170)	36s	19s	16m ± 0.15 at 1m	5165

Table 6.1: Summary of the GRB follow-ups and detections by Watcher.

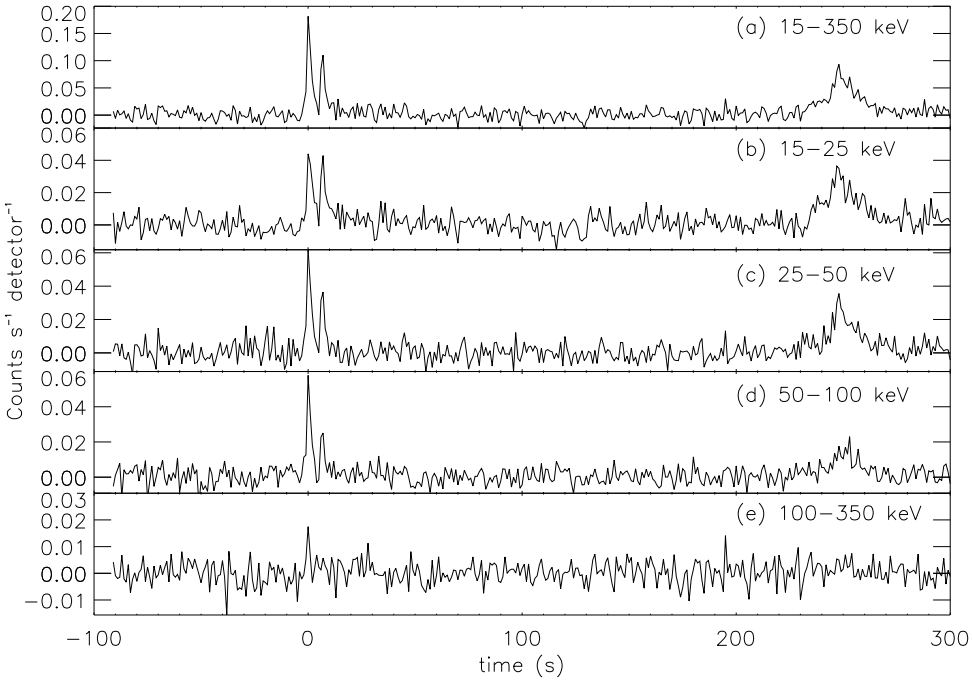

Figure 6.2: Background-subtracted BAT light curve of GRB 060526 in units of counts s^{-1} (fully illuminated detector)$^{-1}$ at 1 s resolution for 5 different energy bands from the top to the bottom: 15-350 keV, 15-25 keV, 25-50 keV, 50-100 keV and 100-350 keV.

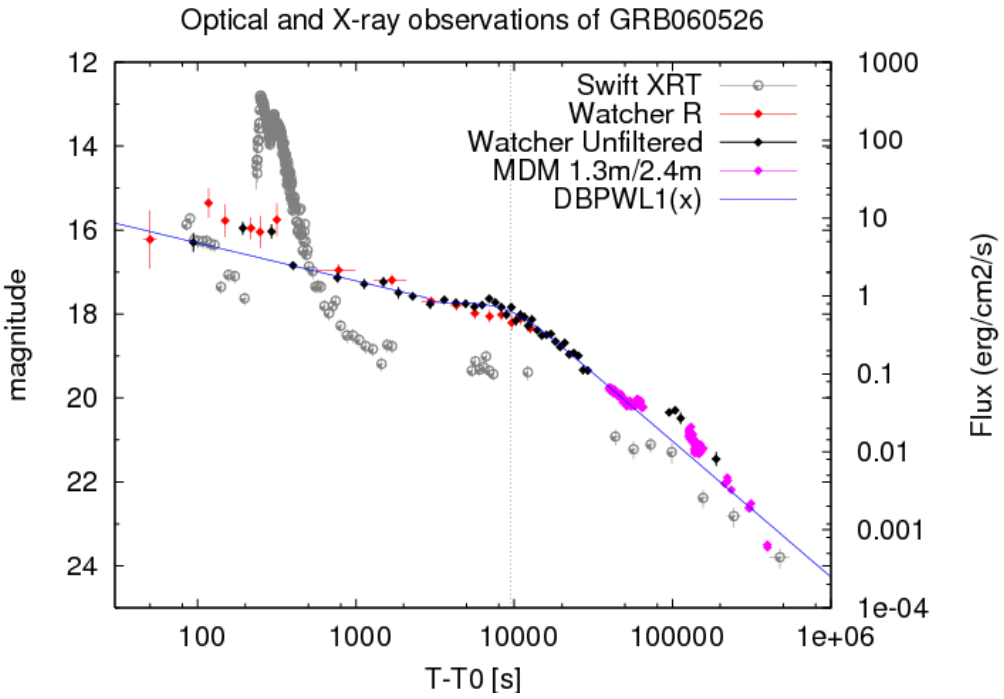

Figure 6.3: Combined observations of GRB 060526 including data from Watcher, *Swift* XRT and MDM

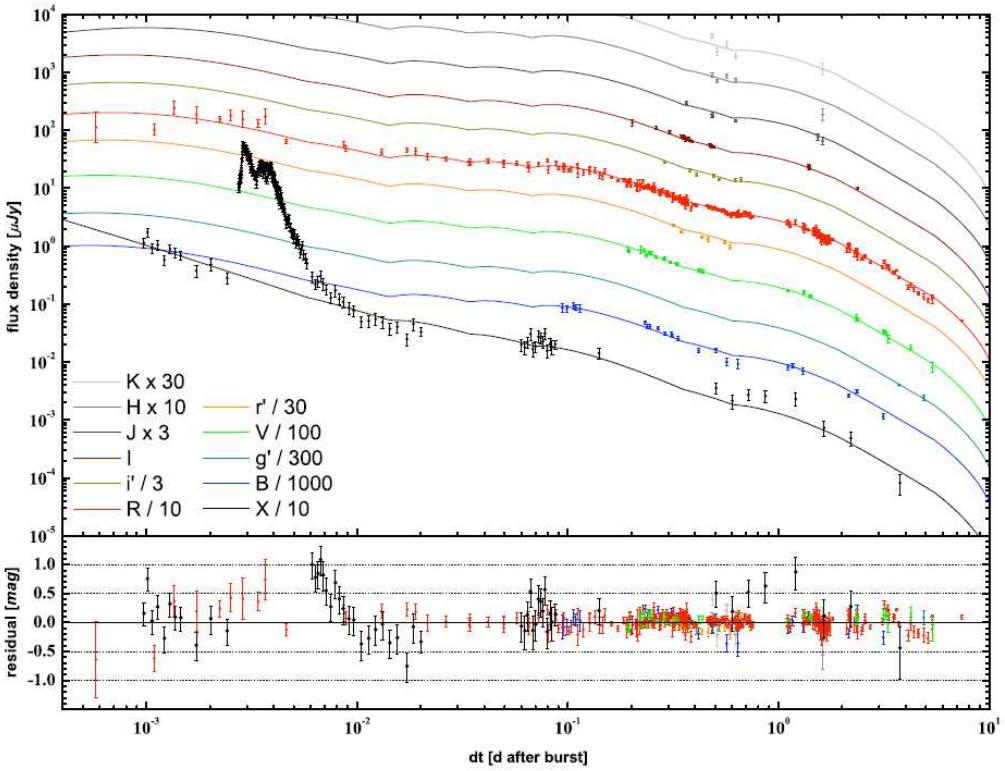

Figure 6.4: Fit to the lightcurve of GRB 060526 in X-ray and optical/NIR $r'Ri'IJHK_S$ bands including a total of six energy injections. The strong X-ray flare is excluded from the modelling. The light curves have been offset by constant factors. *Credit: Jóhannesson et al. (2009).*

The prompt data obtained by Watcher for GRB 060526 is shown in Figure 6.3 along with data from other optical observatories and the *Swift* XRT. The dense sampling and long coverage of the prompt and early afterglow of this GRB have permitted detailed modelling of the highly variable lightcurve in terms of energy injections. The code proposed by Jóhannesson et al. (2006) was used to model the afterglow lightcurve by applying several energy injection episodes as a possible scenario to explain the rebrightenings and shallow decay of the afterglow. Figure 6.4 shows the best fit (χ^2/d.o.f. = 2.8) found using a model with a total of six energy injections: at 0.006, 0.015, 0.04, 0.09, 0.4 and 0.6 days. The initial energy injected into the outflow is $E_0 = 5^{+3}_{-2} \times 10^{49}$ erg[2]. The energy injections then add 0.8, 1.7, 2.6, 5, 8, and finally 13 times the initial energy release E_0 to the afterglow, for a total energy release in the afterglow of $1.5^{+1.1}_{-0.7} \times 10^{51}$ erg (Thoene et al., 2008).

The first four injections are responsible for the shallow afterglow decay between 0.008 and 0.25 days. The quality of the data does not allow to discriminate between this four-injection scenario and a continuous injection (French et al. in prep.). Also, since there are no direct indications of injections in the lightcurve, the time of each of the four injections is not well determined. A direct consequence of this is that the energy of each individual injection in this phase is not well determined, while the total energy released is fairly consistent. The time and energy of the last two injections are, however, better constrained by the data.

6.1.1.2 GRB 080905b

GRB 080905b was detected by the Fermi GBM, with a T_{90} duration (20 - 1000 keV) of 159 s (Fig 6.5(a)) (Bhat et al., 2008). Burst emission up to 100 keV persisted up to 90 s post-trigger (Stroh et al., 2008). In Figure 6.5(c) the Watcher lightcurve of GRB 080905b is shown, along with the limiting magnitude in each frame. Watcher's early detections beginning at T_0 + 50 s are therefore evidence of prompt optical emission coincident with the weaker second and third pulses of this GRB. The broad optical peak between 300 and 600 s post-trigger does not seem to be matched by similar behaviour in the X-ray afterglow lightcurve, which instead exhibits an early steep decay followed by a flattening beginning at roughly 250 s and then a further less steep decay which begins at roughly 2700 s (Fig. 6.5(b)) (Stroh, 2008). Watcher did not detect the afterglow beyond about 8000 s. Further details of these observations are described in Ferraro et al., (in prep).

6.2 GRB 060904b

On September 4th, 2006 at 02:31:03 UT the BAT instrument on-board the *Swift* spacecraft detected GRB 060904b (Grupe et al., 2006). The BAT light curve (Fig. 6.6(a)) showed a double-peak event, with an initial fast rise exponential decay pulse followed by a second, weaker peak T_0 + 120 s later. The initial peak lasted for 9 s and started 2 s before the BAT

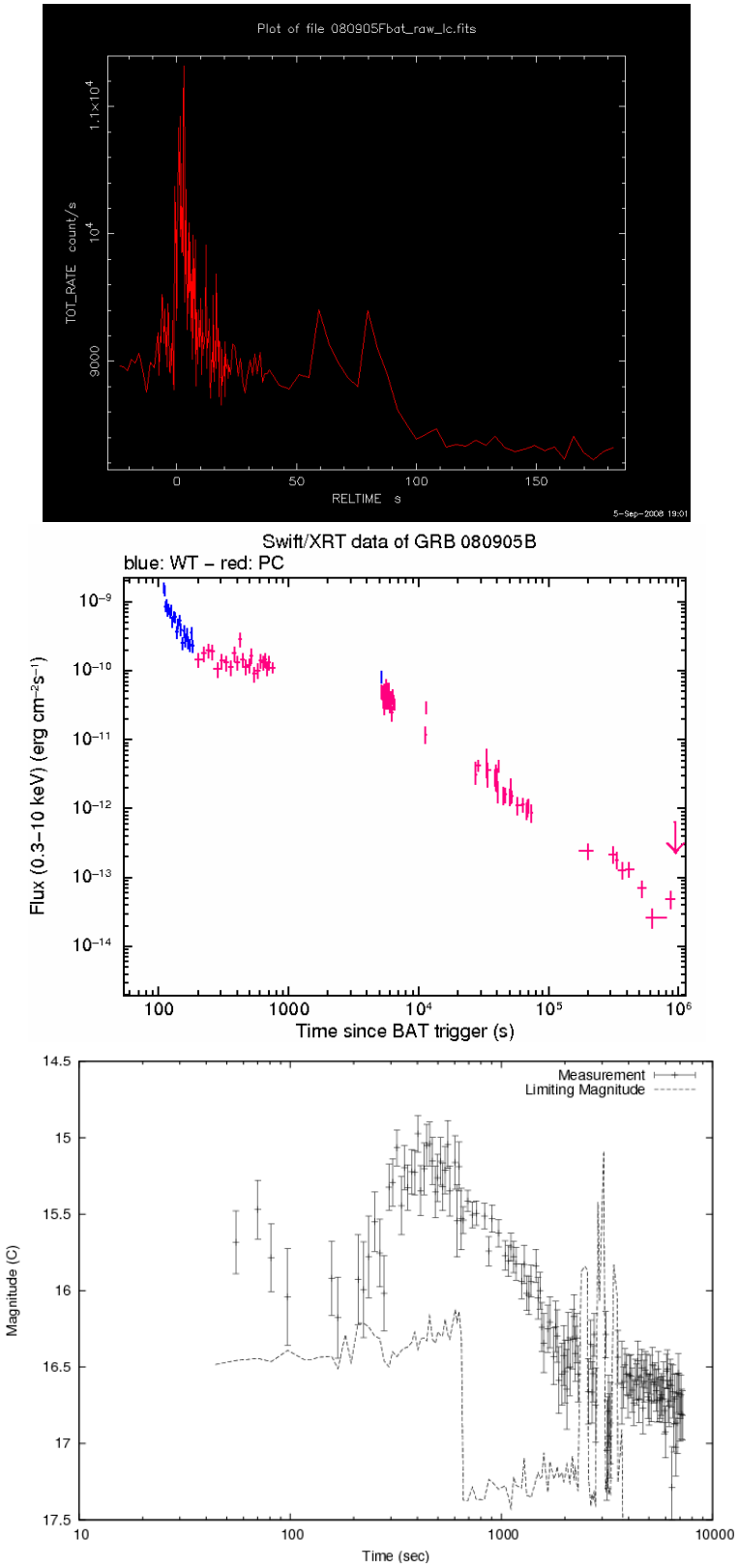

Figure 6.5: (a) GBM lightcurve of GRB 080905b (*Credit: http://www.mpe.mpg.de/ jcg/-grb080905B.html*) (b) XRT lightcurve of GRB 080905b (*Credit: This work made use of data supplied by the UK Swift Science Data Centre at the University of Leicester (Evans et al., 2007, 2008)*) (c) Watcher R_C lightcurve of GRB 080905b.

trigger, while the second peak, detected within the 15-25 keV band, covered T_0 + 120 s to T_0 + 220 s, peaking at T_0 + 155 s. The T_{90} of the burst (15-350 keV) was 192 ± 5 s. *Swift*-XRT began observing the source at T_0 + 69 s and detected a major flare coincident with the 2nd pulse of the prompt gamma emission (Fig. 6.6). Ground based optical follow-up observations began with ROTSE-IIIc detecting a source at RA = 03 h 52 m 50.52 s and Dec = -00° 43' 30.85" (J2000) with R = 17.3 mag at T_{90} + 18.5 s (Rykoff et al., 2006b). Watcher automatically responded to the GCN alert and began observations in R, I and clear (C) filters at T_0 + 63 s, detecting an afterglow candidate at R = 16.8 mag (Table 6.2). Watcher continued observations until dawn at ~04:18:00 UT. Fugazza et al. (2006) performed optical spectroscopy on the target with VLT + FORS1 at T_0 + 5.15 hours and determined a redshift of z = 0.703.

6.2.1 The Optical Afterglow

Fig. 6.8 shows the optical lightcurve of GRB 060904b. The optical emission began to rise before the end of the prompt phase and a power-law function was fit to the data with a slope of $\alpha_1 = -0.79$ from +90 s to + 550 s post-trigger, reaching R=16.7 mag (Watcher) at + 502 s. The reduced χ^2 for the fit over this time interval was 0.635 with 6 d.o.f. The flux then declined with a slope of $\alpha_2 = 0.81$ to R = 18.19 mag (Skvarc, 2006) at + 1380 s. The reduced χ^2 for the fit was 1.1 with 15 d.o.f. From this point the flux remained at a constant level until just before dawn when Watcher recorded a slight bump in the lightcurve, peaking at R = 17.39 mag. Late observations detected the afterglow fading with a decay index of $\alpha_4 = 1.08$ from ~15 hours after the trigger up to ~1.9 days. These results are consistent with those found by TAROT (Klotz et al., 2008) and are discussed in detail in § 6.2.3.2.

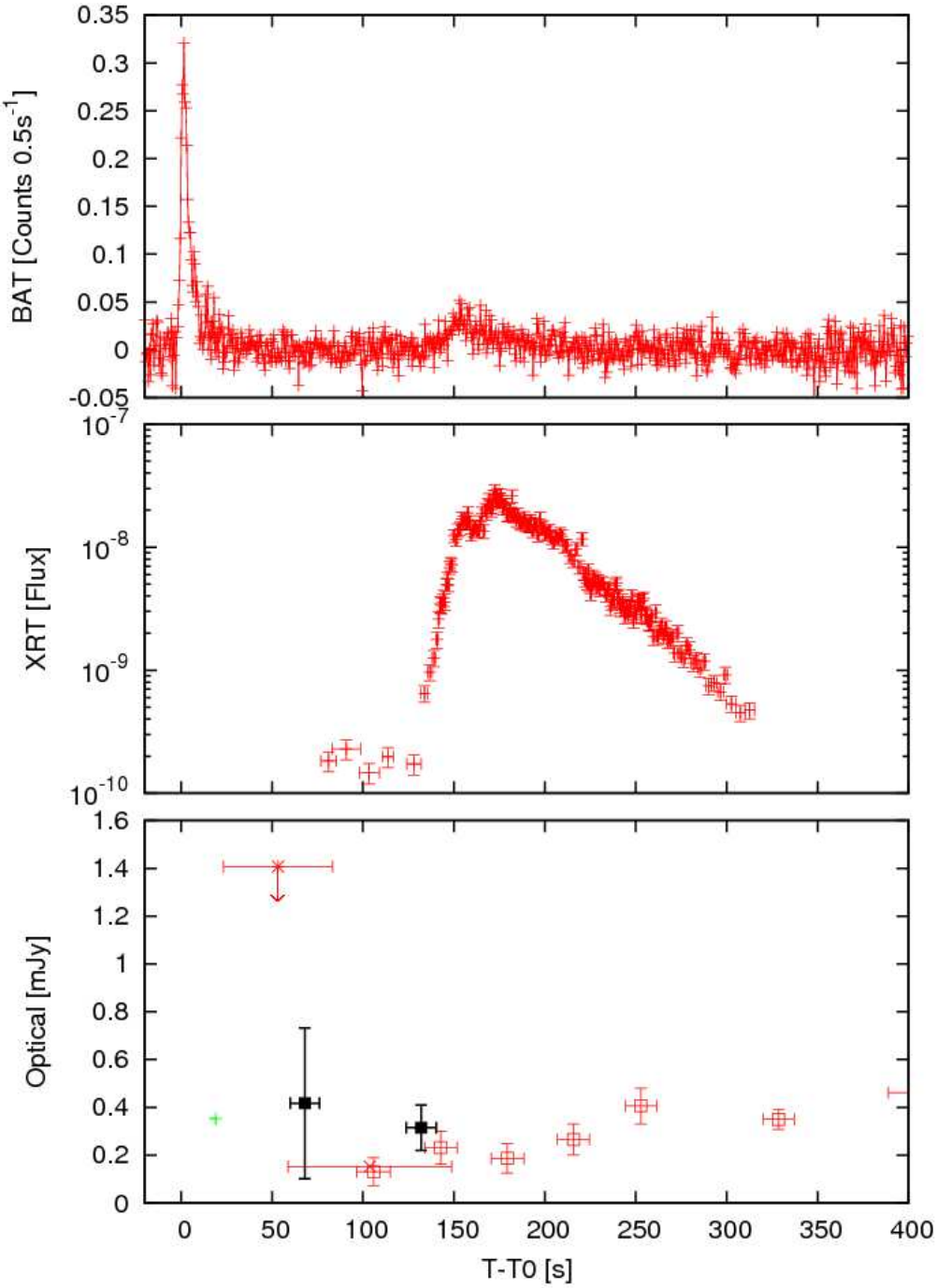

Figure 6.6: (a) BAT lightcurve (counts $0.5\,s^{-1}$), (b) XRT lightcurve (Flux (0.3-10 keV)(erg cm^{-2} s^{-1})) and (c) optical lightcurve (mJy) - including data from Watcher (black solid squares), ROTSE-III (green plus) and TAROT (red X's and empty squares) - for 060904b showing the time of the peak of the emission in each band. *Credit: BAT, XRT, GCN*

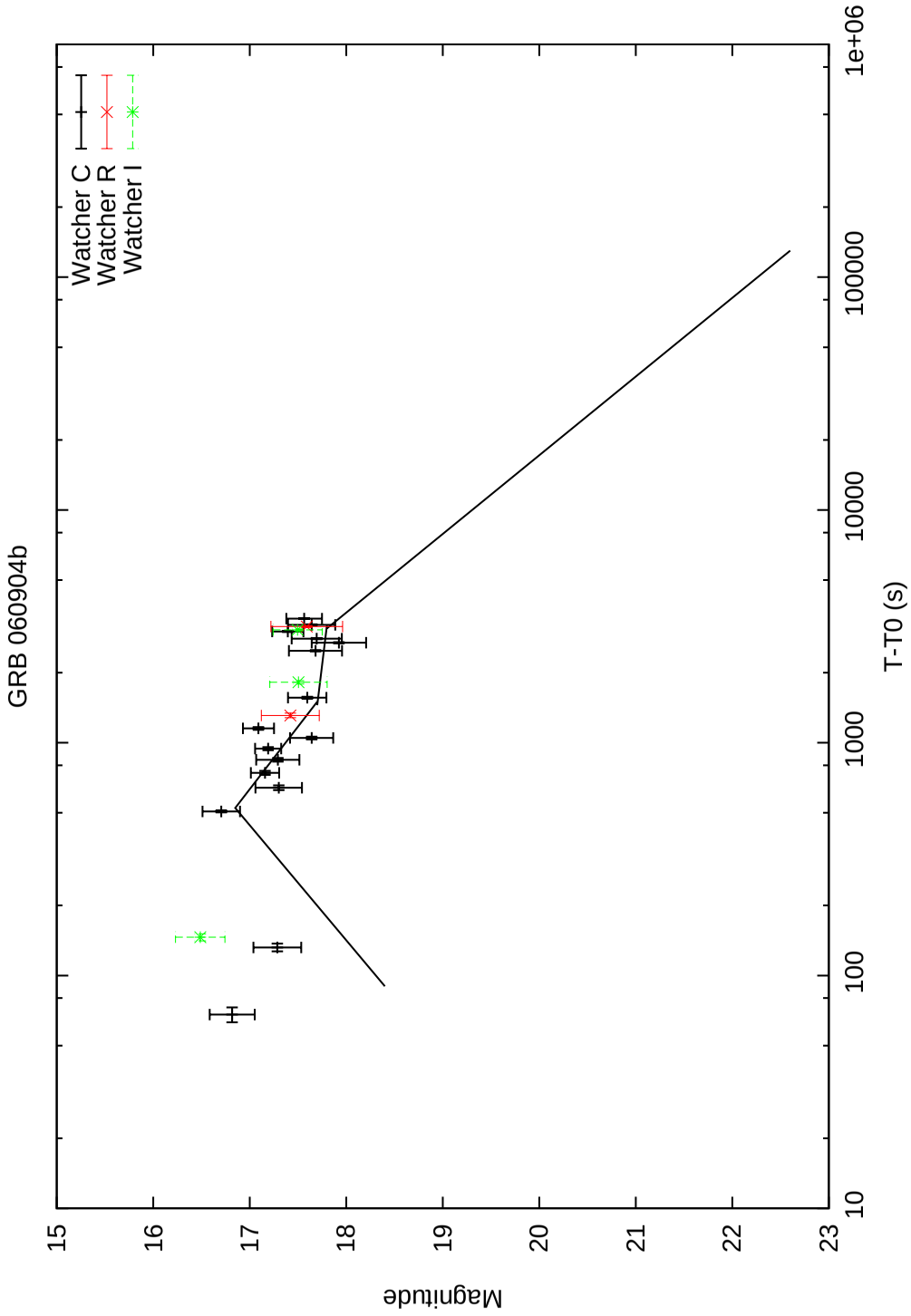

Figure 6.7: Optical lightcurve for 060904b - Watcher data.

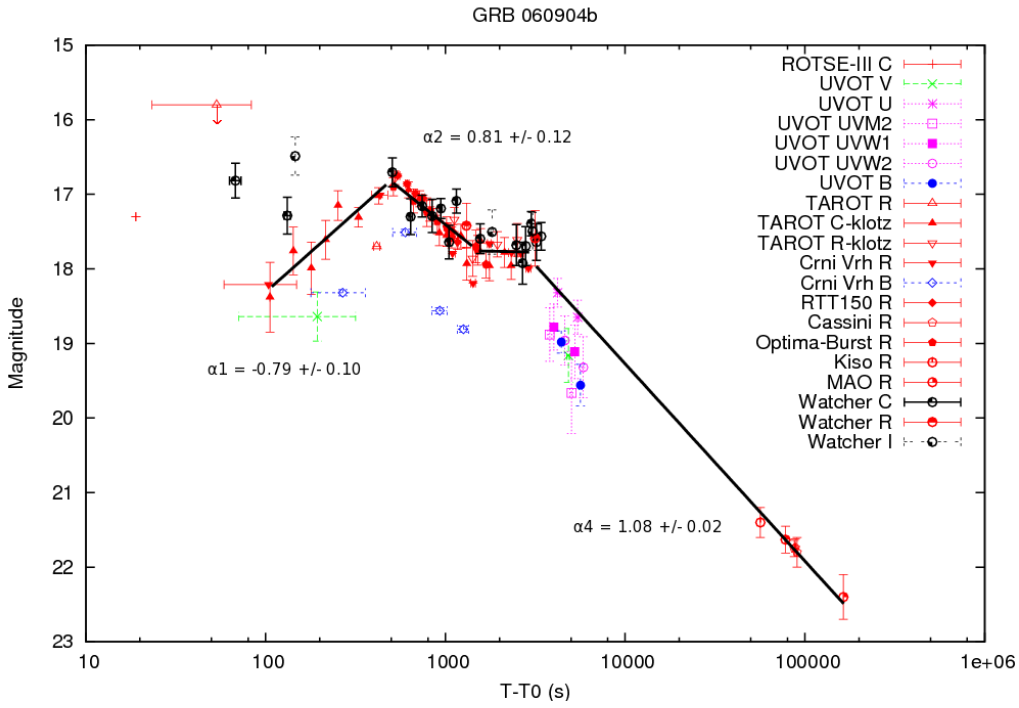

Figure 6.8: Optical lightcurve for 060904b including Watcher data with data from the GCN *Credit: (Rykoff et al., 2006b; Grupe et al., 2006; Klotz et al., 2006b; Skvarc, 2006; Oates and Grupe, 2006; Mescheryakov et al., 2006; Greco et al., 2006; Prymak et al., 2006; Soyano et al., 2006; Asfandyarov et al., 2006)*

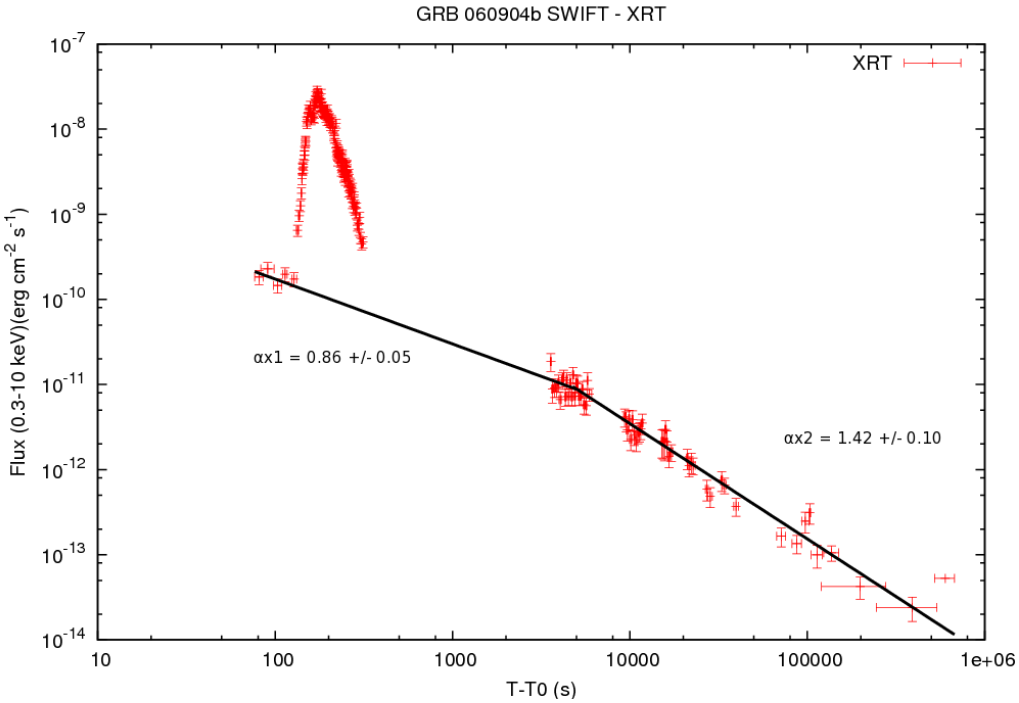

Figure 6.9: XRT lightcurve for 060904b. *Credit: This work made use of data supplied by the UK Swift Science Data Centre at the University of Leicester (Evans et al., 2007, 2008)*

T - T_0 (s)	Exp (s)	Filter	Mag	Δ Mag
63	10	C	16.81	0.23
127	10	C	17.30	0.24
141	10	I	16.48	0.25
502	10	C	16.70	0.19
626	30	C	17.30	0.24
728	30	C	17.15	0.14
830	30	C	17.29	0.22
928	30	C	17.18	0.13
1033	30	C	17.64	0.22
1137	30	C	17.19	0.16
1280	60	R	17.42	0.29
1546	30	C	17.59	0.19
1788	60	I	17.50	0.29
2470	30	C	17.68	0.27
2673	30	C	17.92	0.28
2991	30	C	17.39	0.16
3024	60	I	17.49	0.25
3128	60	R	17.59	0.37
3194	30	C	17.64	0.24
3398	30	C	17.56	0.18

Table 6.2: Watcher detections of GRB 060904b. T-T_0 is the time in seconds from the burst trigger to the start of the exposure, Exp is the duration of the exposure, Mag is the brightness of the OT in magnitudes and Δ Mag is the 1σ error on the magnitude.

6.2.2 X-Ray Emission

Fig. 6.9 shows the X-ray lightcurve for GRB 060904b, starting 69 s after the BAT trigger (Grupe et al., 2006). The light curve shows an initial shallow decay between 77.3 s and ~138 s followed by a giant flare with a duration of 490 s. This flare has a 0.3-10.0 keV mean flux of 2.2×10^{-9} erg s^{-1} cm^{-2} and a total fluence of 8.8×10^{-7} erg cm^{-2} (Klotz et al., 2008). Data taken from before ~300 s to after ~3500 s excluding the flare, shows a smooth power-law decay with index $\alpha_{x1} = 0.86 \pm 0.05$ until ~5000 s. At this point there is a break and the flux continues to decay with a new index $\alpha_{x2} = 1.42 \pm 0.1$. There is no evidence for a plateau phase.

6.2.3 Discussion

6.2.3.1 The Giant X-Ray Flare

The giant X-ray flare associated with GRB 060904b has been observed in many other GRBs (see Chincarini et al. (2007) for a review). The flare from GRB 050502b was studied in detail by (Falcone et al., 2006) and is similar to GRB 060904b. For example the spectrum of GRB 060904b during the flare cannot be fit by a power-law, as is the case for GRB 050502b. The temporal decay observed before the flare can be extrapolated to ~5000 s after the trigger suggesting that the X-ray flare could be produced by an additional mechanism, independent of the one generating the underlying afterglow emission.

Thus the Band model together with a cut-off model were used to accurately model the spectrum (Klotz et al., 2008). The consistency with the Band model (or cut-off power-law) suggests that the flare could be caused by the same mechanism powering the prompt emission, as in a late time internal shock scenario, which was suggested to explain the GRB 050502b giant flare. This combination can be explained as the superposition of a decaying prompt and a rising X-ray afterglow component, as suggested by Willingale et al. (2007) to interpret the typical "steep-flat-steep" behaviour of *Swift* XRT light curves. The break in the light curve at ~5000 s could denote the transition from the "flat phase" to the "steep" afterglow-dominated phase.

The steepening in the X-ray lightcurve ($\Delta\alpha = 0.56 \pm 0.11$) at ~5000 s is not consistent with a spectral break within a standard afterglow scenario (the standard steepening is $\alpha_{x1} - \alpha_{x2} = 0.25$) nor with an achromatic jet break (the optical light curve extrapolates without a break from ~3000 s to late times, see Fig. 6.8). The late-time optical-to-X-ray temporal decay indices ($\alpha_{xo} = \alpha_x - \alpha_o$) also verify the closure relations expected in a standard afterglow scenario, when ν_m is below the optical band and ν_c is between the optical and the X-ray band (Zhang and Mészáros (2004)).

6.2.3.2 Optical Afterglow Behaviour

The optical emission of GRB 060904b was observed to increase during the whole X-ray flare, showing a maximum after the end of the flare at ∼500 s. One could consider the possibility that the X-ray flare is correlated with the optical rise. In fact, the broad band data suggest a temporal sequence, with a flare moving from the γ-ray band to the optical band (Fig. 6.6). In such a case the X-ray and optical emission are produced by the same mechanism (internal shock), with the peak of the emission moving from the BAT to optical bands. Hence, near the peak of the emission one should expect the same spectro-temporal behaviour. However, the observed X-ray rise and decay temporal slopes are significantly steeper than the optical ones. This suggests that the optical flare and the BAT-XRT flare are not correlated.

A similar rise was observed in the near infrared light curves of GRB 060418 and GRB 060607a (Molinari et al., 2007), together with simultaneous X-ray emission characterised by the presence of various flares. In these cases, the optical rise was interpreted as the peak of the afterglow emission which, in the standard thin shell case, is predicted to occur around the deceleration time $t_{dec} \sim t_{peak}$ (Sari and Piran, 1999c; Kobayashi and Zhang, 2007). Up to now, only a small fraction of optical afterglows has been observed sufficiently early, and time-sampled sufficiently well for the optical rising to be clearly identified. Theoretically, if the rise is ascribed to the beginning of the afterglow, in a standard ISM scenario the temporal index α_1 is expected to be ≤ -2 (Sari and Piran, 1999c), much steeper than our observed value of $\alpha_1 = -0.79 \pm 0.10$. In the case of a fireball expanding in a wind environment, the rise could be less steep and also followed by a plateau (Wu et al., 2003). In such a case, the late optical light curve should decrease with the same temporal index, or more steeply, than in the X-ray. However, if the X-ray emission at ∼5000 s is interpreted as the link to the "standard" afterglow phase, then the hypothesis of an expansion in a wind environment does not agree with the late time observations. In fact, at $T_0 + 5000$ s, the X-ray decay is steeper than the optical one.

Other scenarios can also explain a late rising of the optical afterglow:

- An off-axis line of sight (Granot et al., 2002) as was supposed in the case of GRB 060206 by Woźniak et al. (2006). In this case the X-ray and the optical light curves must follow the same behaviour, which is not the case for GRB 060904b.

- The circumstellar medium could be very dense and the extinction very high at the beginning of the optical afterglow, and could decrease later because of the dust destruction implied by the burst blast wave (Perna and Loeb, 1998). This is probably not the case of GRB 060904b because optical emission was detected by ROTSE during the prompt emission and color indexes do not show a red excess near t_{peak}.

- Reverse shock emission. In this scenario, it could be interpreted that the optical flare of GRB 060904b at ∼500 s is an optical flash, and the following plateau is the combined result of forward and reverse shock emission (Sari and Piran, 1999c). However, in such a case, the power-law behaviour of both the rise and decay of the reverse shock optical emission are expected to be somewhat steeper than those observed in this case (Sari and Piran, 1999c; Kobayashi and Zhang, 2007).

- The optical rise and decay temporal indexes of $\alpha_1 = -0.79 \pm 0.109$ and $\alpha_2 = 0.81 \pm 0.12$, could be marginally accommodated within a standard afterglow scenario, if ν_m were to cross the optical band during the flare.

6.2.3.3 Optical Plateau

Some GRBs exhibit an optical plateau that consists of a phase of very shallow decay starting a few minutes after the trigger (typically 5 min in the burst rest frame) and lasting a few more minutes. The plateau can appear simultaneously in the optical and in the X-ray band (e.g GRB 050801; de Pasquale et al. (2007)). In some cases an early re-brightening rather than a plateau is observed, while in other events a plateau appears in the optical on longer time-scales, e.g GRB 060206 (Stanek et al., 2007; Monfardini et al., 2006) having no correlation with any X-ray flattening. GRB 060904b shows some evidence of an optical plateau (Fig. 6.8). Several scenarios could explain such a plateau. In the standard

fireball scenario a nearly flat optical light curve (temporal decay index $\alpha = -0.25$) can be produced by the forward shock when the fireball is in the fast cooling regime with the observational frequency between the cooling frequency ν_c and the injection frequency ν_m (Sari and Piran, 1999c). This ordering of characteristic emission frequencies cannot be reconciled with the late ($T_0 + 5000$ s) optical-to-X-ray data. Another possibility is that the plateau is produced by a patchy jet, i.e by a collimated fireball characterised by a non-uniform distribution of energy (Kumar and Panaitescu, 2000). In such a case a large bump is expected, followed by a plateau as observed in GRB 060904b. However, the same behaviour should be seen roughly simultaneously in all bands, which is inconsistent with the GRB 060904b X-ray data. A last hypothesis for the origin of the optical plateau is that it is produced by a late energy injection in the fireball. Late energy injection can be ascribed to a long lasting central engine activity, or to a refreshed shock associated with a short-lived central engine that is releasing its energy with a variety of Lorentz factors (Rees and Mészáros, 1998). This hypothesis was also proposed by de Pasquale et al. (2007) to explain the plateau observed simultaneously in optical and X-ray in GRB 050801.

6.2.4 Conclusions

The optical emission of GRB 060904b is found to increase from the end of the prompt phase, reaching a maximum brightness at $t_{peak} = 9.2$ min and then decreasing. A large optical plateau and a huge X-ray flare are also associated with this burst. It has been argued that the X-ray flare occurring near t_{peak} is produced by extended internal engine activity. Its presence during the optical rise is thought to be only a coincidence, and is not related to the optical flare. It is also proposed that the nature of the optical plateau of GRB 060904b, while not completely elucidated, could be related to late energy injection.

Chapter 7

Soft γ-ray Repeaters and The Curious Case of SWIFT J195509 + 261406

7.1 Introduction

On June 10th 2007 at T_0 = 20:52:26 UT the BAT instrument on-board the *Swift* satellite triggered on a possible GRB candidate. Initially the burst appeared to be a standard cosmic GRB (Pagani et al., 2007) with Galactic coordinates (l, b) = (63.5, -1.0). The burst had a $T_{90} = 4.6 \pm 0.4$ s, power-law photon index = 1.76 ± 0.25 and fluence = 2.4 ± 0.4 x 10^{-7} erg cm^{-2} (Tueller et al., 2007). The X-Ray Telescope (XRT) on board *Swift* detected an X-ray counterpart 3200 s later (Pagani and Kennea, 2007) with a column density slightly lower than the Galactic value. The delay in X-ray observations was caused by an Earth limb constraint, which meant the spacecraft could not slew promptly to the BAT position.

An optical counterpart was detected by the OPTIMA-Burst instrument on the 1.3 m telescope at Kryoneri T_0+ 57 s after the trigger with a magnitude of 19 ± 0.4 (Stefanescu et al., 2007). The source then faded until T_0+ 476 s, when observations with the fibre-fed, single-photon-counting high-time-resolution main instrument of OPTIMA-Burst showed a flaring activity that lasted about 80 s and consisted of three to four overlapping spikes

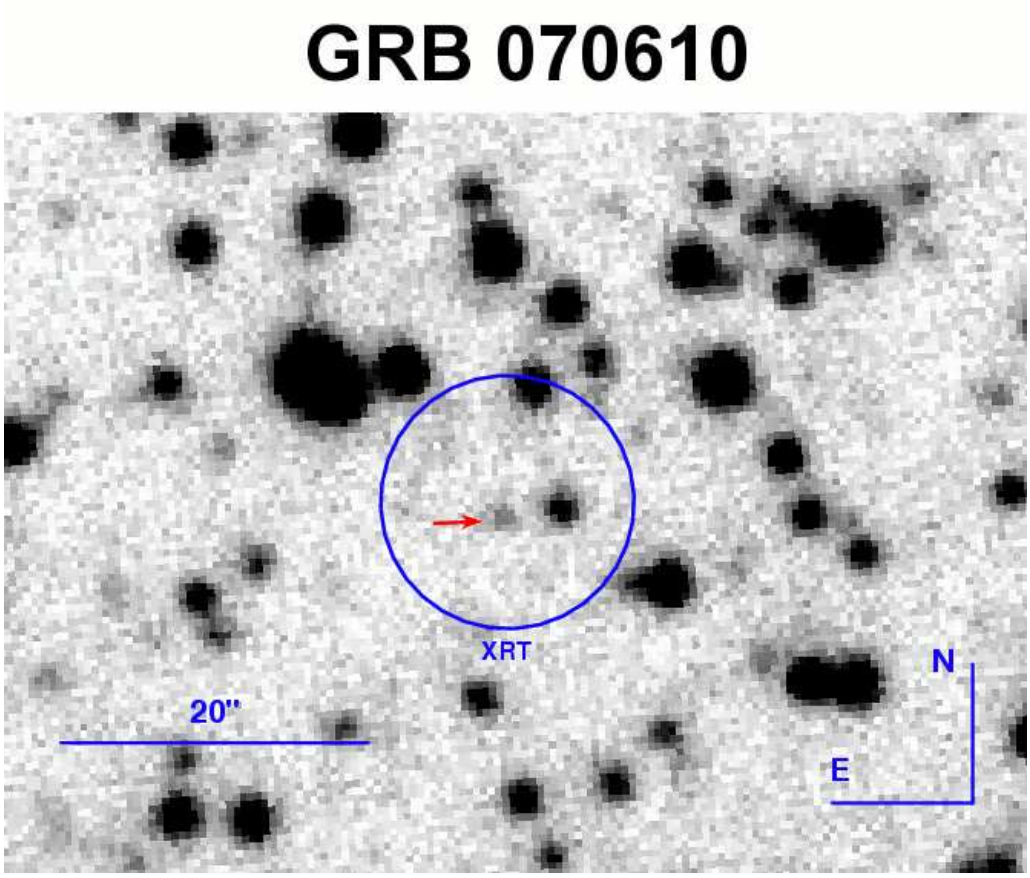

Figure 7.1: Optical counterpart of GRB 070610, the only uncatalogued source within the XRT error circle. *Credit: A. J. Castro-Tirado.*

and a slow decay (Stefanescu et al., 2007). The counterpart was confirmed by the 1.5 m OSN telescope in Granada (Spain) 5.87 hours after the burst (Fig. 7.1) with a detected magnitude of R ∼21.5 mag (Postigo et al., 2007).

Observations with the Tautenburg 1.34 m Schmidt Telescope detected the optical transient (OT) in only 3 of 9 images, indicating rapid, short-lived flaring behaviour, atypical for a GRB afterglow (Kann et al., 2007). Furthermore, the X-ray afterglow flux remained almost constant, with some flares (Fig. 7.2). The unusual behaviour of the source in both the optical and the X-ray regime as well as its location in the Galactic plane provide evidence for this being a new transient source located within the Galaxy, rather than a cosmic GRB and its associated afterglow (Kann et al., 2007).

Overall, more than 40 flaring episodes were detected in the optical band over a time span of three days, and a faint infrared flare 11 days later, after which the source re-

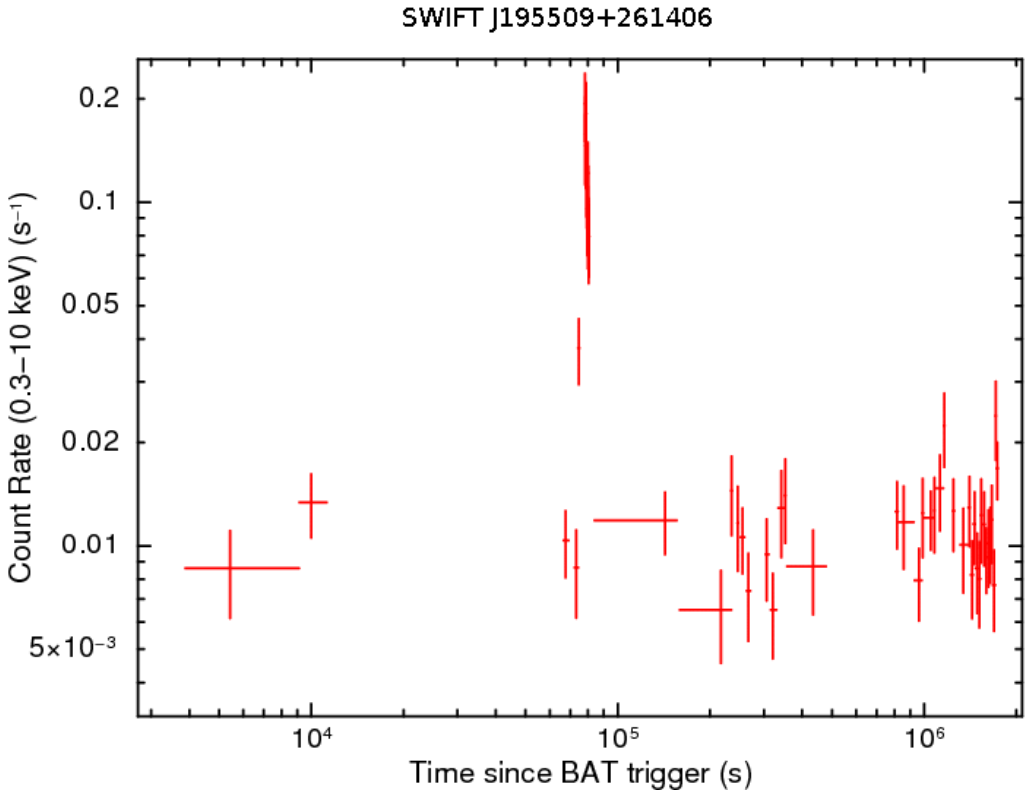

Figure 7.2: X-Ray lightcurve of 070610, showing constant behaviour, with small flares. *Credit: http://www.swift.ac.uk/xrt_curves/00281993/index.php*.

turned to quiescence. Radio observations confirmed a Galactic nature for the source and established a lower distance limit of ~3.7 kpc. It is suggested that the source could be an isolated magnetar whose bursting activity has been detected at optical wavelengths, and for which the long-term X-ray emission is short-lived (Castro-Tirado et al., 2008). In this case, a new manifestation of magnetar activity has been recorded and it can be considered that SWIFT J195509 + 261406 is a link between the 'persistent' Soft γ-ray Repeaters (SGRs) / Anomalous X-ray Pulsars (AXPs) and dim isolated neutron stars.

In this chapter an overview of SGRs and AXPs is presented to set the observations in context. The Watcher observations of the source are described in Section § 7.5.2 and the detailed description and interpretation of the source behaviour is presented in Section § 7.5.3.

7.2 Soft Gamma-Ray Repeaters

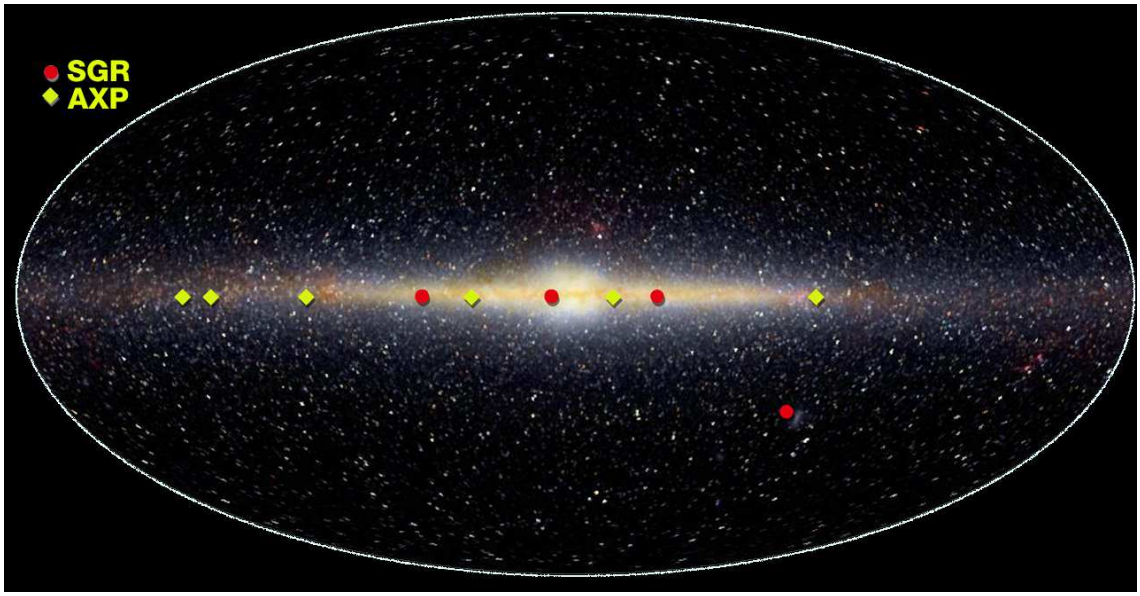

Figure 7.3: Galactic plane distribution of confirmed SGRs and AXPs. *Credit: http://science.nasa.gov/newhome/headlines/ast05mar99_1a.htm*.

Soft γ-ray repeaters (SGRs) were originally thought to be a sub-class of GRBs, with shorter durations and softer spectra than classical bursts (Mazets et al., 1981). They differ from GRBs, however, due to their propensity to produce multiple bursting episodes over years (Fig. 7.4), unlike GRBs which have never been seen to repeat, and are distributed along the galactic plane (Fig. 7.3), unlike GRBs which are isotropically distributed. SGRs have significantly softer spectra than GRBs, usually best described by a thermal bremsstrahlung model with energies of $\sim$30 keV. The first SGR was discovered in 1979, along with two others that year. It was not until the reactivation of SGR 1806-20 in 1983, however, that the independent nature of these sources, distinct from GRBs, was fully appreciated (Laros et al., 1987). The massive flare on March 5th 1979 was the most energetic γ-ray emission episode ever recorded at the time (Mazets et al., 1979). Fig. 7.4 shows a histogram of the flares over the last 15 years of the confirmed SGRs. The time intervals between bursting episodes have been shown to be lognormally distributed (Hurley et al., 1995).

A summary of the confirmed SGRs and AXPs is shown in Table 7.1.

Name SGR	RA (J2000)	Dec (J2000)	Distance (kpc)	Period (s)	dP/dt (10^{-11} s s^{-1})	B_{surf} (10^{14} G)	Association	L_x (2-10 keV) (10^{35} erg s^{-1})
SGR 1806-20	18 h 08 m 39.329 s	-20° 24′ 39.94″	$15.1^{+1.8}_{-1.3}$	7.56	54.9	21	W31	4.4
SGR 0526-66	05 h 26 m 00.89 s	-66° 04′ 36.3″	50	8.047	6.5	7.3	SNR N49	2.1
SGR 1900+14	19 h 07 m 14.33 s	+09° 19′ 20.1″	12 - 15	5.169	7.78	6.4	massive star cluster	1.8 - 2.8
SGR 1627-41	16 h 35 m 51.84 s	-47° 35′ 23.3″	11	2.594	1.9	2.2	CTB 33	0.039
AXP								
1E 1547.0-5408	15 h 50 m 54.11 s	-54° 18′ 23.7″	9	2.069	2.318	2.2	SNR G327.24-0.13	0.031
XTE J1810-197	18 h 09 m 51.08 s	-19° 43′ 51.74″	5	5.539	0.81	1.7	-	0.39
1E 1048.1-5937	10 h 50 m 07.14 s	-59° 53′ 21.4″	2.7	6.452	2.7	4.2	GSH 288.3-0.5-2.8	0.054
1E 2259+586	23 h 01 m 08.29 s	+58° 52′ 44.45″	3	6.978	0.048	0.59	SNR CTB 109	0.18
CXOU J010043.1-721134	01 h 00 m 43.14 s	-72° 11′ 33.8″	57	8.02	1.88	3.9	SMC	0.78
4U 0142+61	01 h 46 m 22.44 s	+61° 45′ 03.3″	> 2.5	8.68	0.196	1.3	-	> 0.53
CXO J164710.2-455216	16 h 47 m 10.2 s	-45° 52′ 16.9″	5	10.61	0.24	1.6	Westerlund 1	0.26
1RXS J170849.0-400910	17 h 08 m 46.87 s	-40° 08′ 52.44″	8	10.99	1.94	4.7	-	1.9
1E 1841-045	18 h 41 m 19.34 s	-04° 56′ 11.16″	$8.5^{+1.5}_{-1}$	11.77	4.155	7.1	SNR Kes 73	2.2

Table 7.1: Summary of confirmed SGRs and AXPs. *Credit: http://www.physics.mcgill.ca/ pulsar/magnetar/main.html*

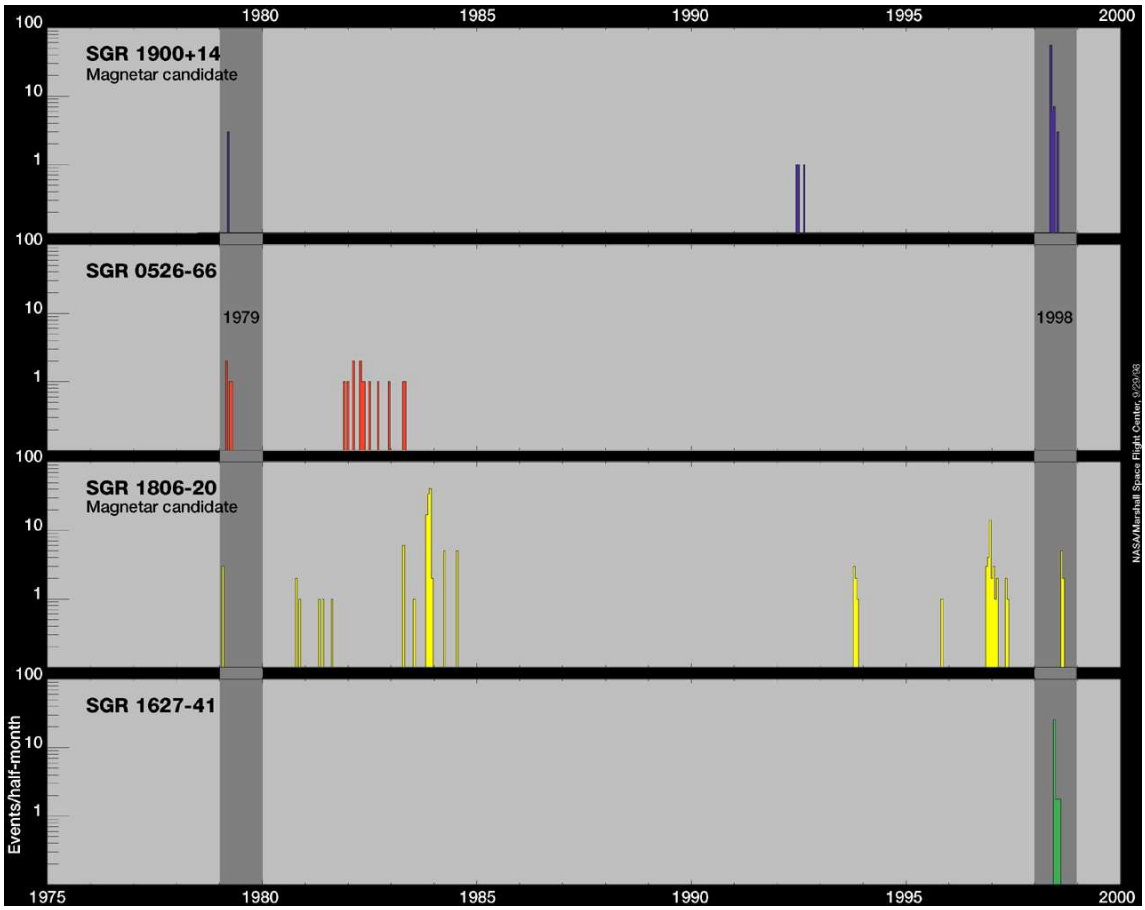

Figure 7.4: Summary of the flares from the 4 confirmed SGRs from 1975 to 2000. *Credit: http://science.nasa.gov/newhome/headlines/ast05mar99_1a.htm*.

- **SGR 1806-20:** The first SGR discovered, SGR 1806-20, was detected by the Venera space-craft on January 7th 1979 from a source in the constellation Sagittarius, near the Galactic centre. In 1983 the source began a long period of intense activity, with over 100 flares detected (Laros et al., 1987), which distinguished it from a standard GRB and prompted a review of the nature of this source. SGR 1806-20 flared again on December 27th 2004 (Hurley et al., 2005) and was detected by the International Gamma-Ray Astrophysics Laboratory (INTEGRAL), the Reuven Ramaty High Energy Solar Spectroscopic Imager (RHESSI), *Swift* and γ-ray detectors on board Mars Odyssey. A ~1 s precursor was observed 142 s before the flare, with a roughly flat-topped profile, which was unusual for an SGR episode (Fig. 7.5). The peak luminosity of the main burst in the first 0.125 s was $L = 2 \times 10^{47}\, d_{15}^2$ erg s^{-1}

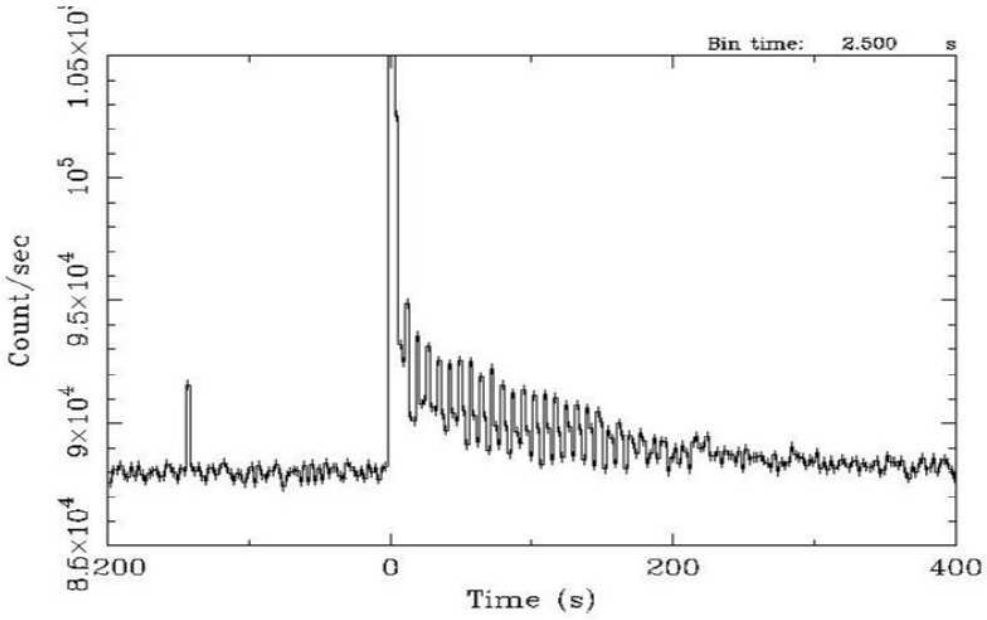

Figure 7.5: Lightcurve of SGR 0526-66, 27th December 2004, showing a ∼1 s precursor 142 s before the flare. *Credit: Mereghetti et al. (2005).*

where $d_{15} = (d/15\,\mathrm{kpc})$, and d is the distance to SGR 1806-20 (Hurley et al., 2005). The likely distance to SGR 1806-20 is $0.8 < d_{15} < 1$, based on the apparent association of the SGR with a compact (∼10 arcsec) stellar cluster at that distance (Corbel and Eikenberry, 2004). The flare's luminosity briefly exceeded all the stars in the Galaxy combined by a factor of $\sim 10^3$. The flare was followed by a hard X-ray tail with a 7.56 s pulsation period, suggesting that the progenitor may be a rotating neutron star.

- **SGR 0526-66:** The extremely bright SGR 0526-66 was detected on 5th March 1979 (Mazets et al., 1979). This extraordinary event began with an extremely bright spike peaking at $\sim 10^{45}\,\mathrm{erg\,s^{-1}}$ (Golenetskii et al., 1984), followed by a 3 minute train of periodic 8 s pulsations (Fig. 7.6) whose flux decayed in a quasi-exponential manner (Feroci et al., 2001). The burst was well localised at the edge of the supernova remnant (SNR) N49 in the Large Magellanic Cloud (Cline et al., 1982). Over the next four years, 17 SGR-type bursts were seen from this source (Mazets et al., 1979; Golenetskii et al., 1984) but no subsequent periodic pulsations were detected. The

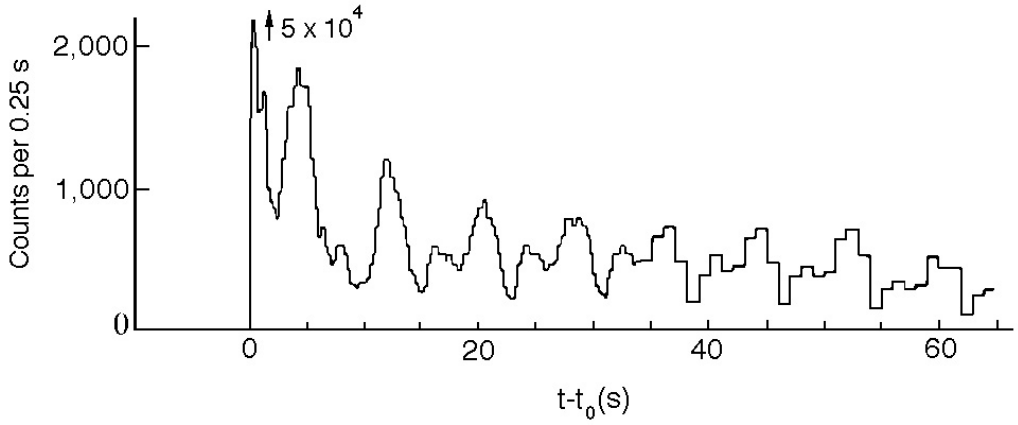

Figure 7.6: Lightcurve of SGR 0526-66, 5th March 1979, showing periodic pulsations of ~8 s. *Credit: Mazets et al. (1979).*

high luminosity, strong pulsations, and apparent association with a SNR strongly suggested that the source is a young, magnetised neutron star with a spin period of 8 s.

- **SGR 1900+14:** The third and final SGR to be discovered in 1979 was SGR 1900+14, first detected with three flares over two days in mid-March. The source remained quiet until 1992 when it emitted another 3 bursts. On 27th August 1998, SGR 1900+14 flared again, this time with one of the brightest events ever recorded outside our solar system (Hurley et al., 1999a). This flare was nearly a carbon-copy of the March 5th event, with both characterised by a brief, hard spike of very intense γ-rays, followed by a soft oscillating tail. As shown in Fig. 7.7, the August 27th event displayed a high initial luminosity and was followed by a ~300 s long tail with a soft energy spectrum and a 5.16 s period (Hurley et al., 1999a).

  The massive flare allowed SGR 1900+14 to be accurately localised to just outside the edge of a young (10,000 yr) SNR within our Galaxy (Feroci et al., 2001). It is thought that the supernova that formed this remnant imparted a kick velocity of ~1500 - 2000 km s^{-1} to the SGR, allowing it to overtake the expanding shell of hot gas from the supernova.

- **SGR 1627-41:** Discovered on June 15th, 1998, SGR 1627-41 emitted about 100

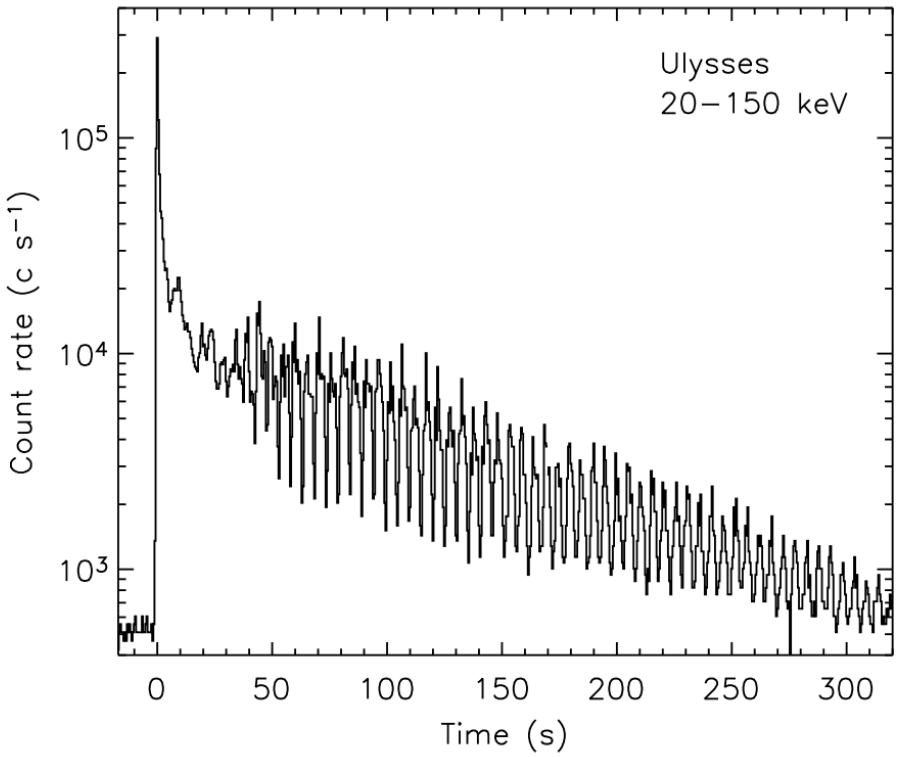

Figure 7.7: The giant flare from SGR 1900+14 as observed with the γ-ray detector aboard Ulysses (20-150 keV). Note the strong 5.16 s pulsations clearly visible during the decay. *Credit: Hurley et al. (1999a).*

bursts from June to July 1998 and was detected by several satellites (e.g. CGRO, Woods et al. (1999b); Ulysses, Hurley et al. (1999b); Wind, Mazets et al. (1999)). The peak flare had a maximum luminosity of $\sim 8 \times 10^{43}$ ergs s^{-1} assuming isotropic emission (Mazets et al., 1999), which is smaller but of a similar magnitude to the March 5th 1979 and August 27th 1998 events. However, this very energetic burst differed significantly from the other giant outbursts. It exhibited no separate initial pulse with a fast rise time, no extended tail, and no pulsations (Fig. 7.8; Mazets et al. (1999)). The position of the source was found to be consistent with the Galactic supernova remnant G337.0-0.1 (Hurley et al., 1999b). The location within the supernova remnant suggests that the SGR has a transverse velocity of ~200 - 2000 km s^{-1} (Hurley et al., 1999b).

A variety of models have been proposed to explain SGRs, including accretion onto

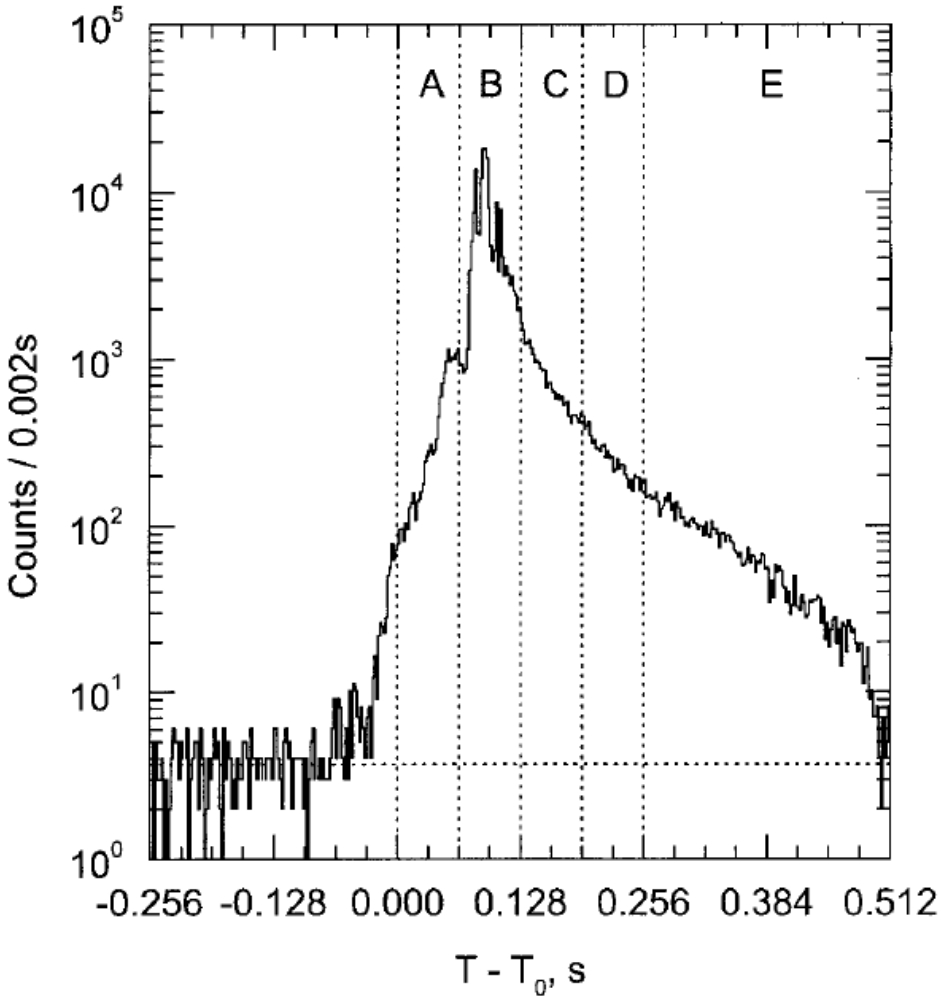

Figure 7.8: The giant flare from SGR 1627-41 which differs from other giant SGR flares, exhibiting no separate initial pulse with a fast rise time, no extended tail, and no pulsations. *Credit: Mazets et al. (1999).*

magnetised neutron stars (Livio and Taam, 1987; Katz et al., 1994), cometary accretion onto quark stars (Alcock et al., 1986) as well as thermonuclear energy release on a magnetised neutron star (Woosley and Wallace, 1982). These models failed to adequately explain both the common recurrent bursts and the occasional giant flares (e.g. the March 5th event). The discovery of persistent X-ray emission from the three known SGRs at the time aided in the understanding of the nature of SGRs (Murakami et al., 1994; Rothschild et al., 1994; Vasisht et al., 1994). Around the same time, the magnetar model § 7.4 was put forward to explain the high-luminosity bursts of the SGRs (Duncan and Thompson, 1992;

Paczynski, 1992; Thompson and Duncan, 1995) and the persistent X-ray emission of both the SGRs and the AXPs (Thompson and Duncan, 1996). The model predicted slow pulsations and rapid spin down from the quiescent X-ray counterparts of the SGRs. Shortly after this (Kouveliotou et al., 1998) discovered 7.5 s pulsations and rapid spin down in the X-ray counterpart to SGR 1806-20. This was interpreted as the magnetic braking of an isolated neutron star with a $\sim 10^{15}$ G dipole magnetic field (Kouveliotou et al., 1998).

7.3 Anomalous X-Ray Pulsars

Anomalous X-ray Pulsars (AXPs) were first reported by Fahlman and Gregory (1981) who discovered pulsations from the X-ray source 1E 2259+586 at the centre of the SNR CTB 109. The object was originally interpreted as a peculiar X-ray binary, with an energy spectrum much softer than is typical of accreting pulsars, and no optical counterpart. The source was subsequently found to be spinning down in a secular manner (Koyama et al., 1987). AXPs are characterised by several features including: a narrow range of spin periods (2 - 12 s), fairly constant X-ray luminosities ($\sim 10^{35}$ - 10^{36} erg s^{-1}), no (or very small) long term variability, lack of evidence of binary companions, relatively soft X-ray spectra, absence of radio emission and a secular spin-down on time-scales of 10^3 – 10^5 years (Table 7.1) (Mereghetti, 2008). As noted by Thompson and Duncan (1996), their 'anomalous' property is the unclear mechanism powering their X-ray emission.

AXPs appear to be too young to be low-mass binaries as some are associated with SNR and have a small scale height above the Galactic plane (van Paradijs et al., 1995). The AXP 1E 2259+586, and subsequently the entire AXP population, was identified with isolated magnetars powered by the decay of a $\sim 10^{15}$ G magnetic field. The principal competing model postulated that AXPs are neutron stars surrounded by fossil disks that were acquired during supernova collapse or during a common-envelope interaction (Corbet et al., 1995; van Paradijs et al., 1995; Chatterjee et al., 2000; Chatterjee and Hernquist, 2000).

A useful discriminator between the fossil disk and magnetar models is provided by the detection of optical and near infrared counterparts to the AXPs, beginning with 4U 0142+61 (Hulleman et al., 2000). Dim counterparts have now been detected for several AXPs, with an optical/IR luminosity typically one thousandth of that emitted in 2-10 keV X-rays. This constrains any remnant accreting disk to be very compact (Perna et al., 2000). A key prediction of the magnetar model was confirmed by the detection of X-ray bursts similar to SGR bursts from at least one, and possibly two, AXPs. Two weak bursts were observed from the direction of 1E 1048.1-5937 (Gavriil et al., 2002) and more than 80 SGR-like bursts were detected from 1E 2259+586 during a single, brief (~11 ks) observation of the source (Kaspi et al., 2003). Transient releases of energy appear to power at least 10% of the X-ray output of 1E 2259+586 and a much larger fraction in some other AXPs.

Originally, one of the defining characteristics of AXPs was the steadiness of their X-ray emission over a fairly narrow range of luminosities 10^{35} - 10^{36} erg s^{-1}. With recent observations, however, it has become clear that at least half, and possibly most, magnetar candidates are variable X-ray sources. Some of the observed variability could be driven by burst activity, but at least a few sources have shown large changes in luminosity with little or no detected burst activity. For example, XTE J1810-197 was discovered in 2003 with a luminosity of $\sim 2\times10^{36}$ erg s^{-1} (Ibrahim et al., 2004), but archival observations from the 1990's detected the source in a "low state" with a luminosity two orders of magnitude smaller (Gotthelf et al., 2004).

The realisation that SGRs and AXPs can enter low states with luminosities of order 10^{33} - 10^{34} erg s^{-1} for extended periods of time has important implications for the total number of magnetar candidates in the Galaxy. Their duty cycle as bright X-ray sources is presently unknown, especially as a function of age. There is still much to be learned about the similarities and differences between magnetar candidates in their dim states, and other low-luminosity X-ray sources in the Galaxy such as Isolated Neutron Stars.

7.4 The Magnetar Model

The similarities in the observed properties of SGRs and AXPs has made it clear that they are, fundamentally, the same type of object - a neutron star. Their distinguishing characteristics compared to 'normal' neutron stars is that magnetism is the likely source of energy for their radiative emissions. The behaviour of SGRs and AXPs is now best described by the magnetar model, in which the decay of an ultra-strong magnetic field ($B > 10^{14}$ G) powers the high-luminosity bursts and also a substantial fraction of the persistent X-ray emission.

Progress in the understanding of these objects was hampered for many years by the lack of detection of radio pulsars with magnetic fields much exceeding 10^{13} G. It was noted early on that fields as strong as 10^{14} - 10^{15} G could be present in neutron stars as the result of flux conservation from the progenitor star (Woltjer, 1964). The production of ultra-strong magnetic fields generated in a rotating SN collapse was also proposed as a possible catalyst for energetic outflows (LeBlanc and Wilson, 1970; Symbalisty, 1984). A related possibility is that ordinary radio pulsars could contain intense toroidal magnetic fields arising from strong differential rotation in the nascent neutron star (Ardelyan et al., 1987). Later it was realised that appropriate conditions for true dynamo action could exist in proto-neutron stars (Thompson and Duncan, 1993), leading to the formation of a class of ultra-magnetic neutron stars with dissipative properties distinct from those of radio pulsars (Duncan and Thompson, 1992).

Young magnetars undergo a rapid spin down due to their strong magnetic dipole radiation losses, reaching periods of several seconds in a few thousands years. A turbulent dynamo amplification occurring either in a newly born, differentially rotating proto-neutron star, or in the convective regions of its progenitor star could form very high magnetic fields, in principle up to 3×10^{17} G. The dynamo responsible for the high magnetic field generation requires that magnetars be born with very short rotation periods, of the order of $P_o \sim 1 - 2$ ms, and that convection is present in the core. This formation scenario

was predicted to have the two observational consequences (a) magnetars could have large spatial velocities, of the order of $\sim 10^3$ km s^{-1} and (b) their associated supernovae should be more energetic than ordinary core collapse supernovae (Duncan and Thompson, 1992).

Early in their life, magnetars slow down to the point that their magnetic energy, $E_{mag} \sim 10^{47}\ (B/10^{15}\,\mathrm{G})^2\ (R/10\,\mathrm{km})^3$, is much larger than their rotational energy, $\sim 10^{46}$ $(P/5\,\mathrm{s})\ (\dot{P}/10^{-11}\,\mathrm{s\,s^{-1}})$ ergs. Such a huge energy reservoir is sufficient to power the persistent X-ray emission for $\sim 10^4$ years. Persistent emission can be induced by the twisting of the external magnetic field caused by the motions of the star interior, where the magnetic field is dominated by a toroidal component larger than the external dipole. The twisting motion of the crust sustains steady electric currents in the magnetosphere, which provide an additional source of heating for the surface of the star (Thompson et al., 2000). The short, soft bursts can be triggered by cracking of the crust caused by the strong magnetic field. The crust fractures perturb the magnetosphere and inject fireballs. The bursts duration is dictated by the cooling time, but it depends also on the vertical expansion of surface layers (Thompson et al., 2002) and/or depth of heating (Lyubarsky et al., 2002).

The strong magnetic field ($\sim 10^{14}$ G) stresses the iron surface of the neutron star, to which it is anchored. It is believed that the magnetar internal field is tightly wound up in a toroidal configuration and is up to a factor $\sim$10 stronger than the external field (Thompson et al., 2002). The surface, a crustal lattice with a finite shear modulus, undergoes localised cracking, twisting the field lines and injecting energy into the magnetosphere (Fig. 7.10). A twisted, force-free magnetosphere supports electrical currents flowing along open field lines in normal pulsars (Thompson et al., 2002). The strong flow of charged particles heats the neutron star crust and produces a significant optical depth for resonant cyclotron scattering in the magnetosphere. Repeated scattering of the thermal photons emitted at the star surface can give rise to significant high-energy tails of $\sim 10^{40}$ - 10^{41} erg.

The magnetar starquakes and twisting magnetic field lead to the formation of an $e^{\pm}$ corona in the closed magnetosphere. The corona consists of closed flux tubes, anchored on both ends to the neutron star surface and permeated by currents driven by the twisting

motion of their footpoints. The persistent hard X-ray emission extending up to ∼100 keV originates in a transition layer between the corona and the atmosphere, while the optical and IR are emitted by curvature radiation in the corona (Beloborodov and Thompson, 2007). The gradual dissipation of the magnetospheric currents can also provide plausible mechanisms for the generation of persistent soft γ-ray emission (Thompson and Beloborodov, 2005). In recent years, pulsar searches have largely closed the observational gap between the dipole fields of radio pulsars and magnetar candidates (Manchester, 2004).

7.4.1 Neutron Stars and Magnetars

Baade and Zwicky (1934) were the first to propose the formation of neutron stars as the end product of a supernova explosion. Their forward thinking was not vindicated for another three decades, with the discovery of the first radio pulsars by Bell and Hewish (Hewish et al., 1968). As the core of a massive star (∼4 - 8 $M_\odot$) is compressed during a supernova, it collapses into a neutron star, with a radius of ∼10 km. The outer layers of the star expand rapidly outwards, creating a supernova remnant, leaving the core with a mass of ∼1.5 - 2 $M_\odot$. A neutron star is mostly made of a dense liquid of neutrons, with a trace of protons and electrons. The outer layer consists of a thick (∼100 m) crust, most probably composed of heavy atomic ions, such as iron (Fig. 7.9). The angular momentum of the parent star is mostly preserved during the collapse, resulting in a rapid rotational period which gradually slows down as the star ages (neutron star rotation periods have been observed from 1.4 ms to 30 s). For a pure magnetic dipole the rate of loss of energy is related to the angular velocity ω by:

$$\frac{d}{dt}\left(\frac{1}{2}I\omega^2\right) = I\omega\dot{\omega} = \frac{2}{3}M_\perp^2\omega^4 c^{-3} \tag{7.1}$$

where $M_\perp$ is the component of the magnetic dipole moment orthogonal to the spin axis and I is the moment of inertia. The slowdown may be expressed as a power-law:

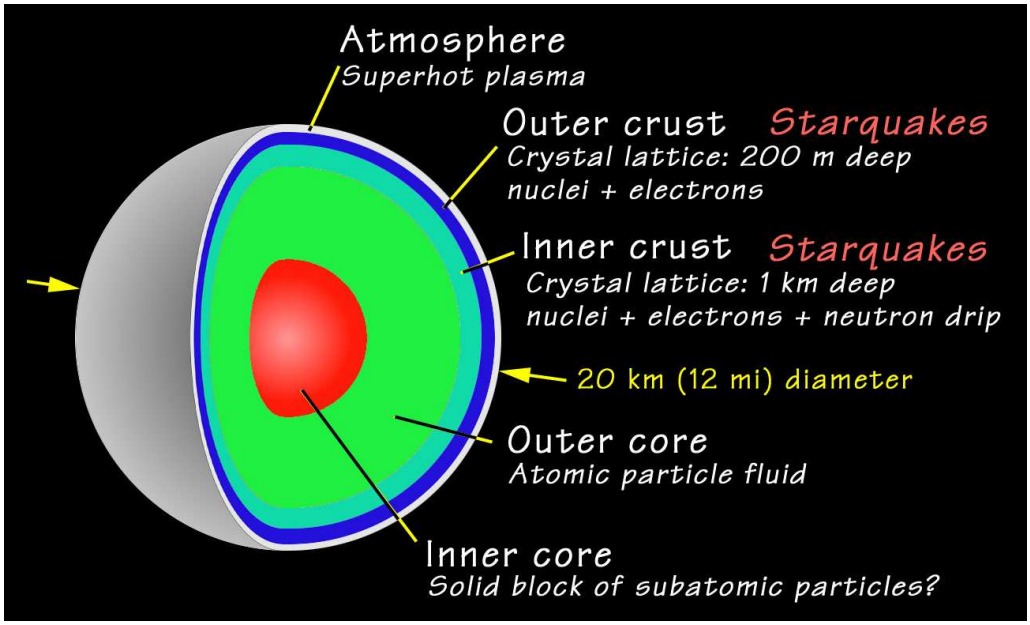

Figure 7.9: Diagram of the the structure of a neutron star. *Credit: http://science.msfc.nasa.gov/newhome/headlines/ast20may98_1.htm*

$$\dot{\omega} = -k\omega^n \tag{7.2}$$

where k is a constant and n is referred to as the 'braking index'. If the slowdown follows Eq. 7.1 then $n = 3$. If we assume the pulsar has an angular velocity which is initially very high, and a constant magnetic field, its age, t, may be determined by integrating Eq. 7.2 to give:

$$t = -(n-1)^{-1}\omega\dot{\omega}^{-1} = (n-1)^{-1}P\dot{P}^{-1} \tag{7.3}$$

where P is the period of the pulsar.

In some rare supernova explosions, a neutron star is born with a fast rotation period (~ms). The fluid in the core, which is rapidly rotating, convecting, and electrically conducting, causes a dynamo to be established which maintains the strong magnetic field of the star. Differential rotation and magnetic braking quickly slow the period down to the 5 - 10 s range (Thompson and Duncan, 1993). Magnetic diffusion and dissipation heat the neutron star surface, which radiates X-rays. The X-radiation is always present, regardless

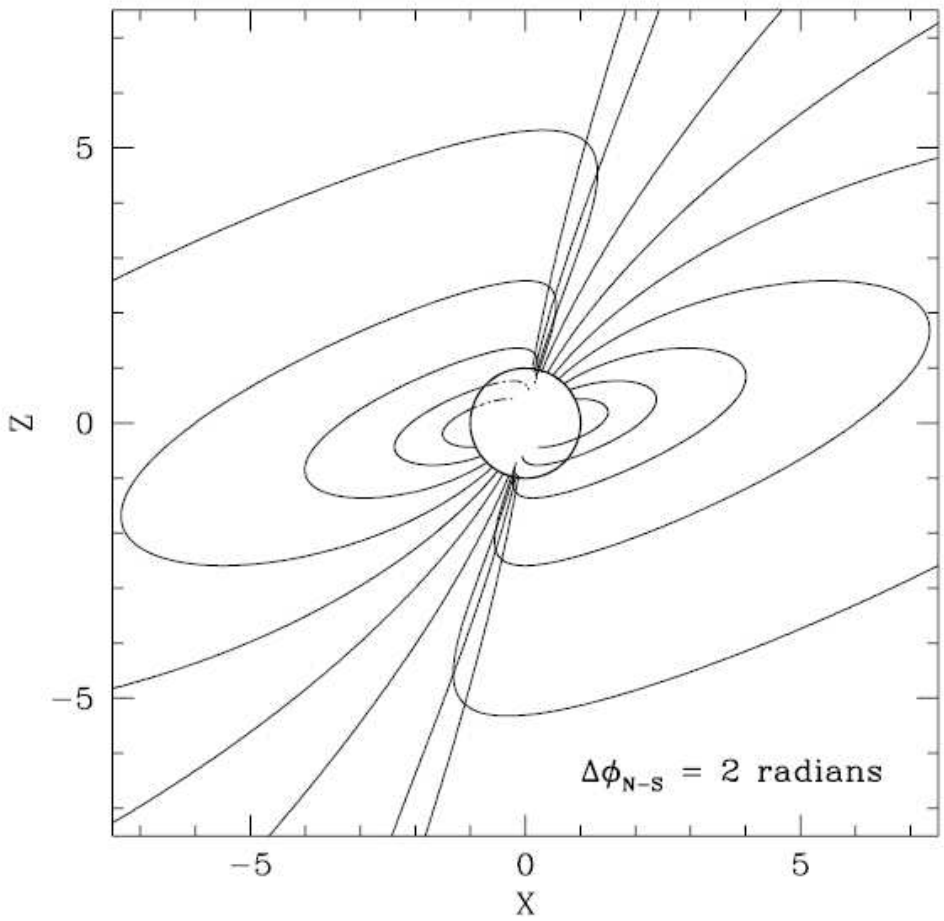

Figure 7.10: Stresses applied to the solid crust of a magnetar from the intense magnetic field creates a twisted dipole magnetic field, generating X-ray emission. The twist angle between the northern and southern hemisphere is $\Delta\Phi_{N-S} = 2\,\mathrm{rad}$. Dashed lines indicate the part of the field lines behind the neutron star. *Credit: (Thompson et al., 2002).*

of the bursting activity, so magnetars are quiescent X-ray sources. In addition, increased dissipation at the poles creates hot spots on the surface, and a periodic component whose amplitude is ~10% of the total is superimposed. Thus magnetars are quiescent, periodic X-ray sources.

Localised cracking of the crust cannot relieve all the stress which the magnetic field exerts on the surface, and it continues to build for decades. The built-up stress eventually ruptures the surface of the star profoundly, resulting in a giant flare. Magnetic field lines accelerate electrons and positrons, filling the magnetosphere with a hot pair plasma. The initial spike in the giant flare is radiation from the entire magnetosphere (a field of B

$> 10^{14}$ G is required to contain the pair plasma). The ∼5 minute long, periodic component of the flare comes from hot spots on the surface of the neutron star.

The most direct evidence for the link between SGRs and magnetars was the discovery of pulsations in the persistent X-ray flux of SGR 1806-20, with a period of 7.47 s (Kouveliotou et al., 1998). These pulsations are most likely caused by bright and dim zones on the surface of a neutron star and in its surrounding magnetosphere rotating in and out of our view. This pulsar was found to have a large spin-down rate of 2.6×10^{-3} s yr^{-1} due to magnetic dipole emission. From this, the age of the pulsar and dipolar magnetic field strength were calculated to be ∼1,500 years and 8×10^{14} G, respectively (Kouveliotou et al., 1998), in agreement with predictions of the magnetar model. These findings were reinforced when SGR 1900+14 became active again in June 1998 after a long period of quiescence. Rossi X-Ray Timing Explorer (RXTE) observations of the source during the episodes confirmed the pulsation period of 5.16 s and also found a secular spin-down of the pulse period at an average rate of 1.1×10^{-10} s s^{-1} (Kouveliotou et al., 1999). This spin-down rate was also attributed to magnetic dipole radiation and allowed an estimate of the pulsar dipolar magnetic field, calculated to be 2 - 8×10^{14} G. These findings proved the existence of magnetars, confirmed the theory that SGRs are magnetars and supported suggestions that SGR bursts are caused by neutron star 'crustquakes' produced by magnetic stresses.

7.5 SWIFT J195509 + 261406

Following the initial detection of SWIFT J195509 + 261406 as a single 'GRB' lasting about 4.6 s and its bizarre X-ray counterpart, a multi-wavelength observing campaign was mounted. Starting ∼1 min after the burst trigger time and continuing to ∼1 yr, the data set includes: Radio observations from RATAN-600 and 100 m Effelsberg; Millimetre observations from Plateau de Bure and IRAM; NIR imaging from 8.2 m VLT (including AO); optical data from Watcher, 0.3 m BOOTES-2, 1.5 m OSN, 1.34 m TLS, 6.0 m BTA

and 8.2 m VLT; X-ray data from *Swift*/XRT and XMM-Newton. Fig. 7.11 shows a colour composite optical image of the field taken by the 1.5 m OSN telescope.

The durations of the flares from SWIFT J195509 + 261406 ranged from tens of seconds to a few minutes and flux amplitudes ranged up to about 100 times the 'outburst' baseline flux (or $\geq 10^4$ times the quiescent state). After 13 June, the activity decayed abruptly and no further flares were seen until 22 June, when a late-time, lower brightness flare was detected in the near-infrared using the 8.2 m Very Large Telescope. A late-time observation by the XMM-Newton spacecraft ~173 days after the burst failed to detect the source, imposing an upper limit ($3\,\sigma$) on any underlying X-ray flux of $L_X \leq 3.1 \times 10^{-14}$ erg cm^2 s^{-1} (0.2 - 10 keV). The $^{12}CO(J = 1 - 0)$ spectrum observed in the direction of SWIFT J195509 + 261406 reveals a molecular cloud (MC) in the range +25 km s^{-1} and +30 km s^{-1}, inferring a lower limit to the kinematic distance to the *Swift* source of 3.7 kpc.

7.5.1 Optical and X-ray Observations

Fig. 7.12 shows the optical and X-ray data taken of SWIFT J195509 + 261406 from June to November 2007. Both light curves show there was strong activity during the first three days, reaching a maximum around one day after the 'GRB' and gradually decaying after the third day until the source became undetectable. The X-ray observations made by *Swift* do not overlap with the times of any of the recorded optical flares. However, observations in both X-ray and optical agree that the strongest flaring activity occurred around one day after the γ-ray event. A short (~30 s) powerful X-ray flare, in which the flux increased by a factor of $\Delta f/f \approx 100$ on a time-scale of $\Delta t/t \approx 10^{-4}$, was followed by several optical flares of similar amplitude. The X-ray data beginning one day after the giant flare event (excluding minor flaring-like activity) can be fitted by a power-law decay $F \propto t^{\alpha}$ with $\alpha = -0.75 \pm 0.25$, consistent with the values seen in the decline phase of the anomalous X-ray pulsar XTE J1810-197 (Ibrahim et al., 2004) and the transient magnetar SGR 1627-41 (Mereghetti et al., 2006).

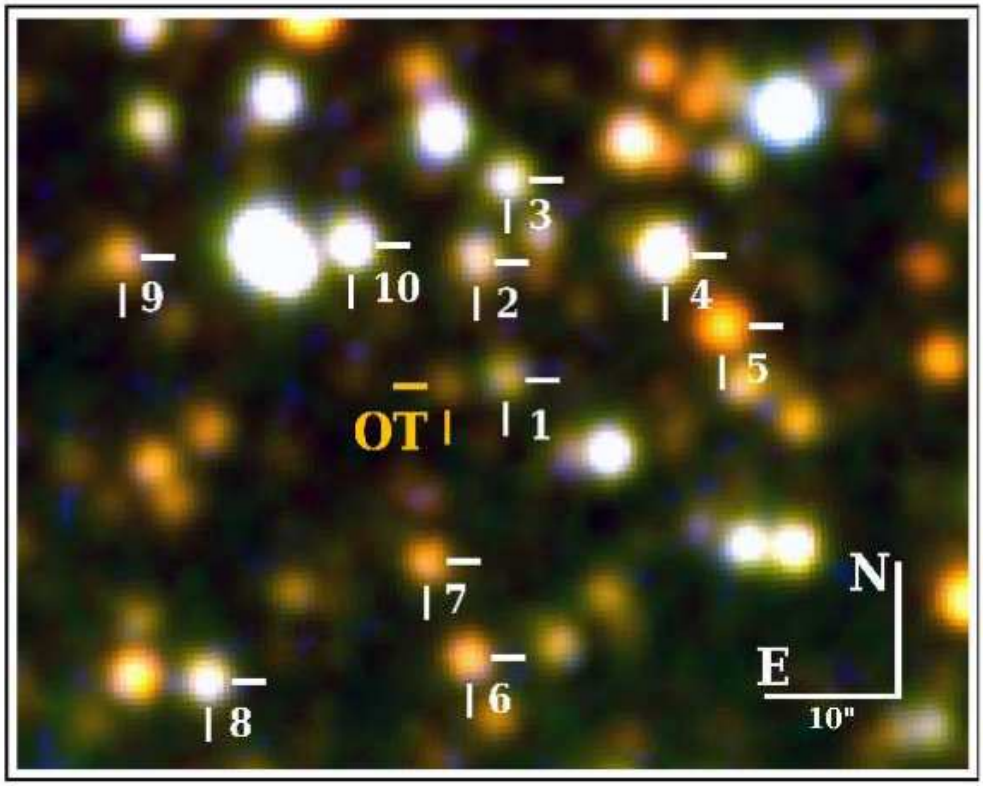

Figure 7.11: Colour composite made from V, Rc and Ic band imaging of SWIFT J195509 + 261406 at the 1.5m OSN telescope (labelled as OT for optical transient. Calibration stars used for the photometry, numbered from 1 to 10. *Credit: (Castro-Tirado et al., 2008)*

The baseline X-ray luminosity of SWIFT J195509 + 261406 during the first 8,000 s that followed the initial γ-ray spike was $\sim 1.2 \times 10^{34}\,(D/5\,kpc)^2\,\mathrm{erg\,s^{-1}}$ whereas the quiescent X-ray luminosity was $\leq 9.0 \times 10^{31}\,(D/5\,kpc)^2\,\mathrm{erg\,s^{-1}}$ (0.2 - 10 keV) at the late-time X-ray observation after ∼173 days. The quiescent X-ray luminosity is significantly smaller than the values of $\sim 4 \times 10^{33}\,\mathrm{erg\,s^{-1}}$ and $\sim 1.3 \times 10^{35}\,\mathrm{erg\,s^{-1}}$ derived for SGR 1627-41 and some anomalous X-ray pulsars, respectively.

7.5.2 Watcher Data

Watcher automatically began observations of SWIFT J195509 + 261406 at 20:53:31 UT, 53.5 s after the *Swift*/BAT detection and continued observing the target throughout the two nights that followed. The calibration of the Watcher exposures was done using two

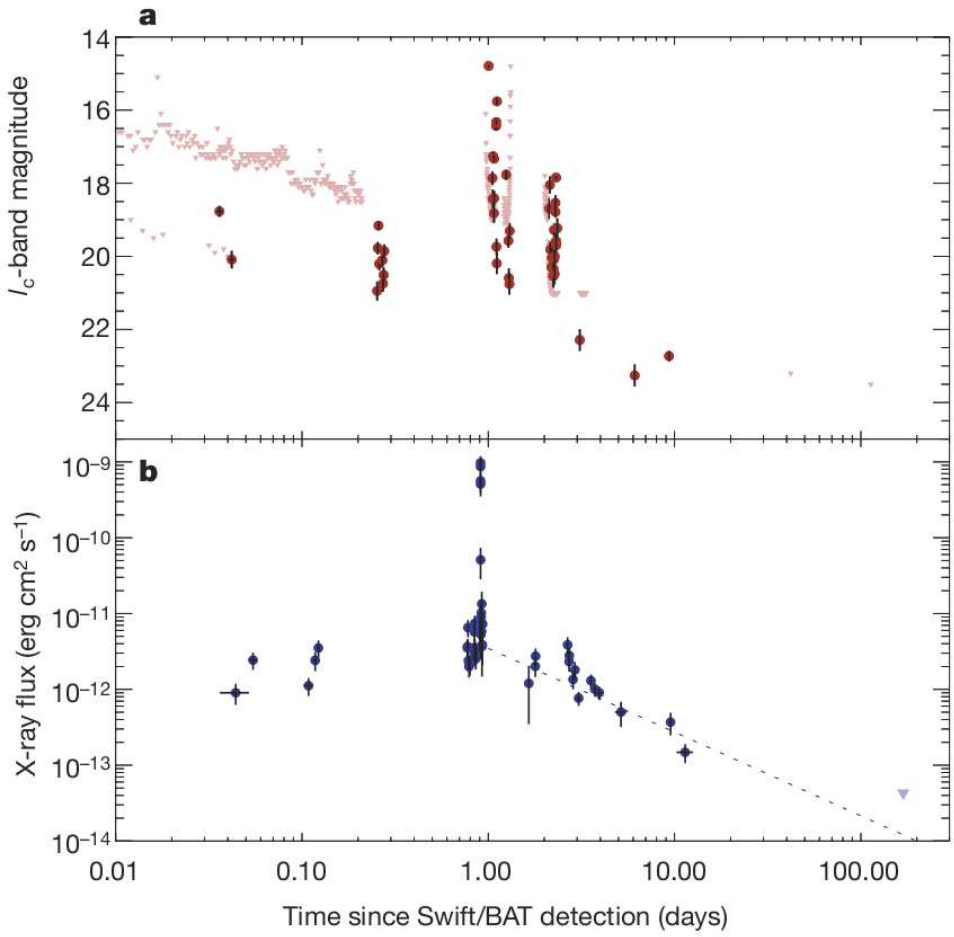

Figure 7.12: Optical and X-ray light curves of SWIFT J195509 + 261406 (June - November 2007). (a) Optical detections (Ic-band magnitudes, filled circles, with $1\,\sigma$ error bars) are shown together with $3\,\sigma$ upper limits (triangles). (b) *Swift* X-ray data (0.2 - 10 keV, filled circles, with $1\,\sigma$ error bars) together with the late-time $3\,\sigma$ limit obtained with XMM-Newton (triangle). *Credit: (Castro-Tirado et al., 2008)*

reference stars at the following coordinates (J2000): star A at R.A.= 19:55:07.77, Dec.= +26:16:34.6, with R_c = 12.14 and I_c = 11.13 and star B at R.A.= 19:55:28.016, Dec.= +26:13:49.94, with R_c = 13.88 and I_c = 12.84. In order to compare with observations by other telescopes, mostly obtained in the I_c-band, and taking into account the red colour of the source, the unfiltered frames were calibrated using I_c reference stars. Initially no optical transient was discovered, but later several bright, flaring episodes were detected. In total Watcher detected 4 flares not seen by other telescopes during the night of June 11th (Fig. 7.13). Four other detections are only marginally significant. The brightest flare detected by Watcher exhibited an increase in brightness from below the detection limit of

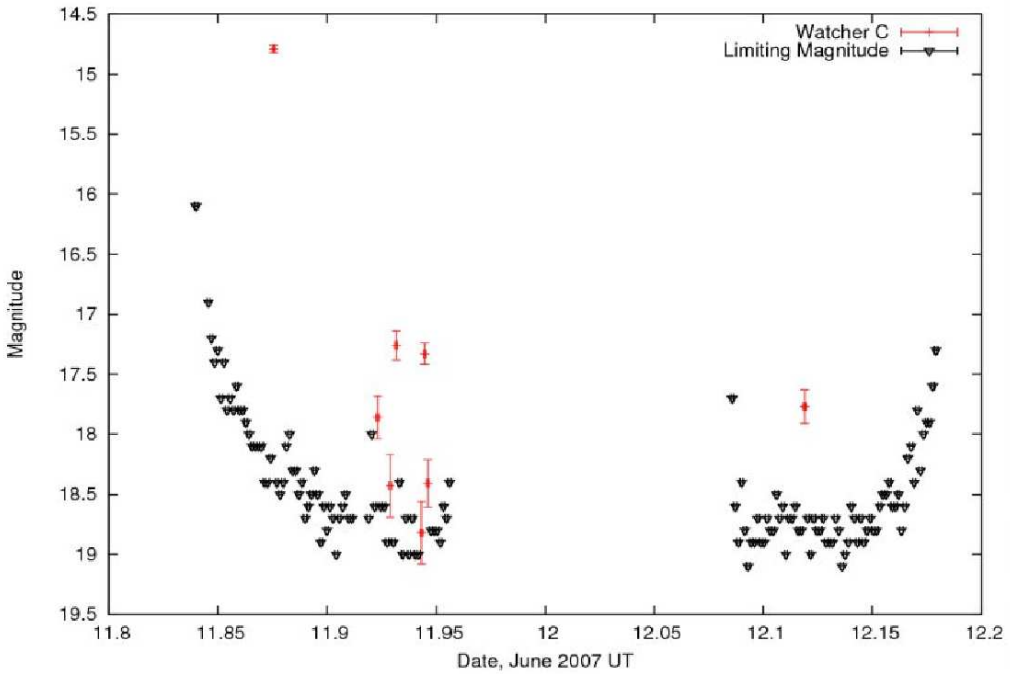

Figure 7.13: Bright flares from SWIFT J195509 + 261406 detected by Watcher on 11th and 12th June 2007. Upper limits vary depending on time of night, seeing quality etc. A gap in the data exists for ~2 hrs about midnight due to Watcher automatically responding to another GRB alert.

~18 mag to 14.7 mag within a timescale of 2 minutes. The image has been examined for cosmic rays and other possible defects and no evidence was found that the detection is not genuine. The full Watcher data is shown in Tables 7.2 and 7.3.

7.5.3 Discussion

The unusual properties of this newly discovered source make it difficult to classify. One possibility is that the source is a 'bursting pulsar', similar to GRO J1744-28 (Kouveliotou et al., 1996). However, *Swift*/BAT did not record any other γ-ray burst from SWIFT J195509 + 261406 after the initial one.

A second possibility is based on the proposed similarity to the black hole candidate V4641 Sgr (Markwardt et al., 2007; Revnivtsev et al., 2002). This black hole, orbiting an intermediate-mass companion (a B9 subgiant), was suggested as the first member of the 'fast X-ray novae' group (Uemura et al., 2002), and it has been proposed that SWIFT

J195509 + 261406 is a member of this class (Kasliwal et al., 2008). However, several lines of evidence indicate otherwise. First, the lack of further detections of the baseline (non-flaring) flux during the outburst phase at γ-ray (*Swift*/BAT), millimetre (during the outburst, <0.6 mJy, 3σ) and centimetre wavelengths (Kasliwal et al., 2008) (during the decline phase, <0.09 mJy, 3σ) implies a different physical mechanism, because considerable γ-ray and radio emission (the latter arising from a collimated jet) was recorded at the time of the V4641 Sgr outbursts (Hjellming et al., 2000). As shown in Fig. 7.14, there is no evidence for an underlying supernova remnant or a massive star cluster. Four anomalous X-ray pulsars have been detected at near-infrared wavelengths[1] but no *H*-band counterpart of any SGR is known. SGR 1806-20, which is hidden by more than 30 mag of visual extinction, was only seen in the *K*-band when it was in an active state (Israel et al., 2005). The other three known SGRs have no near-infrared counterparts. The near-infrared limit imposed on the quiescent counterpart of SWIFT J195509 + 261406 (H > 23; that is, $M_H > 8.1$ assuming $D \approx 5$ kpc and $E(B-V) = 1.9\pm 0.6$ towards the source) constrains the spectral type of any companion to be a main-sequence star with spectral type later than M5V (that is $\leq 0.12\,M_\odot$Dahn et al. (2002)) unless the donor was a hydrogen-poor (semi-) degenerate star in an ultra-compact X-ray binary with orbital period less than 1 hr (in't Zand et al., 2007).

Another method of explaining both the observed baseline flux and the flaring episodes in X-ray and optical wavelengths is an ultra-compact low-mass X-ray binary with blobs of homogeneous synchrotron-emitting plasma of size $\sim 10^7$ cm and magnetic fields of strength $\sim 10^5$ G. This third scheme allows such blobs to be found in a magnetised corona which is an extended region of low-density, X-ray irradiated material above and below the accretion disk (Merloni et al., 2000) or a wind, rather than in the outer regions of a collimated jet. Thus, SWIFT J195509 + 261406 could be part of such a system.

The final possibility is that the *Swift* source is an isolated compact object that is a new magnetar in our Galaxy, which displays activity like that of a soft γ-ray repeater in the

[1]McGill Pulsar Group SGR/AXP online catalogue. http://www.physics.mcgill.ca/ pulsar/magnetar/-main.html

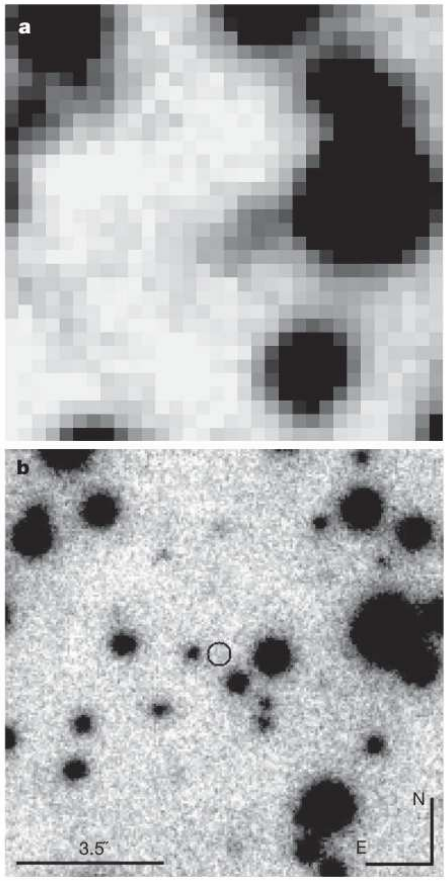

Figure 7.14: Deep, late observations of the SWIFT J195509 + 261406 field. (a) Deep I_c-band image obtained with the 6.0 m Big Telescope Altazimuthal (using SCORPIO) on 12 October 2007. (b) Deep H-band image obtained on 30 September 2007 with the 8.2 m Very Large Telescope (using NACO) using laser guide-star adaptive optics. Both images show that the source has disappeared. The location for SWIFT J195509 + 261406 is marked with a circle (error radius of 0.26"). The limiting magnitudes are $I_c > 23.5$ and $H > 23.0$. *Credit: (Castro-Tirado et al., 2008)*

optical and from which only one hard burst was recorded in γ-rays, near the onset of its bursting activity. If this is the case, SWIFT J195509 + 261406 is the first SGR detected at optical wavelengths. This is supported by the burst durations and the timing properties of the flares (Stefanescu et al., 2008). Fig. 7.15 shows the magnitude distribution of the optical flares detected in the I_c-band. The flare fluxes are found to be log-normally distributed similar to the high-energy flares of SGR 1806-20 (Hurley et al., 1995) and SGR 1900+14 (Göğüş et al., 1999). The observed data are well fitted by a truncated normal distribution (solid line) with

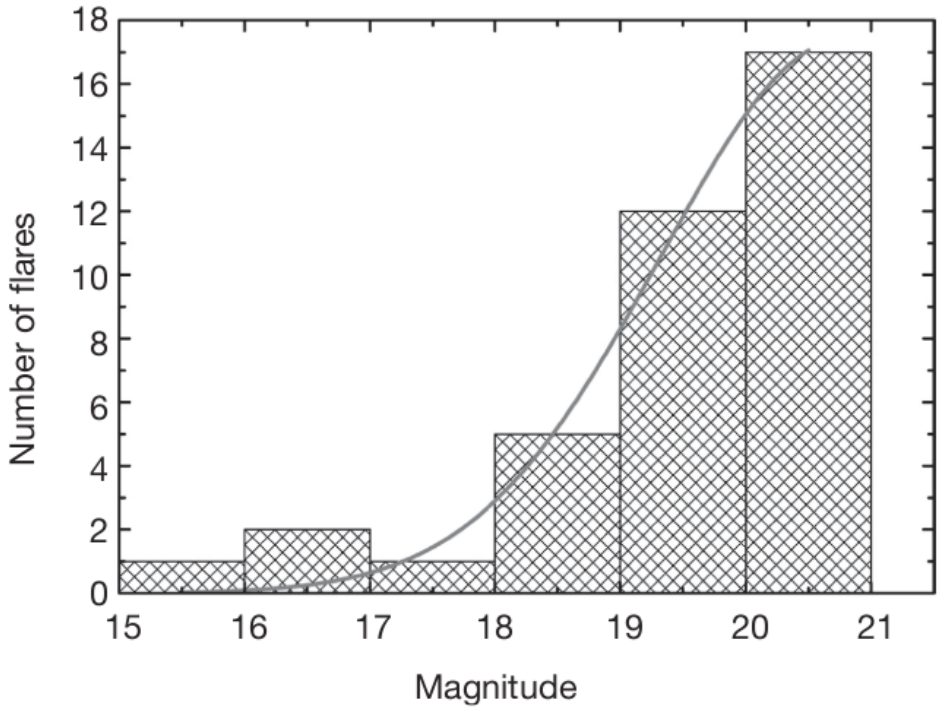

Figure 7.15: Log-normal distribution of flare fluxes for SWIFT J195509 + 261406. The magnitude distribution of the optical flares detected in the I_c-band is shown. Using all I_c-band detections of the source, the flare fluxes are found to be log-normally distributed as seen in the high-energy flares of SGR 1806-20 and SGR 1900+14, supporting the claim that SWIFT J195509 + 261406 is a new SGR, although this is not conclusive. *Credit: (Castro-Tirado et al., 2008)*

$$N = \frac{A}{w\sqrt{\frac{\pi}{2}}} e^{\frac{-2(x-x_c)^2}{w^2}} \tag{7.4}$$

where N is the number of flares in a one-magnitude bin, x is the magnitude, x_c is the centre of the distribution, w is the width and A is the amplitude. The fit is moderately acceptable with $\chi^2 = 49.7$ for 35 degrees of freedom, and parameters $x_c = 20.80 \pm 0.61$ mag, $w = 2.96 \pm 0.76$ mag and $A = 64.5 \pm 22.7$ The truncation of the distribution is a natural result of the limiting magnitude of the observations. In addition, intermediate-duration bursts (~1 - 30 s) recorded from SGR 1900+14 show two events, at ~7 kpc and lasting about 1 s, displaying unusual hard power-law spectra similar and comparable in energy, $E = (6.5 - 11) \times 10^{39}$ erg (Woods et al., 1999a), to GRB 070610, the burst of γ-rays associated with SWIFT J195509 + 261406 ($E = 1.9 \times 10^{39} (D/5\,kpc)^2$ erg) (Tueller

et al., 2007). Thus, both the initial γ-ray burst duration and the log-normal distribution of the optical flares strengthen the association of the *Swift* source with a magnetar, although the lack of detected persistent X-ray pulses (which would allow determination of the spin period derivative and thus the magnetic field) currently prevents the possibility of proving the existence of an extreme magnetic field typical of magnetars for this source.

7.6 Conclusion

A deeper X-ray observation together with a detailed study of future activity periods of SWIFT J195509 + 261406, including simultaneous X-ray/optical monitoring, could shed light onto its nature and discern whether the source is an ultra-compact low-mass X-ray binary or an isolated neutron star displaying a new manifestation of magnetar activity. In the latter case, it would represent a link between 'persistent' SGRs/AXPs (with $L_X < (2-4) \times 10^{35}\,\mathrm{erg\,s^{-1}}$ and $\sim(0.2-5) \times 10^{35}\,\mathrm{erg\,s^{-1}}$ respectively) and dim isolated neutron stars (with $L_X < (2-20) \times 10^{30}\,\mathrm{erg\,s^{-1}}$) (Treves et al., 2000), and would be one of a few hundred Galactic magnetars to become active in the past $\sim 10^4$ years (Muno et al., 2008).

Date June 2007 UT	Filter	Exp (s)	Mag
11.839213	C	120	> 16.1
11.844942	C	120	> 16.9
11.846366	C	120	> 17.2
11.847789	C	120	> 17.4
11.849213	C	120	> 17.3
11.850637	C	120	> 17.7
11.852049	C	120	> 17.4
11.853495	C	120	> 17.8
11.854942	C	120	> 17.7
11.856400	C	120	> 17.8
11.857870	C	120	> 17.6
11.859271	C	120	> 17.8
11.860683	C	120	> 17.8
11.862106	C	120	> 17.9
11.863530	C	120	> 18.0
11.864942	C	120	> 18.1
11.866400	C	120	> 18.1
11.867824	C	120	> 18.1
11.869248	C	120	> 18.1
11.870671	C	120	> 18.4
11.872095	C	120	> 18.4
11.873507	C	120	> 18.2
11.874942	C	120	14.79 ± 0.03
11.876366	C	120	> 18.4
11.877836	C	120	> 18.5
11.879294	C	120	> 18.4
11.880706	C	120	> 18.1
11.882130	C	120	> 18.0
11.883553	C	120	> 18.3
11.884965	C	120	> 18.3
11.886389	C	120	> 18.5
11.887847	C	120	> 18.4
11.889306	C	120	> 18.7
11.890775	C	120	> 18.6
11.892188	C	120	> 18.5
11.893611	C	120	> 18.3
11.895023	C	120	> 18.5
11.896458	C	120	> 18.9
11.897882	C	120	> 18.6
11.899294	C	120	> 18.8
11.900718	C	120	> 18.6
11.902153	C	120	> 18.7
11.903576	C	120	> 19.0
11.905000	C	120	> 18.7
11.906412	C	120	> 18.6
11.907836	C	120	> 18.5
11.909259	C	120	> 18.7
11.910718	C	120	> 18.7
11.918356	C	120	> 18.7
11.919769	C	120	> 18.0
11.921181	C	120	> 18.6
11.922616	C	120	17.86 ± 0.18
11.924086	C	120	> 18.6
11.925498	C	120	> 18.6
11.926910	C	120	> 18.9
11.928333	C	120	18.43 ± 0.26
11.929757	C	120	> 18.9
11.931169	C	120	17.26 ± 0.12
11.932593	C	120	> 18.4
11.934016	C	120	> 19.0
11.935486	C	120	> 18.7
11.936944	C	120	> 19.0
11.938426	C	120	> 18.7
11.939873	C	120	> 19.0
11.941296	C	120	> 19.0
11.942720	C	120	18.82 ± 0.26
11.944132	C	120	17.33 ± 0.09
11.945556	C	120	18.41 ± 0.20
11.946979	C	120	> 18.8
11.948426	C	120	> 18.8
11.949838	C	120	> 18.8
11.951262	C	120	> 18.9
11.952685	C	120	> 18.6
11.954109	C	120	> 18.7
11.955532	C	120	> 18.4

Table 7.2: Watcher photometric data of the optical counterpart of SWIFT J195509 + 261406 for the night of June 11th.

Date June 2007 UT	Filter	Exp (s)	Mag
12.085116	C	120	> 17.7
12.086528	C	120	> 18.6
12.087975	C	120	> 18.9
12.089433	C	120	> 18.4
12.090891	C	120	> 18.8
12.092373	C	120	> 19.1
12.093831	C	120	> 18.9
12.095289	C	120	> 18.9
12.096725	C	120	> 18.7
12.098206	C	120	> 18.9
12.099664	C	120	> 18.9
12.101123	C	120	> 18.7
12.102569	C	120	> 18.8
12.104005	C	120	> 18.8
12.105440	C	120	> 18.5
12.106863	C	120	> 18.7
12.083704	C	120	> 13.5
12.108287	C	120	> 18.6
12.109711	C	120	> 19.0
12.111134	C	120	> 18.7
12.112558	C	120	> 18.7
12.114005	C	120	> 18.6
12.115417	C	120	> 18.8
12.116840	C	120	> 18.8
12.118264	C	120	17.77 ± 0.14
12.119676	C	120	> 18.7
12.121100	C	120	> 19.0
12.122535	C	120	> 18.7
12.123947	C	120	> 18.8
12.125370	C	120	> 18.8
12.126794	C	120	> 18.7
12.128206	C	120	> 18.9
12.129641	C	120	> 18.9
12.131111	C	120	> 18.9

Date June 2007 UT	Filter	Exp (s)	Mag
12.132558	C	120	> 18.7
12.134016	C	120	> 18.8
12.135428	C	120	> 19.1
12.136852	C	120	> 19.0
12.138275	C	120	> 18.9
12.139688	C	120	> 18.6
12.141111	C	120	> 18.7
12.142558	C	120	> 18.9
12.144016	C	120	> 18.7
12.145475	C	120	> 18.9
12.146944	C	120	> 18.8
12.148391	C	120	> 18.7
12.149850	C	120	> 18.8
12.151319	C	120	> 18.8
12.152778	C	120	> 18.6
12.154236	C	120	> 18.5
12.155671	C	120	> 18.5
12.157083	C	120	> 18.4
12.158507	C	120	> 18.6
12.159931	C	120	> 18.6
12.161354	C	120	> 18.5
12.162778	C	120	> 18.8
12.164213	C	120	> 18.6
12.165648	C	120	> 18.2
12.167118	C	120	> 18.1
12.168530	C	120	> 18.4
12.169954	C	120	> 17.8
12.171377	C	120	> 18.3
12.172789	C	120	> 18.0
12.174225	C	120	> 17.9
12.175648	C	120	> 17.9
12.177060	C	120	> 17.6
12.178484	C	120	> 17.3

Table 7.3: Watcher photometric data of the optical counterpart of SWIFT J195509 + 261406 for the night of June 12th.

Chapter 8

Conclusions & Future Work

8.1 Conclusions

Watcher is a robotic optical telescope system capable of carrying out unmanned long-term observation plans as well as automated rapid follow-up observations of transient events, such as GRBs. It was developed on a small budget with limited manpower, and made use of existing commercially available hardware and utilises the open-source robotic observatory management software RTS2.

The system has been operating fully robotically since May 2006, and routinely carries out early observations of GRB error boxes on timescales of tens of seconds to minutes. The system has detected 6 optical transients, three of which were observed while the GRB was still active in γ-rays, and has determined early upper limits to optical emission for a number of other GRBs (see § 6.1). Some of the highlights of Watcher's observations have been the detection of prompt optical emission from GRB 060526 and GRB 060904b and the detection of multiple flaring episodes from Swift J195509 + 261406.

The *quick* software suite was developed as an automated reduction and photometric analysis pipeline for the rapid production of lightcurves for astrophysical transient objects, such as GRBs. It is written in `bash` and utilises IRAF, Octave and Gnuplot and can be installed freely on any Linux-based system. The suite was intended primarily for use with

data from Watcher but can be easily adapted to accommodate data from any telescope. A modular-based design was used, whereby a number of complex high-level 'main' scripts depend on several lower-level 'core' scripts.

8.2 Future Work

8.2.1 Watcher

One of the areas in which Watcher has been active, other than GRB follow-ups, is in blazar monitoring. Combining optical data with radio and high energy observations can contribute to the understanding of the continuum emission of blazars. This emission, which is observed to be extremely intense and to vary rapidly, is thought to originate in a relativistic plasma jet which is accelerated by a billion solar mass black hole. Watcher has also been involved in the monitoring of cataclysmic variables (CVs), in conjunction with Simon Jeffery of Armagh Observatory. CVs are close binaries in which a low-mass companion (a star of late spectral type) transfers material onto a compact object, which may be a white dwarf, neutron star, or black hole. Violent outbursts are often observed in these systems. Multi-wavelength observations can contribute to the understanding of the underlying processes. It is intended to expand Watcher's involvement in such monitoring campaigns in the future. Future observing campaigns could also include the search for extrasolar planets using the 'transit' method (the periodic dimming of a star that occurs when a close-in planet passes in front of its parent star as seen from Earth). Another way in which Watcher's productivity could be maximised is by becoming part of a network of robotic telescopes. The VOEventNet project (§ 3.1.6) in particular could allow Watcher to carry out rapid follow-up observations of other transient sources such as supernovae and microlensing events.

In June 2009 the Apogee AP6e camera on Watcher was replaced with an Andor iXon EMCCD (Electron Multiplying Charged Couple Device) (Fig. 8.3). EMCCDs operate by amplifying weak signal events (down to single photons) to a signal level that is well clear

of the read noise floor of the camera, at any readout speed. Importantly, this 'on-chip' amplification process is realized without sacrificing the photon collection capability of the sensor, with back-illuminated sensors offering up to 95% quantum efficiency. Unlike a conventional CCD, an EMCCD is not limited by the readout noise of the output amplifier, even when operated at high readout speeds. This is achieved by adding a solid state Electron Multiplying (EM) register to the end of the normal serial register. This register allows weak signals to be multiplied before any readout noise is added by the output amplifier, hence rendering the read noise negligible. The EMCCD also makes use of a frame transfer system, whereby the data is quickly transfered to a storage area before being read off the chip (Fig. 8.1). This allows the EMCCD to move on to the next exposure very quickly, increasing the duty cycle of the telescope.

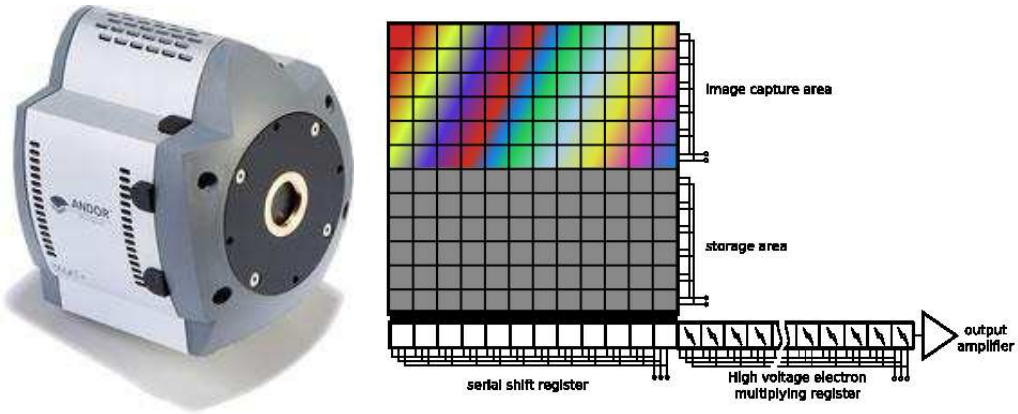

Figure 8.1: (a) The Andor iXon EMCCD. (b) Electrons are transferred from the image capture area to the storage area and are then transferred serially through the gain stages making up the multiplication register of an EMCCD. *Credit: www.andor.com*

The next upgrade for Watcher would most likely be a larger telescope and mount. The NTM-500 (Fig. 8.2(a)), produced by Astelco Systems[1], is a german equatorial mount with a load capacity of > 90 kg (plus counter weights), a maximum slewing speed of $\sim 100^\circ\ s^{-1}$ and pointing accuracy of < 5″ RMS. It is designed for robotic use and supports a wide range of software, with drivers available for both Windows and Linux. It is ideal for use with a larger 60 cm telescope, such as the light-weight Classical Cassegrain models

[1] www.astelco.com

provided by Astelco Systems (Fig. 8.2(b)). A system such as this would increase GRB response times, allow Watcher to probe to deeper magnitudes and, combined with the EMCCD, increase temporal resolution.

Figure 8.2: (a) The Astelco NTM-500. (b) The Astelco Classical Cassegrain 60 cm telescope, as seen on Bootes-3 located in New Zealand. *Credit: www.astelco.com*

8.2.2 Automated Reduction & Analysis Software & RTS2

Currently the main area of human involvement in the Watcher's routine operations is the reduction and analysis of data. Part of this process is already automated: object frames are sent to a processing queue as soon as they are taken, and an astrometric fit is performed on them using the `past` program, part of the `JIBARO` package (de Ugarte Postigo et al., 2005), which utilises `SExtractor` (Bertin and Arnouts, 1996). Astrometric data is then stored in the database as image metadata, and positional corrections, if necessary, are fed back to the mount control program. The *quick* suite currently reduces the level of human involvement in the reduction and analysis stages to a minimum. The next step is to fully integrate this process into RTS2, whereby the system could intelligently create master calibration frames, reduce the raw image frames and perform accurate photometry on specific targets of interest within the images. This would greatly improve the speed of analysis and aid in the production of GCNs.

Development of RTS2 is ongoing, with additional features and support for new devices being added regularly. One key improvement which is plannned is the addition of a merit function in the scheduler which will favour targets that are in the vicinity of the current *Swift* pointing, thereby improving follow-up times to GRB alerts generated by *Swift*. Much of the present development work is focused on the development of a web-based GUI for managing observations in order to improve the system's user-friendliness. An increasing number of groups are planning to develop robotic telescope systems based on RTS2.

8.2.3 Education & Outreach

A small robotic telescope can provide a valuable practical element to undergraduate astronomy studies (Percy, 2003). The UCD School of Physics has recently established an undergraduate degree programme in Physics with Astronomy and Space Science. The course has a substantial emphasis on hands–on experience in astronomical techniques, which will include planning observations with Watcher and analysing the resulting data. It is also intended that Watcher will contribute to the very active and expanding outreach programme at Boyden Observatory.

8.2.4 The Future Role of Robotic Telescopes in GRB Astronomy

Robotic optical telescopes are particularly well suited to the study of GRBs. The unpredictable and transient nature of these events precludes the scheduling of observations and demands automated responses on the shortest possible time-scales. Small ($< 1\,\mathrm{m}$) telescopes are sensitive enough to detect the optical emission in many cases, particularly since they can carry out observations at very early times when an optical counterpart will be at its brightest. The enhanced quality of observations in the *Swift* era has revealed unexpected complexity and variety in the optical behaviour of GRBs, and has allowed the early-time regime to be explored in greater detail than was previously possible. The

complexity of optical light curves in the *Swift* era and the unexpectedly large fraction of bursts for which no optical counterpart has been detected raises new questions which will require a large sample of well-observed bursts to address.

Figure 8.3: The Watcher Robotic Telescope including the Andor iXon EMCCD - Summer 2009. *Credit: Riccardo Felletti*.

Appendix A

Publication List of the Author

Refereed Publications

1. *"A photometric redshift of $z = 1.8^{+0.4}_{-0.3}$ for the AGILE GRB 080514B"*

   A. Rossi, A. de Ugarte Postigo, P. Ferrero, D. A. Kann, S. Klose, S. Schulze, J. Greiner, P. Schady, R. Filgas, E. E. Gonsalves, A. Küpcü Yoldaş, T. Krühler, G. Szokoly, A. Yoldaş, P. M. J. Afonso, C. Clemens, J. S. Bloom, D. A. Perley, J. P. U. Fynbo, A. J. Castro-Tirado, J. Gorosabel, P. Kubánek, A. C. Updike, D. H. Hartmann, A. Giuliani, S. T. Holland, L. Hanlon, M. Bremer, J. French, **G. Melady**, D. A. García-Hernández.

   Astronomy and Astrophysics, Volume 491, Issue 2, 2008, pp.L29-L32

2. *"Assessment of a pixel-to-pixel metrological approach to the measurement of astronomical magnitudes"*

   A. Ferrero, L. Hanlon, J. French, **G. Melady**, B. McBreen, J. Campos A. Pons.

   Metrologia, Volume 46, 2009, S228-S232

3. *"Flares from a candidate Galactic magnetar suggest a missing link to dim isolated neutron stars"*

   A. J. Castro-Tirado, A. de Ugarte Postigo, J. Gorosabe1, M. Jelínek, T. A. Fatkhullin, V. V. Sokolov, P. Ferrero, D. A. Kann, S. Klose, D. Sluse, M. Bremer, J. M. Win-

ters, D. Nuernberger, D. Pérez-Ramírez, M. A. Guerrero, J. French, **G. Melady**, L. Hanlon, B. McBreen, K. Leventis, S. B. Markoff, S. Leon, A. Kraus, F. J. Aceituno, R. Cunniffe, P. Kubánek, S. Vítek, S. Schulze, A. C. Wilson, R. Hudec, M. Durant, J. M. González-Pérez, T. Shahbaz, S. Guziy, S. B. Pandey, L. Pavlenko, E. Sonbas, S. A. Trushkin, N. N. Bursov, N. A. Nizhelskij, C. Sánchez-Fernández, L. Sabau-Graziati.

Nature, Volume 455, Issue 7212, 2008, pp. 506-509

4. *"Integral Constraints on Gamma-Ray Burst Polarization and on the Population of Nearby, Low-Luminosity Bursts"*

   L. Hanlon, S. Foley, S. McGlynn, B. McBreen, J. French, **G. Melady**, S. McBreen, A. J. Dean, D. J. Clark, A. J. Bird, D. Willis.

   International Journal of Modern Physics D, Volume 17, Issue 09, 2008, pp. 1351-1357

5. *"Gamma-ray bursts detected by INTEGRAL"*

   S. Foley, S. McGlynn, S. McBreen, L. Hanlon, B. McBreen, J. French, **G. Melady**, R. O'Connor.

   Il Nuovo Cimento B, Volume 121, November 2006, pp. 10551059

Papers in Preparation

1. *"The Watcher robotic telescope"*

   J. French, L. Hanlon, B. McBreen, **G. Melady**, Petr Kubánek, Martin Jelínek, S. McBreen, P. Meintjes M. Hoffmann, H. Calitz, A. J .Castro-Tirado, A. de Ugarte Postigo.

   To be submitted to *PASP*.

2. *"Early optical observations of GRB 060526 with the Watcher robotic telescope"*

   J. French, L. Hanlon, Petr Kubánek, Martin Jelínek, B. McBreen, **G. Melady**, S.

McBreen, G. Jóhannesson, C. Thöne, A. Kann, P. Meintjes M. Hoffmann, H. Calitz. To be submitted to *Astronomy and Astrophysics*.

Submitted Papers

1. *"The Photometry Pipeline of the Watcher Robotic Telescope"*
   A. Ferrero, L. Hanlon, R. Felletti, J. French, **G. Melady**, S. McBreen, P. Kubánek, M. Jelínek, B. McBreen, P. Meintjes, J. Calitz, M. Hoffman
   Submitted to *Advances in Astronomy*.

Non-Refereed Publications

1. *"Watcher Robotic Telescope Follow-Ups of GRBs"*
   G. Melady, J. French, L. Hanlon, B. McBreen, S. Foley, A. Ferrero, R. Felletti, S. McBreen, P. Kubánek, M. Jelínek, P. Meintjes, M. Hoffman, J. Calitz, N. Smith. GAMMA-RAY BURSTS: Sixth Huntsville Symposium. *AIP Conference Proceedings,* Volume 1133, 2009, pp. 67-69

2. *"INTEGRAL detection and follow-up observations of GRBs 080414 and 080603"*
   A. Martin-Carrillo, L. Hanlon, S. McGlynn, S. Foley, S. McBreen, **G. Melady**, J. French, P. Kubánek, A. Ferrero, B. McBreen, S. Molkov, R. Preece, A. von Kienlin. AN INTEGRAL VIEW OF COMPACT OBJECTS: 7th INTEGRAL Workshop, Copenhagen, 2008, p. 16

3. *"GRB 070610: Flares from a peculiar Galactic source"*
   A. de Ugarte Postigo, A. J. Castro-Tirado, J. Gorosabel, T. A. Fatkhullin, V. V. Sokolov, M. Jelínek, D. Sluse, P. Ferrero, D. A. Kann, S. Klose, M. Bremer, J. M. Winters, D. Nurenberger, D, Pérez-Ramírez, M. A. Guerrero, J. French, **G. Melady**, L. Hanlon, B. McBreen, F. J. Aceituno, R. Cunniffe, P. Kubánek, S. Vitek, S, Schulze, A. C. Wilson, R. Hudec, J. M. González-Pérez, T. Shahbaz, S. Guziy,

L. Pavlenko, E. Sonbas, S. Trushki, N. Bursov, N. A. Nizhelskij, L. Sabau-Graziati. GAMMA-RAY BURSTS 2007: Proceedings of the Santa Fe Conference. *AIP Conference Proceedings*, Volume 1000, 2008, pp. 337-341

4. *"Observations of Gamma-Ray Bursts with INTEGRAL"*
   S. McGlynn, S. McBreen, L. Hanlon, B. McBreen, S. Foley, J. French, **G. Melady**, A. von Kienlin, R. Preece.
   GAMMA-RAY BURSTS IN THE SWIFT ERA: Sixteenth Maryland Astrophysics Conference, *AIP Conference Proceedings*, Volume 836, May 2006, pp. 165-168

5. 11 Gamma-Ray Burst Coordinates Network (GCN) notices on Watcher GRB follow-up observations.
   GCN numbers: 8303, 8216, 8207, 6586, 6562, 6538, 6528, 6500, 5257, 5247, 4960.

Appendix B

The *quick* Code

All codes are located in /home/gmelady/apps/bin on the SSAMR lab network.

Main Scripts

quick_phot

```
#!/bin/bash

#-------------------------------------------------------
# quick_phot updated script using quick_core scripts (quick_phot_core,
    quick_calc_core)
# header to be updated
#
# Gary Melady 22-05-08
#
# 18-06-09: Removed "exposure" from the titles of output files
#                Removed instrumental magnitude output files - no longer
    needed
#-------------------------------------------------------


# -------------------- Initial setup --------------------
# Threshold sigma level value.
# If the detection level is below this value,
# the script will calculate the limiting magnitude of the image
threshold_sigma=2

# Make sure there is an input list of targets
roi=`ls *.roi | head -1` 2>/dev/null
if [ ! $roi ]
then
        echo "Need a region of interest file in x.roi containing T0 and
            coordinates of target"
```

```
25          exit
    fi
27
    # Get T0 from targets file
29  T0_temp=`grep T0 $roi`

31  # Check if there is a T0 in the file
    if [ ! $T0_temp ]
33  then
            echo "Cannot find T0 in $roi, please input initial time of
                event"
35          exit
    else
37          T0=${T0_temp#*=}
            echo $T0>T0
39  fi

41  # Get some info for header
    #(Will only work properly if all images in directory are for same
        object, filter & exposure)
43  img=`ls *.fits|head -1`

45  # Check if there are any images
    if [ ! $img ]
47  then
            echo "Cannot find any fits images, exiting"
49          exit
    fi
51
    title_fil=`gethead $img FILTER`
53  target=`gethead $img OBJECT`
    title_target=`gethead $img OBJECT|awk '{print $1_$2}'`
55  #title_exp=`gethead $img EXPOSURE`

57  # Create temp file for heading of magnitude and sn files later
    printf "#$title_target\n#Filter=$title_fil\n#JD T-T0 EXP MAG MAG_ERR S/
        N SIGMA\n" > header
59  printf "#$title_target\n#Filter=$title_fil\n#JD T-T0 EXP CAT_MAG
        INST_MAG INST_MAG_ERR S/N SIGMA\n" > lim_header

61  printf "Performing aperture photometry on: "

63  for img in $*
    do
65          printf "\n - $img"
            imgroot=`fileroot $img`
67
    #       -------------------- Time info --------------------
69
            # Calculate T-T0
71          JD=`gethead $img JD`
            EXPOSURE=`gethead $img EXPOSURE`
73          printf "$JD $EXPOSURE\n" > time_temp

75          # Call to quick_time_core to calculate T-T0
```

```
        quick_time_core
77
        # Check if it worked
79      if [ ! -e curr_img_time ]
        then
81              echo "quick_time_core failed, exiting"
                continue
83      fi

85      mv curr_img_time $imgroot.time

87 #    -------------------- Photometry --------------------

89      # Calculate optimal aperture
        quick_ape $img
91      ape=`awk '{print $1}' $imgroot.ape_opt`

93      # Get the coordinates of the targets from the target file
        # and convert it to xy coords for each frame
95      rm $imgroot.coor 2>/dev/null

97      cat $roi $imgroot.refstar | grep '^[^#]' | while read n ra dec
            mag
        do
99              sky2xy $img $ra $dec |  awk '{print $5,$6}' >> $imgroot
                    .coor
        done
101
        # Call to quick_phot_core to do the photometry on current image
103     quick_phot_core $img $ape

105     # Check if it worked

107     #if [ $? -ne 0 ]
        #then
109     #         echo "quick_phot_core failed, exiting"
        #         continue
111     #fi

113     # Rename file so octave can read it later
        cp $imgroot.mag.2 curr_img_info
115
    #   ------- 1st Check for Limiting Magnitude -------
117
        # If the target was not detected at all calculate the limiting
            magnitude of the frame
119
        if [ `head -1 $imgroot.mag.2 | awk '{print $1}'` = INDEF ]
121     then
                printf " - No detection \n   - Calculating limiting
                    magnitude"
123
                # Delete curr_img_info generated by quick_phot_core
125             # Clean up files from previous runs of quick_phot
                rm $imgroot.mag* curr_img_info 2>/dev/null
```

```
127
                # Call to quick_lim_mag6 to calculate the limiting
                    magnitude
129             quick_lim_mag6 $img

131             # Check if it worked
                if [ -s lim_mag ]
133             then
                        cat lim_mag >> lim_mag.dat
135                     rm lim_mag
                        printf "Done "
137                     continue
                else
139                     echo " quick_lim_mag6 failed, exiting"
                        continue
141             fi
        fi
143

145 #       ---------- Calculate apparent magnitudes --------

147     # If object was detected continue with photometry

149     # Get catalog magnitude values for reference stars from refstar
            file
        grep '^[^#]' $imgroot.refstar | while read n ra dec mag
151     do
            echo $mag >> cat_mag
153     done

155     # Call to quick_aphot_core to do the apparent photometry
        #cat curr_img_info
157     quick_aphot_core

159     # Check if it worked
        if [ $? -ne 0 ]
161     then
                echo "quick_aphot_core failed"
163             continue
        fi
165
        mv curr_img_app $imgroot.app 2>/dev/null
167     rm cat_mag

169 #       ---------- Calculate confidence levels ----------

171     # Call to quick_confidence_core to calculate the s/n and sigma
            levels
        quick_confidence_core
173

175     # Check if it worked
        if [ $? -ne 0 ]
177     then
                echo "quick_confidence_core failed"
```

```
179                 continue
            fi
181
            mv curr_img_sn $imgroot.sn 2>/dev/null
183
#       --------- Limiting Magnitude Again ------------
185
            # If the sigma level of the source is below a threshold value,
                get the limiting magnitude of the image
187         head -n1 $imgroot.sn | while read SN SIG
            do
189                 SIGMA=`printf %.0f $SIG`
                    if [ $SIGMA -le $threshold_sigma ]
191                 then
                            printf " - Detection below threshold \n   -
                                Calculating limiting magnitude"
193
                            # Delete curr_img_info quick_phot_core
195                         rm $imgroot.mag* curr_img_info 2>/dev/null

197                         # Call to quick_lim_mag6 to calculate the
                                limiting magnitude
                            quick_lim_mag6 $img
199                 fi
            done
201

203         # Check if it worked
            if [ -s lim_mag ]
205         then
                    cat lim_mag >> lim_mag.dat
207                 rm lim_mag
                    printf "Done "
209                 continue
            fi
211
#       -------------------- Clean up ------------------
213
            # Append all info to appropriate files
215         #Apparent photomtery:
            if [ -e $imgroot.app ]
217         then
                    echo "`sed -n 1p $imgroot.time` `sed -n 1p $imgroot.app
                        ` `sed -n 1p $imgroot.sn`" >> app_phot
219         fi

221         # Instrumental photometry
            i=1
223         j=`cat $imgroot.mag.2 2>/dev/null | wc -l`
            while [ $i -le $j ]
225         do
                    echo "`sed -n 1p $imgroot.time` `sed -n "$i"p $imgroot.
                        mag.2 | awk '{print $1,$2}'` `sed -n "$i"p $imgroot
                        .sn`" >> inst_phot.$i
227                 i=`expr $i + 1`
```

```
        done
229
        printf "Done "
231
done
233
# Add headers to output files
235 # Apparent Photometry
if [ -e app_phot ]
237 then
        cat header app_phot | column -t > apparent_magnitude_"
            $title_target"_"$title_fil"
239 #else
#         printf "\nNo apparent magnitude file found"
241 fi

243 # Limiting magnitudes
if [ -e lim_mag.dat ]
245 then
       cat lim_header lim_mag.dat | column -t > limiting_magnitude_"
           $title_target"_"$title_fil"
247 #else
#         printf "\nNo limiting magnitude file found"
249 fi

251 rm curr_img_* 2>/dev/null
rm *.coor *.perror *.sn *.app *.time *.ub1 *.ape_opt 2>/dev/null
253 rm header lim_* T0 uparm* cat_mag tim* app_* inst_* 2>/dev/null
rm *.mag* 2>/dev/null
255
# Plot the results
257 if [ -e apparent_magnitude_"$title_target"_"$title_fil" ] && [ -e
    limiting_magnitude_"$title_target"_"$title_fil" ]
then
259         quick_plot_object_lim_sn

261 elif [ -e apparent_magnitude_"$title_target"_"$title_fil" ]
then
263         quick_plot_sn apparent_magnitude_"$title_target"_"$title_fil"

265 elif [ -e limiting_magnitude_"$title_target"_"$title_fil" ]
then
267         quick_plot_lim_sn limiting_magnitude_"$title_target"_"
            $title_fil"

269 fi

271 printf "\nDone \n"
```

quick_reduce

```
#!/bin/bash

#-----------------------------------------------------------------
# Program to do a quick grb images reduction using iraf.
# Place images in directory "images"
# Place darks in directory "darks"
# Place flats in directory "flats"
# Check darks/flats for problems (e.g. very high counts) using imstat.
# Run program from directory above those created.
#
# Program requirements: fitsname.sh, iraf
#
# Summary:
# - Combines darks into master darks based on exposure.
# - Subtracts master darks from all target images based on exposure.
# - Flat fields all target images based on filter.
#
# Gary Melady June 2007
#
# 21-06-07 Changed from "imcombine" to "darkcombine" to create master
    darks.
# 21-06-07 Changed from "imarith" to "ccdproc" to dark subtract object
    images.
# 21-06-07 Added flat field processing (flatcombine and ccdproc)
# 04-08-07 Fixed flat fielding in reduction
# 12-12-07 Fixed iraf problem in ubuntu (iraf hates tabs for some
    reason)
# 31-01-08 Added sorting of reduced images by filter
# 01-02-08 Added way to remove bad darks (i.e. mean pixel counts above
    some threshold)
# 23-02-08 Changed from fitsname.sh to quick_name (much faster)
#                       Completely removed ability to do dark
    subtraction only if no flats are found
# 08-04-08 Added trimming and bad pixel mask to all images
#
#-----------------------------------------------------------------

# Combine the darks to form master darks for each exposure length
# For grb's exposures are 10s, 30s, 60s and 120s.

dir=`pwd`
dark=`pwd`/darks
flat=`pwd`/flats
image=`pwd`/images

# To change / add exposures /filters do it here
exposure="1 5 10 20 30 60 120"
filter="B V R I C"

# Threshold settings for deciding what's a good dark / flat
dark_lim=500 # upper limit for mean pixel value of darks
flat_lim=500 # lower limit for mean pixel value of flats

# Bad pixel mask
```

```
50
#echo "Starting image reduction"
52 echo "---------------< Darks >---------------"

54 # Test to see if darks directory exists
if [ -d $dark ]
56 then
  cd $dark
58
  # Test for anomalous (high value) darks and move to trash if mean is
      above $dark_lim
60  if [ -d trash ]
  then
62                echo "Quality of darks already tested"
        else
64        printf "Testing quality of darks"
          quick_imstat *.fits &>/dev/null
66
          grep '^[^#]' imstat.dat | while read image npix mean stdev
              min max
68        do
            mean1=${mean%.*}
70          printf "."
            if [ $mean1 -ge $dark_lim ]
72          then
              mkdir trash &>/dev/null
74            printf "\n -- Mean value of $image = $mean > $dark_lim -
                  moving to $dark/trash"
              mv $image trash
76          fi
          done
78              printf "Done\n"
        fi
80

82  # Test if we need to rename the darks
  ls *T*.fits > dnam.dat 2>/dev/null
84  if [ -s dnam.dat ]
  then
86    echo "Darks already renamed"
  else
88    #echo "Renaming darks"
      quick_name *.fits #&>/dev/null
90  fi
  rm dnam.dat
92
        # Trim the images (top 4 rows, right most column)
94      # Fix the bad pixels (as described in badpixmask.dat above)

96      # Test if darks need to be trimmed
        ls tbp*.fits > dtbp.dat 2>/dev/null
98      if [ -s dtbp.dat ]
        then
100             echo "Darks already trimmed"
        else
```

```
                echo "Trimming the darks..."
                ls *.fits > list.dat 2>/dev/null

                echo 'noao
                imred
                ccdred
                unlearn ccdproc
                ccdproc @list.dat output="tbp_@list.dat" ccdtype=""
                    fixpix- oversca- trim+ zerocor- darkcor- flatcor-
                    trimsec="[1:1023,1:1020]"
                logout' | ecl | grep ERROR
        fi

        rm list.dat dtbp.dat logfile up* 2>/dev/null
        mkdir originals 2>/dev/null
        mv dark*.fits originals 2>/dev/null

  # Combine darks using iraf darkcombine
  for exp in $exposure
  do
    if [ -e mdark_"$exp".fits ]
    then
      echo "$exp s master dark already exists"
    else
      x=`ls tbp*_"$exp".fits 2>/dev/null |head -1`
      if [ -e "$x" ]
      then
        echo "Creating master $exp s dark..."
        ls tbp*_"$exp".fits > dark_"$exp".dat

        echo 'noao
        imred
        ccdred
        unlearn darkcombine
        darkcombine @dark_'$exp'.dat output="mdark_'$exp'.fits" combine
            ="median" reject="crreject" process- gain="8.0"
        logout' | ecl | grep ERROR

        # Clean up
        rm $dark/*.dat
      #else
        #echo "Cannot find any $exp s darks"
      fi
    fi
  done
  cd $dir
else
  echo "Cannot find 'darks' directory"
  echo "Exiting"
  exit
fi

# Combine flats to form master flats based on filter
# Filters are $filter but for grb's it's usually C.
```

```
154 echo "---------------< Flats >---------------"

156 # Test to see if flats directory exists
    # TO DO get mkskycor working to eliminate illumination gradient
158 if [ -d $flat ]
    then
160   cd $flat

162         # Test for anomalous (low value) flats and move to trash if
              mean is below $flat_lim
      if [ -d trash ]
164   then
            echo "Quality of flats already tested"
166         else
            printf "Testing quality of flats"
168         quick_imstat *.fits &>/dev/null

170         grep '^[^#]' imstat.dat | while read image npix mean stdev
              min max
            do
172           mean1=${mean%.*}
              printf "."
174           if [ $mean1 -le $flat_lim ]
              then
176             mkdir trash &>/dev/null
                printf "\n -- Mean value of $image = $mean < $flat_lim -
                  moving to $flat/trash"
178             mv $image trash
              fi
180         done
                    printf "Done\n"
182         fi

184   # Test if we need to rename the flats
      ls *T*.fits > fnam.dat 2>/dev/null
186   if [ -s fnam.dat ]
      then
188           echo "Flats already renamed"
            else
190     #echo "Renaming flats"
        quick_name *.fits #&>/dev/null
192   fi
      rm fnam.dat
194
      # Trim the images (top 4 rows, right most column)
196         # Fix the bad pixels (as described in badpixmask.dat above)

198         # Test if flats need to be trimmed
            ls tbp*.fits > ftbp.dat 2>/dev/null
200         if [ -s ftbp.dat ]
            then
202                 echo "Flats already trimmed"
            else
204                 echo "Trimming the flats..."
                    ls *.fits > list.dat 2>/dev/null
```

```
206
        echo 'noao
208     imred
        ccdred
210     unlearn ccdproc
        ccdproc @list.dat output="tbp_@list.dat" ccdtype="" fixpix-
            oversca- trim+ zerocor- darkcor- flatcor- trimsec="
            [1:1023,1:1020]"
212     logout' | ecl | grep ERROR
        fi
214
        rm list.dat ftbp.dat logfile up* 2>/dev/null
216     mkdir originals 2>/dev/null
        mv flat*.fits originals 2>/dev/null
218
  # Combine flats using iraf flatcombine
220 #echo "Creating master flats"

222 for fil in $filter
  do
224   if [ -e mflat_"$fil".fits ]
    then
226   echo "$fil band master flat already exists"
    else
228   x=`ls tbp*_"$fil".fits 2>/dev/null |head -1`
      if [ -e "$x" ]
230   then
        echo "Creating master $fil band flat..."
232     ls tbp*_"$fil".fits > flat_"$fil".dat

234                     echo 'noao
                        imred
236                     ccdred
                        unlearn flatcombine
238                     flatcombine @flat_'$fil'.dat output="mflat_'
                            $fil'.fits" combine="median" reject="
                            crreject" process- gain="8.0"
                        logout' | ecl | grep ERROR
240
        # Clean up
242     rm $flat/*.dat
      #else
244     #echo "Cannot find any $fil band flats"
      fi
246   fi
  done
248 cd $dir
else
250 echo "Cannot find 'flats' directory"
  echo "Exiting"
252 exit
fi
254
echo "----------------< Images >----------------"
256
```

```
# Process target images
# Flat field and subtract master darks from images according to filter
    and exposure
# Test to see if images directory exists
if [ -d $image ]
then
  cd $image
  x=`ls *.fits 2>/dev/null | head -1`
  if [ -e "$x" ]
  then

          # Test if we need to rename the images
          ls *T*.fits > inam.dat 2>/dev/null
          if [ -s inam.dat ]
          then
            echo "Images already renamed"
          else
            #echo "Renaming images"
            quick_name *.fits #&>/dev/null
          fi

                # Trim the images (top 4 rows, right most column)
                # Fix the bad pixels (as described in badpixmask.dat
                    above)

                # Test if images need to be trimmed
                ls tbp*.fits > itbp.dat 2>/dev/null
                if [ -s itbp.dat ]
                then
                        echo "Images already trimmed"
                else
                        echo "Trimming the images..."
                        ls *.fits > list.dat 2>/dev/null

                        echo 'noao
                        imred
                        ccdred
                        unlearn ccdproc
                        ccdproc @list.dat output="tbp_@list.dat"
                            ccdtype="" fixpix- oversca- trim+ zerocor-
                            darkcor- flatcor- trimsec="[1:1023,1:1020]"
                        logout' | ecl | grep ERROR
                fi

                rm list.dat itbp.dat logfile up* 2>/dev/null
                mkdir originals 2>/dev/null
                #mv dark*.fits originals

          cp $dark/mdark_*.fits $image
          cp $flat/mflat_*.fits $image

          for fil in $filter
          do
            fla=`ls mflat_"$fil".fits 2>/dev/null |head -1`
            #echo "Master flat: $fla"
```

```
308
            if [ -e "$fla" ]
310         then

312           for exp in $exposure
              do
314             dar=`ls mdark_"$exp".fits 2>/dev/null | head -1`
                #echo "Master dark: $dar"
316             img=`ls *_"$fil"_"$exp".fits 2>/dev/null |head -1`
                #echo "test: $img"
318
                if [ -e "$dar" ]
320             then
                  if [ -e "$img" ]
322               then
                    echo "Performing $fil band $exp s image reduction
                        ..."
324                 ls tbp*_"$fil"_"$exp".fits > image_"$fil"_"$exp".
                        dat

326                 # Do not put ".fits" at the end of the name of the
                        master flat
                    echo 'noao
328                 imred
                    ccdred
330                 unlearn ccdproc
                    ccdproc @image_'$fil'_'$exp'.dat output=
                        fd_@image_'$fil'_'$exp'.dat fixpix- oversca
                        - trim- zerocor- dark="mdark_'$exp'.fits"
                        flat="mflat_'$fil'"
332                 logout' | ecl | grep ERROR

334               #else
                    #echo "No $fil band $exp s exposure images found"
336               fi

338             #else
                  #echo "Cannot find $exp s master dark - Cannot
                      perform $fil band $exp s image reduction"
340             fi
              done
342           #else
                #echo "Cannot find $fil band master flat - Cannot perform
                    $fil band flat fielding"
344           fi
            done
346
            cd $dir
348   else
            echo "Cannot find any fits images in $image"
350         echo "Exiting"
            exit
352       fi

354 else
```

```
  echo "Cannot find 'images' directory"
  echo "Exiting"
        exit
fi

# Move reduced images to $images/reduced

cd $image
# Remove master darks and flats
rm m*.*

if [ -e reduced ]
then
  mv fd_*.fits reduced/ 2>/dev/null
else
  mkdir reduced
  mv fd_*.fits reduced/ 2>/dev/null
fi

# Keep the original unreduced files in $images/originals

if [ -e originals ]
then
  mv *.fits originals/
else
  mkdir originals
  mv *.fits originals/
fi

# Organise reduced images by filter and exposure
cd $image/reduced
# Quick check on quality of all reduced images
ls *.fits > check.dat 2>/dev/null
if [ -s check.dat ]
then
        quick_imstat -p *.fits
else
        echo "No reduced images found, quick_reduce failed"

        # Clean up
        rm *.dat
        cd $image
        rm *.dat

        exit
fi

for fil in $filter
do
  for img1 in *.fits
  do
    echo $img1 | grep _$fil>$fil.dat

    # Organise by filter
    if [ -s $fil.dat ]
```

```
410     then
          mkdir $fil 2>/dev/null
412       mv $img1 $fil
        fi
414   done
      #cd $image/reduced
416 done

418 # Clean up
    rm *.dat
420 cd $image
    rm *.dat
422
    cd $dir
424 printf "\n"
    echo "Original images saved to $image/originals"
426 echo "Reduced images saved to $image/reduced"
    printf "\nDone\n"
```

quick_reference_star

```
#!/bin/bash

#-------------------------------------------------------------
# Program to:
# - automatically select reference stars from a catalogue
# - detect the stars in all the input fits images
# - remove any stars that are not detected in all frames
# - remove the stars that are detected but have low sigma level (below
    threshold_sigma)
# - output list of useable reference stars in target file for use with
    quick_phot
#
# Requirements:
# - quick_time_core, quick_cat_core_ref, quick_phot_core,
    quick_confidence_core, quick_region
# - iraf (phot, txdump)
# - wcstools (scat, gethead, fileroot, sky2xy)
# - octave
# - coordinates of target in x.targets file (placed in current dir)
#
# Gary Melady 23-12-08
#
# - 17-06-09 Fixed 3 bugs:
#       - changed "exit" to "continue" in success tests
#       - made sure the word INDEF is removed from all files needed by
    octave
#       - made provision for the posibility that no suitable reference
    stars are found
#-------------------------------------------------------------

# For filtering by sigma level
# (The sigma threshold number must be an integer)
threshold_sigma=2

# Get input file
target=`ls *.roi|head -1`

# Check if a roi file exists
if [ ! $target ]
then
        echo "Cannot find roi file"
        echo "Exiting"
        exit
fi

# Get T0 (Tzero) from input file
T0_temp=`cat $target |grep T0`

# Check if there is a T0 in the file
if [ ! $T0_temp ]
then
        echo "Cannot find T0 in $targets, please input initial time of
            event"
        exit
```

```
49 else
        T0=${T0_temp#*=}
51      echo $T0>T0
fi
53
# Get filter (only works if all images are the same filter in the
    current dir)
55 img1=`ls *.fits|head -1`

57 # Check if there are any images
if [ ! $img1 ]
59 then
        echo "Cannot find any fits images, exiting"
61      exit
fi
63
filter=`gethead $img1 FILTER`
65
# Get coordinates of target
67 ra=`grep '^[^#]' $target | grep object | awk '{print $2}'`
dec=`grep '^[^#]' $target | grep object | awk '{print $3}'`
69
# ------------------- Search The Catalogue --------------------
71
printf "Searching catalogue for reference stars around RA: $ra, DEC:
    $dec, in filter $filter"
73 quick_cat_core_ref $ra $dec $filter

75 # Check if it worked
if [ ! -s refstar.dat ]
77 then
        echo "Cannot find refstar.dat, quick_cat_core failed"
79      echo "Exiting"
        exit
81 fi

83 printf "\nPerforming aperture photometry on:"
# Do photometry on all targets in all images, calculate s/n and sigma
85 # filter results to remove inappropriate candidates

87 for img in $*
do
89      printf "\n - $img"

91 #       -------------------- Initial info --------------------

93      imgroot=`fileroot $img`

95      # Calculate T-T0
        JD=`gethead $img JD`
97      EXPOSURE=`gethead $img EXPOSURE`
        printf "$JD $EXPOSURE\n" > time_temp
99
        # Call to quick_time_core to calculate T-T0
101     quick_time_core
```

```
103         # Check if it worked
            if [ $? -ne 0 ]
105         then
                echo "quick_time_core failed, exiting"
107             continue
            fi
109
            mv curr_img_time $imgroot.time
111
#           ------------------- Photometry -------------------
113
            # Get the coordinates of the targets from the target file
115         # and convert it to xy coords for each frame

117         grep '^[^#]' refstar.dat | while read ra dec mag
            do
119             sky2xy $img $ra $dec | awk '{print $5,$6}' >> $imgroot
                    .coor
            done
121
            # Call to quick_phot_core to do the photometry on current image
123         quick_phot_core $img

125         # Check if it worked
            #if [ $? -ne 0 ]
127         #then
            #   echo "quick_phot_core failed, exiting"
129         #   exit
            #fi
131
            # Organise result into file with columns: CAT_RA, CAT_DEC,
                CAT_MAG, INST_MAG, INST_ERROR
133         i=1
            cat refstar.dat | while read RA DEC CATMAG
135         do
                echo "$RA $DEC $CATMAG `sed -n "$i"p $imgroot.mag.2|awk
                    '{print $1,$2}'`" >> $imgroot.ref.1
137             i=`expr $i + 1`
            done
139
            # Clean up file so octave can read it later - remove lines that
                contain the word "INDEF"
141         grep -v INDEF $imgroot.mag.2 > $imgroot.mag.3
            grep -v INDEF $imgroot.ref.1 > $imgroot.ref.2
143         cp $imgroot.mag.3 curr_img_info

145 #       ---------- Calculate confidence levels ----------

147         # Call to quick_confidence_core to calculate the s/n and sigma
                levels
            quick_confidence_core
149
            # Check if it worked
151         if [ $? -ne 0 ]
```

```
        then
153             echo "quick_confidence_core failed, exiting"
                continue
155     fi

157     mv curr_img_sn $imgroot.sn

159 #   ------------------- Clean up files -------------------

161     # Append confidence results onto x.ref.2 file
        # With cols: CAT_RA, CAT_DEC, CAT_MAG, INST_MAG, INST_ERROR, SN
            , SIGMA
163     i=1
        cat $imgroot.ref.2 | while read RA DEC CATMAG IMAG IERR
165     do
                echo "$RA $DEC $CATMAG $IMAG $IERR `sed -n "$i"p
                    $imgroot.sn`" >> $imgroot.ref.3
167             i=`expr $i + 1`
        done
169
        # Check if the sigma level is above the $threshold_sigma
171     # If so, keep the star, if not delete it.

173     i=1
        cat $imgroot.ref.3 | while read RA DEC CATMAG IMAG IERR SN SIG
175     do
                SIGMA=`printf %.0f $SIG`
177             if [ $SIGMA -ge $threshold_sigma ]
                then
179                     printf "$i $RA $DEC" >> $imgroot.refstar
                        printf " %.3f " $CATMAG >> $imgroot.refstar
181                     printf "\n" >> $imgroot.refstar

183                     i=`expr $i + 1`
                fi
185     done

187     # Check if any suitable reference stars were found
        if [ -s $imgroot.refstar ]
189     then
                # Create region file of reference stars
191             quick_region $imgroot.refstar 1>/dev/null
        else
193             printf " - No suitable reference stars found, moving
                    image to trash - "
                mkdir trash &>/dev/null
195             mv $imgroot.fits trash
        fi
197
        printf "Done"
199
    done
201
    # Clean up
203 #rm *.coor *.mag* *.time *.ref.* *.sn 2>/dev/null
```

```
#rm refstar* T0 time* up* curr*
205
printf "\nDone\n"
```

Core Scripts

quick_ape

```
#!/bin/bash

#
# Script to calculate the optimal aperture for photometry
#
# Gary Melady 20-01-09
#

# Aperture range
ape_min=2.5
ape_max=5.5
ape_step=0.3

# Create integer counters for the while loop
# (it can't handle floating point numbers - lame)
j_temp=`echo "($ape_max - $ape_min)/$ape_step + 1"|bc -l`
j=`printf %.0f $j_temp`

printf ".("
printf "Aperture optimization"

for img in $*
do
        #printf "\n - $img"
        imgroot=`fileroot $img`

        # Make sure there is an input list of targets
        targets=$imgroot.refstar
        if [ ! $targets ]
        then
                echo "Need a list of targets in $imgroot.refstar file"
                continue
        fi

        # Get coordinates in xy
        rm $imgroot.coor 2>/dev/null
        head -1 $targets | while read n ra dec mag
        do
                sky2xy $img $ra $dec |  awk '{print $5,$6}' >> $imgroot
                    .coor
        done

        i=1
        ape=$ape_min
        while [ $i -le $j ]
        do
                # Run photometry on the image also passing the aperture
                     size
                quick_phot_core $img $ape

                #printf " $ape "
```

```
51                  # Save output to different file
                    mv $imgroot.mag.2 "$imgroot"_"$ape".ape
53                  cp "$imgroot"_"$ape".ape curr_img_info
                    rm $imgroot.mag.1
55
                    # Call to quick_confidence_core to calculate the s/n
                        and sigma levels
57                  quick_confidence_core

59                  # Check if it worked
                    if [ $? -ne 0 ]
61                  then
                            echo "quick_confidence_core failed"
63                          continue
                    fi
65
                    mv curr_img_sn "$imgroot"_"$ape".ape_sn 2>/dev/null
67
                    obj=1 #Temp counter
69                  # Organise results by object and aperture with cols:
                        APERTURE SN SIGMA
                    cat "$imgroot"_"$ape".ape_sn | while read SN SIGMA
71                  do
                          echo "$ape $SN $SIGMA" >> "$imgroot"_object_"$obj
                              ".ape_sn
73                        obj=`expr $obj + 1`
                    done
75
                    # Increment counters
77                  ape=`echo "$ape + $ape_step"|bc -l`
                    i=`expr $i + 1`
79          done

81          # Select the aperture that gives the highest sigma
            sort -rk3 "$imgroot"_object_"$obj".ape_sn | head -1 > "$imgroot
                ".ape_opt
83
            ape=`awk '{print $1}' $imgroot.ape_opt`
85          printf "Aperture=$ape)"

87          #printf "Done"
    done
89
    # Clean up
91  rm *.ape *.ape_sn curr_img_info up* *.coor
    #printf "Done\n"
```

quick_aphot_core

```
#!/bin/bash

#
# quick_aphot_core
#
# Script to calculate apparent photometry of target object in a frame
# This is a core script to be called by other scripts
#
# Requirements:
# - Octave
# - outputs from quick_phot_core
#
# Gary Melady 03-06-08
#

# Test for existance of necessary files:

if [ ! -e curr_img_info ]
then
        echo "quick_aphot_core: Cannot find curr_img_info, exiting"
        exit
fi

if [ ! -e cat_mag ]
then
        echo "quick_aphot_core: Cannot find cat_mag, exiting"
        exit
fi

printf "."

# Calculations for apparent magnitude:
# grb value:
# average((grb-(ref1-mag1)),...,(grb-(refn-magn)))
# grb error:
# average((sqrt(grb_err^2+ref1_err^2),...,sqrt(grb_err^2+refn_err^2)))

echo 'format short;
        #cat_mag_err=0.3 #Catalogue error

        load curr_img_info;
                target_inst_mag=curr_img_info(1,1);
                target_inst_mag_err=curr_img_info(1,2);
                inst_mag=curr_img_info(:,1);
                inst_mag_err=curr_img_info(:,2);
        load cat_mag;

        # Create blank arrays for later
        index=zeros(size(cat_mag));
        app_mag_temp=zeros(size(index));
        app_mag_err_temp=zeros(size(index));

        for i=1:length(cat_mag);
```

```
                app_mag_temp(i)=(target_inst_mag -(inst_mag(i+1)-cat_mag
                    (i)));
55              #app_mag_err_temp(i)=(sqrt(target_inst_mag_err^2+
                    inst_mag_err(i+1)^2+cat_mag_err^2));
                app_mag_err_temp(i)=(sqrt(target_inst_mag_err^2+
                    inst_mag_err(i+1)^2));
57          endfor;

59          app_mag=mean(app_mag_temp);
            app_mag_err=mean(app_mag_err_temp);
61
            # save to files
63          app_mag_obj=[app_mag,app_mag_err];
            save -text curr_img_app_temp app_mag_obj;
65
quit'|octave 1>/dev/null
67
# Cut the comment lines off
69 grep '^[^#]' curr_img_app_temp > curr_img_app 2>/dev/null
rm curr_img_app_temp 2>/dev/null
```

quick_cat_core_lim

```
#!/bin/bash

#-------------------------------------------------------
# quick_cat_core_lim
# Program to search a catalogue and provide results for possible
    limiting magnitudes
# Based on filter of input image
#
# Gary Melady 12-06-08
#
# 26-06-09 Took out averaging between R1, R2, B1, B2 columns in USNO-B1
     cat, just using col R2 B2 now
#       (col2 is more recent observations)
#-------------------------------------------------------

if [ ! $1 ]
then
        echo "Please enter image for catalogue search"
        echo Exiting
        exit
fi

# Get the centre coordinates of each image and search the catalogue for
     all stars in the field using scat (wcstools)


#-------------------- Initial variables --------------------
bright_mag_lim=14
faint_mag_lim=20
num_star=500

#echo "Searching catalogue for stars in $1"

for img in $*
do
        printf "."

        imgroot=`fileroot $img`

#       ----------------- Get some initial info -----------------

        JD=`gethead $img JD`
        EXPOSURE=`gethead $img EXPOSURE`
        FILTER=`gethead $img FILTER`

        if [ $FILTER = V ]
        then
                echo "Catalogue USNO-B1 does not have info for $FILTER
                    band magnitudes"
                exit
        fi

#       ----------------- Get targets from catalogue -----------------
```

```
51          # Catalogue search parameters

53          # Get ra and dec coordinates of centre pixel of image
            XAXIS=`gethead $img NAXIS1`
55          XPLATE=`gethead $img XPLATE`
            YAXIS=`gethead $img NAXIS2`
57          YPLATE=`gethead $img YPLATE`

59          imagex=$[ XAXIS / 2 ] #pixels
            imagey=$[ YAXIS / 2] #pixels
61          catradius=`echo "sqrt(($imagex * $XPLATE)^2 + ($imagey *
               $YPLATE)^2)" | bc -l` #arcsec
            #echo "Radius = $catradius"
63
            ra=`xy2sky $img $imagex $imagey | awk '{print $1}'`
65          dec=`xy2sky $img $imagex $imagey | awk '{print $2}'`
            #echo "RA = $ra DEC = $dec"
67
            #printf "$img centre = $ra $dec"
69
            # Set the path to search the usno-B1 catalogue
71          export UB1_PATH=http://tdc-www.harvard.edu/cgi-bin/scat

73          # Search the catalogue
            scat -jw -o $imgroot -m2 $bright_mag_lim[,$faint_mag_lim] -r
               $catradius -c ub1 -n $num_star $ra $dec
75
            # Check if it worked
77          if [ ! -e $imgroot.ub1 ]
            then
79                  echo "quick_cat_core_lim: catalogue search failed"
                    exit
81          fi

83  #      -------------------- Sort results by filter --------------------

85          # USNO-B1 outoputs a file with cols: ID RA DEC B1 R1 B2 R2 I
               etc
            # USNO doesn't have V band info (TODO)
87
            # Test for "99.99" in cols
89          # - if col is 99.99 don't use that target
            # Create output file with cols RA DEC MAG
91
            if [ $FILTER = C ] || [ $FILTER = R ]
93          then
                    cat $imgroot.ub1 | awk '{print $2,$3,$7}' >> $imgroot.
                       lim_all_"$FILTER"_radec
95
                    i=1
97                  cat $imgroot.lim_all_"$FILTER"_radec | while read ra
                       dec m1
                    do
99                          mag1=${m1%.*}
```

```
101                     if [ $mag1 != 99 ]
                then
103                     mag=$m1
                        echo "`sed -n "$i"p $imgroot.lim_all_"$FILTER"
                            _radec | awk '{print $1,$2}'` $mag" >>
                            $imgroot.lim_all_"$FILTER"_radec2
105             fi

107                     i=`expr $i + 1`
                done
109
        elif [ $FILTER = B ]
111     then
                cat $imgroot.ub1 | awk '{print $2,$3,$6}' >> $imgroot.
                    lim_all_"$FILTER"_radec
113
                i=1
115             cat $imgroot.lim_all_"$FILTER"_radec | while read ra
                    dec m1 m2
                do
117                     mag1=${m1%.*}

119                     if [ $mag1 != 99 ]
                then
121                     mag=$m1
                        echo "`sed -n "$i"p $imgroot.lim_all_"$FILTER"
                            _radec | awk '{print $1,$2}'` $mag" >>
                            $imgroot.lim_all_"$FILTER"_radec2
123             fi

125                     i=`expr $i + 1`
                done
127
        elif [ $FILTER = I ]
129     then
                cat $imgroot.ub1 | awk '{print $2,$3,$8}' >> $imgroot.
                    lim_all_"$FILTER"_radec
131
                i=1
133             cat $imgroot.lim_all_"$FILTER"_radec | while read ra
                    dec m1
                do
135                     mag1=${m1%.*}

137                     if [ $mag1 != 99 ]
                        then
139                             mag=$m1
                                echo "`sed -n "$i"p $imgroot.lim_all_"
                                    $FILTER"_radec | awk '{print $1,$2
                                    }'` $mag" >> $imgroot.lim_all_"
                                    $FILTER"_radec2
141                     fi

143                     i=`expr $i + 1`
                done
```

```
145         #else
            #         echo "Catalogue USNO-B1 does not have info for $FILTER
                band magnitudes"
147         #         exit
            fi
149
            sort -k3 $imgroot.lim_all_"$FILTER"_radec2 > $imgroot.lim_all_"
               $FILTER"_radec_sorted
151 done
```

quick_cat_core_ref

```
#!/bin/bash

#-------------------------------------------------------------
# quick_cat_core_ref
# Program to search a catalogue around an input RA and DEC for possible reference stars
# Filters by radius and magnitude limits.
# Outputs to x.dat
#
# Gary Melady 12-06-08
#
# 26-06-09 Took out averaging between R1, R2, B1, B2 columns in USNO-B1 cat, just using col R2 B2 now
#       (col2 is more recent observations)
#-------------------------------------------------------------

if [ ! $1 ]
then
        echo "Please enter coordinates and filter for catalogue search"
        echo Exiting
        exit
fi

#-------------------- Initial variables --------------------
ra=$1
dec=$2
FILTER=$3

#echo "Searching catalogue for stars around RA: $ra DEC: $dec in filter $FILTER"

# Catalogue search parameters
bright_mag_lim=14
faint_mag_lim=17
num_star=500
catradius=300
imgroot=refstar

#       ----------------- Get targets from catalogue -----------------
# Set the path to search the usno-B1 catalogue
export UB1_PATH=http://tdc-www.harvard.edu/cgi-bin/scat

# Search the catalogue
scat -jw -o $imgroot -m2 $bright_mag_lim[,$faint_mag_lim] -r $catradius -c ub1 -n $num_star $ra $dec

# Check if it worked
if [ ! -s $imgroot.ub1 ]
then
        echo "quick_cat_core_ref failed, exiting"
        exit
fi

printf "."
```

```
52 #       ---------- Sort results by filter ----------

54 # USNO-B1 outoputs a file with cols: ID RA DEC B1 R1 B2 R2 I etc
   # USNO doesn't have V band info (TODO)
56 # Only using B2, R2 and I

58 # Test for "99.99" in cols
   # - if col is 99.99 don't use that target
60 # Create output file with cols RA DEC MAG

62 if [ $FILTER = C ] || [ $FILTER = R ]
   then
64         cat $imgroot.ub1 | awk '{print $2,$3,$7}' >> $imgroot.lim_all_"
               $FILTER"_radec

66         i=1
           cat $imgroot.lim_all_"$FILTER"_radec | while read ra dec m1
68         do
                   mag1=${m1%.*}
70
                   if [ $mag1 != 99 ]
72                 then
                           mag=$m1
74                         echo "`sed -n "$i"p $imgroot.lim_all_"$FILTER"
                               _radec | awk '{print $1,$2}'` $mag" >>
                               $imgroot.lim_all_"$FILTER"_radec2
                   fi
76
                   i=`expr $i + 1`
78         done
           printf "."
80
   elif [ $FILTER = B ]
82 then
           cat $imgroot.ub1 | awk '{print $2,$3,$6}' >> $imgroot.lim_all_"
               $FILTER"_radec
84
           i=1
86         cat $imgroot.lim_all_"$FILTER"_radec | while read ra dec m1
           do
88                 mag1=${m1%.*}

90
                   if [ $mag1 != 99 ]
92                 then
                           mag=$m1
94                         echo "`sed -n "$i"p $imgroot.lim_all_"$FILTER"
                               _radec | awk '{print $1,$2}'` $mag" >>
                               $imgroot.lim_all_"$FILTER"_radec2
                   fi
96
                   i=`expr $i + 1`
98         done
           printf "."
```

```
100
elif [ $FILTER = I ]
102 then
        cat $imgroot.ub1 | awk '{print $2,$3,$8}' >> $imgroot.lim_all_"
            $FILTER"_radec
104
        i=1
106     cat $imgroot.lim_all_"$FILTER"_radec | while read ra dec m1
        do
108             mag1=${m1%.*}

110             if [ $mag1 != 99 ]
                then
112                     mag=$m1
                        echo "`sed -n "$i"p $imgroot.lim_all_"$FILTER"
                            _radec | awk '{print $1,$2}'` $mag" >>
                            $imgroot.lim_all_"$FILTER"_radec2
114             fi

116             i=`expr $i + 1`
        done
118     printf "."

120 #else
#         echo "Catalogue USNO-B1 does not have info for $FILTER band
    magnitudes"
122 #         exit
fi
124
sort -k3 $imgroot.lim_all_"$FILTER"_radec2 > $imgroot.dat
126 printf "."
```

quick_confidence_core

```
#!/bin/bash

#
# quick_confidence_core
#
# Script to calculate signal to noise ratios and sigma levels of
    objects in a frame
# This is a core script to be called by other scripts
#
# Requirements:
# - Octave
# - outputs from quick_phot_core
#
# Gary Melady 27-05-08
#

# Test for existance of necessary files:
if [ ! -e curr_img_info ]
then
        echo "quick_confidence_core: Cannot find curr_img_info, exiting
            "
        exit
fi

printf "."

# Do the calculations for sigma and s/n in octave
# Equations:
# flux = (total counts in aperture) -((mean backround)*(aperture area))
# s/n = (flux)*gain / sqrt((flux)*gain + (aperture area)*((mean
    backround)*gain + (dark current)*exposure + (read noise)^2))
# sigma = (flux) / sqrt((mean backround)*(aperture area))
# sigma = (flux / (aperture area)) / (mean background)

echo    'format short;
        gain=8;         #Gain
        rn=13;          #Read-noise
        dark=1.5;       #Dark Current

  load curr_img_info;
    msky=curr_img_info(:,3);
    area=curr_img_info(:,4);
    flux=curr_img_info(:,5);

  # Define length of cols for signal/noise etc
  sn=zeros(size(curr_img_info(:,1)));
  sigma=zeros(size(curr_img_info(:,1)));
  signal=zeros(size(curr_img_info(:,1)));
  noise=zeros(size(curr_img_info(:,1)));

  for i=1:length(sn);
    # Signal to Noise Ratio

                signal(i)=flux(i)*gain;
```

```
                noise(i)=sqrt((flux(i)*gain)+area(i)*((msky(i)*gain)+
                    dark+rn^2));
53
                sn(i)=signal(i)/noise(i);
55
                # Sigmal level
57    sigma(i)=flux(i)/sqrt(area(i)*msky(i));

59    #merr(i)=1.0857*noise(i)/signal(i);
  endfor;
61
      # Save to a file
63  sn=[sn,sigma];
  save -text curr_img_sn_temp sn;
65 quit' | octave 1>/dev/null

67 # Cut the comment lines off
  grep '^[^#]' curr_img_sn_temp > curr_img_sn 2>/dev/null
69 rm curr_img_sn_temp 2>/dev/null
```

quick_imstat

```
#!/bin/bash

#-------------------------------------------------------------
# Program to print out the images statistics of all the images in the
    current directory
# Requirements: iraf, gnuoplot, fits images
#
# Gary Melady 10-02-08
#-------------------------------------------------------------

dir=`pwd`
rm imstat.dat list 2>/dev/null

if [ ! $1 ]
then
        echo "Please input fits files for analysis"
        echo "-p to plot results"
        exit

elif [ $1 == "-p" ] && [ ! $2 ]
then
        echo "Please input fits files for analysis"
        echo "-p to plot results"
        exit

elif [ $1 == "-p" ]
then
        plot=yes
        ls $* > list 2>/dev/null
else
        plot=no
        ls $* > list 2>/dev/null
fi

if [ -s list ]
then
  echo 'images
  imutil
  unlearn imstat
  imstat @list
  logout' |cl >imstat_iraf.dat
else
  printf "No fits images found\n"
  printf "Exiting\n"
  exit
fi

# Create temp file for heading of imstat.dat
printf "#$dir\n#IMAGE NPIX MEAN STDDEV MIN MAX\n">header

# Trim off the iraf fat from the output file
x=`cat imstat_iraf.dat|wc -l`
sed -n '15,'$x'p;'$x'q' imstat_iraf.dat > imstat_body.dat
cat header imstat_body.dat | column -t > imstat.dat
```

```
54
if [ $plot == "no" ]
56 then
        cat imstat.dat
58 fi

60 if [ $plot == "yes" ]
then
62        echo 'set xlabel "Image Number"
          set ylabel "Counts"
64
          plot \
66        "imstat.dat" u \
          :($3) \
68        t "Mean Pixel Value"

70        set term post color
          set output "quality_plot.ps"
72        replot' | gnuplot -persist

74 fi

76 # Clean up
rm list header imstat_* *.par
```

quick_lim_mag

```
#!/bin/bash

#
# Program to get the limiting magnitude of a frame
# - searches catalogue for all stars in frame (between magnitude limits)
# - detects the sigma levels of all objects
# - finds the dimmest star with sigma level of 3
#
# Requirements:
# - iraf (phot, txdump)
# - wcstools (scat, fileroot, gethead, sky2xy, xy2sky)
# - octave
#
# Gary Melady 21-04-08
#

# For filtering by sigma level (must be an integer)
threshold_sigma=4

if [ ! $1 ]
then
        echo "Please input fits files to calculate limiting magnitude"
        exit
fi

#printf "\n  - Calculating limiting magnitude of $1"

# Get the centre coordinates of each image and search the catalogue for all stars in the field using scat (wcstools)
# Get the instrumental magnitude of each target using phot (iraf)
# Calculate the sigma levels using octave
# Filter the results to get the faintest detection above $threshold_sigma

for img in $*
do

#       ----------------- Get some initial info -----------------
        imgroot=`fileroot $img`
        JD=`gethead $img JD`
        EXPOSURE=`gethead $img EXPOSURE`
        FILTER=`gethead $img FILTER`
        XAXIS=`gethead $img NAXIS1`
        YAXIS=`gethead $img NAXIS2`

#       ----------------- Get targets from catalogue -----------------

        # Call to quick_cat_core to generate file with cols RA DEC MAG (in appropriate filter)
        quick_cat_core_lim $img

        # Check if it worked
        if [ ! -e $imgroot.ub1 ]
```

```
        then
52              echo "quick_cat_core_lim failed, exiting"
                continue
54      fi

56 #    ----------------- Detect targets in the image -----------------

58      # Get the coordinates of the targets from the target file
  # and convert it to xy coords for each frame
60
        cat $imgroot.lim_all_"$FILTER"_radec_sorted | while read ra dec
            mag
62      do
                coor=`sky2xy $img $ra $dec | awk '{print $5,$6}'`
64    echo "$coor $mag" >> $imgroot.lim_all_"$FILTER"_xy
  done
66
        # Only take targets that are on the ccd
68      i=1
        cat $imgroot.lim_all_"$FILTER"_xy | while read x y mag
70      do
                # Get integer values of x and y positions
72              xint=${x%.*}
                yint=${y%.*}
74
                if [ $xint -ge 0 ] && [ $xint -le $XAXIS ] && [ $yint -
                    ge 0 ] && [ $yint -le $YAXIS ]
76              then
                        sed -n "$i"p $imgroot.lim_all_"$FILTER"_xy >>
                            $imgroot.lim_onframe_"$FILTER"_xy
78              fi
                i=`expr $i + 1`
80      done

82      cp $imgroot.lim_onframe_"$FILTER"_xy $imgroot.coor

84      # Call quick_phot_core to the photometry on current image
  quick_phot_core $img
86
        # Check if it worked
88      #if [ $? -ne 0 ]
        #then
90      #       echo "quick_phot_core failed"
        #       exit
92      #fi

94      # Remove targets that weren't detected
        i=1
96      cat $imgroot.mag.2 | while read mag mag_err msky area flux
        do
98              if [ "$mag" != INDEF ] && [ "$mag_err" != INDEF ] && [
                    "$msky" != INDEF ] && [ "$area" != INDEF ] && [ "
                    $flux" != INDEF ]
                then
```

```
100                         # Create list of detected targets with cols:
                                INST_MAG INST_MAG_ERR MSKY AREA FLUX
                    echo "`sed -n "$i"p $imgroot.mag.2 `" >> $imgroot.
                        lim_detected_targets_info
102
                    # Create list of catalogue magnitudes of detected
                        targets
104                 echo "`sed -n "$i"p $imgroot.lim_onframe_"$FILTER"_xy
                        | awk '{print $3}'`" >> $imgroot.
                        lim_detected_targets_catmag


106
                fi
108             i=`expr $i + 1`
        done
110
        # Rename file so octave can read it later
112     #grep -v INDEF $imgroot.lim_detected_targets_info >
            curr_img_info
    cp $imgroot.lim_detected_targets_info curr_img_info
114
#       ---------- Calculate confidence levels ---------
116
        # Call to quick_confidence_core to calculate the s/n and sigma
            levels
118     quick_confidence_core

120     # Check if it worked
        if [ $? -ne 0 ]
122     then
                echo "quick_confidence_core failed"
124             exit
        fi
126
        mv curr_img_sn $imgroot.sn
128
#       -------------------- Clean up the columns --------------------
130
        # Save all the data into one file with cols: JD T-T0 EXP
            CAT_MAG INST_MAG INST_MAG_ERR S/N SIGMA
132     i=1
        j=`cat $imgroot.lim_detected_targets_info | wc -l`
134     while [ $i -le $j ]
        do
136             echo "`sed -n 1p $imgroot.time` `sed -n "$i"p $imgroot.
                    lim_detected_targets_catmag` `sed -n "$i"p $imgroot
                    .lim_detected_targets_info | awk '{print $1,$2}'`
                    `sed -n "$i"p $imgroot.sn`" >> $imgroot.lim_mag_all

138             # Check if the line has a sigma > $threshold_sigma
                tail -1 $imgroot.lim_mag_all | while read JD TmT0 EXP
                    CAT_MAG INST_MAG INST_MAG_ERR SN SIGMA
140             do
                        # Take the integer part of sigma value
142                     sigma=${SIGMA%.*}
```

```
                        # Round the sigma value to the nearest whole
144                     #sigma=`printf %.0f $SIGMA`

146                     if [ "$sigma" -ge "$threshold_sigma" ]
                        then
148                             echo "`tail -1 $imgroot.lim_mag_all`"
                                   >> $imgroot.lim_mag_overthresh
                        fi
150                 done

152                 i=`expr $i + 1`
            done
154
            if [ -e $imgroot.lim_mag_overthresh ]
156         then
                    tail -1 $imgroot.lim_mag_overthresh >> lim_mag
158         else
                    printf "\n Limiting magnitude search failed"
160         fi

162 done

164 rm *.mag* *.lim* 2>/dev/null

166 #printf "Done\n"
```

quick_name

```
#!/bin/bash

#-------------------------------------------------------------
# Program to rename fits images based on target type
# Requirements: wcstools (gethead)
#
# Image types:
# O = Object
# G = GRB
# f = flat
# d = dark
#
# Gary Melady 22-02-08
#-------------------------------------------------------------

if [ ! $1 ]
then
        echo "Please input fits files to rename"
        exit
fi

printf "Renaming images"
for img in $*
do
        TARTYPE=`gethead $img TARTYPE` 2>/dev/null
        IMAGETYP=`gethead $img IMAGETYP` 2>/dev/null
        OBJECT=`gethead $img OBJECT|awk '{print $1_$2}'` 2>/dev/null
        FILTER=`gethead $img FILTER` 2>/dev/null
        EXPOSURE=`gethead $img EXPOSURE` 2>/dev/null
        TIME=`gethead $img DATE-OBS` 2>/dev/null

        # Rename objects
        if [ $TARTYPE == "O" ] || [ $TARTYPE == "G" ]
        then
                mv $img "$OBJECT"--"$TIME"_"$FILTER"_"$EXPOSURE".fits
                    2>/dev/null

        # Rename the flats
        elif [ $TARTYPE == "f" ]
        then
                mv $img "$IMAGETYP"--"$TIME"_"$FILTER".fits 2>/dev/null

        # Rename darks
        elif [ $TARTYPE == "d" ]
        then
                mv $img "$IMAGETYP"--"$TIME"_"$EXPOSURE".fits 2>/dev/
                    null
        fi

        printf "."
done

printf "Done\n"
```

quick_phot_core

```
1  #!/bin/bash

3  #
   # quick_phot_core
5  # Program to do photometry using iraf phot
   #
7  # This script is a core to be called by other scripts
   # (e.g. quick_phot, quick_reference_star, quick_lim_mag)
9  #
   # Requirements:
11 # - iraf (phot, txdump)
   # - wcstools (gethead)
13 #
   # Gary Melady 22-05-08
15 #

17 img=$1
   ape=$2
19
   imgroot=`fileroot $img`
21
   # Test for existance of necessary files:
23 if [ ! -e $imgroot.coor ]
   then
25         echo "quick_phot_core: Cannot find $imgroot.coor"
           echo Exiting
27         exit
   fi
29
   printf "."
31
   # For phot
33 annulus=10
   dannulus=10
35 cbox=8
   ape_multiplier=1.4 # Set to 1 for faint objects (only used if no
       aperture given as input)
37 gain_val=8
   rnoise_val=13
39
   #       ----------------- Get some initial info -----------------
41
   JD=`gethead $img JD`
43 EXPOSURE=`gethead $img EXPOSURE`
   FILTER=`gethead $img FILTER`
45 MAG_ZERO=`gethead $img MAG_ZERO`

47 # Calculate aperture, gain and readnoise
   # Aperture
49
   if [ -z $ape ]
51 then
           FWHM=`gethead $img FWHM`
53         # Quick and dirty fix if FWHM = 0
```

```
        if [ $FWHM == 0 ]
        then
                FWHM=3.5
        fi

        ape=`echo "$FWHM * $ape_multiplier" | bc -l`
fi

# Gain and read-noise

NCOMBINE=`gethead $img NCOMBINE`

if [ ! $NCOMBINE ]
then
        NCOMBINE=1
fi

gain=`echo "$NCOMBINE * $gain_val" | bc -l`
rnoise=`echo "$rnoise_val / sqrt($NCOMBINE)" | bc -l`

#printf "\n ncombine = $NCOMBINE gain = $gain readnoise = $rnoise fwhm
    = $FWHM aperture = $ape\n"

#       ----------------- Detect targets in image -----------------

# Perform the photometry on the image at the list of coords in $imgroot
    .coor
echo 'noao
digiphot
daophot
phot '$img' '$imgroot'.coor '$imgroot'.mag.1 calgori=centroid cbox='
    $cbox' salgori=mode annulus='$annulus' dannulu='$dannulus' readnoi
    ='$rnoise' epadu='$gain' apertur='$ape' zmag='$MAG_ZERO' sigma=0
    veri-
# Use txdump to sort out data from '$imgroot'.mag.1
bye
bye
digiphot
ptools
unlearn txdump
txdump '$imgroot'.mag.1 MAG,MERR,MSKY,AREA,FLUX expr=yes > '$imgroot'.
    mag.2
#txdump '$imgroot'.mag.1 MSKY,SUM,AREA,FLUX expr=yes > '$imgroot'.sn
#txdump '$imgroot'.mag.1 PERROR expr=yes > '$imgroot'.perror
logout'  |ecl |grep ERROR
```

quick_time_core

```
#!/bin/bash

#
# quick_time_core
#
# Program to calculate T minus Tzero for event and output to file with
    cols: JD T-T0 EXPOSURE
#
# Requirements:
# - Octave
#
# Gary Melady 27-05-08
#

# Test for existance of necessary files:
if [ ! -e time_temp ]
then
        echo "quick_time_core: Cannot find time_temp"
        echo "Exiting"
        exit
fi

# Test if necessary files are present
if [ ! -e T0 ]
then
        echo "quick_time_core: Cannot find T0"
        echo "Exiting"
        exit
fi

printf "."

# Calculate T-T0 and output to file (time) with cols: JD T-T0 EXP

echo 'format long;
        load time_temp
                jd=time_temp(:,1);
                exp=time_temp(:,2);
        load T0
                Tzero=T0(1,1);

        TmT0=round((time_temp(:,1)-Tzero)*86400);

        time=[jd,TmT0,exp];
        save -text curr_img_time_temp time;
quit' | octave 1>/dev/null

grep '^[^#]' curr_img_time_temp > curr_img_time
rm curr_img_time_temp
```

Supplementary Scripts

quick_combine

```
#!/bin/bash

#-----------------------------------------------------------------
# Program to combine reduced images in groups.
# Assumes all images in directory are of the same filter type.
# This program will combine images in groups specified by the user.
# e.g. "quick_combine 10" will stack images in groups of 10.
#
# Gary Melady July 2007
#
# 06-08-07 Added new exposure time calculation and ability to write
# to the fits header.
# 26-02-08 Added another (faster) way of exposure time calculation
    using wcstools
# (gethead, sethead)
#
# Program requirements: iraf, wcstools (gethead, sethead)
#-----------------------------------------------------------------

# Test to see if a number was input by the user
if [ $# -eq 0 ]
then
  echo "Please specify the size of the groups of images to combine"
  echo "e.g. 'quick-combine 10' combines the images in groups of 10"
  exit
fi

tot=`ls *.fits|wc -l`
echo "Stacking $tot images in groups of $1"

mkdir temp 2>/dev/null
mkdir stack_$1 2>/dev/null

i=1
j=`echo $[ $tot / $1 ]`

# Test to see if no. of images is evenly divided by the no. of groups
k=`echo $[ $tot % $1 ]`
if [ $k != 0 ]
then
        j=`expr $j + 1`
        #echo "New j = $j"
fi


while [ $i -le $j ]
do
  echo "Stacking group $i of $j..."
  ls *.fits 2>/dev/null | head -$1 > list$i.dat

        # Combine images using iraf imcombine
```

```
51          echo 'images
            imutil
53          unlearn imcombine
            imcombine @list'$i'.dat output="stack_'$1'_'$i'.fits" combine="
                median" outtype="real" offsets="wcs"
55          logout' |ecl |grep ERROR #1>/dev/null

57          # Calculate new exposure time of image
    exp_counter=0
59  exp_total=0
            imname=`cat list$i.dat`
61          for img in $imname
            do
63                  exp_counter=`gethead $img exposure`
                    exp_total=`echo $[ $exp_counter + $exp_total ]`
65          done

67          sethead stack_$1_$i.fits EXPOSURE=$exp_total
            sethead stack_$1_$i.fits EXPTIME=$exp_total
69
    mv $imname temp/
71  mv stack_$1_$i.fits stack_$1 #2>/dev/null

73  i=`expr $i + 1`

75 done

77 # Rename stacked images based on fits header
   cd stack_$1
79 quick_name *.fits
   cp ../*.roi . &>/dev/null
81 cd - &>/dev/null

83 # Clean up
   rm list*.dat 2>/dev/null
85 mv temp/* .
   rm -r temp/ up*
87
   echo "Done"
```

quick_exptime

```
#!/bin/bash

#
# Program to quickly copy EXPOSURE value to EXPTIME in header of fits
    image
# Requirements:
# - EXPOSURE keyword in header
# - wcstools (gethead, sethead)
#
# Gary Melady 18-02-07
#

if [ ! $1 ]
then
  echo "Please input .fits file"
  exit
fi

echo "Copying EXPOSURE value to EXPTIME for:"

for img in $*
do
  exp=`gethead $img EXPOSURE`
  sethead $img EXPTIME=$exp
  echo "$img EXPTIME = $exp"|column -t
done

echo Done
```

quick_plot

```
#!/bin/bash

#
# Program to plot output file from quick_phot
# Requirements - gnuplot, output file from quick_phot
#
# Gary Melady
#

if [ ! $1 ]
then
    echo "Please specify input file"
    exit
fi

echo '#set logs x
    set xlabel "T-T0"
    set ylabel "Magnitude"
    set yrange [*:*] reverse

    plot \
    "'$1'" u \
    ($2+$3/2):\
    ($4):\
    ($3/2):\
    ($5) \
    w xye t "Target"

    set term post color
    set output "'$1'_plot.ps"
    replot' | gnuplot -persist
```

quick_plot_object_lim_sn

```
#!/bin/bash

#-------------------------------------------------------------
# Program to plot:
# - magnitudes of target object with errors in upper plot
# - signal / noise and sigma information in bottom plot
# Requirements: output from quick_phot (apparent_magnitude_object),
    gnuplot
#
# Gary Melady 04-02-08
#-------------------------------------------------------------

rm apparent_magnitude_*.ps 2>/dev/null

a=`ls apparent_magnitude_* 2>/dev/null | head -1`
l=`ls limiting_magnitude_* 2>/dev/null | head -1`

if [ ! $a ] && [ ! $l ]
then
        echo "quick_plot_object_lim_sn: Cannot find any files to plot,
            exiting"
        exit
else
        cp "$a" app 2>/dev/null
        cp "$l" lim 2>/dev/null
fi

echo '# setup initial conditions
  set grid
  set bars 1
  set lmargin 10
  set rmargin 2
  set xlabel "T-T0 [s]"
  #set format x "%.0s*10^%T"
  set logs x

  set multiplot
  #-----------------------------------------
  # Plot 1 lower s/n plot
  set title ""

  # Set size and origin of lower plot
  set size 1,0.3
  set origin 0.0,0.1

  # You need this so that the plots fit together
  set bmargin 1
  set tmargin 0

  set ylabel "Confidence"
  set mytics 1

  plot \
  "app" u \
```

```
    ($2+$3/2):\
54  ($6) \
    pt 1 t "Signal / Noise", \
56  "app" u \
    ($2+$3/2):\
58  ($7) \
    pt 2 t "Sigma", \
60  "lim" u \
    ($2+$3/2):\
62  ($7) \
    pt 1 not, \
64  "lim" u \
    ($2+$3/2):\
66  ($8) \
    pt 2 not
68

70  #--------------------------------------
    # Plot 2 (upper magnitude plot)
72
    # Remove x-axis labels (they are already printed in 1st plot)
74  set xlabel ""
    set format x ""
76  #set logs x
    #set xlabel "T-T0"
78
    set ylabel "Magnitude"
80  set yrange [*:*] reverse

82  # Set size and origin of upper plot
    set size 1,0.55
84  set origin 0.0,0.4

86  # You need this so that the plots fit together
    set bmargin 0
88  set tmargin 1

90  set ytics 0.5
    set mytics 1
92
    plot \
94  "app" u \
    ($2+$3/2):\
96  ($4):\
    ($3/2):\
98  ($5) \
    w xye t "Watcher", \
100 "lim" u \
    ($2+$3/2):\
102       ($4):\
          ($3/2) \
104       w xe pt 10 lt -1 t "Watcher Limiting Magnitude"

106 unset multiplot
```

```
108   set term postscript enhanced color
      set output "'$a'.ps"
110   replot '| gnuplot -persist

112 rm apparent*.ps 2>/dev/null
    rm app lim 2>/dev/null
```

quick_region

```
#!/bin/bash

#-------------------------------------------------------
# Program to turn list of targets in x.targets file into ds9 region
    file
# Requirements: wcstools (skycoor)
#
# Gary Melady 27-02-08
#-------------------------------------------------------

if [ ! $1 ]
then
        echo "Please input target file to generate ds9 region file"
        exit
fi

# Remove previous files and create header
rm $target.reg 2>/dev/null
printf "global color=green font=\"helvetica 10 normal\" select=1
    highlite=1 edit=1 move=1 delete=1 include=1 fixed=0 source\nfk5\n"
    >> header

printf "Creating region files:\n"

for tar in $*
do
        target=`fileroot $tar`

        grep '^[^#]' $tar | while read n ra dec mag
        do
                if [ $n == "object" ]
                then
                        # Convert ra dec coords to xy
      ra1=`skycoor -d $ra $dec|awk '{print $1}'`
                        dec1=`skycoor -d $ra $dec|awk '{print $2}'`
                        text_dec=`echo "$dec1 - 0.01"|bc -l`

                        echo annulus\($ra1,$dec1,10\"\,15\"\) >>
                            body_$target
                        echo "# text($ra1,$text_dec) text={Target}" >>
                            body_$target

                else
                        ra1=`skycoor -d $ra $dec|awk '{print $1}'`
                        dec1=`skycoor -d $ra $dec|awk '{print $2}'`
                        text_dec=`echo "$dec1 - 0.005"|bc -l`

                        echo circle\($ra1,$dec1,8\"\) >> body_$target
                        echo "# text($ra1,$text_dec) text={$mag}" >>
                            body_$target
                fi
        done

        cat header body_$target > $target.reg
```

```
49          printf "$tar -->  $target.reg\n"
    done
51
    rm header body*
53  echo Done
```

coord_conv

```
#!/bin/bash

#-------------------------------------------------------------
# Program to convert ra and dec from sexagesimal to decimal.
# Gary Melady 30-05-2007
#-------------------------------------------------------------

echo "Program to convert ra and dec from sexagesimal to decimal"

# Read in coordinates
echo -n "Please enter RA coordinates in HH MM SS: "
read ra_hr ra_min ra_sec

echo -n "Please enter DEC coordinates in DD MM SS: "
read dec_deg dec_min dec_sec

echo " "

# Perform calculations (must pipe to bc -l for floating point
    operations)
ra_dec=`echo "($ra_hr*15)+(($ra_min/60)*15)+(($ra_sec/3600)*15)"|bc -l`
echo "RA: $ra_hr $ra_min $ra_sec --> $ra_dec"

# Check if dec is positive or negative

if [ $dec_deg -gt 0 ]
then
  dec_dec=`echo "($dec_deg)+($dec_min/60)+($dec_sec/3600)"|bc -l`
  echo "DEC: $dec_deg $dec_min $dec_sec --> $dec_dec"

else
  dec_dec=`echo "($dec_deg)-($dec_min/60)-($dec_sec/3600)"|bc -l`
        echo "DEC: $dec_deg $dec_min $dec_sec --> $dec_dec"
fi

echo " "
```

mag2jy

```
#!/bin/bash

# To convert magnitude and errors to jansky
# Magnitude and error values must be in cols 4 and 5

if [ ! -e $1 ]
then
        echo "No input file found"
        exit
fi

echo "Converting $1 magnitudes to janskys..."

title_target=`cat $1|head -1`
printf "#$title_target\n#jy\n#T-T0[d] EXP[s] MAG MAG_ERR Jy[mJy] Jy_ERR [mJy]\n" > header
grep ^[^#] $1 | awk '{print $2,$3,$4,$5}' > body
file=`fileroot $1`

echo 'format short
        zp=2941; # Zero Point for Bessel R-band
        #zp=3781; # Zero Point for Bessel V-band
        #zp=1823; # Zero Point for Bessel U-band
        #zp=4130; # Zero Point for Bessel B-band
        #zp=2635; # Zero Point for Bessel I-band

        load body;
                obs=body(:,1);
                exp=body(:,2);
                mag=body(:,3);
                mag_err=body(:,4);

        jy=zeros(size(body(:,1)));
        jy_full=zeros(size(body(:,1)));
        jy_err=zeros(size(body(:,1)));
        jy_err_full=zeros(size(body(:,1)));
        mag_err_high=zeros(size(body(:,1)));
        mag_err_low=zeros(size(body(:,1)));

        for i=1:length(jy);

                # Magnitude in mJy
                jy_full(i)=zp*(10^(-0.4*mag(i)));
                jy=jy_full*1000;

                # Error in mJy
                mag_err_high(i)=mag(i)+mag_err(i);
                mag_err_low(i)=mag(i)-mag_err(i);

                jy_err_full(i)=((zp*10^(-0.4*mag_err_low(i)))-(zp
                    *10^(-0.4*mag_err_high(i))))/2;
                jy_err=jy_err_full*1000;

        endfor;
```

```
53
        # Save to a file
55   result=[obs,exp,mag,mag_err,jy,jy_err];
     save -text body_jy result;
57 quit' | octave 1>/dev/null

59 grep '^[^#]' body_jy > "$file"_body
   cat header "$file"_body | column -t > "$file"_jy.dat
61
   # Clean up
63 rm body* header "$file"_body

65 echo "Done"
```

Bibliography

Akerlof, C., Balsano, R., Barthelmy, S., Bloch, J., Butterworth, P., Casperson, D., Cline, T., Fletcher, S., Frontera, F., Gisler, G., Heise, J., Hills, J., Kehoe, R., Lee, B., Marshall, S., McKay, T., Miller, R., Piro, L., Priedhorsky, W., Szymanski, J., and Wren, J. (1999). Observation of contemporaneous optical radiation from a γ-ray burst. *Nature*, 398:400–402.

Akerlof, C. W., Kehoe, R. L., McKay, T. A., Rykoff, E. S., Smith, D. A., Casperson, D. E., McGowan, K. E., Vestrand, W. T., Wozniak, P. R., Wren, J. A., Ashley, M. C. B., Phillips, M. A., Marshall, S. L., Epps, H. W., and Schier, J. A. (2003). The ROTSE-III Robotic Telescope System. *Publ. Astron. Soc. Pac.*, 115:132–140.

Alcock, C., Farhi, E., and Olinto, A. (1986). Model for the 5 March 1979 gamma-ray transient. *Physical Review Letters*, 57:2088–2091.

Amati, L. (2006). The Ep,i-Eiso correlation in gamma-ray bursts: updated observational status, re-analysis and main implications. *Mon. Not. R. Astron. Soc.*, 372:233–245.

Amati, L., Frontera, F., Tavani, M., in't Zand, J. J. M., Antonelli, A., Costa, E., Feroci, M., Guidorzi, C., Heise, J., Masetti, N., Montanari, E., Nicastro, L., Palazzi, E., Pian, E., Piro, L., and Soffitta, P. (2002). Intrinsic spectra and energetics of BeppoSAX Gamma-Ray Bursts with known redshifts. *Astron. Astrophys.*, 390:81–89.

Andersen, M. I. and Pedersen, H. (2004). Gamma-ray burst optical follow ups with robotic telescopes. *Astronomische Nachrichten*, 325:490–495.

Antonelli, L. A. and Team, R. (2005). The rem telescope: a robotic facility to promptly follow-up grbs and cosmic fast transients. volume 797, pages 173–180. AIP.

Ardelyan, N. V., Bisnovatyi-Kogan, G. S., Popov, Y. P., and Chernigovskii, S. V. (1987). Core Collapse and Formation of a Rapidly Rotating Neutron Star. *Soviet Astronomy*, 31:398–+.

Asfandyarov, I., Ibrahimov, M., and Pozanenko, A. (2006). GRB 060904b: optical observations. *GRB Coordinates Network*, 5741:1–+.

Atkins, R., Benbow, W., Berley, D., Chen, M. L., Coyne, D. G., Dingus, B. L., Dorfan, D. E., Ellsworth, R. W., Evans, D., Falcone, A., Fleysher, L., Fleysher, R., Gisler, G., Gonzalez, M. M., Goodman, J. A., Haines, T. J., Hoffman, C. M., Hugenberger, S., Kelley, L. A., Klein, S., Leonor, I., McCullough, J. F., McEnery, J. E., Miller, R. S., Mincer, A. I., Morales, M. F., Nemethy, P., Ryan, J. M., Samuelson, F. W., Shen, B., Shoup, A., Sinnis, C., Smith, A. J., Sullivan, G. W., Tumer, T., Wang, K., Wascko, M. O., Westerhoff, S., Williams, D. A., Yang, T., and Yodh, G. B. (2003). The High-Energy Gamma-Ray Fluence and Energy Spectrum of GRB 970417a from Observations with Milagrito. *Astrophys. J.*, 583:824.

Atteia, J.-L., Boer, M., Cotin, F., Couteret, J., Dezalay, J.-P., Ehanno, M., Evrard, J., Lagrange, D., Niel, M., Olive, J.-F., Rouaix, G., Souleille, P., Vedrenne, G., Hurley, K., Ricker, G., Vanderspek, R., Crew, G., Doty, J., and Butler, N. (2003). In-Flight Performance and First Results of FREGATE. In Ricker, G. R. and Vanderspek, R. K., editors, *Gamma-Ray Burst and Afterglow Astronomy 2001: A Workshop Celebrating the First Year of the HETE Mission*, volume 662 of *American Institute of Physics Conference Series*, pages 17–24.

Baade, W. and Zwicky, F. (1934). Cosmic Rays from Super-novae. *Proceedings of the National Academy of Science*, 20:259–263.

Bailyn, C., van Dokkum, P., Buxton, M., Cobb, B., and Bloom, J. S. (2003). GRB 031203: SMARTS optical monitoring. *GRB Coordinates Network*, 2486.

Band, D., Matteson, J., Ford, L., Schaefer, B., Palmer, D., Teegarden, B., Cline, T., Briggs, M., Paciesas, W., Pendleton, G., Fishman, G., Kouveliotou, C., Meegan, C., Wilson, R., and Lestrade, P. (1993). BATSE observations of gamma-ray burst spectra. I - Spectral diversity. *Astrophys. J.*, 413:281.

Barbier, L., Barthelmy, S., Cummings, J., Fenimore, E., Gehrels, N., Hullinger, D., Krimm, H., Markwardt, C., Norris, J., Nousek, J., Palmer, D., Parsons, A., Sakamoto, T., Sato, G., Suzuki, M., and Tueller, J. (2005). Swift-BAT detection of GRB 050401. *GRB Coordinates Network*, 3162.

Barthelmy, S., Barbier, L., Cummings, J., Fenimore, E., Gehrels, N., Hullinger, D., Krimm, H., Koss, M., Markwardt, C., Palmer, D., Parsons, A., Sakamoto, T., Sato, G., Stamatikos, M., and Tueller, J. (2006). GRB 060614: Swift-BAT refined analysis. *GRB Coordinates Network*, 5256.

Barthelmy, S. D., Barbier, L. M., Cummings, J. R., Fenimore, E. E., Gehrels, N., Hullinger, D., Krimm, H. A., Markwardt, C. B., Palmer, D. M., Parsons, A., Sato, G., Suzuki, M., Takahashi, T., Tashiro, M., and Tueller, J. (2005). The Burst Alert Telescope (BAT) on the SWIFT Midex Mission. *Space Science Reviews*, 120:143–164.

Barthelmy, S. D., Butterworth, P., Cline, T. L., and Gehrels, N. (1998). Current Status and New Developments with the GRB Coordinates Network (GCN). In *Bulletin of the American Astronomical Society*, volume 30 of *Bulletin of the American Astronomical Society*, page 875.

Barthelmy, S. D., Butterworth, P., Cline, T. L., Gehrels, N., Fishman, G. J., Kouveliotou, C., and Meegan, C. A. (1995). BACODINE, the Real-Time BATSE Gamma-Ray Burst Coordinates Distribution Network. *Astrophys. Space. Sci.*, 231:235–238.

Baruch, J. E. F. (1995). A review of European developments in automated and robotic telescopes for photometry. In Bode, M. F., editor, *Robotic Observatories*, Wiley - Praxis Series in Astronomy and Astrophysics, pages 3–9. John Wiley & Sons. ISBN 0-471-95690-2.

Belczynski, K., Bulik, T., and Kalogera, V. (2002). Merger Sites of Double Neutron Stars and Their Host Galaxies. *Astrophys. J., Lett.*, 571:L147–L150.

Beloborodov, A. M. and Thompson, C. (2007). Corona of Magnetars. *Astrophys. J.*, 657:967–993.

BenZvi, S., Bohacova, M., Connolly, B., Grygar, J., Hrabovsky, M., Karova, T., Mandat, D., Necesal, P., Nosek, D., Nozka, L., Palatka, M., Pech, M., Prouza, M., Ridky, J., Schovanek, P., Smida, R., Travnicek, P., Vitale, P., Westerhoff, S., and for the Pierre Auger Collaboration (2007). New method for atmospheric calibration at the Pierre Auger Observatory using FRAM, a robotic astronomical telescope. *ArXiv e-prints*, 706.

Berger, E. (2008). The Host Galaxies of Short-Duration Gamma-Ray Bursts: Luminosities, Metallicities, and Star Formation Rates. *astro-ph/0805.0306*.

Berger, E., Kulkarni, S. R., and Frail, D. A. (2002). GRB 021004 - unusual Radio-to-Submm spectrum. *GRB Coordinates Network*, 1612.

Bertin, E. and Arnouts, S. (1996). SExtractor: Software for source extraction. *Astron. Astrophys. Suppl. Ser.*, 117:393–404.

Bessell, M. S. (1979). UBVRI photometry. II - The Cousins VRI system, its temperature and absolute flux calibration, and relevance for two-dimensional photometry. *Publ. Astron. Soc. Pac.*, 91:589–607.

Bessell, M. S. (1995). UBVRI Filters for CCD Photometry. *CCD Astronomy*, 2:20–+.

Bhat, P. N., Paciesas, W., and Horst, A. J. v. d. (2008). GRB 080905B: Fermi Gamma-ray Burst Monitor detection. *GCN*, 8205.

Blandford, R. D. and Znajek, R. L. (1977). Electromagnetic extraction of energy from Kerr black holes. *Mon. Not. R. Astron. Soc.*, 179:433–456.

Blinnikov, S. I., Novikov, I. D., Perevodchikova, T. V., and Polnarev, A. G. (1984). Exploding Neutron Stars in Close Binaries. *Soviet Astronomy Letters*, 10:177.

Bloom, J. B., Prochaska, J. X., Pooley, D., Blake, C. W., Foley, R. J., Jha, S., Ramirez-Ruiz, E., Granot, J., Filippenko, A. V., Sigurdsson, S., Barth, A. J., Chen, H. W., Cooper, M. C., Falco, E. E., Gal, R. R., Gerke, B. F., Gladders, M. D., Greene, J., Hennanwi, J., Ho, L. C., Hurley, K., Koester, B. P., Li, W., Lubin, L., Newman, J., Perley, D. A., Squires, G. K., and Wood-Vasey, W. M. (2005). Closing in on a Short-Hard

Burst Progenitor: Constraints from Early-Time Optical Imaging and Spectroscopy of a Possible Host Galaxy of GRB 050509b. volume 37 of *Bulletin of the American Astronomical Society*, page 793.

Bloom, J. S., Frail, D. A., and Kulkarni, S. R. (2003). Gamma-Ray Burst Energetics and the Gamma-Ray Burst Hubble Diagram: Promises and Limitations. *Astrophys. J.*, 594:674–683.

Bloom, J. S., Kulkarni, S. R., and Djorgovski, S. G. (2002). The Observed Offset Distribution of Gamma-Ray Bursts from Their Host Galaxies: A Robust Clue to the Nature of the Progenitors. *Astron. J.*, 123:1111–1148.

Bode, M. F., editor (1995). *Robotic Observatories*, Wiley - Praxis Series in Astronomy and Astrophysics. John Wiley & Sons. ISBN 0-471-95690-2.

Boër, M., Atteia, J. L., Damerdji, Y., Gendre, B., Klotz, A., and Stratta, G. (2006). Detection of a Very Bright Optical Flare from the Gamma-Ray Burst GRB 050904 at Redshift 6.29. *Astrophys. J., Lett.*, 638:L71–L74.

Boer, M., Klotz, A., Atteia, J.-L., Buchholtz, G., Daigne, F., Eysseric, J., Goldoni, P., Jean, P., Lecavelier Des Etangs, A., Lopez, M., Malina, R., Marcowith, A., Marquette, J. B., Mayet, A., Mirabel, F., Mochkovitch, R., Pacheco, J., Pares, L., Paul, J., Pedersen, H., Pinna, H., and Sivan, J.-P. (2003). The Gamma-Ray Burst Hunt at La Silla the TAROT-S Very Fast Moving Telescope. *The Messenger*, 113:45–48.

Briggs, M. S., Band, D. L., Kippen, R. M., Preece, R. D., Kouveliotou, C., van Paradijs, J., Share, G. H., Murphy, R. J., Matz, S. M., Connors, A., Winkler, C., McConnell, M. L., Ryan, J. M., Williams, O. R., Young, C. A., Dingus, B., Catelli, J. R., and Wijers, R. A. M. J. (1999). Observations of GRB 990123 by the Compton Gamma Ray Observatory. *Astrophys. J.*, 524:82–91.

Burrows, D. N., Hill, J. E., Nousek, J. A., Kennea, J. A., Wells, A., Osborne, J. P., Abbey, A. F., Beardmore, A., Mukerjee, K., Short, A. D. T., Chincarini, G., Campana, S., Citterio, O., Moretti, A., Pagani, C., Tagliaferri, G., Giommi, P., Capalbi, M., Tamburelli,

F., Angelini, L., Cusumano, G., Bräuninger, H. W., Burkert, W., and Hartner, G. D. (2005a). The Swift X-Ray Telescope. *Space Science Reviews*, 120:165–195.

Burrows, D. N., Hill, J. E., Nousek, J. A., Kennea, J. A., Wells, A., Osborne, J. P., Abbey, A. F., Beardmore, A., Mukerjee, K., Short, A. D. T., Chincarini, G., Campana, S., Citterio, O., Moretti, A., Pagani, C., Tagliaferri, G., Giommi, P., Capalbi, M., Tamburelli, F., Angelini, L., Cusumano, G., Bräuninger, H. W., Burkert, W., and Hartner, G. D. (2005b). The Swift X-Ray Telescope. *Space Science Reviews*, 120:165–195.

Campana, S., Barthelmy, S., Gehrels, N., Gronwall, C., Krimm, H., Markwardt, C., Page, K., Palmer, D., and Perri, M. (2006a). GRB 060117: Swift-BAT detection of a bright burst. *GRB Coordinates Network*, 4533.

Campana, S., Barthelmy, S. D., Boyd, P. T., Brown, P. J., Burrows, D. N., Cummings, J. R., Guidorzi, C. G., Holland, S. T., Kennea, J. A., Markwardt, C. B., Marshall, F. E., Moretti, A., Page, K. L., Stamatikos, M., Tagliaferri, G., and Berk, D. E. V. (2006b). GRB 060526: Swift detection of a burst with x-ray and optical afterglow. *GRB Coordinates Network*, 5162:1–+.

Castro-Tirado, A. J., Bremer, M., McBreen, S., Gorosabel, J., Guziy, S., Fakthullin, T. A., Sokolov, V. V., González Delgado, R. M., Bihain, G., Pandey, S. B., Jelínek, M., de Ugarte Postigo, A., Misra, K., Sagar, R., Bama, P., Kamble, A. P., Anupama, G. C., Licandro, J., Pérez-Ramírez, D., Bhattacharya, D., Aceituno, F. J., and Neri, R. (2007). The dark nature of ¡ASTROBJ¿GRB 051022¡/ASTROBJ¿ and its host galaxy. *Astron. Astrophys.*, 475:101–107.

Castro-Tirado, A. J., Cunniffe, R., de Ugarte Postigo, A., Jelínek, M., Vitek, S., Kubánek, P., Gorosabel, J., Castillo Carrión, S., Mateo Sanguino, T. J., Riva, A., Conconi, P., di Caprio, V., Zerbi, F., Amado, P., Cárdenas, C., Claret, A., Guziy, S., Martín-Ruiz, S., Sánchez, M. A., García Teodoro, P., Castro Cerón, J. M., Díaz Verdejo, J., Hudec, R., López Soler, J. M., Berná Galiano, J. Á., Casares, J., Fabregat, J., Páta, P., Sánchez Fernández, C., Sabau-Graziati, M. D., Trigo-Rodríguez, J. M., and Vitali, F. (2006a). BOOTES-IR: a robotic nIR astronomical observatory devoted to follow-up of transient phenomena. In Stepp, L. M., editor, *Ground-based and Airborne Telescopes*,

pp. 62670I, volume 6267 of *Presented at the Society of Photo-Optical Instrumentation Engineers (SPIE) Conference*.

Castro-Tirado, A. J., de Ugarte Postigo, A., Gorosabel, J., Jelínek, M., Fatkhullin, T. A., Sokolov, V. V., Ferrero, P., Kann, D. A., Klose, S., Sluse, D., Bremer, M., Winters, J. M., Nuernberger, D., Pérez-Ramírez, D., Guerrero, M. A., French, J., Melady, G., Hanlon, L., McBreen, B., Leventis, K., Markoff, S. B., Leon, S., Kraus, A., Aceituno, F. J., Cunniffe, R., Kubánek, P., Vítek, S., Schulze, S., Wilson, A. C., Hudec, R., Durant, M., González-Pérez, J. M., Shahbaz, T., Guziy, S., Pandey, S. B., Pavlenko, L., Sonbas, E., Trushkin, S. A., Bursov, N. N., Nizhelskij, N. A., Sánchez-Fernández, C., and Sabau-Graziati, L. (2008). Flares from a candidate Galactic magnetar suggest a missing link to dim isolated neutron stars. *Nature*, 455:506–509.

Castro-Tirado, A. J., Jelínek, M., Mateo Sanguino, T. J., de Ugarte Postigo, A., and the BOOTES team (2004). BOOTES: A stereoscopic robotic ground support facility. *Astronomische Nachrichten*, 325:679–679.

Castro-Tirado, A. J., Jelínek, M., Pandey, S. B., McBreen, S., de Jong, J., Sahu, D. K., Ferrero, P., Caballero, J. A., Gorosabel, J., Kann, D. A., Klose, S., de Ugarte Postigo, A., Anupama, G. C., Gry, C., Guziy, S., Srividya, S., Valdivielso, L., Vanniarajan, S., and Henden, A. A. (2006b). ¡ASTROBJ¿GRB 051028¡/ASTROBJ¿: an intrinsically faint gamma-ray burst at high redshift? *Astron. Astrophys.*, 459:763–767.

Chatterjee, P. and Hernquist, L. (2000). The Spin Period, Luminosity, and Age Distributions of Anomalous X-Ray Pulsars. *Astrophys. J.*, 543:368–372.

Chatterjee, P., Hernquist, L., and Narayan, R. (2000). An Accretion Model for Anomalous X-Ray Pulsars. *Astrophys. J.*, 534:373–379.

Chen, W. P., Lemme, C., and Paczynski, B., editors (2001). *Small Telescope Astronomy on Global Scales*, volume 246 of *Astronomical Society of the Pacific Conference Series*.

Chevalier, R. A. and Li, Z.-Y. (1999). Gamma-Ray Burst Environments and Progenitors. *Astrophys. J., Lett.*, 520:L29–L32.

Chevalier, R. A. and Li, Z.-Y. (2000). Wind Interaction Models for Gamma-Ray Burst Afterglows: The Case for Two Types of Progenitors. *Astrophys. J.*, 536:195–212.

Chincarini, G., Moretti, A., Romano, P., Falcone, A. D., Morris, D., Racusin, J., Campana, S., Covino, S., Guidorzi, C., Tagliaferri, G., Burrows, D. N., Pagani, C., Stroh, M., Grupe, D., Capalbi, M., Cusumano, G., Gehrels, N., Giommi, P., La Parola, V., Mangano, V., Mineo, T., Nousek, J. A., O'Brien, P. T., Page, K. L., Perri, M., Troja, E., Willingale, R., and Zhang, B. (2007). The First Survey of X-Ray Flares from Gamma-Ray Bursts Observed by Swift: Temporal Properties and Morphology. *Astrophys. J.*, 671:1903–1920.

Cline, T. L., Desai, U. D., Teegarden, B. J., Evans, W. D., Klebesadel, R. W., Laros, J. G., Barat, C., Hurley, K., Niel, M., and Weisskopf, M. C. (1982). Precise source location of the anomalous 1979 March 5 gamma-ray transient. *Astrophys. J., Lett.*, 255:L45–L48.

Colgate, S. A. (1968). Prompt gamma rays and X-rays from supernovae. *Canadian Journal of Physics*, 46:476–+.

Corbel, S. and Eikenberry, S. S. (2004). The connection between W31, SGR 1806-20, and LBV 1806-20: Distance, extinction, and structure. *Astron. Astrophys.*, 419:191–201.

Corbet, R. H. D., Smale, A. P., Ozaki, M., Koyama, K., and Iwasawa, K. (1995). The spectrum and pulses of 1E 2259+586 from ASCA and BBXRT observations. *Astrophys. J.*, 443:786–794.

Costa, E., Frontera, F., Heise, J., Feroci, M., in't Zand, J., Fiore, F., Cinti, M. N., Dal Fiume, D., Nicastro, L., Orlandini, M., Palazzi, E., Rapisarda, M., Zavattini, G., Jager, R., Parmar, A., Owens, A., Molendi, S., Cusumano, G., Maccarone, M. C., Giarrusso, S., Coletta, A., Antonelli, L. A., Giommi, P., Muller, J. M., Piro, L., and Butler, R. C. (1997). Discovery of an X-ray afterglow associated with the γ-ray burst of 28 February 1997. *Nature*, 387:783.

Coward, D. M., Guetta, D., Burman, R. R., and Imerito, A. (2008). Where are the missing gamma-ray burst redshifts? *Mon. Not. R. Astron. Soc.*, 386:111–116.

Cummings, J., Barbier, L., Barthelmy, S., Hullinger, D., Fenimore, E., Gehrels, N., Krimm, H., Markwardt, C., Palmer, D., Parsons, A., Sakamoto, T., Sato, G., and Tueller, J. (2005). GRB 050820A BAT observations of second, larger episode of emission. *GRB Coordinates Network*, 3858.

Dahn, C. C., Harris, H. C., Vrba, F. J., Guetter, H. H., Canzian, B., Henden, A. A., Levine, S. E., Luginbuhl, C. B., Monet, A. K. B., Monet, D. G., Pier, J. R., Stone, R. C., Walker, R. L., Burgasser, A. J., Gizis, J. E., Kirkpatrick, J. D., Liebert, J., and Reid, I. N. (2002). Astrometry and Photometry for Cool Dwarfs and Brown Dwarfs. *Astronomical Journal*, 124:1170–1189.

Dai, Z. G. and Cheng, K. S. (2001). Afterglow Emission from Highly Collimated Jets with Flat Electron Spectra: Application to the GRB 010222 Case? *Astrophys. J., Lett.*, 558:L109–L112.

D'Alessio, V., Piro, L., and Rossi, E. M. (2006). Properties of X-ray rich gamma ray bursts and X-ray flashes detected with BeppoSAX and Hete-2. *Astron. Astrophys.*, 460:653–664.

Dar, A. and de Rújula, A. (2004). Towards a complete theory of gamma-ray bursts. *Phys. Rep.*, 405:203–278.

de Angelis, A. (2001). GLAST, the Gamma-Ray Large Area Space Telescope. In Mourao, A. M., Pimenta, M., Sa, P. M., and Velhinho, J. M., editors, *New worlds in astroparticle physics*, pages 140–+.

de Pasquale, M., Oates, S. R., Page, M. J., Burrows, D. N., Blustin, A. J., Zane, S., Mason, K. O., Roming, P. W. A., Palmer, D., Gehrels, N., and Zhang, B. (2007). Early afterglow detection in the Swift observations of GRB 050801. *Mon. Not. R. Astron. Soc.*, 377:1638–1646.

de Ugarte Postigo et al. (2005). JIBARO: Un conjunto de utilidades para la reducción y análisis automatizado de imágenes. In Castro-Tirado, A. J., de la Morena, B., and Torresi, J., editors, *Astrofísica Robótica en España*, pages 35–50. Ed. Sirius, Madrid.

Della Valle, M. (2005). Supernovae shedding light on gamma-ray bursts. *Nuovo Cimento C Geophysics Space Physics C*, 28:563.

Della Valle, M., Chincarini, G., Panagia, N., Tagliaferri, G., Malesani, D., Testa, V., Fugazza, D., Campana, S., Covino, S., Mangano, V., Antonelli, L. A., D'Avanzo, P., Hurley, K., Mirabel, I. F., Pellizza, L. J., Piranomonte, S., and Stella, L. (2006a). An enigmatic long-lasting γ-ray burst not accompanied by a bright supernova. *Nature*, 444:1050–1052.

Della Valle, M., Malesani, D., Benetti, S., Testa, V., Hamuy, M., Antonelli, L. A., Chincarini, G., Cocozza, G., Covino, S., D'Avanzo, P., Fugazza, D., Ghisellini, G., Gilmozzi, R., Lazzati, D., Mason, E., Mazzali, P., and Stella, L. (2003). Evidence for supernova signatures in the spectrum of the late-time bump of the optical afterglow of GRB 021211. *Astron. Astrophys.*, 406:L33–L37.

Della Valle, M., Malesani, D., Bloom, J. S., Benetti, S., Chincarini, G., D'Avanzo, P., Foley, R. J., Covino, S., Melandri, A., Piranomonte, S., Tagliaferri, G., Stella, L., Gilmozzi, R., Antonelli, L. A., Campana, S., Chen, H.-W., Filliatre, P., Fiore, F., Fugazza, D., Gehrels, N., Hurley, K., Mirabel, I. F., Pellizza, L. J., Piro, L., and Prochaska, J. X. (2006b). Hypernova Signatures in the Late Rebrightening of GRB 050525A. *Astrophys. J., Lett.*, 642:L103–L106.

Dingus, B. L. (2003). Observations of the Highest Energy Gamma Rays from Gamma-Ray Bursts. In Ricker, G. R. and Vanderspek, R. K., editors, *Gamma-Ray Burst and Afterglow Astronomy 2001: A Workshop Celebrating the First Year of the HETE Mission*, volume 662 of *American Institute of Physics Conference Series*, page 240.

Donaghy, T. Q., Lamb, D. Q., Sakamoto, T., Norris, J. P., Nakagawa, Y., Villasenor, J., Atteia, J. ., Vanderspek, R., Graziani, C., Kawai, N., Ricker, G. R., Crew, G. B., Doty, J., Prigozhin, G., Jernigan, J. G., Shirasaki, Y., Suzuki, M., Butler, N., Hurley, K., Tamagawa, T., Yoshida, A., Matsuoka, M., Fenimore, E. E., Galassi, M., Boer, M., Dezalay, J. ., Olive, J. ., Levine, A., Martel, F., Morgan, E., Sato, R., Woosley, S. E., Braga, J., Manchanda, R., Pizzichini, G., Takagishi, K., and Yamauchi, M. (2006). HETE-2

Localizations and Observations of Four Short Gamma-Ray Bursts: GRBs 010326B, 040802, 051211 and 060121. *astro-ph/0605570*.

Drake, A. J., Djorgovski, G., Graham, M., Williams, R., Mahabal, A., Donalek, C., Glikman, E., Bloom, J., Vastrand, T., White, R., Rabinowitz, D., and Baltay, C. (2006). VOEventNet: Event Messaging for Astronomy. In *Bulletin of the American Astronomical Society*, volume 38 of *Bulletin of the American Astronomical Society*, page 1002.

Duncan, R. C. and Thompson, C. (1992). Formation of very strongly magnetized neutron stars - Implications for gamma-ray bursts. *Astrophys. J., Lett.*, 392:L9–L13.

Eaton, J. A., Henry, W., and Fekel, F. C. (2003). Advantages of automated observing with small telescopes. In Oswalt, T. D., editor, *The Future of Small Telescopes in the New Millennium*, volume II, pages 189–207. Kluwer Academic Publishers.

Eichler, D., Livio, M., Piran, T., and Schramm, D. N. (1989). Nucleosynthesis, neutrino bursts and gamma-rays from coalescing neutron stars. *Nature*, 340:126–128.

Evans, P. A., Beardmore, A. P., Page, K. L., Osborne, J. P., O'Brien, P. T., Willingale, R., Starling, R. L. C., Burrows, D. N., Godet, O., Vetere, L., Racusin, J., Goad, M. R., Wiersema, K., Angelini, L., Capalbi, M., Chincarini, G., Gehrels, N., Kennea, J. A., Margutti, R., Morris, D. C., Mountford, C. J., Pagani, C., Perri, M., Romano, P., and Tanvir, N. (2008). Methods and results of an automatic analysis of a complete sample of Swift-XRT observations of GRBs. *ArXiv e-prints*.

Evans, P. A., Beardmore, A. P., Page, K. L., Tyler, L. G., Osborne, J. P., Goad, M. R., O'Brien, P. T., Vetere, L., Racusin, J., Morris, D., Burrows, D. N., Capalbi, M., Perri, M., Gehrels, N., and Romano, P. (2007). An online repository of Swift/XRT light curves of γ-ray bursts. *Astron. Astrophys.*, 469:379–385.

Fahlman, G. G. and Gregory, P. C. (1981). An X-ray pulsar in SNR G109.1-1.0. *Nature*, 293:202–204.

Falcone, A. D., Burrows, D. N., Lazzati, D., Campana, S., Kobayashi, S., Zhang, B., Mészáros, P., Page, K. L., Kennea, J. A., Romano, P., Pagani, C., Angelini, L., Beardmore, A. P., Capalbi, M., Chincarini, G., Cusumano, G., Giommi, P., Goad, M. R.,

Godet, O., Grupe, D., Hill, J. E., La Parola, V., Mangano, V., Moretti, A., Nousek, J. A., O'Brien, P. T., Osborne, J. P., Perri, M., Tagliaferri, G., Wells, A. A., and Gehrels, N. (2006). The Giant X-Ray Flare of GRB 050502B: Evidence for Late-Time Internal Engine Activity. *Astrophys. J.*, 641:1010–1017.

Fan, Y. Z., Zhang, B., and Wei, D. M. (2005). Early Optical-Infrared Emission from GRB 041219a: Neutron-rich Internal Shocks and a Mildly Magnetized External Reverse Shock. *Astrophys. J., Lett.*, 628:L25–L28.

Feroci, M., Hurley, K., Duncan, R. C., and Thompson, C. (2001). The Giant Flare of 1998 August 27 from SGR 1900+14. I. An Interpretive Study of BeppoSAX and Ulysses Observations. *Astrophys. J.*, 549:1021–1038.

Fishman, G. J. and Meegan, C. A. (1995). Gamma-Ray Bursts. *Ann. Rev. Astron. Astrophys.*, 33:415.

Foley, S., McGlynn, S., Hanlon, L., McBreen, S., and McBreen, B. (2008). Global characteristics of GRBs observed with INTEGRAL and the inferred large population of low-luminosity GRBs. *Astron. Astrophys.*, 484:143–157.

Fox, D. B., Frail, D. A., Price, P. A., Kulkarni, S. R., Berger, E., Piran, T., Soderberg, A. M., Cenko, S. B., Cameron, P. B., Gal-Yam, A., Kasliwal, M. M., Moon, D.-S., Harrison, F. A., Nakar, E., Schmidt, B. P., Penprase, B., Chevalier, R. A., Kumar, P., Roth, K., Watson, D., Lee, B. L., Shectman, S., Phillips, M. M., Roth, M., McCarthy, P. J., Rauch, M., Cowie, L., Peterson, B. A., Rich, J., Kawai, N., Aoki, K., Kosugi, G., Totani, T., Park, H.-S., MacFadyen, A., and Hurley, K. C. (2005). The afterglow of GRB 050709 and the nature of the short-hard γ-ray bursts. *Nature*, 437:845.

Frail, D. A., Kulkarni, S. R., Nicastro, L., Feroci, M., and Taylor, G. B. (1997). The radio afterglow from the γ-ray burst of 8 May 1997. *Nature*, 389:261.

Frail, D. A., Kulkarni, S. R., Sari, R., Djorgovski, S. G., Bloom, J. S., Galama, T. J., Reichart, D. E., Berger, E., Harrison, F. A., Price, P. A., Yost, S. A., Diercks, A., Goodrich, R. W., and Chaffee, F. (2001). Beaming in Gamma-Ray Bursts: Evidence for a Standard Energy Reservoir. *Astrophys. J., Lett.*, 562:L55–L58.

Fruchter, A. S., Levan, A. J., Strolger, L., Vreeswijk, P. M., Thorsett, S. E., Bersier, D., Burud, I., Castro Cerón, J. M., Castro-Tirado, A. J., Conselice, C., Dahlen, T., Ferguson, H. C., Fynbo, J. P. U., Garnavich, P. M., Gibbons, R. A., Gorosabel, J., Gull, T. R., Hjorth, J., Holland, S. T., Kouveliotou, C., Levay, Z., Livio, M., Metzger, M. R., Nugent, P. E., Petro, L., Pian, E., Rhoads, J. E., Riess, A. G., Sahu, K. C., Smette, A., Tanvir, N. R., Wijers, R. A. M. J., and Woosley, S. E. (2006). Long γ-ray bursts and core-collapse supernovae have different environments. *Nature*, 441:463–468.

Fryer, C. L., Woosley, S. E., and Hartmann, D. H. (1999). Formation Rates of Black Hole Accretion Disk Gamma-Ray Bursts. *Astrophys. J.*, 526:152.

Fugazza, D., D'Avanzo, P., Malesani, D., Tagliaferri, G., Chincarini, G., Stella, L., Fynbo, J. P. U., Lidman, C., and Sana, H. (2006). GRB 060904B: VLT redshift. *GCN*, 5513.

Fynbo, J. P. U., Hjorth, J., Sollerman, J., Mxller, P., Gorosabel, J., Grundahl, F., Jensen, B. L., Andersen, M. I., Vreeswijk, P., Castro-Tirado, A., and Grace Collaboration (2004). The GRB-SN Connection: GRB 030329 and XRF 030723. In *AIP Conf. Proc. 727: Gamma-Ray Bursts: 30 Years of Discovery*, page 301.

Fynbo, J. P. U., Watson, D., Thöne, C. C., Sollerman, J., Bloom, J. S., Davis, T. M., Hjorth, J., Jakobsson, P., Jørgensen, U. G., Graham, J. F., Fruchter, A. S., Bersier, D., Kewley, L., Cassan, A., Castro Cerón, J. M., Foley, S., Gorosabel, J., Hinse, T. C., Horne, K. D., Jensen, B. L., Klose, S., Kocevski, D., Marquette, J.-B., Perley, D., Ramirez-Ruiz, E., Stritzinger, M. D., Vreeswijk, P. M., Wijers, R. A. M., Woller, K. G., Xu, D., and Zub, M. (2006). No supernovae associated with two long-duration γ-ray bursts. *Nature*, 444:1047–1049.

Fynbo, J. U., Jensen, B. L., Gorosabel, J., Hjorth, J., Pedersen, H., Møller, P., Abbott, T., Castro-Tirado, A. J., Delgado, D., Greiner, J., Henden, A., Magazzù, A., Masetti, N., Merlino, S., Masegosa, J., Østensen, R., Palazzi, E., Pian, E., Schwarz, H. E., Cline, T., Guidorzi, C., Goldsten, J., Hurley, K., Mazets, E., McClanahan, T., Montanari, E., Starr, R., and Trombka, J. (2001). Detection of the optical afterglow of GRB 000630: Implications for dark bursts. *Astron. Astrophys.*, 369:373–379.

Gal-Yam, A., Fox, D. B., Price, P. A., Ofek, E. O., Davis, M. R., Leonard, D. C., Soderberg, A. M., Schmidt, B. P., Lewis, K. M., Peterson, B. A., Kulkarni, S. R., Berger, E., Cenko, S. B., Sari, R., Sharon, K., Frail, D., Moon, D.-S., Brown, P. J., Cucchiara, A., Harrison, F., Piran, T., Persson, S. E., McCarthy, P. J., Penprase, B. E., Chevalier, R. A., and MacFadyen, A. I. (2006). A novel explosive process is required for the γ-ray burst GRB 060614. *Nature*, 444:1053–1055.

Galama, T. J., Vreeswijk, P. M., van Paradijs, J., Kouveliotou, C., Augusteijn, T., Bohnhardt, H., Brewer, J. P., Doublier, V., Gonzalez, J.-F., Leibundgut, B., Lidman, C., Hainaut, O. R., Patat, F., Heise, J., in 't Zand, J., Hurley, K., Groot, P. J., Strom, R. G., Mazzali, P. A., Iwamoto, K., Nomoto, K., Umeda, H., Nakamura, T., Young, T. R., Suzuki, T., Shigeyama, T., Koshut, T., Kippen, M., Robinson, C., de Wildt, P., Wijers, R. A. M. J., Tanvir, N., Greiner, J., Pian, E., Palazzi, E., Frontera, F., Masetti, N., Nicastro, L., Feroci, M., Costa, E., Piro, L., Peterson, B. A., Tinney, C., Boyle, B., Cannon, R., Stathakis, R., Sadler, E., Begam, M. C., and Ianna, P. (1998). An unusual supernova in the error box of the gamma-ray burst of 25 April 1998. *Nature*, 395:670.

Gavriil, F. P., Kaspi, V. M., and Woods, P. M. (2002). Magnetar-like X-ray bursts from an anomalous X-ray pulsar. *Nature*, 419:142–144.

Gehrels, N., Cannizzo, J. K., and Norris, J. P. (2007). Gamma-ray bursts in the Swift era. *New Journal of Physics*, 9:37–+.

Gehrels, N., Chincarini, G., Giommi, P., Mason, K. O., Nousek, J. A., Wells, A. A., White, N. E., Barthelmy, S. D., Burrows, D. N., Cominsky, L. R., Hurley, K. C., Marshall, F. E., Mészáros, P., Roming, P. W. A., Angelini, L., Barbier, L. M., Belloni, T., Campana, S., Caraveo, P. A., Chester, M. M., Citterio, O., Cline, T. L., Cropper, M. S., Cummings, J. R., Dean, A. J., Feigelson, E. D., Fenimore, E. E., Frail, D. A., Fruchter, A. S., Garmire, G. P., Gendreau, K., Ghisellini, G., Greiner, J., Hill, J. E., Hunsberger, S. D., Krimm, H. A., Kulkarni, S. R., Kumar, P., Lebrun, F., Lloyd-Ronning, N. M., Markwardt, C. B., Mattson, B. J., Mushotzky, R. F., Norris, J. P., Osborne, J., Paczynski, B., Palmer, D. M., Park, H.-S., Parsons, A. M., Paul, J., Rees, M. J., Reynolds, C. S., Rhoads, J. E., Sasseen, T. P., Schaefer, B. E., Short, A. T., Smale, A. P., Smith,

I. A., Stella, L., Tagliaferri, G., Takahashi, T., Tashiro, M., Townsley, L. K., Tueller, J., Turner, M. J. L., Vietri, M., Voges, W., Ward, M. J., Willingale, R., Zerbi, F. M., and Zhang, W. W. (2004). The Swift Gamma-Ray Burst Mission. *Astrophys. J.*, 611:1005–1020.

Gehrels, N., Sarazin, C. L., O'Brien, P. T., Zhang, B., Barbier, L., Barthelmy, S. D., Blustin, A., Burrows, D. N., Cannizzo, J., Cummings, J. R., Goad, M., Holland, S. T., Hurkett, C. P., Kennea, J. A., Levan, A., Markwardt, C. B., Mason, K. O., Mészáros, P., Page, M., Palmer, D. M., Rol, E., Sakamoto, T., Willingale, R., Angelini, L., Beardmore, A., Boyd, P. T., Breeveld, A., Campana, S., Chester, M. M., Chincarini, G., Cominsky, L. R., Cusumano, G., de Pasquale, M., Fenimore, E. E., Giommi, P., Gronwall, C., Grupe, D., Hill, J. E., Hinshaw, D., Hjorth, J., Hullinger, D., Hurley, K. C., Klose, S., Kobayashi, S., Kouveliotou, C., Krimm, H. A., Mangano, V., Marshall, F. E., McGowan, K., Moretti, A., Mushotzky, R. F., Nakazawa, K., Norris, J. P., Nousek, J. A., Osborne, J. P., Page, K., Parsons, A. M., Patel, S., Perri, M., Poole, T., Romano, P., Roming, P. W. A., Rosen, S., Sato, G., Schady, P., Smale, A. P., Sollerman, J., Starling, R., Still, M., Suzuki, M., Tagliaferri, G., Takahashi, T., Tashiro, M., Tueller, J., Wells, A. A., White, N. E., and Wijers, R. A. M. J. (2005). A short γ-ray burst apparently associated with an elliptical galaxy at redshift z = 0.225. *Nature*, 437:851–854.

Ghirlanda, G., Ghisellini, G., and Celotti, A. (2004). The spectra of short gamma-ray bursts. *Astron. Astrophys.*, 422:L55.

Golenetskii, S. V., Ilinskii, V. N., and Mazets, E. P. (1984). Recurrent bursts in GBS0526 - 66, the source of the 5 March 1979 gamma-ray burst. *Nature*, 307:41–43.

Gorosabel, J., Lund, N., Brandt, S., Westergaard, N. J., and Castro Cerón, J. M. (2004). The potential of INTEGRAL for the detection of high redshift GRBs. *Astron. Astrophys.*, 427:87–93.

Gotthelf, E. V., Halpern, J. P., Buxton, M., and Bailyn, C. (2004). Imaging X-Ray, Optical, and Infrared Observations of the Transient Anomalous X-Ray Pulsar XTE J1810-197. *Astrophys. J.*, 605:368–377.

Göğüş , E., Woods, P. M., Kouveliotou, C., van Paradijs, J., Briggs, M. S., Duncan, R. C., and Thompson, C. (1999). Statistical Properties of SGR 1900+14 Bursts. *Astrophys. J., Lett.*, 526:L93–L96.

Granot, J., Panaitescu, A., Kumar, P., and Woosley, S. E. (2002). Off-Axis Afterglow Emission from Jetted Gamma-Ray Bursts. *Astrophys. J., Lett.*, 570:L61–L64.

Granzer, T. (2004). What makes an automated telescope robotic? *Astronomische Nachrichten*, 325:513–518.

Greco, G., Terra, F., Bartolini, C., Guarnieri, A., Piccioni, A., Nanni, D., Bernabei, S., Sclavi, S., and Pizzichini, G. (2006). GRB 060904b, optical observations. *GRB Coordinates Network*, 5526:1–+.

Groot, P. J., Galama, T. J., Vreeswijk, P. M., Wijers, R. A. M. J., Pian, E., Palazzi, E., van Paradijs, J., Kouveliotou, C., in 't Zand, J. J. M., Heise, J., Robinson, C., Tanvir, N., Lidman, C., Tinney, C., Keane, M., Briggs, M., Hurley, K., Gonzalez, J.-F., Hall, P., Smith, M. G., Covarrubias, R., Jonker, P., Casares, J., Frontera, F., Feroci, M., Piro, L., Costa, E., Smith, R., Jones, B., Windridge, D., Bland-Hawthorn, J., Veilleux, S., Garcia, M., Brown, W. R., Stanek, K. Z., Castro-Tirado, A. J., Gorosabel, J., Greiner, J., Jaeger, K., Bohm, A. B., and Fricke, K. J. (1998). The Rapid Decay of the Optical Emission from GRB 980326 and Its Possible Implications. *Astrophys. J., Lett.*, 502:L123.

Grupe, D., Barthelmy, S. D., Chester, M. M., Cummings, J. R., Holland, S. T., Hunsberger, S. D., Kennea, J. A., Krimm, H. A., Markwardt, C. B., Marshall, F. E., Palmer, D. M., Stamatikos, M., and Stroh, M. C. (2006). GRB 060904B: Swift detection of a burst with optical counterpart. *GRB Coordinates Network*, 5505:1–+.

Gullixson, C. A. (1992). Two Dimensional Imagery. In Howell, S. B., editor, *Astronomical CCD Observing and Reduction Techniques*, volume 23 of *Astronomical Society of the Pacific Conference Series*, pages 130–+.

Hakkila, J., Giblin, T. W., Young, K. C., Fuller, S. P., Peters, C. D., Nolan, C., Sonnett, S. M., Haglin, D. J., and Roiger, R. J. (2007). A Gamma-Ray Burst Database of

BATSE Spectral Lag and Internal Luminosity Function Values. *Astrophys. J., Suppl. Ser.*, 169:62–74.

Harrison, F. A., Bloom, J. S., Frail, D. A., Sari, R., Kulkarni, S. R., Djorgovski, S. G., Axelrod, T., Mould, J., Schmidt, B. P., Wieringa, M. H., Wark, R. M., Subrahmanyan, R., McConnell, D., McCarthy, P. J., Schaefer, B. E., McMahon, R. G., Markze, R. O., Firth, E., Soffitta, P., and Amati, L. (1999). Optical and Radio Observations of the Afterglow from GRB 990510: Evidence for a Jet. *Astrophys. J., Lett.*, 523:L121–L124.

Heise, J., in't Zand, J., Kippen, R. M., and Woods, P. M. (2001). X-Ray Flashes and X-Ray Rich Gamma Ray Bursts. In Costa, E., Frontera, F., and Hjorth, J., editors, *Gamma-ray Bursts in the Afterglow Era*, page 16.

Henry, G. W. and Eaton, J. A., editors (1994). *Robotic Telescopes: Current Capabilities, Present Developments, and Future Prospects for Automated Astronomy*, volume 79 of *Astronomical Society of the Pacific Conference Series*.

Hewish, A., Bell, S. J., Pilkington, J. D., Scott, P. F., and Collins, R. A. (1968). Observation of a Rapidly Pulsating Radio Source. *Nature*, 217:709–+.

Higdon, J. C. and Lingenfelter, R. E. (1990). Gamma-ray bursts. *Ann. Rev. Astron. Astrophys.*, 28:401–436.

Hjellming, R. M., Rupen, M. P., Hunstead, R. W., Campbell-Wilson, D., Mioduszewski, A. J., Gaensler, B. M., Smith, D. A., Sault, R. J., Fender, R. P., Spencer, R. E., de la Force, C. J., Richards, A. M. S., Garrington, S. T., Trushkin, S. A., Ghigo, F. D., Waltman, E. B., and McCollough, M. (2000). Light Curves and Radio Structure of the 1999 September Transient Event in V4641 Sagittarii (=XTE J1819-254=SAX J1819.3-2525). *Astrophys. J.*, 544:977–992.

Hjorth, J., Sollerman, J., Gorosabel, J., Granot, J., Klose, S., Kouveliotou, C., Melinder, J., Ramirez-Ruiz, E., Starling, R., Thomsen, B., Andersen, M. I., Fynbo, J. P. U., Jensen, B. L., Vreeswijk, P. M., Castro Cerón, J. M., Jakobsson, P., Levan, A., Pedersen, K., Rhoads, J. E., Tanvir, N. R., Watson, D., and Wijers, R. A. M. J. (2005a).

GRB 050509B: Constraints on Short Gamma-Ray Burst Models. *Astrophys. J., Lett.*, 630:L117–L120.

Hjorth, J., Sollerman, J., Møller, P., Fynbo, J. P. U., Woosley, S. E., Kouveliotou, C., Tanvir, N. R., Greiner, J., Andersen, M. I., Castro-Tirado, A. J., Castro Cerón, J. M., Fruchter, A. S., Gorosabel, J., Jakobsson, P., Kaper, L., Klose, S., Masetti, N., Pedersen, H., Pedersen, K., Pian, E., Palazzi, E., Rhoads, J. E., Rol, E., van den Heuvel, E. P. J., Vreeswijk, P. M., Watson, D., and Wijers, R. A. M. J. (2003). A very energetic supernova associated with the γ-ray burst of 29 March 2003. *Nature*, 423:847.

Hjorth, J., Watson, D., Fynbo, J. P. U., Price, P. A., Jensen, B. L., Jørgensen, U. G., Kubas, D., Gorosabel, J., Jakobsson, P., Sollerman, J., Pedersen, K., and Kouveliotou, C. (2005b). The optical afterglow of the short γ-ray burst GRB 050709. *Nature*, 437:859.

Horváth, I., Balázs, L. G., Bagoly, Z., Ryde, F., and Mészáros, A. (2006). A new definition of the intermediate group of gamma-ray bursts. *Astron. Astrophys.*, 447:23.

Howell, S. B. (1989). Two-dimensional aperture photometry - Signal-to-noise ratio of point-source observations and optimal data-extraction techniques. *Astronomical Society of the Pacific, Publications*, 101:616–622.

Howell, S. B. (2000a). *Handbook of CCD Photometry*, page 47. Cambridge University Press.

Howell, S. B. (2000b). *Handbook of CCD Photometry*, pages 40 – 44. Cambridge University Press.

Huchra, J. (2003). The importance of small telescopes to cosmological research. In Oswalt, T. D., editor, *The Future of Small Telescopes in the New Millennium*, volume III, pages 343–354. Kluwer Academic Publishers.

Hulleman, F., van Kerkwijk, M. H., and Kulkarni, S. R. (2000). An optical counterpart to the anomalous X-ray pulsar 4U0142+61. *Nature*, 408:689–692.

Hullinger, D., Barbier, L., Barthelmy, S., Cummings, J., Fenimore, E., Gehrels, N., Krimm, H., Koss, M., Markwardt, C., Palmer, D., Parsons, A., Sakamoto, T., Sato, G., Stamatikos, M., and Tueller, J. (2006). GRB 060505 BAT refined analysis. *GRB Coordinates Network*, 5142.

Hurley, K., Boggs, S. E., Smith, D. M., Duncan, R. C., Lin, R., Zoglauer, A., Krucker, S., Hurford, G., Hudson, H., Wigger, C., Hajdas, W., Thompson, C., Mitrofanov, I., Sanin, A., Boynton, W., Fellows, C., von Kienlin, A., Lichti, G., Rau, A., and Cline, T. (2005). An exceptionally bright flare from SGR 1806-20 and the origins of short-duration γ-ray bursts. *Nature*, 434:1098–1103.

Hurley, K., Cline, T., Mazets, E., Barthelmy, S., Butterworth, P., Marshall, F., Palmer, D., Aptekar, R., Golenetskii, S., Il'Inskii, V., Frederiks, D., McTiernan, J., Gold, R., and Trombka, J. (1999a). A giant periodic flare from the soft γ-ray repeater SGR1900+14. *Nature*, 397:41–43.

Hurley, K., Kouveliotou, C., Woods, P., Mazets, E., Golenetskii, S., Frederiks, D. D., Cline, T., and van Paradijs, J. (1999b). Precise Interplanetary Network Localization of a New Soft Gamma Repeater, SGR 1627-41. *Astrophys. J., Lett.*, 519:L143–L145.

Hurley, K., Sari, R., and Djorgovski, S. G. (2002). Cosmic Gamma-Ray Bursts, Their Afterglows, and Their Host Galaxies. [astro-ph/0211620 Review article for the book *Compact Stellar X-Ray Sources*, Editors W. Lewin and M. van der Klis, to be published by Cambridge University Press].

Hurley, K. J., McBreen, B., Delaney, M., and Britton, A. (1995). Lognormal Properties of SGR 1806-20 and Implications for Other SGR Sources. *Astrophys. Space. Sci.*, 231:81–84.

Ibrahim, A. I., Markwardt, C. B., Swank, J. H., Ransom, S., Roberts, M., Kaspi, V., Woods, P. M., Safi-Harb, S., Balman, S., Parke, W. C., Kouveliotou, C., Hurley, K., and Cline, T. (2004). Discovery of a Transient Magnetar: XTE J1810-197. *Astrophys. J., Lett.*, 609:L21–L24.

in't Zand, J. J. M., Jonker, P. G., and Markwardt, C. B. (2007). Six new candidate ultra-compact X-ray binaries. *Astron. Astrophys.*, 465:953–963.

Israel, G., Covino, S., Mignani, R., Stella, L., Marconi, G., Testa, V., Mereghetti, S., Campana, S., Rea, N., Götz, D., Perna, R., and Lo Curto, G. (2005). Discovery and monitoring of the likely IR counterpart of SGR 1806-20 during the 2004 γ-ray burst-active state. *Astron. Astrophys.*, 438:L1–L4.

Jakobsson, P., Hjorth, J., Fynbo, J. P. U., Watson, D., Pedersen, K., Björnsson, G., and Gorosabel, J. (2004). Swift Identification of Dark Gamma-Ray Bursts. *Astrophys. J., Lett.*, 617:L21–L24.

Janesick, J. and Elliott, T. (1992). History and Advancement of Large Array Scientific CCD Imagers. In Howell, S. B., editor, *Astronomical CCD Observing and Reduction Techniques*, volume 23 of *Astronomical Society of the Pacific Conference Series*, pages 1–+.

Jaroszynski, M. (1996). Hot tori around black holes as sources of gamma ray bursts. *Astron. Astrophys.*, 305:839–+.

Jelínek, M., Castro-Tirado, A. J., Postigo, A. d. U., Kubánek, P., Vitek, S., Gorosabel, J., Guziy, S., Hudec, R., Ceron, J. M. C., Pata, P., and Bernas, M. (2005). GRB 050904: BOOTES early R-band detection. *GRB Coordinates Network*, 3929.

Jelínek, M., Kubánek, P., Nekola, M., and Hudec, R. (2004). BART: an intelligent GRB and sky monitoring telescope (2000-2004). *Astronomische Nachrichten*, 325:678–678.

Jelínek, M., Kubánek, P., Prouza, M., Nekola, M., and Hudec, R. (2006a). GRB 060117: FRAM refined analysis. *GRB Coordinates Network*, 4536.

Jelínek, M., Prouza, M., Kubánek, P., Hudec, R., Nekola, M., Řídký, J., Grygar, J., Boháčová, M., Castro-Tirado, A. J., Gorosabel, J., Hrabovský, M., Mandát, D., Nosek, D., Nožka, L., Palatka, M., Pandey, S. B., Pech, M., Schovánek, P., Šmída, R., Trávníček, P., de Ugarte Postigo, A., and Vítek, S. (2006b). The bright optical flash from GRB 060117. *Astron. Astrophys.*, 454:L119–L122.

Jóhannesson, G., Björnsson, G., and Gudmundsson, E. H. (2006). Energy Injection in Gamma-Ray Burst Afterglow Models. *Astrophys. J.*, 647:1238–1249.

Jóhannesson, G., Thöne, C. C., Kann, D. A., Selj, J. H., Jaunsen, A., Fynbo, J. P. U., Hanlon, L., and French, J. (2009). Detailed Study of the Variable Afterglow of GRB 060526. In Meegan, C., Kouveliotou, C., and Gehrels, N., editors, *American Institute of Physics Conference Series*, volume 1133 of *American Institute of Physics Conference Series*, pages 221–223.

Kann, D. A., Klose, S., and Zeh, A. (2006). Signatures of Extragalactic Dust in Pre-Swift GRB Afterglows. *Astrophys. J.*, 641:993–1009.

Kann, D. A., Wilson, A. C., Schulze, S., Klose, S., Henze, M., Ludwig, F., Laux, U., and Greiner, J. (2007). GRB 070610: TLS RRM sees flaring behaviour - Galactic transient? *GRB Coordinates Network*, 6505:1–+.

Kasliwal, M. M., Cenko, S. B., Kulkarni, S. R., Cameron, P. B., Nakar, E., Ofek, E. O., Rau, A., Soderberg, A. M., Campana, S., Bloom, J. S., Perley, D. A., Pollack, L. K., Barthelmy, S., Cummings, J., Gehrels, N., Krimm, H. A., Markwardt, C. B., Sato, G., Chandra, P., Frail, D., Fox, D. B., Price, P. A., Berger, E., Grebenev, S. A., Krivonos, R. A., and Sunyaev, R. A. (2008). GRB 070610: A Curious Galactic Transient. *Astrophys. J.*, 678:1127–1135.

Kaspi, V. M., Gavriil, F. P., Woods, P. M., Jensen, J. B., Roberts, M. S. E., and Chakrabarty, D. (2003). A Major Soft Gamma Repeater-like Outburst and Rotation Glitch in the No-longer-so-anomalous X-Ray Pulsar 1E 2259+586. *Astrophys. J., Lett.*, 588:L93–L96.

Katz, J. I., Toole, H. A., and Unruh, S. H. (1994). Yet another model of soft gamma repeaters. *Astrophys. J.*, 437:727–732.

Kawai, N., Yamada, T., Kosugi, G., Hattori, T., and Aoki, K. (2005). GRB 050904: Subaru Optical Spectroscopy. *GRB Coordinates Network*, 3937.

Kawai, N., Yoshida, A., Matsuoka, M., Shirasaki, Y., Tamagawa, T., Torii, K., Sakamoto, T., Takahashi, D., Fenimore, E., Galassi, M., Tavenner, T., Lamb, D. Q., Graziani, C.,

Donaghy, T., Vanderspek, R., Yamauchi, M., Takagishi, K., and Hatsukade, I. (2003). In-Orbit Performance of WXM (Wide-Field X-Ray Monitor). In Ricker, G. R. and Vanderspek, R. K., editors, *Gamma-Ray Burst and Afterglow Astronomy 2001: A Workshop Celebrating the First Year of the HETE Mission*, volume 662 of *American Institute of Physics Conference Series*, pages 25–32.

King, A., Olsson, E., and Davies, M. B. (2007). A new type of long gamma-ray burst. *Mon. Not. R. Astron. Soc.*, 374:L34–L36.

Klebesadel, R. W., Strong, I. B., and Olson, R. A. (1973). Observations of Gamma-Ray Bursts of Cosmic Origin. *Astrophys. J., Lett.*, 182:L85.

Klotz, A., Boer, M., and Atteia, J. L. (2006a). GRB 060111B: TAROT optical observation. *GRB Coordinates Network*, 4495.

Klotz, A., Boer, M., and Atteia, J. L. (2006b). GRB 060904B: TAROT optical counterpart observations. *GRB Coordinates Network*, 5508:1–+.

Klotz, A., Gendre, B., Stratta, G., Atteia, J. L., Boër, M., Malacrino, F., Damerdji, Y., and Behrend, R. (2006c). Continuous optical monitoring during the prompt emission of ¡ASTROBJ¿GRB 060111B¡/ASTROBJ¿. *Astron. Astrophys.*, 451:L39–L42.

Klotz, A., Gendre, B., Stratta, G., Galli, A., Corsi, A., Preger, B., Cutini, S., Pélangeon, A., Atteia, J. L., Boër, M., and Piro, L. (2008). Early emission of rising optical afterglows: the case of GRB 060904B and GRB 070420. *Astron. Astrophys.*, 483:847–855.

Kobayashi, S. and Zhang, B. (2007). The Onset of Gamma-Ray Burst Afterglow. *Astrophys. J.*, 655:973–979.

Kocevski, D. and Liang, E. (2003). The Connection between Spectral Evolution and Gamma-Ray Burst Lag. *Astrophys. J.*, 594:385–389.

Kouveliotou, C., Dieters, S., Strohmayer, T., van Paradijs, J., Fishman, G. J., Meegan, C. A., Hurley, K., Kommers, J., Smith, I., Frail, D., and Murakami, T. (1998). An X-ray pulsar with a superstrong magnetic field in the soft γ-ray repeater SGR1806 - 20. *Nature*, 393:235–237.

Kouveliotou, C., Meegan, C. A., Fishman, G. J., Bhat, N. P., Briggs, M. S., Koshut, T. M., Paciesas, W. S., and Pendleton, G. N. (1993). Identification of two classes of gamma-ray bursts. *Astrophys. J., Lett.*, 413:L101.

Kouveliotou, C., Strohmayer, T., Hurley, K., van Paradijs, J., Finger, M. H., Dieters, S., Woods, P., Thompson, C., and Duncan, R. C. (1999). Discovery of a Magnetar Associated with the Soft Gamma Repeater SGR 1900+14. *Astrophys. J., Lett.*, 510:L115–L118.

Kouveliotou, C., van Paradijs, J., Fishman, G. J., Briggs, M. S., Kommers, J., Harmon, B. A., Meegan, C. A., and Lewin, W. H. G. (1996). A new type of transient high-energy source in the direction of the Galactic Centre. *Nature*, 379:799–801.

Koyama, K., Hoshi, R., and Nagase, F. (1987). X-ray observations of the extraordinary pulsar 1E 2259 + 586. *Publ. Astron. Soc. Jpn.*, 39:801–807.

Kubánek, P., Jelínek, M., Prouza, M., Nekola, M., and Hudec, R. (2006a). GRB 060117: FRAM optical afterglow candidate. *GRB Coordinates Network*, 4535.

Kubánek, P., Jelínek, M., Vítek, S., de Ugarte Postigo, A., Nekola, M., and French, J. (2006b). RTS2: a powerful robotic observatory manager. In Lewis, H. and Bridger, A., editors, *Advanced Software and Control for Astronomy*, volume 6274 of *Presented at the Society of Photo-Optical Instrumentation Engineers (SPIE) Conference*.

Kumar, P. and Panaitescu, A. (2000). Afterglow Emission from Naked Gamma-Ray Bursts. *Astrophys. J., Lett.*, 541:L51–L54.

Lamb, D. Q. (2001). The Role of Dust in GRB Afterglows. In Costa, E., Frontera, F., and Hjorth, J., editors, *Gamma-ray Bursts in the Afterglow Era*, page 297.

Lamb, D. Q., Donaghy, T. Q., and Graziani, C. (2004). A unified jet model of X-ray flashes and γ-ray bursts. *New Astronomy Review*, 48:459–464.

Landolt, A. U. (1992). UBVRI photometric standard stars in the magnitude range 11.5-16.0 around the celestial equator. *Astronomical Journal*, 104:340–371.

Laros, J. G., Fenimore, E. E., Klebesadel, R. W., Atteia, J.-L., Boer, M., Hurley, K., Niel, M., Vedrenne, G., Kane, S. R., Kouveliotou, C., Cline, T. L., Dennis, B. R., Desai, U. D., Orwig, L. E., Kuznetsov, A. V., Sunyaev, R. A., and Terekhov, O. V. (1987). A new type of repetitive behavior in a high-energy transient. *Astrophys. J., Lett.*, 320:L111–L115.

Le Floc'h, E., Duc, P.-A., Mirabel, I. F., Sanders, D. B., Bosch, G., Diaz, R. J., Donzelli, C. J., Rodrigues, I., Courvoisier, T. J.-L., Greiner, J., Mereghetti, S., Melnick, J., Maza, J., and Minniti, D. (2003). Are the hosts of gamma-ray bursts sub-luminous and blue galaxies? *Astron. Astrophys.*, 400:499–510.

LeBlanc, J. M. and Wilson, J. R. (1970). A Numerical Example of the Collapse of a Rotating Magnetized Star. *Astrophys. J.*, 161:541–+.

Li, W., Filippenko, A. V., Chornock, R., and Jha, S. (2003). The Early Light Curve of the Optical Afterglow of GRB 021211. *Astrophys. J.*, 586:L9–L12.

Livio, M. and Taam, R. E. (1987). Possible models for the high-energy transient GB790107. *Nature*, 327:398–400.

Lloyd, N. M. and Petrosian, V. (2000). Synchrotron Radiation as the Source of Gamma-Ray Burst Spectra. *Astrophys. J.*, 543:722–732.

Lloyd-Ronning, N. M. and Petrosian, V. (2002). Interpreting the Behavior of Time-resolved Gamma-Ray Burst Spectra. *Astrophys. J.*, 565:182.

Lund, N., Budtz-Jørgensen, C., Westergaard, N. J., Brandt, S., Rasmussen, I. L., Hornstrup, A., Oxborrow, C. A., Chenevez, J., Jensen, P. A., Laursen, S., Andersen, K. H., Mogensen, P. B., Rasmussen, I., Omø, K., Pedersen, S. M., Polny, J., Andersson, H., Andersson, T., Kämäräinen, V., Vilhu, O., Huovelin, J., Maisala, S., Morawski, M., Juchnikowski, G., Costa, E., Feroci, M., Rubini, A., Rapisarda, M., Morelli, E., Carassiti, V., Frontera, F., Pelliciari, C., Loffredo, G., Martínez Núñez, S., Reglero, V., Velasco, T., Larsson, S., Svensson, R., Zdziarski, A. A., Castro-Tirado, A., Attina, P., Goria, M., Giulianelli, G., Cordero, F., Rezazad, M., Schmidt, M., Carli, R., Gomez,

C., Jensen, P. L., Sarri, G., Tiemon, A., Orr, A., Much, R., Kretschmar, P., and Schnopper, H. W. (2003). JEM-X: The X-ray monitor aboard INTEGRAL. *Astron. Astrophys.*, 411:L231–L238.

Lyubarsky, Y., Eichler, D., and Thompson, C. (2002). Diagnosing Magnetars with Transient Cooling. *Astrophys. J., Lett.*, 580:L69–L72.

Mészáros, P. and Rees, M. J. (1993). Relativistic fireballs and their impact on external matter - Models for cosmological gamma-ray bursts. *Astrophys. J.*, 405:278.

MacFadyen, A. I. and Woosley, S. E. (1999). Collapsars: Gamma-Ray Bursts and Explosions in "Failed Supernovae". *Astrophys. J.*, 524:262–289.

Mackay, C. D. (1986). Charge-coupled devices in astronomy. *Annual Review of Astronomy and Astrophysics*, 24:255–283.

Malesani, D., Tagliaferri, G., Chincarini, G., Covino, S., Della Valle, M., Fugazza, D., Mazzali, P. A., Zerbi, F. M., D'Avanzo, P., Kalogerakos, S., Simoncelli, A., Antonelli, L. A., Burderi, L., Campana, S., Cucchiara, A., Fiore, F., Ghirlanda, G., Goldoni, P., Götz, D., Mereghetti, S., Mirabel, I. F., Romano, P., Stella, L., Minezaki, T., Yoshii, Y., and Nomoto, K. (2004). SN 2003lw and GRB 031203: A Bright Supernova for a Faint Gamma-Ray Burst. *Astrophys. J., Lett.*, 609:L5–L8.

Manchester, R. N. (2004). Observational Properties of Pulsars. *Science*, 304:542–547.

Markwardt, C. B., Pagani, C., Evans, P., Gavriil, F. P., Kennea, J. A., Krimm, H. A., Landsman, W., and Marshall, F. E. (2007). SWIFT J195509.6+261406 / GRB 070610: A Potential Galactic Transient. *The Astronomer's Telegram*, 1102:1–+.

Martinez, P. and Klotz, A. (1998). *A practical guide to CCD astronomy*. A practical guide to CCD astronomy , by Martinez, Patrick.; Klotz, Alain. Cambridge ; New York, NY, USA : Cambridge University Press, 1998. Practical astronomy handbook series ; 8.

Mas-Hesse, J. M., Giménez, A., Culhane, J. L., Jamar, C., McBreen, B., Torra, J., Hudec, R., Fabregat, J., Meurs, E., Swings, J. P., Alcacera, M. A., Balado, A., Beiztegui, R., Belenguer, T., Bradley, L., Caballero, M. D., Cabo, P., Defise, J. M., Díaz, E., Domingo,

A., Figueras, F., Figueroa, I., Hanlon, L., Hroch, F., Hudcova, V., García, T., Jordan, B., Jordi, C., Kretschmar, P., Laviada, C., March, M., Martín, E., Mazy, E., Menéndez, M., Mi, J. M., de Miguel, E., Muñoz, T., Nolan, K., Olmedo, R., Plesseria, J. Y., Polcar, J., Reina, M., Renotte, E., Rochus, P., Sánchez, A., San Martín, J. C., Smith, A., Soldan, J., Thomas, P., Timón, V., and Walton, D. (2003). OMC: An Optical Monitoring Camera for INTEGRAL. Instrument description and performance. *Astron. Astrophys.*, 411:L261–L268.

Massey, P. and Jacoby, G. H. (1992). CCD Data: The Good, The Bad, and The Ugly. In Howell, S. B., editor, *Astronomical CCD Observing and Reduction Techniques*, volume 23 of *Astronomical Society of the Pacific Conference Series*, pages 240–+.

Matheson, T. (2005). The Supernovae Associated with Gamma-Ray Bursts. In *ASP Conf. Ser. 332: The Fate of the Most Massive Stars*, page 416.

Mazets, E. P., Aptekar, R. L., Butterworth, P. S., Cline, T. L., Frederiks, D. D., Golenetskii, S. V., Hurley, K., and Il'Inskii, V. N. (1999). Unusual Burst Emission from the New Soft Gamma Repeater SGR 1627-41. *Astrophys. J., Lett.*, 519:L151–L153.

Mazets, E. P., Golenetskii, S. V., Ilyinskii, V. N., Panov, V. N., Aptekar, R. L., Guryan, Y. A., Proskura, M. P., Sokolov, I. A., Sokolova, Z. Y., Kharitonova, T. V., Dyatchkov, A. V., and Khavenson, N. G. (1981). Catalog of cosmic gamma-ray bursts from the KONUS experiment data. *Astrophys. Space. Sci.*, 80:119–143.

Mazets, E. P., Golentskii, S. V., Ilinskii, V. N., Aptekar, R. L., and Guryan, I. A. (1979). Observations of a flaring X-ray pulsar in Dorado. *Nature*, 282:587–589.

McBreen, S., Hanlon, L., McGlynn, S., McBreen, B., Foley, S., Preece, R., von Kienlin, A., and Williams, O. R. (2006). Observations of the intense and ultra-long burst GRB 041219a with the Germanium spectrometer on INTEGRAL. *Astron. Astrophys.*, 455:433–440.

McBreen, S., Quilligan, F., McBreen, B., Hanlon, L., and Watson, D. (2001). Temporal properties of the short gamma-ray bursts. *Astron. Astrophys.*, 380:L31.

McGlynn, S., Clark, D. J., Dean, A. J., Hanlon, L., McBreen, S., Willis, D. R., McBreen, B., Bird, A. J., and Foley, S. (2007). Polarisation studies of the prompt gamma-ray emission from GRB 041219a using the spectrometer aboard INTEGRAL. *Astron. Astrophys.*, 466:895–904.

McNamara, B. J., Harrison, T. E., and Williams, C. L. (1995). Directions for Future X-Ray, Optical, and Radio Follow-up Observations of Gamma-Ray Burst Counterparts. *Astrophys. J., Lett.*, 452:L25.

Medvedev, M. V. (2000). Theory of "Jitter" Radiation from Small-Scale Random Magnetic Fields and Prompt Emission from Gamma-Ray Burst Shocks. *Astrophys. J.*, 540:704–714.

Meegan, C., Bhat, N., Connaughton, V., Briggs, M., Diehl, R., Fishman, G., Greiner, J., Kippen, R. M., von Kienlin, A., Kouveliotou, C., Lichti, G., Paciesas, W., Preece, R., Steinle, H., and Wilson-Hodge, C. (2007). The GLAST Burst Monitor. In Ritz, S., Michelson, P., and Meegan, C. A., editors, *The First GLAST Symposium*, volume 921 of *American Institute of Physics Conference Series*, page 13.

Meegan, C. A., Fishman, G. J., Wilson, R. B., Horack, J. M., Brock, M. N., Paciesas, W. S., Pendleton, G. N., and Kouveliotou, C. (1992). Spatial distribution of gamma-ray bursts observed by BATSE. *Nature*, 355:143.

Mereghetti, S. (2008). The strongest cosmic magnets: soft gamma-ray repeaters and anomalous X-ray pulsars. *Astron. Astrophys. Rev.*, 15:225–287.

Mereghetti, S., Esposito, P., Tiengo, A., Turolla, R., Zane, S., Stella, L., Israel, G. L., Feroci, M., and Treves, A. (2006). XMM-Newton observations of the Soft Gamma Ray Repeater SGR 1627-41 in a low luminosity state. *Astron. Astrophys.*, 450:759–762.

Mereghetti, S., Götz, D., von Kienlin, A., Rau, A., Lichti, G., Weidenspointner, G., and Jean, P. (2005). The First Giant Flare from SGR 1806-20: Observations Using the Anticoincidence Shield of the Spectrometer on INTEGRAL. *Astrophys. J., Lett.*, 624:L105–L108.

Merline, W. J. and Howell, S. B. (1995). A Realistic Model for Point-sources Imaged on Array Detectors: The Model and Initial Results. *Experimental Astronomy*, 6:163–210.

Merloni, A., Di Matteo, T., and Fabian, A. C. (2000). Magnetic flares and the optical variability of the X-ray transient XTE J1118+480. *Mon. Not. R. Astron. Soc.*, 318:L15–L19.

Mescheryakov, A., Burenin, R., Pavlinsky, M., Sunyaev, R., Khamitov, I., Aslan, Z., Kiziloglu, U., Gogus, E., Bikmaev, I., and Sakhibullin, N. (2006). GRB 060904B: RTT150 optical observations. *GRB Coordinates Network*, 5524:1–+.

Mészáros, P. (2002). Theories of Gamma-Ray Bursts. *Ann. Rev. Astron. Astrophys.*, 40:137–169.

Mészáros, P. and Rees, M. J. (1997). Optical and Long-Wavelength Afterglow from Gamma-Ray Bursts. *Astrophys. J.*, 476:232.

Metzger, M. R., Djorgovski, S. G., Kulkarni, S. R., Steidel, C. C., Adelberger, K. L., Frail, D. A., Costa, E., and Frontera, F. (1997). Spectral constraints on the redshift of the optical counterpart to the γ-ray burst of 8 May 1997. *Nature*, 387:878–880.

Molinari, E., Vergani, S. D., Malesani, D., Covino, S., D'Avanzo, P., Chincarini, G., Zerbi, F. M., Antonelli, L. A., Conconi, P., Testa, V., Tosti, G., Vitali, F., D'Alessio, F., Malaspina, G., Nicastro, L., Palazzi, E., Guetta, D., Campana, S., Goldoni, P., Masetti, N., Meurs, E. J. A., Monfardini, A., Norci, L., Pian, E., Piranomonte, S., Rizzuto, D., Stefanon, M., Stella, L., Tagliaferri, G., Ward, P. A., Ihle, G., Gonzalez, L., Pizarro, A., Sinclaire, P., and Valenzuela, J. (2007). REM observations of GRB 060418 and GRB 060607A: the onset of the afterglow and the initial fireball Lorentz factor determination. *Astron. Astrophys.*, 469:L13–L16.

Monfardini, A., Kobayashi, S., Guidorzi, C., Carter, D., Mundell, C. G., Bersier, D. F., Gomboc, A., Melandri, A., Mottram, C. J., Smith, R. J., and Steele, I. A. (2006). High-Quality Early-Time Light Curves of GRB 060206: Implications for Gamma-Ray Burst Environments and Energetics. *Astrophys. J.*, 648:1125–1131.

Mortara, L. and Fowler, A. (1981). Evaluations of Charge-Coupled Device / CCD / Performance for Astronomical Use. In *Society of Photo-Optical Instrumentation Engineers (SPIE) Conference Series*, volume 290 of *Society of Photo-Optical Instrumentation Engineers (SPIE) Conference Series*, pages 28–+.

Mundell, C. G., Melandri, A., Guidorzi, C., Kobayashi, S., Steele, I. A., Malesani, D., Amati, L., D'Avanzo, P., Bersier, D. F., Gomboc, A., Rol, E., Bode, M. F., Carter, D., Mottram, C. J., Monfardini, A., Smith, R. J., Malhotra, S., Wang, J., Bannister, N., O'Brien, P. T., and Tanvir, N. R. (2007). The Remarkable Afterglow of GRB 061007: Implications for Optical Flashes and GRB Fireballs. *Astrophys. J.*, 660:489–495.

Muno, M. P., Gaensler, B. M., Nechita, A., Miller, J. M., and Slane, P. O. (2008). A Search for New Galactic Magnetars in Archival Chandra and XMM-Newton Observations. *Astrophys. J.*, 680:639–653.

Murakami, T., Tanaka, Y., Kulkarni, S. R., Ogasaka, Y., Sonobe, T., Ogawara, Y., Aoki, T., and Yoshida, A. (1994). X-Ray Identification of the Soft Gamma-Ray Repeater 1806-20. *Nature*, 368:127–+.

Narayan, R., Paczynski, B., and Piran, T. (1992). Gamma-ray bursts as the death throes of massive binary stars. *Astrophys. J., Lett.*, 395:L83–L86.

Narayan, R., Piran, T., and Shemi, A. (1991). Neutron star and black hole binaries in the Galaxy. *Astrophys. J., Lett.*, 379:L17–L20.

Norris, J. P. (2002). Implications of the Lag-Luminosity Relationship for Unified Gamma-Ray Burst Paradigms. *Astrophys. J.*, 579:386.

Norris, J. P. and Bonnell, J. T. (2006). Short Gamma-Ray Bursts with Extended Emission. *Astrophys. J.*, 643:266.

Norris, J. P., Marani, G. F., and Bonnell, J. T. (2000). Connection between Energy-dependent Lags and Peak Luminosity in Gamma-Ray Bursts. *Astrophys. J.*, 534:248.

Nysewander, M., LaCluyze, A., Reichart, D., Crain, J. A., Foster, A., and Ivarson, K. (2006). GRB 060117: PROMPT Observations. *GRB Coordinates Network*, 4548.

Nysewander, M., Reichart, D. E., Crain, J. A., Foster, A., Haislip, J., Ivarsen, K., Lacluyze, A., and Trotter, A. (2007). PROMPT Observations of the Early-Time Optical Afterglow of GRB 060607A. *astro-ph/0708.3444*.

Oates, S. R. and Grupe, D. (2006). GRB 060904b: Optical observations with Swift/UVOT. *GRB Coordinates Network*, 5519:1–+.

Ofek, E. O., Cenko, S. B., Gal-Yam, A., Fox, D. B., Nakar, E., Rau, A., Frail, D. A., Kulkarni, S. R., Price, P. A., Schmidt, B. P., Soderberg, A. M., Peterson, B., Berger, E., Sharon, K., Shemmer, O., Penprase, B. E., Chevalier, R. A., Brown, P. J., Burrows, D. N., Gehrels, N., Harrison, F., Holland, S. T., Mangano, V., McCarthy, P. J., Moon, D.-S., Nousek, J. A., Persson, S. E., Piran, T., and Sari, R. (2007). GRB 060505: A Possible Short-Duration Gamma-Ray Burst in a Star-forming Region at a Redshift of 0.09. *Astrophys. J.*, 662:1129–1135.

Oswalt, T. D., editor (2003). *The Future of Small Telescopes in the New Millennium*. Kluwer Academic Publishers. ISBN 1-4020-0948-8.

Paciesas, W. S., Meegan, C. A., Pendleton, G. N., Briggs, M. S., Kouveliotou, C., Koshut, T. M., Lestrade, J. P., McCollough, M. L., Brainerd, J. J., Hakkila, J., Henze, W., Preece, R. D., Connaughton, V., Kippen, R. M., Mallozzi, R. S., Fishman, G. J., Richardson, G. A., and Sahi, M. (1999). The Fourth BATSE Gamma-Ray Burst Catalog (Revised). *Astrophys. J., Suppl. Ser.*, 122:465.

Paczynski, B. (1986). Gamma-ray bursters at cosmological distances. *Astrophys. J., Lett.*, 308:L43.

Paczynski, B. (1991). Cosmological gamma-ray bursts. *Acta Astronomica*, 41:257–267.

Paczynski, B. (1992). GB 790305 as a very strongly magnetized neutron star. *Acta Astronomica*, 42:145–153.

Paczynski, B. (1998). Are Gamma-Ray Bursts in Star-Forming Regions? *Astrophys. J., Lett.*, 494:L45.

Paczynski, B. and Rhoads, J. E. (1993). Radio Transients from Gamma-Ray Bursters. *Astrophys. J., Lett.*, 418:L5.

Pagani, C., Barthelmy, S. D., Cummings, J. R., Gehrels, N., Grupe, D., Holland, S. T., Kennea, J. A., Markwardt, C. B., Marshall, F. E., O'Brien, P. T., Palmer, D. M., Parsons, A. M., Stamatikos, M., and Vetere, L. (2007). GRB 070610: Swift detection of a burst. *GRB Coordinates Network*, 6489:1–+.

Pagani, C. and Kennea, J. A. (2007). GRB 070610; Swift-XRT position. *GRB Coordinates Network*, 6490:1–+.

Page, M., Burrows, D., Beardmore, A., Palmer, D., J, ., Kennea, ., Gehrels, N., Markwardt, C., Page, K., Sakamoto, T., Chester, M., and Boyd, P. (2005). Subject: GRB 050820: Swift detection of a GRB. *GRB Coordinates Network*, 3830.

Pal'shin, V. and Frederiks, D. (2005). GRB 050820a - corrections to GCN 3846. *GRB Coordinates Network*, 3852.

Panaitescu, A. (2008). Gev emission from gamma-ray burst afterglows. *MON.NOT.ROY.ASTRON.SOC.*, 385:1628.

Panaitescu, A. and Kumar, P. (2001). Fundamental Physical Parameters of Collimated Gamma-Ray Burst Afterglows. *Astrophys. J., Lett.*, 560:L49–L53.

Panaitescu, A. and Mészáros, P. (2000). Gamma-Ray Bursts from Upscattered Self-absorbed Synchrotron Emission. *Astrophys. J., Lett.*, 544:L17–L21.

Panaitescu, A. and Vestrand, W. T. (2008). Taxonomy of gamma-ray burst optical light curves: identification of a salient class of early afterglows. *Mon. Not. R. Astron. Soc.*, 387:497–504.

Pe'er, A. (2008). Temporal Evolution of Thermal Emission from Relativistically Expanding Plasma. *Astrophys. J.*, 682:463–473.

Percy, J. R. (2003). Small telescopes in astronomy education. In Oswalt, T. D., editor, *The Future of Small Telescopes in the New Millennium*, volume I, pages 113–123. Kluwer Academic Publishers.

Perna, R., Hernquist, L., and Narayan, R. (2000). Emission Spectra of Fallback Disks around Young Neutron Stars. *Astrophys. J.*, 541:344–350.

Perna, R. and Loeb, A. (1998). Identifying the Environment and Redshift of Gamma-Ray Burst Afterglows from the Time Dependence of Their Absorption Spectra. *Astrophys. J.*, 501:467–+.

Perri, M., Barthelmy, S., Boyd, P., Burrows, D., Cummings, J., Gehrels, N., Gronwall, C., Kennea, J., Krimm, H., Markwardt, C., Marshall, F., Palmer, D., and Sakamoto, T. (2006). GRB 060111B: Swift detection of a burst. *GRB Coordinates Network*, 4487.

Piran, T. (1992). The implications of the Compton (GRO) observations for cosmological gamma-ray bursts. *Astrophys. J., Lett.*, 389:L45–L48.

Piran, T. (2005). The physics of gamma-ray bursts. *Reviews of Modern Physics*, 76:1143–1210.

Piran, T., Sari, R., and Zou, Y.-C. (2008). Observational Limits on Inverse Compton Processes in GRBs. *astro-ph/0807.3954*.

Piro, L., Frail, D. A., Gorosabel, J., Garmire, G., Soffitta, P., Amati, L., Andersen, M. I., Antonelli, L. A., Berger, E., Frontera, F., Fynbo, J., Gandolfi, G., Garcia, M. R., Hjorth, J., in 't Zand, J., Jensen, B. L., Masetti, N., Møller, P., Pedersen, H., Pian, E., and Wieringa, M. H. (2002). The Bright Gamma-Ray Burst of 2000 February 10: A Case Study of an Optically Dark Gamma-Ray Burst. *Astrophys. J.*, 577:680–690.

Pogson, N. (1856). Magnitudes of Thirty-six of the Minor Planets for the first day of each month of the year 1857. *"Monthly Notices of the Royal Astronomical Society"*, 17:1–+.

Poirier, J., D'Andrea, C., Fragile, P. C., Gress, J., Mathews, G. J., and Race, D. (2003). Search for sub-TeV gamma rays in coincidence with gamma ray bursts. *Physical Review D*, 67(4):042001.

Postigo, A. d. U., Castro-Tirado, A. J., and Aceituno, F. (2007). GRB 070610: Optical observations from OSN. *GRB Coordinates Network*, 6501:1–+.

Preece, R. D., Briggs, M. S., Giblin, T. W., Mallozzi, R. S., Pendleton, G. N., Paciesas, W. S., and Band, D. L. (2002). On the Consistency of Gamma-Ray Burst Spectral Indices with the Synchrotron Shock Model. *Astrophys. J.*, 581:1248–1255.

Preece, R. D., Briggs, M. S., Mallozzi, R. S., Pendleton, G. N., Paciesas, W. S., and Band, D. L. (2000). The BATSE Gamma-Ray Burst Spectral Catalog. I. High Time Resolution Spectroscopy of Bright Bursts Using High Energy Resolution Data. *Astrophys. J., Suppl. Ser.*, 126:19.

Prymak, N., Kanbach, G., Steinle, H., Stefanescu, A., Duscha, S., Schrey, F., and Muehlegger, M. (2006). GRB 060904b optical detections (delayed report due to internet outage). *GRB Coordinates Network*, 5541:1–+.

Qin, Y.-P., Xie, G.-Z., Xue, S.-J., Liang, E.-W., Zheng, X.-T., and Mei, D.-C. (2000). The Hardness-Duration Correlation in the Two Classes of Gamma-Ray Bursts. *Publ. Astron. Soc. Jpn.*, 52:759.

Quilligan, F., McBreen, B., Hanlon, L., McBreen, S., Hurley, K. J., and Watson, D. (2002). Temporal properties of gamma ray bursts as signatures of jets from the central engine. *Astron. Astrophys.*, 385:377.

Rees, M. J. (1999). Some comments on triggers, energetics and beaming. *Astron. Astrophys. Suppl. Ser.*, 138:L491.

Rees, M. J. and Mészáros, P. (1992). Relativistic fireballs - Energy conversion and timescales. *Mon. Not. R. Astron. Soc.*, 258:41.

Rees, M. J. and Mészáros, P. (1998). Refreshed Shocks and Afterglow Longevity in Gamma-Ray Bursts. *Astrophys. J., Lett.*, 496:L1.

Reichart, D., Nysewander, M., Moran, J., Bartelme, J., Bayliss, M., Foster, A., Clemens, J. C., Price, P., Evans, C., Salmonson, J., Trammell, S., Carney, B., Keohane, J., and Gotwals, R. (2005). PROMPT: Panchromatic Robotic Optical Monitoring and Polarimetry Telescopes. *Nuovo Cimento C Geophysics Space Physics C*, 28:767–+.

Revnivtsev, M., Gilfanov, M., Churazov, E., and Sunyaev, R. (2002). Super-Eddington outburst of V4641 Sgr. *Astron. Astrophys.*, 391:1013–1022.

Ricker, G. R., Atteia, J.-L., Crew, G. B., Doty, J. P., Fenimore, E. E., Galassi, M., Graziani, C., Hurley, K., Jernigan, J. G., Kawai, N., Lamb, D. Q., Matsuoka, M., Pizzichini, G., Shirasaki, Y., Tamagawa, T., Vanderspek, R., Vedrenne, G., Villasenor, J., Woosley, S. E., and Yoshida, A. (2003). The High Energy Transient Explorer (HETE): Mission and Science Overview. In Ricker, G. R. and Vanderspek, R. K., editors, *Gamma-Ray Burst and Afterglow Astronomy 2001: A Workshop Celebrating the First Year of the HETE Mission*, volume 662 of *American Institute of Physics Conference Series*, pages 3–16.

Rieke, G. H. and Visnovsky, K. (1994). *Detection of Light, From the Ultraviolet to the Submillimeter*. Cambridge University Press, 1994. ISBN 0521410282.

Roming, P. W. A., Kennedy, T. E., Mason, K. O., Nousek, J. A., Ahr, L., Bingham, R. E., Broos, P. S., Carter, M. J., Hancock, B. K., Huckle, H. E., Hunsberger, S. D., Kawakami, H., Killough, R., Koch, T. S., McLelland, M. K., Smith, K., Smith, P. J., Soto, J. C., Boyd, P. T., Breeveld, A. A., Holland, S. T., Ivanushkina, M., Pryzby, M. S., Still, M. D., and Stock, J. (2005). The Swift Ultra-Violet/Optical Telescope. *Space Science Reviews*, 120:95–142.

Roming, P. W. A., Schady, P., Fox, D. B., Zhang, B., Liang, E., Mason, K. O., Rol, E., Burrows, D. N., Blustin, A. J., Boyd, P. T., Brown, P., Holland, S. T., McGowan, K., Landsman, W. B., Page, K. L., Rhoads, J. E., Rosen, S. R., Vanden Berk, D., Barthelmy, S. D., Breeveld, A. A., Cucchiara, A., De Pasquale, M., Fenimore, E. E., Gehrels, N., Gronwall, C., Grupe, D., Goad, M. R., Ivanushkina, M., James, C., Kennea, J. A., Kobayashi, S., Mangano, V., Mészáros, P., Morgan, A. N., Nousek, J. A., Osborne, J. P., Palmer, D. M., Poole, T., Still, M. D., Tagliaferri, G., and Zane, S. (2006). Very Early Optical Afterglows of Gamma-Ray Bursts: Evidence for Relative Paucity of Detection. *Astrophys. J.*, 652:1416–1422.

Rothschild, R. E., Kulkarni, S. R., and Lingenfelter, R. E. (1994). Discovery of an X-Ray Source Coincident with the Soft Gamma-Repeater 0425-66. *Nature*, 368:432–+.

Rykoff, E. S., Mangano, V., Yost, S. A., Sari, R., Aharonian, F., Akerlof, C. W., Ashley, M. C. B., Barthelmy, S. D., Burrows, D. N., Gehrels, N., Göğüş, E., Güver, T., Horns, D., Kızıloğlu, Ü., Krimm, H. A., McKay, T. A., Özel, M., Phillips, A., Quimby, R. M., Rowell, G., Rujopakarn, W., Schaefer, B. E., Smith, D. A., Swan, H. F., Vestrand, W. T., Wheeler, J. C., Wren, J., and Yuan, F. (2006a). The Anomalous Early Afterglow of GRB 050801. *Astrophys. J., Lett.*, 638:L5–L8.

Rykoff, E. S., Rujopakarn, W., and Yuan, F. (2006b). GRB 060904B: ROTSE-III Detection of Optical Counterpart. *GRB Coordinates Network*, 5504:1–+.

Rykoff, E. S., Yost, S. A., Krimm, H. A., Aharonian, F., Akerlof, C. W., Alatalo, K., Ashley, M. C. B., Barthelmy, S. D., Gehrels, N., Göğüş, E., Güver, T., Horns, D., Kızıloğlu, Ü., McKay, T. A., Özel, M., Phillips, A., Quimby, R. M., Rujopakarn, W., Schaefer, B. E., Smith, D. A., Swan, H. F., Vestrand, W. T., Wheeler, J. C., and Wren, J. (2005). Prompt Optical Detection of GRB 050401 with ROTSE-IIIa. *Astrophys. J., Lett.*, 631:L121–L124.

Sakamoto, T., Barbier, L., Barthelmy, S. D., Cummings, J. R., Fenimore, E. E., Gehrels, N., Hullinger, D., Krimm, H. A., Markwardt, C. B., Palmer, D. M., Parsons, A. M., Sato, G., and Tueller, J. (2006). Confirmation of the Esrcpeak-Eiso (Amati) Relation from the X-Ray Flash XRF 050416AObserved by the Swift Burst Alert Telescope. *Astrophys. J., Lett.*, 636:L73–L76.

Sakamoto, T., Lamb, D. Q., Kawai, N., Yoshida, A., Graziani, C., Fenimore, E. E., Donaghy, T. Q., Matsuoka, M., Suzuki, M., Ricker, G., Atteia, J.-L., Shirasaki, Y., Tamagawa, T., Torii, K., Galassi, M., Doty, J., Vanderspek, R., Crew, G. B., Villasenor, J., Butler, N., Prigozhin, G., Jernigan, J. G., Barraud, C., Boer, M., Dezalay, J.-P., Olive, J.-F., Hurley, K., Levine, A., Monnelly, G., Martel, F., Morgan, E., Woosley, S. E., Cline, T., Braga, J., Manchanda, R., Pizzichini, G., Takagishi, K., and Yamauchi, M. (2005). Global Characteristics of X-Ray Flashes and X-Ray-Rich Gamma-Ray Bursts Observed by HETE-2. *Astrophys. J.*, 629:311.

Sari, R. and Piran, T. (1999a). GRB 990123: The Optical Flash and the Fireball Model. *Astrophys. J., Lett.*, 517:L109–L112.

Sari, R. and Piran, T. (1999b). Predictions for the Very Early Afterglow and the Optical Flash. *Astrophys. J.*, 520:641–649.

Sari, R. and Piran, T. (1999c). Predictions for the Very Early Afterglow and the Optical Flash. *Astrophys. J.*, 520:641–649.

Sari, R., Piran, T., and Narayan, R. (1998). Spectra and Light Curves of Gamma-Ray Burst Afterglows. *Astrophys. J., Lett.*, 497:L17.

Schmidt, B., Wieringa, M., Frail, D. A., and Soderberg, A. (2006). GRB 060117 - ATCA 3/6cm radio limits - correction. *GRB Coordinates Network*, 4547.

Shao, L. and Dai, Z. G. (2005). A Reverse-Shock Model for the Early Afterglow of GRB 050525A. *Astrophys. J.*, 633:1027–1030.

Skvarc, J. (2006). GRB 060904B: Optical observations at Crni Vrh. *GRB Coordinates Network*, 5511:1–+.

Soderberg, A. M., Kulkarni, S. R., Berger, E., Fox, D. W., Sako, M., Frail, D. A., Gal-Yam, A., Moon, D. S., Cenko, S. B., Yost, S. A., Phillips, M. M., Persson, S. E., Freedman, W. L., Wyatt, P., Jayawardhana, R., and Paulson, D. (2004). The sub-energetic γ-ray burst GRB 031203 as a cosmic analogue to the nearby GRB 980425. *Nature*, 430:648–650.

Soyano, T., Mito, H., and Urata, Y. (2006). GRB 060904B: Kiso Optical observation. *GRB Coordinates Network*, 5548:1–+.

Stanek, K. Z., Dai, X., Prieto, J. L., An, D., Garnavich, P. M., Calkins, M. L., Serven, J., Worthey, G., Hao, H., Dobrzycki, A., Howk, C., and Matheson, T. (2007). "Anomalous" Optical Gamma-Ray Burst Afterglows Are Common: Two z ˜ 4 Bursts, GRB 060206 and GRB 060210. *Astrophys. J., Lett.*, 654:L21–L24.

Stanek, K. Z., Matheson, T., Garnavich, P. M., Martini, P., Berlind, P., Caldwell, N., Challis, P., Brown, W. R., Schild, R., Krisciunas, K., Calkins, M. L., Lee, J. C., Hathi, N., Jansen, R. A., Windhorst, R., Echevarria, L., Eisenstein, D. J., Pindor, B., Olszewski,

E. W., Harding, P., Holland, S. T., and Bersier, D. (2003). Spectroscopic Discovery of the Supernova 2003dh Associated with GRB 030329. *Astrophys. J., Lett.*, 591:L170.

Stefanescu, A., Kanbach, G., Słowikowska, A., Greiner, J., McBreen, S., and Sala, G. (2008). Very fast optical flaring from a possible new Galactic magnetar. *Nature*, 455:503–505.

Stefanescu, A., Slowikowska, A., Kanbach, G., Duscha, S., Schrey, F., Steinle, H., and Ioannou, Z. (2007). GRB 070610: OPTIMA-Burst high-time-resolution optical observations. *GRB Coordinates Network*, 6492:1–+.

Stroh, M. C. (2008). GRB 080905B: Swift-XRT Refined Analysis. *GCN*, 8193.

Stroh, M. C., Barthelmy, S. D., Baumgartner, W. H., and et al. (2008). GRB 080905B: Swift detection of a burst with possible optical counterpart. *GCN*, 8182.

Symbalisty, E. M. D. (1984). Magnetorotational iron core collapse. *Astrophys. J.*, 285:729–746.

Szabados, L. (2003). Variable star research with small telescopes. In Oswalt, T. D., editor, *The Future of Small Telescopes in the New Millennium*, volume III, pages 207–223. Kluwer Academic Publishers.

Tavani, M. (1996). A Shock Emission Model for Gamma-Ray Bursts. II. Spectral Properties. *Astrophys. J.*, 466:768–+.

Tavani, M., Barbiellini, G., Argan, A., Basset, M., Boffelli, F., Bulgarelli, A., Caraveo, P., Chen, A., Costa, E., De Paris, G., Del Monte, E., Di Cocco, G., Donnarumma, I., Feroci, M., Fiorini, M., Foggetta, L., Froysland, T., Frutti, M., Fuschino, F., Galli, M., Gianotti, F., Giuliani, A., Labanti, C., Lapshov, I., Lazzarotto, F., Liello, F., Lipari, P., Longo, F., Marisaldi, M., Mastropietro, M., Mattaini, E., Mauri, F., Mereghetti, S., Morelli, E., Morselli, A., Pacciani, L., Pellizzoni, A., Perotti, F., Picozza, P., Pittori, C., Pontoni, C., Porrovecchio, G., Prest, M., Pucella, G., Rapisarda, M., Rossi, E., Rubini, A., Soffitta, P., Traci, A., Trifoglio, M., Trois, A., Vallazza, E., Vercellone, S., Zambra, A., and Zanello, D. (2006). The AGILE mission and its scientific instrument. In *Space*

Telescopes and Instrumentation II: Ultraviolet to Gamma Ray. Edited by Turner, Martin J. L.; Hasinger, Günther., volume 6266 of *Presented at the Society of Photo-Optical Instrumentation Engineers (SPIE) Conference*.

Thoene, C. C., Kann, D. A., Johannesson, G., Selj, J. H., Jaunsen, A., Fynbo, J. P. U., Baliyan, K. S., Bartolini, C., Bikmaev, I. F., Bloom, J. S., Burenin, R. A., Cobb, B. E., Covino, S., Curran, P. A., Dahle, H., French, J., Ganesh, S., Greco, G., Guarnieri, A., Hanlon, L., Hjorth, J., Ibrahimov, M., Israel, G. L., Jakobsson, P., Jensen, B. L., Jorgensen, U. G., Khamitov, I. M., Malesani, D., Masetti, N., Naranen, J., Pakstiene, E., Pavlinsky, M. N., Perley, D. A., Piccioni, A., Pizzichini, G., Pozanenko, A., Nanni, D., Rumyantsev, V., Sharapov, D., Starr, D., Sunyaev, R. A., Terra, F., Vreeswijk, P. M., and Wilson, A. C. (2008). Photometry and Spectroscopy of GRB 060526: A detailed study of the afterglow and host of a high-redshift gamma-ray burst. *ArXiv e-prints*.

Thompson, C. and Beloborodov, A. M. (2005). High-Energy Emission from Magnetars. *Astrophys. J.*, 634:565–569.

Thompson, C. and Duncan, R. C. (1993). Neutron star dynamos and the origins of pulsar magnetism. *Astrophys. J.*, 408:194–217.

Thompson, C. and Duncan, R. C. (1995). The soft gamma repeaters as very strongly magnetized neutron stars - I. Radiative mechanism for outbursts. *Mon. Not. R. Astron. Soc.*, 275:255–300.

Thompson, C. and Duncan, R. C. (1996). The Soft Gamma Repeaters as Very Strongly Magnetized Neutron Stars. II. Quiescent Neutrino, X-Ray, and Alfven Wave Emission. *Astrophys. J.*, 473:322–+.

Thompson, C., Duncan, R. C., Woods, P. M., Kouveliotou, C., Finger, M. H., and van Paradijs, J. (2000). Physical Mechanisms for the Variable Spin-down and Light Curve of SGR 1900+14. *Astrophys. J.*, 543:340–350.

Thompson, C., Lyutikov, M., and Kulkarni, S. R. (2002). Electrodynamics of Magnetars: Implications for the Persistent X-Ray Emission and Spin-down of the Soft Gamma Repeaters and Anomalous X-Ray Pulsars. *Astrophys. J.*, 574:332–355.

Treves, A., Turolla, R., Zane, S., and Colpi, M. (2000). Isolated Neutron Stars: Accretors and Coolers. *Publ. Astron. Soc. Pac.*, 112:297–314.

Tueller, J., Barbier, L., Barthelmy, S. D., Cummings, J., Fenimore, E., Gehrels, N., Krimm, H., Markwardt, C., Pagani, C., Palmer, D., Parsons, A., Sakamoto, T., Sato, G., Stamatikos, M., and Ukwatta, T. (2007). GRB 070610, Swift-BAT refined analysis. *GRB Coordinates Network*, 6491:1–+.

Ubertini, P., Lebrun, F., Di Cocco, G., Bazzano, A., Bird, A. J., Broenstad, K., Goldwurm, A., La Rosa, G., Labanti, C., Laurent, P., Mirabel, I. F., Quadrini, E. M., Ramsey, B., Reglero, V., Sabau, L., Sacco, B., Staubert, R., Vigroux, L., Weisskopf, M. C., and Zdziarski, A. A. (2003). IBIS: The Imager on-board INTEGRAL. *Astron. Astrophys.*, 411:L131–L139.

Uemura, M., Kato, T., Watanabe, T., Stubbings, R., Monard, B., and Kawai, N. (2002). The 1999 Optical Outburst of the Fast X-Ray Nova, V4641 Sagittarii. *Publ. Astron. Soc. Jpn.*, 54:95–101.

Usov, V. V. (1992). Millisecond pulsars with extremely strong magnetic fields as a cosmological source of gamma-ray bursts. *Nature*, 357:472–474.

van Breda, I. G. (1995). Monitoring of active galactic nuclei. In Bode, M. F., editor, *Robotic Observatories*, Wiley - Praxis Series in Astronomy and Astrophysics, pages 101–105. John Wiley & Sons.

van Paradijs, J., Groot, P. J., Galama, T., Kouveliotou, C., Strom, R. G., Telting, J., Rutten, R. G. M., Fishman, G. J., Meegan, C. A., Pettini, M., Tanvir, N., Bloom, J., Pedersen, H., Nørdgaard-Nielsen, H. U., Linden-Vørnle, M., Melnick, J., van der Steene, G., Bremer, M., Naber, R., Heise, J., in't Zand, J., Costa, E., Feroci, M., Piro, L., Frontera, F., Zavattini, G., Nicastro, L., Palazzi, E., Bennet, K., Hanlon, L., and Parmar, A. (1997). Transient optical emission from the error box of the γ-ray burst of 28 February 1997. *Nature*, 386:686.

van Paradijs, J., Taam, R. E., and van den Heuvel, E. P. J. (1995). On the nature of the 'anomalous' 6-s X-ray pulsars. *Astron. Astrophys.*, 299:L41+.

Vasisht, G., Kulkarni, S. R., Frail, D. A., and Greiner, J. (1994). Supernova remnant candidates for the soft gamma-ray repeater 1900+14. *Astrophys. J., Lett.*, 431:L35–L38.

Vedrenne, G., Roques, J.-P., Schönfelder, V., Mandrou, P., Lichti, G. G., von Kienlin, A., Cordier, B., Schanne, S., Knödlseder, J., Skinner, G., Jean, P., Sanchez, F., Caraveo, P., Teegarden, B., von Ballmoos, P., Bouchet, L., Paul, P., Matteson, J., Boggs, S., Wunderer, C., Leleux, P., Weidenspointner, G., Durouchoux, P., Diehl, R., Strong, A., Cassé, M., Clair, M. A., and André, Y. (2003). SPI: The spectrometer aboard INTEGRAL. *Astron. Astrophys.*, 411:L63–L70.

Vestrand, W. T., Borozdin, K. N., Brumby, S. P., Casperson, D. E., Fenimore, E. E., Galassi, M. C., McGowan, K., Perkins, S. J., Priedhorsky, W. C., Starr, D., White, R., Wozniak, P., and Wren, J. A. (2002). The RAPTOR experiment: a system for monitoring the optical sky in real time. In Kibrick, R. I., editor, *Advanced Global Communications Technologies for Astronomy II*, volume 4845 of *Presented at the Society of Photo-Optical Instrumentation Engineers (SPIE) Conference*, pages 126–136.

Vestrand, W. T., Theiler, J., and Woznia, P. R. (2004). Unsolved problems in observational astronomy. II. Focus on rapid response - mining the sky with "thinking" telescopes. *Astronomische Nachrichten*, 325:477–482.

Vestrand, W. T., Wozniak, P. R., Wren, J. A., Fenimore, E. E., Sakamoto, T., White, R. R., Casperson, D., Davis, H., Evans, S., Galassi, M., McGowan, K. E., Schier, J. A., Asa, J. W., Barthelmy, S. D., Cummings, J. R., Gehrels, N., Hullinger, D., Krimm, H. A., Markwardt, C. B., McLean, K., Palmer, D., Parsons, A., and Tueller, J. (2005). A link between prompt optical and prompt γ-ray emission in γ-ray bursts. *Nature*, 435:178–180.

Vestrand, W. T., Wren, J. A., Wozniak, P. R., Aptekar, R., Golentskii, S., Pal'Shin, V., Sakamoto, T., White, R. R., Evans, S., Casperson, D., and Fenimore, E. (2006). Energy input and response from prompt and early optical afterglow emission in γ-ray bursts. *Nature*, 442:172–175.

Villasenor, J. N., Dill, R., Doty, J. P., Monnelly, G., Vanderspek, R., Kissel, S., Prigozhin, G., Crew, G. B., and Ricker, G. R. (2003). An Overview of the HETE Soft X-ray Camera. In Ricker, G. R. and Vanderspek, R. K., editors, *Gamma-Ray Burst and Afterglow Astronomy 2001: A Workshop Celebrating the First Year of the HETE Mission*, volume 662 of *American Institute of Physics Conference Series*, pages 33–37.

Wang, X. and Loeb, A. (2000). Variability of Gamma-Ray Burst Afterglows due to Interstellar Turbulence. *Astrophys. J.*, 535:788–797.

Wei, D. M., Yan, T., and Fan, Y. Z. (2006). The Optical Flare and Afterglow Light Curve of GRB 050904 at Redshift z=6.29. *Astrophys. J., Lett.*, 636:L69–L72.

White, R. R., Allan, A., Barthelmy, S., Bloom, J., Graham, M., Hessman, F. V., Marka, S., Rots, A., Scholberg, K., Seaman, R., Stoughton, C., Vestrand, W. T., Williams, R., and Wozniak, P. R. (2006). Astronomical network event and observation notification. *Astronomische Nachrichten*, 327:775–+.

Williams, R. J. and Mulherin, J. (2001). The Development of Advanced-Technology Automated/Robotic Telescope Systems and the Future of Small-Telescope Astronomy. In Paczynski, B., Chen, W.-P., and Lemme, C., editors, *IAU Colloq. 183: Small Telescope Astronomy on Global Scales*, volume 246 of *Astronomical Society of the Pacific Conference Series*, page 95.

Willingale, R., O'Brien, P. T., Osborne, J. P., Godet, O., Page, K. L., Goad, M. R., Burrows, D. N., Zhang, B., Rol, E., Gehrels, N., and Chincarini, G. (2007). Testing the Standard Fireball Model of Gamma-Ray Bursts Using Late X-Ray Afterglows Measured by Swift. *Astrophys. J.*, 662:1093–1110.

Winkler, C., Courvoisier, T. J.-L., Di Cocco, G., Gehrels, N., Giménez, A., Grebenev, S., Hermsen, W., Mas-Hesse, J. M., Lebrun, F., Lund, N., Palumbo, G. G. C., Paul, J., Roques, J.-P., Schnopper, H., Schönfelder, V., Sunyaev, R., Teegarden, B., Ubertini, P., Vedrenne, G., and Dean, A. J. (2003). The INTEGRAL mission. *Astron. Astrophys.*, 411:L1–L6.

Woltjer, L. (1964). X-Rays and Type i Supernova Remnants. *Astrophys. J.*, 140:1309–1313.

Woods, P. M., Kouveliotou, C., van Paradijs, J., Briggs, M. S., Hurley, K., Göğüş, E., Preece, R. D., Giblin, T. W., Thompson, C., and Duncan, R. C. (1999a). Hard Burst Emission from the Soft Gamma Repeater SGR 1900+14. *Astrophys. J., Lett.*, 527:L47–L50.

Woods, P. M., Kouveliotou, C., van Paradijs, J., Hurley, K., Kippen, R. M., Finger, M. H., Briggs, M. S., Dieters, S., and Fishman, G. J. (1999b). Discovery of a New Soft Gamma Repeater, SGR 1627-41. *Astrophys. J., Lett.*, 519:L139–L142.

Woosley, S. E. (1993). Gamma-ray bursts from stellar mass accretion disks around black holes. *Astrophys. J.*, 405:273–277.

Woosley, S. E. and Wallace, R. K. (1982). The thermonuclear model for gamma-ray bursts. *Astrophys. J.*, 258:716–732.

Woźniak, P. R., Vestrand, W. T., Wren, J. A., White, R. R., Evans, S. M., and Casperson, D. (2006). RAPTOR Observations of Delayed Explosive Activity in the High-Redshift Gamma-Ray Burst GRB 060206. *Astrophys. J., Lett.*, 642:L99–L102.

Wu, X. F., Dai, Z. G., Huang, Y. F., and Lu, T. (2003). Optical flashes and very early afterglows in wind environments. *Mon. Not. R. Astron. Soc.*, 342:1131–1138.

Yi, T., Liang, E., Qin, Y., and Lu, R. (2006). On the spectral lags of the short gamma-ray bursts. *Mon. Not. R. Astron. Soc.*, 367:1751.

Yost, S. A., Yuan, F., Swan, H., and Akerlof, C. (2006). GRB 060111B: ROTSE-III Detection of Optical Counterpart Flare. *GRB Coordinates Network*, 4488.

Zhang, B., Fan, Y. Z., Dyks, J., Kobayashi, S., Mészáros, P., Burrows, D. N., Nousek, J. A., and Gehrels, N. (2006). Physical Processes Shaping Gamma-Ray Burst X-Ray Afterglow Light Curves: Theoretical Implications from the Swift X-Ray Telescope Observations. *Astrophys. J.*, 642:354–370.

Zhang, B. and Mészáros, P. (2002). Gamma-Ray Bursts with Continuous Energy Injection and Their Afterglow Signature. *Astrophys. J.*, 566:712–722.

Zhang, B. and Mészáros, P. (2004). Gamma-Ray Bursts: progress, problems and prospects. *International Journal of Modern Physics A*, 19:2385–2472.

Zhang, B.-B., Liang, E.-W., and Zhang, B. (2007). A Comprehensive Analysis of Swift XRT Data. I. Apparent Spectral Evolution of Gamma-Ray Burst X-Ray Tails. *Astrophys. J.*, 666:1002–1011.